Mixtures of ultracold gases: Fermi sea and Bose-Einstein condensate of Lithium isotopes

Florian Schreck

To cite this version:

Florian Schreck. Mixtures of ultracold gases: Fermi sea and Bose-Einstein condensate of Lithium isotopes. Atomic Physics [physics.atom-ph]. Université Pierre et Marie Curie - Paris VI, 2002. English. NNT : . tel-00001340v2

HAL Id: tel-00001340

https://theses.hal.science/tel-00001340v2

Submitted on 17 May 2002

HAL is a multi-disciplinary open access archive for the deposit and dissemination of scientific research documents, whether they are published or not. The documents may come from teaching and research institutions in France or abroad, or from public or private research centers.

L'archive ouverte pluridisciplinaire **HAL**, est destinée au dépôt et à la diffusion de documents scientifiques de niveau recherche, publiés ou non, émanant des établissements d'enseignement et de recherche français ou étrangers, des laboratoires publics ou privés.

PHYSICS DEPARTMENT OF THE
ÉCOLE NORMALE SUPÉRIEURE

LABORATOIRE KASTLER BROSSEL

DOCTORAL THESIS OF THE UNIVERSITÉ PARIS VI
speciality : quantum physics

presented by
Florian SCHRECK

to obtain the title
Docteur de l'Université Paris VI

Subject of the thesis :

MIXTURES OF ULTRACOLD GASES: FERMI SEA AND BOSE-EINSTEIN CONDENSATE OF LITHIUM ISOTOPES
-
MELANGES DE GAZ ULTRAFROIDS: MER DE FERMI ET CONDENSAT DE BOSE-EINSTEIN DES ISOTOPES DU LITHIUM

Defended the 21 january 2002 in front of the jury consisting of :

M.	A. ASPECT	Rapporteur
M.	R. GRIMM	Rapporteur
M.	C. COHEN-TANNOUDJI	Président
M.	G. SHLYAPNIKOV	Examinateur
M.	R. COMBESCOT	Examinateur
M.	C. SALOMON	Directeur de thèse

To my friends.

Contents

Introduction

All particles, elementary particles as well as composite particles such as atoms, belong to one of two possible classes: they are either fermions or bosons. Which class a particle belongs to is determined by its spin. If the spin is an odd multiple of $\hbar/2$, the particle is a fermion. For even multiples it is a boson. Examples of fermions are electrons or ^{6}Li atoms. ^{7}Li and photons are bosons. The quantum properties of a particle are influenced by its bosonic or fermionic nature. For a system of identical particles the many particle wavefunction must be symmetric under the exchange of two particles for bosons and anti-symmetric under the exchange of two particles for fermions. A direct consequence of this (anti-)symmetrization postulate is that it is impossible for fermions to occupy the same quantum state. This is called the Pauli exclusion principle. No process can add a fermion to an already occupied state. The process is inhibited by *Pauli blocking*. For bosons it is favorable to occupy the same state and the more bosons that are already in this state, the higher the probability that another boson is transferred to it. This property is called Bose enhancement.

Bose enhancement leads to a phase transition at high phase-space densities, corresponding to low temperatures and/or high densities. When the phase-space density is increased past a certain critical value, the occupation of the ground-state rapidly becomes macroscopic. This effect, called Bose-Einstein condensation was predicted in 1924 by S. Bose and A. Einstein [1, 2, 3]. In cold atom experiments, the temperature of a harmonically trapped, weakly interacting gas is lowered until the phase transition occurs at a critical temperature T_C

$$T_C = \frac{\hbar\bar{\omega}}{k_B}\left(\frac{N}{1.202}\right)^{1/3}, \tag{1}$$

where $\bar{\omega}$ is the geometrical mean of the trap oscillation frequencies, k_B the Boltzmann constant and N the number of trapped atoms. Below this temperature a macroscopic fraction of the atoms occupy the ground state of the trap [4]. The behavior of each of these atoms can be described by the same wavefunction. Thus a gas under these conditions is called a degenerate gas. The atoms in the ground state are called the Bose-Einstein condensate (in the following called *condensate* or BEC). Atoms in higher energy levels belong to what is termed the thermal cloud. For temperatures below the temperature corresponding to the harmonic oscillator energy level splitting $T_{\bar{\omega}} = \hbar\bar{\omega}/k_B$, even a classical gas would occupy the ground state macroscopically. But the critical temperature can be much higher than this temperature ($T_c > T_{\bar{\omega}}$). Therefore the phenomenon is not a classical one.

The first experiments involving Bose-Einstein condensates were performed with liquid ^{4}He [5]. Below 2 K, the liquid becomes superfluid. Low-temperature superconductivity can be explained similarly by the condensation of paired electrons [6]. In these liquid and solid systems the bosons interact strongly with their neighbors, making a theoretical description much more complicated than Einstein's first work. In 1995 the group of C. Wieman and E. Cornell at JILA and the group of W. Ketterle at MIT succeeded in producing condensates of ultracold dilute rubidium and sodium gases [7, 8]. In 2001 they received the Nobel prize for their work. The interaction between the atoms gives rise to a mean field energy which depends on the scattering length and the density of the gas. This energy can easily be included in the theoretical description of the gas [9, 10]. The mean field gives rise to interesting phenomena. For positive scattering length, the condensate becomes bigger than the ground state wave function of the gas. For negative scattering length, a density larger than a critical value can provoke collapse of the gas [11, 12]. Since the production of the first condensates, a tremendous variety of experiments have been performed, testing different aspects of the physics of Bose-Einstein condensation. A few of the most important ones are briefly mentioned in the following. Initial studies investigated the properties of the phase transition, the influence of the mean field on the shape of the wavefunction, and its free expansion after release from a trap [13, 14]. Interference experiments showed the phase coherence of the condensate [15]. A coherent atomic beam, called the atom laser, was produced by quasi-continuously releasing atoms from the trapped condensate [16, 17]. The frequency and damping of vibrational excitations such as the quadrupole mode or the scissors mode (a response to a sudden change in an axis of the trap) were measured [18, 19]. The interaction of condensates with light were used to construct interferometers or matter wave amplifiers [20, 21]. The existence of a critical velocity, typical for superfluidity, was found [22]. Spinor mixtures of condensates were studied [23, 24]. Dark solitons, vortices and vortice lattices were generated and studied [25, 26, 27, 28, 29, 30]. Recently, condensates restricted to lower dimensions and in optical lattices have been studied [31, 32, 33]. Another research direction is to simplify the method of production of condensates, which led to condensation in an optical trap [34] or in microtraps [35, 36]. Condensates have the possibility to improve high precision measurements; some groups are testing interferometers to this end [37]. Today more than 30 research groups have produced condensates in hydrogen, metastable helium, lithium, sodium, potassium and most often in rubidium [7, 38, 39, 40, 41, 42, 43, 44, 45]. Several machines capable of producing condensates are under construction. This research field will certainly be fascinating for several years to come.

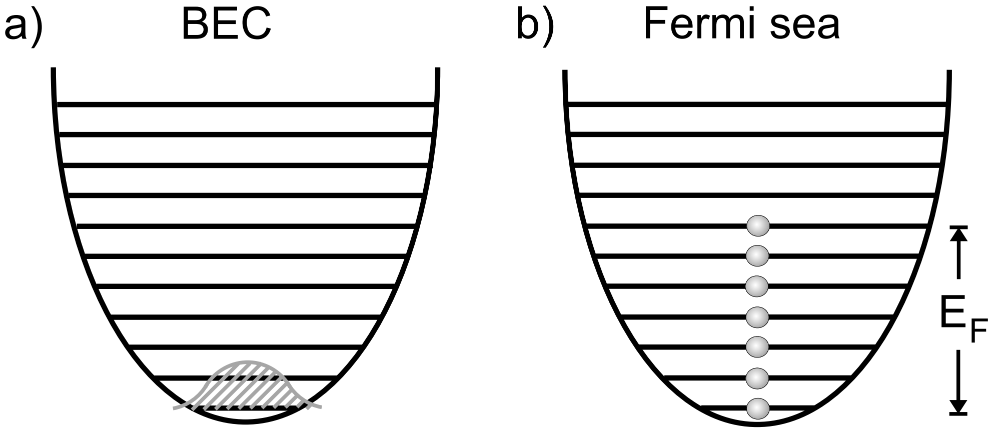

Figure 1: *Comparison of a Bose-Einstein condensate with a Fermi sea, both at zero temperature and trapped in a harmonic potential. a) All bosons occupy the ground state wave function of the potential. b) The fermions fill up in the lowest energy states up to the Fermi energy* E_F.

Fermionic systems behave in a radically different manner from bosonic systems (see figure 1). At zero temperature the fermions fill up the lowest energy states of the system, since only one fermion can occupy each state. This situation is called a degenerate Fermi gas or a *Fermi sea*. It was first described theoretically in 1926 by E. Fermi [46, 47]. The energy of the highest occupied state is the Fermi energy E_F. All states above this energy are empty. At finite temperature this rectangular energy distribution is smeared out around the Fermi energy with a characteristic width of the order of $k_B T$. In order to be significantly different from a classical distribution, the temperature must be lower than the Fermi temperature $T_F = E_F/k_B$. The degeneracy parameter T/T_F is a measure for the deviation from a classical distribution. For a harmonically trapped gas the Fermi temperature is

$$T_F = \frac{\hbar\bar{\omega}}{k_B}(6N)^{1/3}\,, \tag{2}$$

a factor 1.7 higher than the critical temperature for a bosonic gas under the same conditions [48]. No phase transition between the classical and the quantum degenerate regime occurs. By decreasing T/T_F the system transitions smoothly from classical to non-classical behavior.

Degenerate fermionic systems are very common in nature. Examples are electrons in metals or atoms, neutron stars, and liquid ^{3}He. Many properties of these systems are governed by the Pauli exclusion principle. Its effect in neutron stars, called Fermi pressure, counterbalances attractive gravitational forces and stabilizes the star. It guarantees the stability of atoms and requires that only two electrons with opposing spin can occupy each orbit. An intriguing phenomenon in degenerate Fermi systems is the Bardeen-Cooper-Schrieffer (BCS) transition [49, 50]. Here two fermions are coupled by an attractive interaction. The pair of fermions, called a Cooper pair, behaves like a boson, since its spin is a multiple of $\hbar$. Thus Cooper pairs can Bose condense and form a superfluid phase in a degenerate Fermi gas. This is the basis of low temperature superconductivity in metals and superfluid ^{3}He. Metals and ^{3}He have been extensively studied, but the systems are complicated because of the strong interaction between the fermions.

Creating a degenerate Fermi gas in a dilute atomic vapor opens new possibilities. In comparison with ^{3}He or metals it is much easier to change the environment in which the fermions reside. The properties of the Fermi sea can be observed in a more direct, visual way. Because of the diluteness of the gas, a theoretical description is easier. The interaction between the atoms can often be approximated by a mean field. The fermionic properties of the gas influence not only the experimental results, but also the cooling method with which a degenerate gas is produced. Up to now the only known cooling method, capable of producing degenerate gases is evaporative cooling. It cools by removing the atoms with the highest energy from a trapped sample. Elastic collisions thermalize the gas and produce again new high energetic atoms that can be removed. A problem occurs when applying this cooling scheme to fermions. Because of the requirement of anti-symmetry for the many particle wave function, collisions with zero angular momentum are forbidden. Only these kind of collisions can take place at very low temperatures. This means that particles in a gas of identical fermions do not collide with each other at low temperatures. This makes evaporative cooling impossible.

The solution to this problem is to cool a mixture of distinguishable particles. Then the anti-symmetrization of the wave function is not required and the atoms can collide even at low temperatures. This cooling scheme is called sympathetic cooling and was first proposed for two-component plasmas [51]. It was often used for cooling ions confined in electromagnetic traps [52, 53]. Neutral atoms and molecules have been cooled *via* cryogenically cooled Helium [54, 55, 56]. Sympathetic cooling using ^{87}Rb atoms in two different internal states has led to the production of two overlapping condensates [57, 58, 59]. For fermions, the s-wave scattering limitation was overcome by using two distinct Zeeman substates, both of which were evaporatively cooled. D. Jin's group used this method in 1999 to reach temperatures on the order of $\sim 300\,\mathrm{nK} \sim 0.4\,T_F$ in a gas of ^{40}K atoms [60]. In our experiment, we use sympathetic cooling of ^{6}Li fermions *via* collisions with evaporatively cooled ^{7}Li bosons and reach temperatures of $\sim 1\,\mu\mathrm{K} \sim 0.2(1)\,T_F$, which are among the best reached worldwide. The same approach was chosen by the group of R. Hulet, achieving similar results [61]. One of the main differences between the lithium and the potassium experiments is the following. The potassium experiment uses two Fermi gases to provide elastic collisions. In this way, two degenerate Fermi gases are produced together. We used a bosonic and a fermionic component and produced a condensate immersed in a Fermi sea. This has important consequences for the efficiency of the cooling process in the regime of quantum degeneracy. In this regime most of the lowest energy states are occupied. Because of Pauli blocking this reduces the number of possible final states after a collision and thus the number of possible collisions. By using two Fermi gases, the Pauli blocking occurs twice. Using a Fermi and a Bose gas, it acts only once, which is unavoidable since one degenerate Fermi gas is the goal of the experiment. Thus, sympathetic cooling should work better for a boson-fermion mixture.

During the last year new experiments using sympathetic cooling have been successful. ^{85}Rb was cooled by ^{87}Rb [58], Potassium condensed by sympathetic cooling with Rubidium [43] and ^{7}Li was cooled by ^{133}Cs in an optical trap [62]. Fermionic ^{6}Li was cooled to degeneracy by ^{23}Na [63] or by mixing two different states in an optical trap [64].

Interesting experiments can now be performed with these degenerate Fermi gases. First of all the degeneracy of the Fermi gas must be shown. One method is to observe the slight change in the spatial distribution between a classical and a degenerate gas. We can also compare the behavior of fermions and bosons, in the case that both species coexist, as in our experiments. The size of a harmonically trapped degenerate Fermi gas is determined by its Fermi energy, as a result of Fermi pressure. The size of a non-degenerate Bose gas by contrast is determined by its temperature. When both gases are in thermal equilibrium the difference in size gives a measure for the fermionic degeneracy T/T_F. A study of this effect is presented in the result section (3.3.4). Other experiments can be performed to detect the effects of Pauli blocking on scattering of atoms or light. The suppression of collisions described above can be detected and even used to determine the temperature and degeneracy of the Fermi gas [65, 66]. The same mechanism modifies the scattering of light off a degenerate Fermi gas, resulting in a reduction of the line width of the atomic transition and a change in the spatial distribution of scattered light [67, 68, 69]. One of the most fascinating effects to be observed would be a BCS transition. For this a degenerate Fermi gas with attractive interaction between the fermions must be prepared. To do this, we can prepare atoms in our experiment in two different hyperfine states and use a *Feshbach-resonance* to tune the interaction due to elastic collisions to the desired value [70]. One of the open questions is if it is experimentally possible to reach conditions under which the phase transition occurs. Predictions for the BCS transition temperature T_{BCS} range from $T_{BCS}/T_F = 0.025$ to $T_{BCS}/T_F = 0.4$ [71, 72]. Trying to reach the BCS phase transition is one of the main motivations for our work.

Because of the boson-fermion mixture we choose for sympathetic cooling, we also have the possibility to study degenerate Bose gases of ^{7}Li. This atom has interesting scattering properties (see figure 2). In the $|F = 2, m_F = 2\rangle$ state, the scattering length is negative: $a = -27\,a_0$ (where $a_0 = 0.53 \times 10^{-10}$ m is the Bohr radius). Because of this the condensate collapses, if the number of condensed atoms is higher than a critical number. The scattering length of the $|F = 1, m_F = -1\rangle$ state is positive and small: $a = +5.1\,a_0$ [73]. We have used this to produce condensates which do not collapse for any number of atoms, which is new for Lithium. In our very elongated trapping potential, the mean field energy does not change the shape of the wavefunction in the radial directions, which thus stays. This situation is called a quasi-one-dimensional condensate. Furthermore a Feshbach resonance exists in the $|F = 1, m_F = 1\rangle$ state, which made it possible to produce a condensate with tunable scattering length in an optical trap. This in turn was used to produce bright solitons. To this end, a trap which harmonically confined the condensate in the radial directions only was used. The confinement in the axial direction was provided by the attractive mean field, resulting from a slightly negative scattering length. Also the regime of large positive scattering length is interesting. When the scattering length becomes bigger than the harmonic oscillator ground state, the scattering cross section is modified [74].

Mixtures of degenerate fermionic and bosonic gases are also of interest. We have used a mixture of Lithium isotopes not only to perform sympathetic cooling, but also to determine the degree of degeneracy of the Fermi sea and to measure the collision cross section between the two species. In the future the interaction of the two gases due to the mean field might be observable as a spatial phase separation [75].

Several types of evaporative and sympathetic cooling schemes have been employed during this work, first in a magnetic trap, and later in an optical dipole trap. A magnetic trap confines atoms in a magnetic field minimum. Only states which have an energy which increases with the magnetic field can be trapped. By contrast, an optical trap can trap all states. The first series of experiments was performed in a magnetic trap using the stretched hyperfine states ^{7}Li $|F = 2, m_F = 2\rangle$ and ^{6}Li $|F = 3/2, m_F = 3/2\rangle$ (see figure 2). Here the ^{7}Li and the inter-isotope scattering lengths are relatively high ($-27\,a_0$ and $40\,a_0$, respectively) and enable evaporative and sympathetic cooling. In addition, both states can be trapped up to arbitrary energies in a magnetic field minimum. In these experiments, a degenerate Fermi gas together with

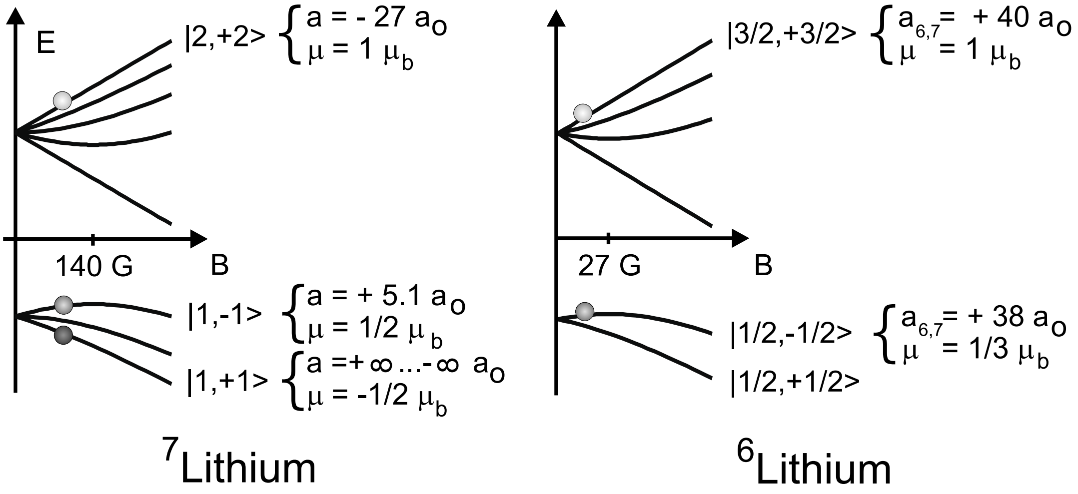

Figure 2: *Energy levels of* ^{7}*Li and* ^{6}*Li ground states in a magnetic field. Relevant scattering lengths, a, and magnetic moments,* μ*, are given.* μ_b *is the Bohr magneton and* $a_0 = 0.53 \times 10^{-10}$ *m the Bohr radius. The* $|1,-1\rangle$ *state (resp.* $|1/2,-1/2\rangle$*) is only trapped in fields weaker than 140 Gauss (resp. 27 Gauss). Light balls: states used in first sympathetic cooling stage, the condensate becomes unstable for too high atom numbers; dark balls: states used in second cooling stage, enabling the production of a condensate stable for any number of atoms. Black ball: state used for evaporation in the optical trap, resulting in a condensate with tunable scattering length and a bright soliton due to a Feshbach resonance.*

a non-degenerate Bose gas was produced and Fermi pressure was visible by comparing the spatial extension of the two clouds.

The next series of experiments was performed in the lower hyperfine states ^{7}Li $|F = 1, m_F = -1\rangle$ and ^{6}Li $|F = 1/2, m_F = -1/2\rangle$, still in a magnetic trap. The advantage of these states is that the ^{7}Li scattering length is positive. But it is impossible to start evaporative cooling in these states, because the maximum trap depth is $k_B \times 2.4\,$mK for ^{7}Li and $k_B \times 330\,\mu$K for ^{6}Li, which is insufficient to confine the gas before evaporative cooling which has a temperature of $> 3\,$mK. Thus it is necessary to cool the gas first in the higher hyperfine states and then transfer the atoms to the lower hyperfine states. The ^{7}Li $|F = 1, m_F = -1\rangle$ scattering length is positive but five times smaller in magnitude than in the $|F = 2, m_F = 2\rangle$ state. This makes evaporative cooling in the lower state impossible. We circumvent this problem by using the inter-isotope collisions to thermalize the gas during evaporative cooling. In this manner a condensate, stable with 10^4 atoms, immersed in a Fermi sea was produced. This is new in ultracold atomic gases. Before, mixtures of bosonic and fermionic degenerate gases existed only in mixtures of liquid ^{3}He with ^{4}He.

After precooling in the higher states to $\sim 10\,\mu$K we can transfer the atoms to an optical trap. Here all states can be trapped. We can transfer the atoms to the $|F = 1, m_F = 1\rangle$ state, for example, for which the scattering length can be tuned by using a Feshbach resonance. By using a scattering length of $\sim 40\,a_0$ we performed evaporative cooling by lowering the depth of the optical trap. In this way we produced a condensate with a tunable scattering length. We chose a scattering length of $\sim -4\,a_0$ and released the cloud in the axial direction. The gas remained confined by its mean field attraction. It slid axially, guided by the radial confinement while maintaining its form. This was the first matter wave soliton ever created.

The presentation of my thesis is divided into three chapters. In the first chapter, I introduce some theoretical background on degenerate fermionic (1.1.2) and bosonic (1.1.6) gases and their mixtures (1.1.13). I discuss evaporative and sympathetic cooling (1.2) and the physics of elastic collisions (1.3). The second chapter is dedicated to the description of the experimental setup. As introduction, it also contains a discussion of the properties of lithium (2.2) and other approaches to producing a degenerate Fermi gas (2.3). The third chapter presents our experimental results. In the first section I discuss the experimental steps that prepare a gas sample for evaporative cooling (3.1). In three sections the results of experiments in the higher (3.3) and lower (3.4) hyperfine states and in the optical trap (3.6) are presented.

Chapter 1

Theory

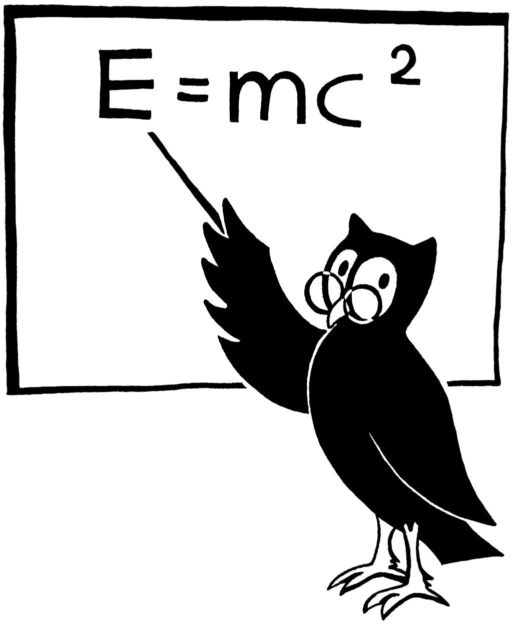

In this chapter some of the theory related to our experiment is introduced. It is divided into three parts. In the first section, properties of fermionic and bosonic gases relevant for the experiment are presented. The next section explains the principle and behavior of evaporative and sympathetic cooling, the cooling methods used to produce degenerate quantum gases. Since these methods rely on elastic collisions the third section is dedicated to this topic. Special attention is payed to the possibility of tuning the scattering length by applying a magnetic field and to the suppression of scattering under certain conditions for ^{7}Li.

1.1 Theory of quantum gases

Every particle falls into one of two categories: if its spin is $\hbar/2$ it is called a fermion; if it is $\hbar$ it is called a boson. This is as true of composite particles such as atoms as it is of elementary particles like electrons. The quantum mechanical properties of both classes are very different: the many-particle wavefunction of identical fermions must be anti-symmetric under the exchange of two particles, while the bosonic wavefunctionmust be symmetric. For fermions, this leads to the Pauli exclusion principle: two fermions may never occupy the same quantum state. This can be seen in the following way. Let ϕ, χ be single particle wavefunctions. Two identical particles in these states are described by $\Psi_{1,2}^{+/-} = (\phi_1\chi_2 \pm \phi_2\chi_1)/\sqrt{2}$. The +(-) makes the wavefunction symmetric (anti-symmetric) and describes bosons (fermions). The wavefunction $\Psi_{1,2}^{-}$ describing two fermions in the same state $\phi = \chi$ vanishes: $\Psi_{1,2}^{-} = (\chi_1\chi_2 - \chi_2\chi_1)/\sqrt{2} = 0$ and is thus unphysical. Two fermions can not occupy the same state. The link between the spin and the statistics of a particle is the spin-statistics theorem, which can be derived using relativistic quantum mechanics.

The statistical and the scattering properties are dominated by this (anti-) symmetrization requirement. At zero temperature, trapped fermions occupy, one by one, the lowest energy states, forming a Fermi sea, whereas (non-interacting) bosons are condensed in the lowest state as a Bose-Einstein condensate (see figure 1). The scattering of distinguishable particles is possible in all angular momentum orders. But only the even angular momentum orders (s,d,...), which correspond to symmetric wavefunctions are permitted for identical bosons. Only odd orders (p,f,...), corresponding to anti-symmetric wavefunctions, are permitted for fermions. In the following, the properties of fermionic and bosonic gases relevant for the described experiment such as density distributions, heat capacities etc. are briefly derived. For a more detailed description see [76].

1.1.1 Properties of a classical gas

Before describing the properties of gases of identical particles, we will briefly recall the properties of a gas of distinguishable particles, for which (anti-) symmetrization of the wavefunction is not required. In the limit of low phase-space densities, a fermionic gas, a bosonic gas and a gas of distinguishable particles all behave in the same manner. This limit is called a classical gas. We consider N non-interacting particles with mass m trapped in a cylindrical harmonic potential with trapping frequencies ω_{rad} radially and $\omega_{ax} = \lambda\omega_{rad}$ axially. The energy distribution is the Boltzmann distribution

$$f(\epsilon, T, C) = Ce^{-\beta\epsilon}, \tag{1.1}$$

where $\beta = 1/k_B T$, k_B the Boltzmann constant and C a normalization constant. The hamiltonian describing the gas is

$$H(\overrightarrow{r}, \overrightarrow{k}) = \frac{\hbar^2 \overrightarrow{k}^2}{2m} + \frac{m\omega_{rad}^2}{2}\rho^2 \quad ; \quad \rho = (x^2 + y^2 + \lambda^2 z^2)^{1/2} \,. \tag{1.2}$$

The constant C is determined using the normalization

$$N = \int dr^3 dk^3\, f(\epsilon = H(\overrightarrow{r}, \overrightarrow{k}), T, C) \tag{1.3}$$

and yields $C = N\lambda/(2\pi)^3\sigma_x^3\sigma_k^3$ with $\sigma_x = \sqrt{k_B T/m\omega_{rad}^2}$ and $\sigma_k = \sqrt{2\pi}/\lambda_{dB}$ where $\lambda_{dB} = h/\sqrt{2\pi m k_B T}$ is the de Broglie wavelength. The distribution in momentum and in real space decouple and are both gaussian:

$$f(\overrightarrow{r}, \overrightarrow{k}, T) = \frac{N\lambda}{(2\pi)^3\sigma_x^3\sigma_k^3} \exp\left(-\beta\frac{\hbar^2 \overrightarrow{k}^2}{2m}\right) \exp\left(-\beta\frac{m\omega_{rad}^2}{2}\rho^2\right) . \tag{1.4}$$

The momentum distribution is isotropic with the RMS size $\sigma_p = \hbar\sigma_k$. The spatial distribution follows the anisotropy of the trap and has the RMS size $\sigma_i = \sqrt{k_B T/m\omega_i^2}$. For $\omega_{rad} > \omega_{ax}$ the gas is distributed in a cigar shape and has the aspect ratio λ.

A property which is very important for sympathetic cooling (see section 1.2.2) is the specific heat capacity of the gas. It is defined as $C_F \equiv \frac{\partial E}{\partial T}\big|_N$ and is a measure for the amount of energy that must be dissipated, to cool the sample by ΔT. The heat capacity of a classical gas is $C_{cl} = 3Nk_B$ [76].

1.1.2 Properties of a fermionic gas

Now we will discuss the properties of N identical non-interacting fermions with mass m trapped as above in a cylindrical harmonic potential with trapping frequencies ω_{rad} radially and $\omega_{ax} = \lambda\omega_{rad}$ axially. At zero temperature, fermions occupy one by one the N lowest lying energy states due to the Pauli principle. The energy of the highest occupied state is called the Fermi energy E_F. This energy, together with the energy corresponding to the temperature $k_B T$ and the two oscillator energies $\hbar\omega_{rad}$ and $\hbar\omega_{ax}$ are the four energy scales of the system. In the following we will always assume $k_B T$ and $E_F \gg \hbar\omega_{rad}, \hbar\omega_{ax}$. Then the energy distribution has no structure on the scale of the energy level splitting and effects due to the discreteness of the energy level spectrum are negligible. Thus we are left with two energy scales E_F and T. We may define a parameter T/T_F called the degeneracy parameter, with $T_F = E_F/k_B$ being the Fermi temperature.

In the case $T/T_F \gg 1$ the occupation probability of the quantum states is low and thus it is very improbable that two particles occupy the same state, independent of the particle statistic. Thus a Fermi gas will behave classically.

We are here more interested in the case $T/T_F < 1$, in which case the gas is called degenerate. This term is used in analogy with the degenerate Bose gas, but without the notion of having all the atoms in the same energy level, a notion that is normally associated with the word degenerate. For a classical or bosonic gas at low temperature, the probability to find several particles in the lowest states is high. This is forbidden for fermions and thus the properties of the fermionic degenerate gas are nonclassical and differ also from the bosonic case. The shape of the cloud is no longer gaussian. Its characteristic size is given by the Fermi radius R_F which corresponds to the maximum distance from the trap center, that a particle with energy E_F can reach in the radial direction

$$R_F \equiv \sqrt{\frac{2E_F}{m\omega_{rad}^2}}\,. \tag{1.5}$$

This size exceeds the size of a classical gas, which means that by cooling a gas from the classical to the degenerate regime, its size will stop shrinking when degeneracy is reached. This is the effect of the Fermi pressure, a direct consequence of the Pauli exclusion principle. Its observation is one of the main results of this work. The momentum distribution is position dependent and the heat capacity is reduced in comparison to a classical gas.

In the following the discussed properties will be exactly derived in the case of zero temperature and finite temperature results are cited. The complete treatment and a discussion of the approximations applied may be found in the useful article by Butts and Rokhsar [77].

Energy distribution

From the Pauli principle it is easy to derive the energy distribution of fermions, the Fermi-Dirac distribution

$$f(\epsilon) = \frac{1}{e^{\beta(\epsilon-\mu)}+1}\,, \tag{1.6}$$

where μ is the chemical potential (see *e.g.* [76]). The latter is determined by the normalization condition

$$N = \int d\epsilon\, f(\epsilon) g(\epsilon)\,, \tag{1.7}$$

where $g(\epsilon)$ is the density of energy states which, for a harmonic potential, is $g(\epsilon) = \epsilon^2/(2\lambda(\hbar\omega_{rad})^3)$. The Fermi-Dirac distribution never exceeds 1, reflecting the Pauli exclusion principle. At zero temperature the energy distribution $f(\epsilon) = 1$ below the Fermi energy $E_F \equiv \mu(T = 0, N)$ and 0 above. For lower degeneracies, this step function is smeared out around E_F with a width of the order of $E_F\,T/T_F$ (figure 1.1a).

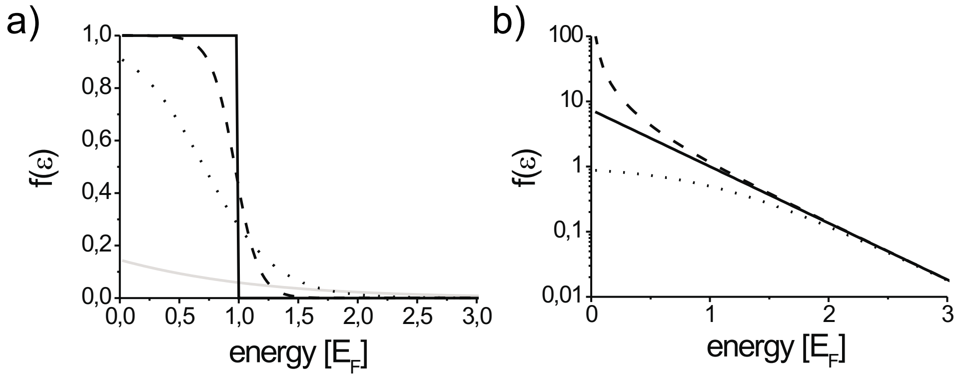

Figure 1.1: *Behavior of the Fermi-Dirac energy distribution. a) Dependence on the degeneracy:* $T/T_F = 0$, 0.1, 0.3, 1 *(solid, dashed, dotted, gray, calculated for 3D harmonic potential). The step-function for* $T/T_F = 0$ *is smeared out around* E_F *with lowering degeneracy and approaches a classical distribution. b) Comparison of a Fermi-Dirac distribution for* $T/T_F = 0.5$ *(dotted) with a classical distribution (solid) and a Bose-Einstein distribution (dashed) having the same asymptotic behavior.*

For high temperatures or energies higher than the Fermi energy, $f(\epsilon)$ can be approximated by the classical Boltzmann distribution, $f(\epsilon) = e^{-\beta(\epsilon-\mu)}$. The same is true for the bosonic energy distribution function (see 1.1.6). The three distribution functions are compared in figure 1.1b). This behavior leads to a simple detection scheme for quantum degeneracy. A classical gaussian distribution is fitted to the high energy part of the spatial or momentum distribution and to the whole distribution. For quantum degenerate gases the resulting width differ, in contrast to a classical gas (see section 1.1.5 and figure 3.20).

By integrating equation (1.7) for $T = 0$ the Fermi energy is found to be

$$E_F = \hbar\omega_{rad}(6N\lambda)^{1/3}\,. \tag{1.8}$$

To obtain a high Fermi energy it is necessary to use a strongly confining trap and to cool a large number of atoms. The Fermi energy corresponds to a wave number

$$k_F \equiv \sqrt{\frac{2mE_F}{\hbar^2}} = (48N\lambda)^{1/6}\sigma_r^{-1}\,, \tag{1.9}$$

with $\sigma_r = \sqrt{\hbar/(m\omega_{rad})}$ the radial width of the gaussian ground state of the trap. $\hbar k_F$ is the maximum momentum reached in the Fermi gas.

Spatial and momentum distribution

To derive the spatial and momentum distributions it is convenient to apply the semiclassical, also called the Thomas-Fermi, approximation. Particles are distributed in phase-space according to the Fermi-Dirac distribution. The density of states is $(2\pi)^{-3}$ and sums over states are replaced by integrals. The number density in phase-space is

$$w(\overrightarrow{r}, \overrightarrow{k}; T, \mu) = \frac{1}{(2\pi)^3} \frac{1}{e^{\beta(H(\overrightarrow{r}, \overrightarrow{k})-\mu)} + 1}, \tag{1.10}$$

with the Hamiltonian

$$H(\overrightarrow{r}, \overrightarrow{k}) = \frac{\hbar^2 \overrightarrow{k}^2}{2m} + \frac{m\omega_{rad}^2}{2}\rho^2 \quad ; \quad \rho = (x^2 + y^2 + \lambda^2 z^2)^{1/2}. \tag{1.11}$$

The chemical potential is determined using the normalization

$$N = \int d\overrightarrow{r} d\overrightarrow{k}\, w(\overrightarrow{r}, \overrightarrow{k}; T, \mu). \tag{1.12}$$

After determination of μ the spatial and momentum densities can be calculated by integrating over the momentum or spatial degrees of freedom, respectively:

$$n(\overrightarrow{r}, T) = \int d\overrightarrow{k}\, w(\overrightarrow{r}, \overrightarrow{k}; T, \mu), \tag{1.13}$$

$$\tilde{n}(\overrightarrow{k}, T) = \int d\overrightarrow{r}\, w(\overrightarrow{r}, \overrightarrow{k}; T, \mu). \tag{1.14}$$

This method gives solutions for all temperatures, but can only be applied numerically. For $T = 0$ it is easy to calculate the distributions analytically. For each spatial point in phase-space we can determine the local Fermi wave number using

$$\frac{\hbar^2 k_F(\overrightarrow{r})^2}{2m} + V(\overrightarrow{r}) = E_F, \tag{1.15}$$

with $V(\overrightarrow{r}) = \frac{1}{2} m\omega_r^2 \rho^2$ being the potential. All momentum states corresponding to the position $\overrightarrow{r}$ are filled up to the momentum $\hbar k_F(\overrightarrow{r})$. This expresses the fact that all states up to E_F are occupied according to the definition of the Fermi energy. E_F is constant over the sample since any position dependence would provoke a flow of atoms in phase-space and the sample is already defined to be in equilibrium. Equation (1.15) shows that position and momentum distributions do not decouple. At the outer edges of the cloud, the atoms have a lower momentum then in the middle, in contrast to a classical distribution. The density at each point is the number of states that fit in the Fermi sphere with radius k_F in k space, which is the volume of the Fermi sphere multiplied by the density of states $(2\pi)^{-3}$

$$\begin{aligned} n(\overrightarrow{r}, T=0) &= \frac{4\pi k_F(\overrightarrow{r})^3}{3(2\pi)^3} = \frac{1}{6\pi^2}\left(\frac{2m}{\hbar^2}(E_F - V(r))\right)^{3/2} &(1.16)\\ &= \frac{N\lambda}{R_F^3}\frac{8}{\pi^2}\left(1-\frac{\rho^2}{R_F^2}\right)^{3/2} &(1.17)\end{aligned}$$

for $\rho < R_F$ and 0 else. Here the definition of the Fermi radius (1.5) has been used. The distribution of the cloud is a cigar shaped ellipsoid with length $2R_F/\lambda$ and diameter 2 R_F (for $\omega_{rad} > \omega_{ax}$). The same aspect ratio λ is also obtained for a classical gas.

Measuring the spatial and momentum distribution

In the experiment, the density distribution is probed by sending a probe beam through the gas cloud and measuring the absorption. The measured quantity is the optical density

$$D_{opt} = -ln\left(\frac{I(y,z)}{I_0(y,z)}\right) = \sigma_0 \int dx\, n(x,y,z) = \sigma_0 n^{2D}(y,z)\,, \tag{1.18}$$

where $I_0(y,z)$ is the initial probe beam intensity, $I(y,z)$ the intensity after passage through the cloud and σ_0 the absorption cross section. This quantity is proportional to the column density $n^{2D}(y,z)$. Normally it is not possible to resolve the radial direction and a second integration is necessary, leaving only $n^{1D}(z) = \int dy\, n^{2D}(y,z)$. These distributions take the form

$$n^{2D}(y,z) = \frac{3N\lambda}{\pi R_F^2}\left(1-\frac{y^2+\lambda^2 z^2}{R_F^2}\right)^2\,, \tag{1.19}$$

$$n^{1D}(z) = \frac{48N\lambda}{15\pi R_F}\left(1-\frac{\lambda^2 z^2}{R_F^2}\right)^{5/2}\,. \tag{1.20}$$

These distributions are non-gaussian, but the difference from the classical gaussian distribution is always small and diminishes with more integrations, as demonstrated in figure 1.2.

By suddenly switching off the trap and allowing an expansion of the gas, it is also possible to observe the momentum distribution of the cloud. It can be derived, for $T=0$ analogous to equation (1.17) and is

$$\tilde{n}(\overrightarrow{k}, T=0) = \frac{N}{K_F^3}\frac{8}{\pi^2}\left(1-\frac{k^2}{K_F^2}\right)^{3/2}\,, \tag{1.21}$$

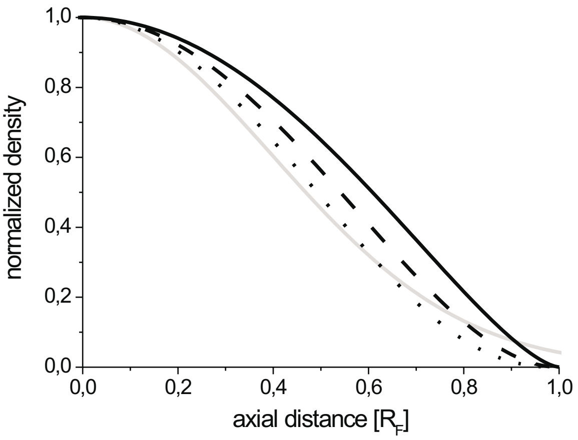

Figure 1.2: *Comparison of density profiles of a degenerate Fermi gas at zero temperature. A cut through the 3D density distribution* n^{3D} *(black solid line) is compared to a cut through the one (*n^{2D}*, dashed line) or two (*n^{1D}*, dotted line) times integrated distribution. For comparison a gaussian fit to* n^{1D}*, corresponding to a classical distribution, is plotted in gray. With more integrations the density profile becomes more "classical". Only integrated distributions can be recorded in the experiment, making it more difficult to detect the effects of degeneracy.*

with formulas analogous to (1.19) and (1.20) for the integrated distributions. The distributions have the same functional form because position and momentum enter both quadratically in the Hamiltonian. However, the momentum distribution is isotropic, similar to that of a classical gas, unlike the momentum distribution of a BEC. Again the difference between the classical and the quantum degenerate solution is small.

Finite temperature distributions

To study the dependence of the position and momentum distributions on degeneracy, one must solve equation (1.7) and calculate (1.13) or (1.14) numerically. For $T/T_F \gg 1$ the classical gaussian distributions are obtained. As $T/T_F \to 0^+$, where $T/T_F < 1$, the distributions approach the parabolic distributions (1.17) and (1.21). In the degenerate but finite temperature regime, the center of the distribution is well approximated by the $T = 0$ solution, whereas the wings are better approximated by a gaussian (figure 1.3a).

To characterize the effects of the Fermi pressure quantitatively we fit gaussian distributions to the spatial distributions $n^{1D}(T/T_F)$ and trace σ^2/R_F^2 over T/T_F, where σ is the root mean square size of the gaussian fits (figure 1.3b). For a classical gas

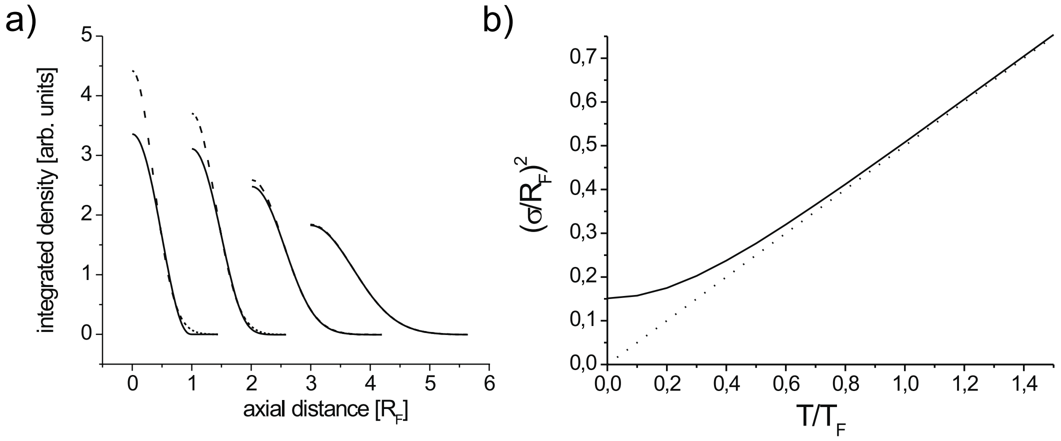

Figure 1.3: *a) Density profiles* $n^{1D}(z)$ *for* $T/T_F = 0, 0.2, 0.5, 1$ *(solid line). A classical distribution (gaussian) has been fitted to the wings of the density profiles (dotted line), showing the effect of Fermi pressure. b) Variance of gaussian fits to Fermi distributions normalized by the Fermi radius squared traced over the degeneracy (solid line). Dotted line: same treatment for Boltzmann gas.*

this treatment results in a straight line, with slope 0.5, which has a y-intercept of zero. Taking the correct fermionic distributions, one obtains asymptotically the same behavior in the high temperature regime. For $T = 0$ the curve turns upwards to intercept the y axis at a constant value of 0.15 instead of 0, which is a result of the Fermi pressure. Inbetween these limits one may interpolate. This has also been applied to experimental data (see figure 3.22 in section 3.3.4). In addition to the gaussian fit to the fermionic distribution for the determination of σ, a good method of measuring the temperature and the atom number must be used in order to determine T/T_F and R_F experimentally.

Heat capacity

The heat capacity $C_F \equiv \frac{\partial E}{\partial T}\big|_N$ can be calculated using the expression

$$E = \int d\epsilon\, \epsilon f(\epsilon) g(\epsilon) \tag{1.22}$$

for the total energy. For the high temperature region the classical result $C_{Cl} = 3Nk_B$ is obtained, whereas for low temperatures the heat capacity is smaller, $C_F = \pi^2 N k_B (T/T_F)$. This is due to the fact that at high degeneracies most atoms are already at their $T = 0$ position. Only in a region of size $k_B T$ around E_F will the atoms still change their energy levels. For a power law density of states the fraction of atoms in this region is proportional to T/T_F, leading to the T/T_F suppression in C_F. The dependence of the heat capacity on degeneracy is an interpolation between these two cases.

The effect of the discreteness of the harmonic oscillator states

If the temperature is smaller than the level spacing and the number of atoms stays small enough, the parabolic density distribution of the degenerate Fermi gas is slightly modified and shows a modulation pattern. This comes from the population of discrete energy shells in the Fermi sea. It also shows up in the heat capacity, which is strongly modulated in dependence of the particle number [78].

1.1.3 The effect of interactions on the degenerate Fermi gas

Until now we have considered a gas of noninteracting fermions. In our system this accurately models the experiment at low temperature, when all fermions are in the same internal state (see section 1.3), since then elastic collisions are suppressed. With respect to the phenomenon of Cooper pairing it is interesting to consider an interacting Fermi gas ([79] ,[80]). Mediated through an attractive interaction, the fermions pair, forming bosonic quasiparticles, which may then undergo a BEC transition. This will be discussed in section (1.1.14). Here we are interested in the shape change of a degenerate Fermi gas at zero temperature due to interactions. In experiments this interaction can be due to the magnetic dipole-dipole interaction or the s-wave interaction between fermions in different internal states. This case is particularly interesting in lithium, since the s-wave scattering length may be arbitrarily tuned using a Feshbach resonance.

We consider fermions in two different spins states $|\uparrow\rangle$ and $|\downarrow\rangle$. The $|\uparrow\rangle$ state experiences a mean field potential $gn_\downarrow(\overrightarrow{r})$ from the interaction with the $|\downarrow\rangle$ atoms, which have the density distribution $n_\downarrow(\overrightarrow{r})$. g is the coupling constant which is linked to the scattering length $a_{\uparrow\downarrow}$ through $g = 4\pi\hbar^2 a_{\uparrow\downarrow}/m$. The mean field potential must be added to the external potential in equation 1.16, resulting in

$$n_\uparrow = \frac{1}{6\pi^2}\left(\frac{2m}{\hbar^2}(E_{F\uparrow} - V_{ext} - gn_\downarrow)\right)^{3/2} \tag{1.23}$$

or

$$\frac{\hbar^2}{2m}(6\pi^2 n_\uparrow)^{2/3} + V_{ext} + gn_\downarrow = E_{F\uparrow} \tag{1.24}$$

and similarly

$$\frac{\hbar^2}{2m}(6\pi^2 n_\downarrow)^{2/3} + V_{ext} + gn_\uparrow = E_{F\downarrow} \tag{1.25}$$

since the situation is symmetric. This coupled set of equations must be solved numerically by iteration. It can be simplified by assuming $N_\uparrow = N_\downarrow$. Then $E_{F\uparrow} = E_{F\downarrow}$ and $n_\uparrow = n_\downarrow = n$ and we obtain a single equation

$$\frac{\hbar^2}{2m}(6\pi^2 n)^{2/3} + V_{ext} + gn = E_F \,. \tag{1.26}$$

The result of this calculation is shown in figure 1.4. The shape of the integrated distribution is compared for negative (a) and positive (b) values of the interaction strength. Experimentally the interaction strength can be arbitrarily tuned using a Feshbach resonance (see section 1.3.3). A trap with frequencies $\omega_{ax} = 2\pi \times 70\,\mathrm{s}^{-1}$ and $\omega_{rad} = 2\pi \times 5000\,\mathrm{s}^{-1}$ was used in the calculation and 10^5 atoms at $T = 0$ were assumed to be in each state. For negative values the mean field potential confines the atoms more strongly than in the case of an ideal gas, leading to higher densities and a more peaked distribution. If the scattering length approaches $a_{\uparrow\downarrow} = -2100\,a_0$, a very small change in $a_{\uparrow\downarrow}$ provokes a strong change in the size. For slightly smaller values the gas becomes unstable: the strong mean field potential leads to an increase in density which in turn increases the mean field potential, without the increase in kinetic energy being able to counterbalance the collapse.

For positive scattering length the size of the cloud increases. If $a_{\uparrow\downarrow} > 4000\,a_0$ it is energetically favorable to introduce a boundary and form two distinct phases. One state forms a core surrounded by a mixed phase consisting of both states. For high enough mean field the $|\uparrow\rangle$ and $|\downarrow\rangle$ states separate completely. A pure phase of one state forms a core surrounded by a pure phase of the other state. This should be observable experimentally. The experimental signal, distributions integrated in two dimensions, is shown in figure (1.4b). At first glance it might be astonishing that the outer component in the doubly integrated distribution has a completely flat profile in the region of the central component. This can be understood analytically by calculating the doubly integrated density of a hollow sphere, for which the central part of the profile is also flat.

The same calculation has been performed for a trap with frequencies $\omega_{ax} = 2\pi \times 1000\,\mathrm{s}^{-1}$, $\omega_{rad} = 2\pi \times 2000\,\mathrm{s}^{-1}$, corresponding to our crossed dipole trap. The collapse appears at $a_{\uparrow\downarrow} < -1800\,a_0$ and the phase separation occurs at about $a_{\uparrow\downarrow} > 4000\,a_0$.

Until now the calculation has been performed at zero temperature. This does not correspond to the actual experiment where typically degeneracies of $T/T_F = 0.2$ are reached. To obtain an estimate for the uncertainty of the result, the same calculation can be performed for a classical gas by solving

$$n(\overrightarrow{r}) = C\exp(-\beta(V_{ext} + gn(\overrightarrow{r}))) \quad \text{with} \quad N = \int dr^3\, n(\overrightarrow{r})\,. \tag{1.27}$$

The results are qualitatively the same but the collapse and phase separation appear at more extreme values of $a_{\uparrow\downarrow}$. For $T/T_F = 1$ they occur at $a_{\uparrow\downarrow} < -10000\,a_0$ and

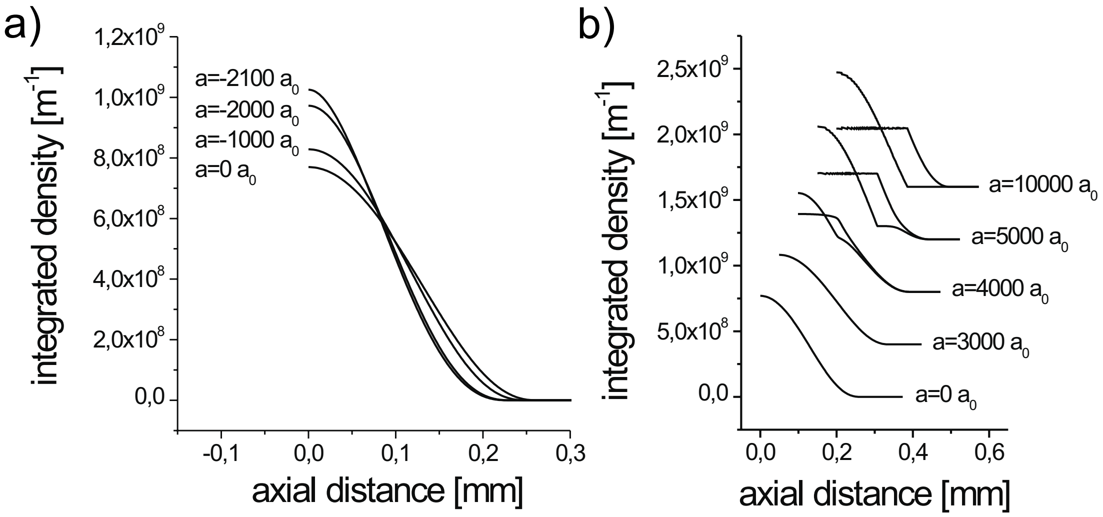

Figure 1.4: *The effect of interactions on a two component Fermi gas at zero temperature. Shown are the doubly integrated density distributions, which correspond to the experimental signal. The calculation is done for* $N = 10^5$ *atoms in each state and trap frequencies* $\omega_{ax} = 2\pi \times 70\,s^{-1}$, $\omega_{rad} = 2\pi \times 5000\,s^{-1}$. *a) For negative scattering length* $a_{\uparrow\downarrow}$ *the mean field is attractive and the gas contracts with decreasing* $a_{\uparrow\downarrow}$. *Above* $a_{\uparrow\downarrow} = 2100\,a_0$ *the gas becomes unstable and undergoes a collapse. b) For positive* $a_{\uparrow\downarrow}$ *the mean field expands the cloud. At* $a_{\uparrow\downarrow} \approx 4000\,a_0$ *the two states start to separate in order to reduce the mean field energy. The distributions of both states are shown. For* $a_{\uparrow\downarrow} = 10000\,a_0$ *the separation is complete: one state occupies the center while the other forms a sphere around it. Only a small region inbetween contains both states. Since doubly integrated density distributions are shown, the density in the inner part of the state forming a shell is not zero, but finite and constant.*

$a_{\uparrow\downarrow} > 40000\ a_0$ respectively when the other parameters are held fix. These values are extreme and would in an experiment probably be accompanied by strong losses.

1.1.4 Pauli blocking

The Pauli exclusion principle leads to a suppression of scattering of light or particles from a degenerate Fermi gas. Consider a scattering process that produces a fermion with less than the Fermi energy. For a zero temperature Fermi gas, all states with this energy are occupied. Thus the scattering process is forbidden by the quantum statistics. This effect is called Pauli blocking [66, 65]. The degree of suppression of collisions depends on the degeneracy of the Fermi gas and on the energy of the incoming particle or photon, called the test particle in the following. If the energy of the test particle is much greater than the Fermi energy, also the majority of scattered fermions will have an energy above E_F, where the occupation of states is low. In this case no modification of the scattering probability is observed, independent of the degeneracy of the Fermi gas. If the energy of the test particle is below the Fermi energy only atoms at the outer edge of the Fermi sphere can participate in the scattering, since these atoms can obtain an energy higher than E_F during the scattering process. For a test particle with zero energy, the scattering rate decreases in proportion to T^3 when compared to the classically expected rate (see figure 1.10a). This effect can be used to measure the degeneracy of the Fermi gas. It is detailed by G. Ferrari in [65], employing a static integration of the Boltzmann collision integral in phase-space. In the experiment the rethermalization of a cold test cloud of impurity atoms in the Fermi gas is observed (see section 3.3.5). This is a dynamic process that has been simulated by solving the coupled energetic Boltzmann equations of the two clouds, as detailed in the section on evaporative cooling (1.2.3). The inhibition of elastic scattering also becomes important at the end of sympathetic cooling as it slows down the cooling process. This is especially true if both components participating in sympathetic cooling are fermionic as is the case in [60].

To observe the effect of Pauli blocking on scattered light, a two-level cycling transition must be used. After the absorption process, the atom undergoes spontaneous emission to its initial state. Atoms in the Fermi sea are in the same state and thus Pauli blocking can occur. Pauli blocking can increase the lifetime of the excited state and thus lead to a narrowing of the linewidth. This effect is analogous to the enhancement of the excited state lifetime in cavity experiments [81], but the enhancement comes from the reduction of atom, not photon, final states. A second effect is the reduction of the scattering rate. Both effects depend on the recoil transmitted to the atom during the scattering process. Since the occupation in a degenerate Fermi gas is highest for low energies, scattering at small angles, corresponding to small momentum transfer, is altered most severely. These effects also depend also strongly on the degeneracy of the Fermi gas. Several articles have been published on this subject: see [67, 68, 69] and references therein.

1.1.5 Detection of a degenerate Fermi gas

Since there is no phase transition from a classical to a degenerate Fermi gas, there is no striking experimental signal for the onset of quantum degeneracy. The system's behavior transitions gradually between that of classical and quantum statistics. Several different methods can be used to measure the degeneracy of a Fermi gas.

The simplest is to look for the change in shape of the spatial or momentum distributions. The easiest way to do this is to fit gaussian distributions to both the wings of the cloud and the whole cloud (see figure 1.3a) and figure 3.20). For a classical distribution the measured RMS sizes are the same. For a degenerate fermionic cloud, less atoms occupy the central part of the cloud due to the Pauli principle. The distribution is slightly flattened in the central part, which shows up in a decrease of the RMS size when fitting less and less of the central part. For a bosonic degenerate gas the opposite is true, due to the Bose-enhanced occupation of low lying states. This dependence of the RMS size with the fit region gives a first indication for quantum degeneracy. To be quantitative, the degeneracy T/T_F has to be determined. Since the high energy wings of the distribution are independent of the statistics, a fit with the classical gaussian distribution to the outer parts of the cloud still gives the correct temperature T. T_F is calculated from the measured trapping frequencies and the atom number. This method is accurate down to degeneracies of $T/T_F = 0.3$ and is demonstrated in section (3.3.2). Below this limit the experimental noise does not allow for an accurate determination of the temperature.

In our experiment there is a bosonic cloud present with the fermionic cloud and we can reach situations in which we know that both distributions are in thermal equilibrium. Both experience the same potential. The size of the degenerate fermionic cloud is related to the Fermi energy, whereas the size of the bosonic cloud depends on temperature. For $T/T_F < 1$ the fermionic cloud thus exceeds the bosonic in size. This is the result of Fermi pressure. As will be demonstrated in the results section (3.3.4), the degeneracy can be seen directly by comparing the bosonic and fermionic distributions, without making a fit. To determine it more precisely, the temperature can be measured from the thermal component of the bosonic distribution. This allows the determination of the degeneracy as long as the bosonic component is not too degenerate and the thermal cloud is visible, which in our experiment currently sets a limit at $T/T_F = 0.2$.

For higher degeneracies the measurement of the rethermalization of a cold test cloud of bosonic atoms which has initially been put in thermal non-equilibrium with the fermionic cloud could be applied. This was discussed in section (1.1.4) in more detail.

1.1.6 The degenerate Bose gas

In the following we will discuss some of the properties of degenerate Bose gases. More detailed information can be found in [76], [82] and [83]. The difference between a Fermi gas and a Bose gas comes from the fact that at most one fermion can occupy a quantum state, whereas an arbitrary number of bosons can exist in the same state. From this fact, the energy distribution function for bosons $f_B(\epsilon)$ can be derived, yielding

$$f_B(\epsilon) = \frac{z}{e^{\beta\epsilon} - z}\,, \tag{1.28}$$

where $z = e^{\beta\mu}$ is the fugacity [76]. By examining equation 1.28 it is clear that z must be between 0 and 1. For any other value the occupation $f(\epsilon = 0)$ becomes negative, which is unphysical. The $\epsilon = 0$ ground state plays a special role. Its occupation

$$f_0 = \frac{z}{1 - z} \tag{1.29}$$

can grow arbitrarily large when z goes to 1. The total occupation of all the other states is bound by a finite value for fixed T. This means that if the number of atoms exceeds a critical number, all atoms added to the system go to the ground state. This effect has the character of a phase transition. The atoms in the ground state are called the Bose-Einstein condensate.

Consider an ideal gas, *i.e.*, a gas without interactions. For a harmonically trapped ideal gas, a phase transition to a Bose-Einstein condensate occurs under the condition

$$n_0\lambda_{dB}^3 = \zeta(3/2) = 2.612...\,, \tag{1.30}$$

where n_0 is the peak density and $\lambda_{dB} = h/\sqrt{2\pi m k_B T}$ the de Broglie wavelength. One may interpret this result as follows. When the atomic de Broglie wavelength becomes larger than the particle distance, the wavepackets describing the atoms overlap and interfere. The behavior of a macroscopic fraction of atoms can then be described by a single wavefunction, the wavefunction of the ground state. Bose-Einstein condensation occurs at a critical temperature $k_B T_C \gg \hbar\omega$, which shows that it is not a classical effect. For $k_B T \ll \hbar\omega$ even a classical gas would macroscopically occupy the ground state. The critical temperature for an ideal gas of N atoms in a harmonic trap with mean frequency $\bar{\omega}$ is

$$T_C = \frac{\hbar\omega}{k_B}\left(\frac{N\lambda}{1.202}\right)^{1/3}\,, \tag{1.31}$$

0.6 times the Fermi temperature of an equivalent Fermi gas. The occupation of the ground state changes with degeneracy T/T_C as

$$\frac{N_0}{N} = 1 - \left(\frac{T}{T_C}\right)^3\,, \tag{1.32}$$

while holding the other parameters constant. The latter is only correct in the limit $N \rightarrow \infty$. For finite atom number the result

$$\frac{N_0}{N} = 1 - \left(\frac{T}{T_C}\right)^3 - \frac{3(\lambda+2)\zeta(2)}{6\lambda^{1/3}[\zeta(3)]^{2/3}}\left(\frac{T}{T_C}\right)^2 N^{-1/3} \tag{1.33}$$

is obtained [82]. The phase transition occurs at a lower temperature. An anisotropic trap ($\lambda \neq 1$) lowers the critical temperature further.

1.1.7 The effect of interactions and the Gross-Pitaevskii equation

The wavefunction of a non-interacting condensate is the ground state wavefunction. For an interacting Bose gas this is no longer true. In addition to the external potential, the mean field potential $g\, n(\overrightarrow{r})$ has to be taken into account, analogous to the treatment in the fermionic case. The coupling constant g is linked to the scattering length a by $g = 4\pi\hbar^2 a/m$. The Schrödinger equation with this mean field potential is called the Gross-Pitaevskii equation (GPE) [9, 10]. Expressing the density $n(\overrightarrow{r})$ in terms of the wavefunction $\Psi(\overrightarrow{r})$ the time dependent GPE reads [83]

$$i\hbar\partial_t\Phi(\overrightarrow{r},t) = \left(-\frac{\hbar\nabla^2}{2m} + V_{ext}(\overrightarrow{r},t) + g|\Phi(\overrightarrow{r},t)|^2\right)\Phi(\overrightarrow{r},t)\,. \tag{1.34}$$

When the gas is at thermal equilibrium, the only time dependence of $\Phi(\overrightarrow{r},t)$ is a global phase. The simplest choice is to assume $\Phi(\overrightarrow{r},t) = \Psi(\overrightarrow{r})\exp(\mu t/i\hbar)$. This ansatz simplifies the time dependent GPE to its time-independent form

$$\mu\Psi(\overrightarrow{r}) = \left(-\frac{\hbar\nabla^2}{2m} + V_{ext}(\overrightarrow{r}) + g|\Psi(\overrightarrow{r})|^2\right)\Psi(\overrightarrow{r})\,. \tag{1.35}$$

It can be shown that μ is the chemical potential [83]. If the mean field energy is much greater than the kinetic energy one may neglect the latter. This is called the Thomas-Fermi approximation. One then finds the solution

$$|\Psi(\overrightarrow{r})|^2 = n(\overrightarrow{r}) = \frac{\mu - V_{ext}(\overrightarrow{r})}{g}\,. \tag{1.36}$$

The chemical potential μ can be found from the normalization condition

$$\int d\overrightarrow{r}\,|\Psi(\overrightarrow{r})|^2 = N\,. \tag{1.37}$$

The spatial distribution of the condensate is determined by an equilibrium between the confining potential and the repulsive interaction of the atoms. For an harmonic potential $V = \frac{m}{2}\sum_{\alpha=x,y,z}\omega_\alpha^2 r_\alpha^2$ it is an inverted parabola

$$\Psi(\vec{r}) = \left(\frac{\mu}{N_0 g}\right)^{1/2}\left(1-\sum_\alpha \frac{r_\alpha^2}{R_\alpha^2}\right)^{1/2}, \tag{1.38}$$

where the Thomas-Fermi radius

$$R_\alpha^2 = \frac{2\mu}{m\omega_\alpha^2} \tag{1.39}$$

has been introduced. The chemical potential is

$$\mu = \frac{1}{2}\hbar\bar{\omega}\left[15\frac{N_0 a}{(\hbar/m\bar{\omega})^{1/2}}\right]^{2/5}, \tag{1.40}$$

where $\bar{\omega}$ is the geometrical mean of the trap frequencies $\bar{\omega} = (\omega_x\omega_y\omega_z)^{1/3}$. The mean field interaction expands the condensate to be larger than the size of the harmonic oscillator ground state $\sigma_{HO} = \sqrt{\hbar/(m\omega)}$.

The mean field interaction also plays an important role during the ballistic expansion of the condensate, during which it is converted to kinetic energy. It can be shown [14, 7, 84] that the shape of the wavefunction stays the same. Only the radii R_α change with time:

$$\begin{aligned} R_{x,y}(t) &= R_{x,y}(0)\sqrt{1+\tau^2} && (1.41)\\ R_z(t) &= R_z(0)\left(1+\lambda^2[\tau\arctan\tau - \ln\sqrt{1+\tau^2}\,]\right), && (1.42)\end{aligned}$$

where $\tau = \omega_{rad}\,t$. The expansion is faster in the direction of the initially stronger confinement. If the trap was initially cigar shaped, then after expansion the BEC becomes pancake shaped. Viewed from the side, this appears as an inversion of ellipticity, a signature for the appearance of a BEC. A classical gas can also show such an inversion, but only if it is in the hydrodynamic regime, which requires that the mean free path between collisions is much smaller than the size of the cloud [85]. This regime is difficult to attain. A classical gas normally shows an isotropic distribution after expansion. If some atoms are not condensed, it is possible to compare the behavior of the condensate with the behavior of these atoms. The latter, called the thermal cloud, expand like a classical gas. The condensate shows the inversion of ellipticity. This contrast is an even clearer signature for the condensate.

1.1.8 BEC with attractive interactions

If the interaction between the atoms is attractive the density can become so large, that no stable solution is possible. The BEC collapses onto itself and its atoms form molecules due to three-body recombination, or undergo dipolar relaxation and are lost. In free space this always occurs before a condensate can be formed [86]. In a trap the kinetic energy which occurs due to the Heisenberg uncertainty principle can counterbalance the attractive interaction up to a certain number of atoms in the condensate and stabilize the BEC. The maximum number of atoms can be found by numerically searching for stable solutions of the GPE with varying number of atoms. In the calculation of [87] no stable solution was found for $N_0 > N_0^c$ with

$$\frac{N_0^c|a|}{\sqrt{\hbar/m\omega}} \simeq +0.57\,. \tag{1.43}$$

1.1.9 One-dimensional degenerate gases

One-dimensional trapping configurations have received a great deal of attention recently, since several types of quantum gases beyond the mean field description employed above are predicted. A radially trapped gas behaves like a one dimensional gas provided that it is not excited radially. This requires that the temperature and the mean field energy are below the radial level spacing: $k_BT \ll \hbar\omega_{rad}$ and $U_{mean1D} = n_{1D}g_{1D} \ll \hbar\omega_{rad}$. Here n_{1D} is the linear density and g_{1D} the 1D interaction strength which depends on the 3D interaction strength g and the radial confinement ω_{rad} [88]. Within the region of quantum degeneracy $n_{1D}\lambda_{dB} > 1$ three different types of trapped degenerate gases can be distinguished ([89] and figure 1.5). For high enough atom numbers the mean field description is valid in the axial direction and the condensate has a Thomas-Fermi shape in this direction (equation 1.38). In a wide temperature region below the critical temperature, the density fluctuations are suppressed, but the phase still fluctuates across the sample. In this regime the condensate is called a quasi-condensate. Quasi-condensates can also exist in 3D for very elongated trap geometries and have recently been observed [90, 91]. To increase the phase coherence length above the size of the sample, the temperature has to be further decreased below a characteristic temperature T_{ph}. Then both density and phase fluctuations are suppressed in the axial direction, as they are for a normal condensate. The third regime is the Tonks gas of impenetrable bosons. It appears when the probability of transmission in boson-boson scattering is low. The bosons remain in their initial order in the one dimensional chain of particles. This is equivalent to the behavior of fermions: there is a one to one mapping between the Hamiltonian describing a fermionic system and a bosonic system under these conditions. For this reason the transition to the Tonks regime is called fermionization. The Boson-Fermion duality is a consequence of the breakdown of the spin-statistical theorem in low dimensions. The condition of low transmission probability can be translated into a condition on the density of atoms. For an infinite waveguide the condition is $n_{1D} \ll 1/\pi|a_{1D}|$, where a_{1D} is the one dimensional scattering length corresponding to the interaction strength g_{1D} [88].

In our experiment, the production of one dimensional condensates is natural due to the elongated trap geometry and the scattering properties of lithium. This will be

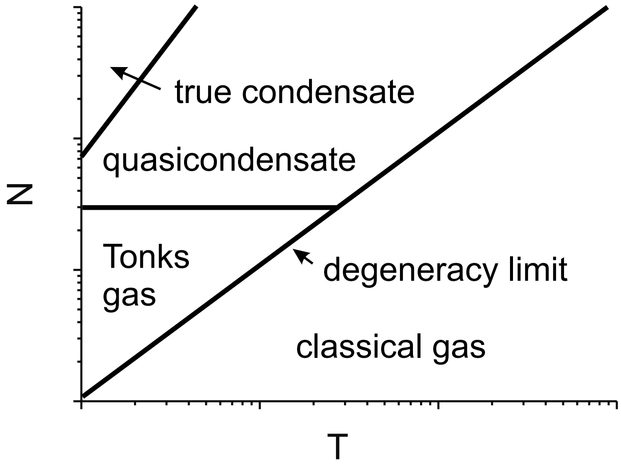

Figure 1.5: *Diagram of states for a trapped 1D gas [89].*

discussed in the next section. The MIT group of W. Ketterle has also recently realized one- and two-dimensional condensates [31].

1.1.10 The 1D condensate

The Thomas-Fermi approximation is only valid if the chemical potential is larger than the level spacing of the harmonic oscillator [83]. The chemical potential (1.40) depends on atom number and scattering length. In some of our experiments the scattering length is very small in comparison with most other experiments, making it easy to obtain a low chemical potential. Together with a strong confinement in the radial directions, our experiment can produce condensates for which the Thomas-Fermi approximation is only valid in the axial direction. The mean field energy in the radial directions is not sufficient to significantly alter the shape of the wavefunction, which remains as the harmonic oscillator ground state wavefunction, a gaussian (see section 3.4.4).

To test this prediction and to calculate the remaining deformation of the radial wavefunction, we minimize the energy of a test wavefunction. Axially we use the parabolic Thomas-Fermi profile obtained above. In the radial directions we retain the gaussian shaped ground state of the harmonic oscillator, with a σ-size that is slightly larger than the one particle ground state size because of the mean field [92]. The ansatz for the wavefunction normalized to 1 is

$$\Psi(x,y,z) = \exp\left(-\frac{x^2+y^2}{4\sigma^2}\right)\sqrt{1-\frac{z^2}{R^2}}\sqrt{\frac{8}{3\pi\sigma^2 R}}\,. \tag{1.44}$$

We minimize the energy regarding the two free parameters σ and R

$$E = \int \frac{\hbar^2}{2m} |grad\,\Psi|^2 + U|\Psi|^2 + \frac{Ng}{2}|\Psi|^4 \,. \tag{1.45}$$

The result of this is

$$\sigma^4 = \frac{\hbar^2}{4m^2\omega_\perp^2}\left[1 + \frac{\sigma}{5}\frac{NA}{R}\right] \tag{1.46}$$

and

$$R^3\sigma^2 = \frac{3}{8\pi}\frac{Ng}{m\omega_{ax}^2} \,. \tag{1.47}$$

This coupled system of equations can be solved iteratively. We will see in the results section (3.4.4) that the radial σ size is increased by only 3% due to the mean field with our experimental parameters. This proves that the ansatz is justified, our BEC is one dimensional. It behaves as an ideal gas in the radial directions. The chemical potential is smaller than the radial level splitting, but the transition temperature is still larger than $\hbar\omega_{rad}$. This means that excitations retain their three-dimensional character and that the calculation of T_C is still valid. However, the ballistic expansion is modified. The radial mean field energy is nearly zero. Instead, the expansion is driven by the Heisenberg uncertainty principle. The radial shape of the wavefunction stays gaussian and expands like a free gaussian wavepacket. The RMS size of the density profile expands like

$$\sigma_{rad}(t) = \sqrt{\frac{\hbar}{2m\omega_{rad}} + \frac{\hbar\omega_{rad}}{2m}t^2} \,. \tag{1.48}$$

1.1.11 The bright soliton

A fascinating behavior may be observed for waves propagating in a nonlinear dispersive medium, the formation of solitary waves which travel without changing their form [93]. Normally dispersion changes the shape of a wavepacket since its constituting frequency components travel at different velocities. This can result in a chirped pulse, where the low frequency part of the pulse arrives before the high frequency part, or the inverse. (One can hear this effect when listening to the noise of ice skates which have travelled through the ice on a lake.) Nonlinearity makes the phase of a wave dependent on the wave's intensity. It can also produce a chirped pulse. Under certain circumstances these effects counterbalance each other and a solitary wave travels without changing its form. This phenomenon was first observed 1834 by J. S. Russell when he followed a water wave in a canal near Edinburgh for eight miles on horseback (read his account of the first sighting in the bibliography section under [94]). These waves are called solitons. They can also exist as light pulses in nonlinear optical fibers where they can be used to transmit information.

Solitons can also exist in one dimensional condensates (see Y. Castin in [83] or [95]). The dispersion is the normal matter wave dispersion $\omega(k) = \hbar k^2/2m$. The nonlinearity comes from the mean field. One distinguishes two types of solitons: dark and bright. Dark solitons are localized intensity minima in a condensate with repulsive interactions. The speed of a dark soliton depends on its depth. A soliton which forms a node is stationary. Its speed increases up to the speed of sound as its depth decreases to zero. Dark solitons were first produced 1999 by the groups of W. Ertmer and B. Phillips and later on by the group of L. Hau, among others [25, 26, 27]. A bright solitons is a localized density maxima which can undergo interactions with other solitons without changing its form. Such solitons can be produced from one dimensional condensates with an attractive mean field. In the non-confined axial direction the soliton is held together due to the mean-field attraction. The attraction is counterbalanced by the kinetic energy, which increases after the Heisenberg uncertainty principle when the wavefunction gets smaller. This phenomenon has not been observed in matter-waves until the work presented in section (3.6.5). A nice property yet to be observed is that solitons can travel through each other and reappear after the collision without having changed their speed or form, but having acquired a phase-shift and a displacement [93].

In the following some of the properties of bright solitons are derived. The starting point is the Gross-Pitaevskii equation (1.34) which we simplify with the ansatz $\Phi(x, y, z, t) = \Psi(z, t)\chi(x)\chi(y)$. Here χ is the gaussian radial harmonic oscillator ground state wavefunction. For an axially open trap ($\omega_{ax} = 0$) one obtains a one-dimensional Gross-Pitaevskii equation for $\Psi(z, t)$:

$$i\hbar\partial_t\Psi(z,t) = -\frac{\hbar^2}{2m}\frac{d^2\Psi}{dz^2} + N_0 g_{1D}|\Psi(z)|^2\Psi(z)\,, \tag{1.49}$$

with the effective 1D interaction strength $g_{1D} = 2a\omega_{rad}\hbar$. The solution of this equation normalized to N is a soliton moving with speed v [96]

$$\Psi(z,t) = \sqrt{\frac{N}{2l}}\mathrm{sech}\left(\frac{z-vt}{l}\right)e^{-i2mvz/\hbar}e^{-ig_{1D}Nt/\hbar 2l}\,, \tag{1.50}$$

with the length l of the soliton

$$l = -\frac{\sigma_{HO}^2}{Na}\,, \tag{1.51}$$

where $\sigma_{HO} = \sqrt{\hbar/(m\omega_{rad})}$ is the radial harmonic oscillator ground state size. The length l is the result of the competition between the kinetic energy per atom $\hbar^2/(ml^2)$ and the interaction energy $g_{1D}N/l$. The density profile is shown in figure (1.6). The chemical potential is

$$\mu = -(Na\omega_{rad})^2 m/2\,, \tag{1.52}$$

which must be smaller than $\hbar\omega_{rad}$ to fulfill the 1D condition. From this condition the maximum number of atoms can be calculated to be $N_{max} = -\sqrt{2}\sigma_{HO}/a$. The size of a soliton with this atom number is $l = \sigma_{HO}/\sqrt{2}$, but for the numerical factor just the radial ground state size. Using equation (1.50) one obtains the maximum density,

$$n_{1D}^{max} = \frac{N^{max}}{2l} = \frac{1}{a}\,, \tag{1.53}$$

which is independent of the radial trap frequency and the atom number. In the center of the soliton the distance of the atoms is the scattering length. Our soliton is produced in the ^{7}Li $|F = 1, m_F = 1\rangle$ state whith a scattering length of $\sim -4\,a_0 = 0.2\,\text{nm}$ in a trap with $\omega_{rad} = 2\pi 700\,\text{Hz}$. The maximum atom number is $N^{max} = 10^4$ and the length under these conditions $l = 1\,\mu\text{m}$. Pictures of the travelling bright soliton are shown in figure (3.36) and compared to the behavior of an ideal gas in figure (3.37).

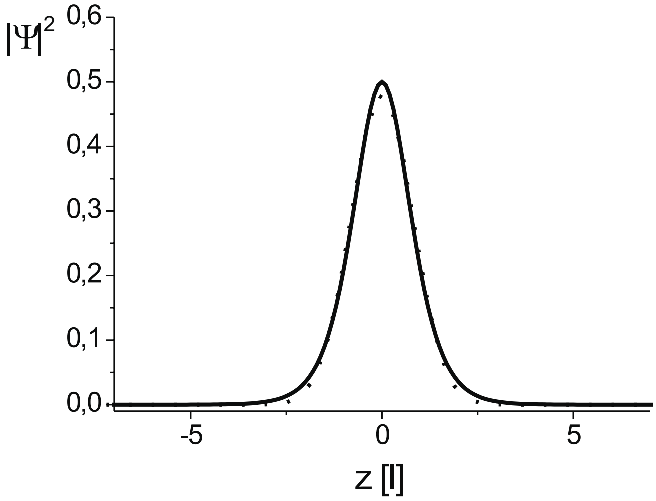

Figure 1.6: *Density distribution of a soliton* $n(z) = |\Psi(z)|^2 = 1/(\cosh(z)\sqrt{2})^2$ *(solid line). For comparison a gaussian has been fitted to this shape (dotted line).*

1.1.12 The effects of Bose statistics on the thermal cloud

The thermal cloud is also effected by the Bose statistics. The shape of the thermal component in the temperature region near and below the critical temperature is no longer gaussian but behaves as

$$n(\overrightarrow{r}) = \frac{1}{\lambda_{dB}^3} g_{3/2}[z\,\exp(-\beta m\omega_{rad}^2\rho^2/2)]\,, \tag{1.54}$$

where $g_{3/2}$ is a Bose-Einstein function and $\rho^2 = x^2 + y^2 + \lambda^2 z^2$. Again, to compare with the experiment, the distribution must be integrated along one or both of the radial directions, yielding

$$n_{2D}(y, z) = \frac{\sigma_x}{\lambda_{dB}^3} \sqrt{\pi} g_2[z \, \exp(-\beta m \omega_{rad}^2 (y^2 + \lambda^2 z^2)/2)] \,, \tag{1.55}$$

$$n_{1D}(z) = \frac{\sigma_x^2}{\lambda_{dB}^3} \pi g_{5/2}[z \, \exp(-\beta m \omega_{ax}^2 z^2)/2)] \,, \tag{1.56}$$

where $\sigma_x = \sqrt{k_B T / m\omega_{rad}^2}$. These functions are fitted to the experimentally measured density distributions to determine the temperature and the number of non-condensed atoms. Below T_C the integrated density distribution of the condensate is simply added, with the condensed fraction N_0/N as an additional fit parameter.

1.1.13 Boson-fermion mixtures

In a mixture of interacting ultracold gases, the phenomenon of phase separation can occur. For certain values of the interaction constants, the atom numbers and the trap frequencies a spatial separation of the different components of the gas can be energetically favorable in comparison with a single mixed phase. This occurs if the gain in mean field interaction energy overweighs the kinetic energy introduced by the boundary. Such phenomena have been experimentally studied in spinor condensates [97, 98].

Our system consists of a mixture of bosonic and fermionic lithium. An analytical calculation in [99] for homogenous gases at zero temperature shows the possibility of phase separation. In a numerical calculation for zero temperature and trapped gases [80], Mølmer predicted phase separation of the two components for extreme interaction parameters. In our system, we actively cool only one component and rely on thermalization between the two components to cool the other. A demixture of the gases would severely limit the thermal contact between them. A reduction in thermal contact can pose a limit on the achievable degeneracies of the passively cooled component. It was important for us to know if a significant phase separation could occur under our experimental conditions, which was not considered in the work of Mølmer. To answer this question, a numerical simulation was carried out using his method, which is analogous to the calculation performed in section 1.1.3 to determine the effect of interactions on a non polarized Fermi gas. Very recently, the group of M.P. Tosi also analyzed the conditions for phase-separation in our experiment [75].

The above approach is valid for zero temperature. The distribution of the bosonic cloud can be computed with the Gross-Pitaevskii equation in the Thomas-Fermi approximation (1.36). In addition to the boson-boson mean field, the mean field potential of the fermions must be taken into account. Similarly, equation (1.26) with an additional boson-fermion mean field term is used to calculate the fermionic distribution. The two equations are as follows:

$$V_{ext}(\overrightarrow{r}) + g_{BB} n_B(\overrightarrow{r}) + g_{BF} n_F(\overrightarrow{r}) = \mu \,, \tag{1.57}$$

$$\frac{\hbar^2}{2m} \left[6\pi^2 n_F(\overrightarrow{r})\right]^{2/3} + V_{ext}(\overrightarrow{r}) + g_{BF} n_B(\overrightarrow{r}) = E_F \,, \tag{1.58}$$

where g_{BF} is the boson-fermion and g_{BB} is the boson-boson interaction strength, n_B the bosonic and n_F the fermionic density distribution. The chemical potential μ and the Fermi energy are found from the normalizations $\int dr^3\, n_B = N_B$ and $\int dr^3\, n_F = N_F$, with N_B and N_F the total number of bosons and fermions. The computation is iterative. First the bosonic distribution is calculated in absence of the fermions. This bosonic distribution adds an extra mean field term to the external trap potential experienced by the fermions. The fermionic distribution is calculated in this total potential. The fermionic mean field on the bosons is added to the external potential to give the total potential for the bosons. The process is repeated starting from the calculation of the bosonic distribution. These iterations continue until the calculated chemical potential and Fermi energy change by less than 10^{-10} during one iteration.

Phase separation is a self-amplifying effect, in which the bosons expel the fermions, creating a potential which confines the bosons more strongly, leading to an even stronger repulsion of the fermions. This is shown in figure (1.7a) for extreme parameters of the atomic interactions ($a_{BF} = 2000\ a_0$, $a_{BB} = 1000\ a_0$) and 10^6 atoms of both species in a trap corresponding to our magnetic trap ($\omega_{ax} = 2\pi \times 80\,\text{Hz}$, $\omega_{rad} = 2\pi \times 5000\,\text{Hz}$ for ^{7}Li). Two different equilibrium distributions can be found, a fermionic sphere around a bosonic core or the inverse. For a smaller interspecies scattering length the phase separation becomes incomplete, and a mixed phase coexists with a pure phase.

The parameters used above are too extreme to be easily reached in our experiment. They were chosen to demonstrate the possibility of phase separation. In figure (1.7c) the case of a more experimentally realistic parameter set is shown ($N_F = N_B = 10^4$, $a_{BF} = 38\ a_0$, $a_{BB} = 5.1\ a_0$, same trap). No phase separation occurs: the fermionic density distribution is only slightly diminished where it overlaps with the condensate. The correct distributions are already well approximated by the undisturbed bosonic distribution and the fermionic distribution calculated with external potential plus the BEC mean field. The back action of the fermions on the bosons is negligible since the fermionic cloud is less dense and more homogenous than the bosonic distribution. Thus no real phase separation takes place. For the fermions to be expelled from the space occupied by the condensate the potential of the boson mean field on the fermions has to be bigger than both the Fermi energy and the temperature of the fermionic cloud

$$U_{BF} = \frac{g_{BF}}{g_{BB}} \mu > E_F, k_B T \,. \tag{1.59}$$

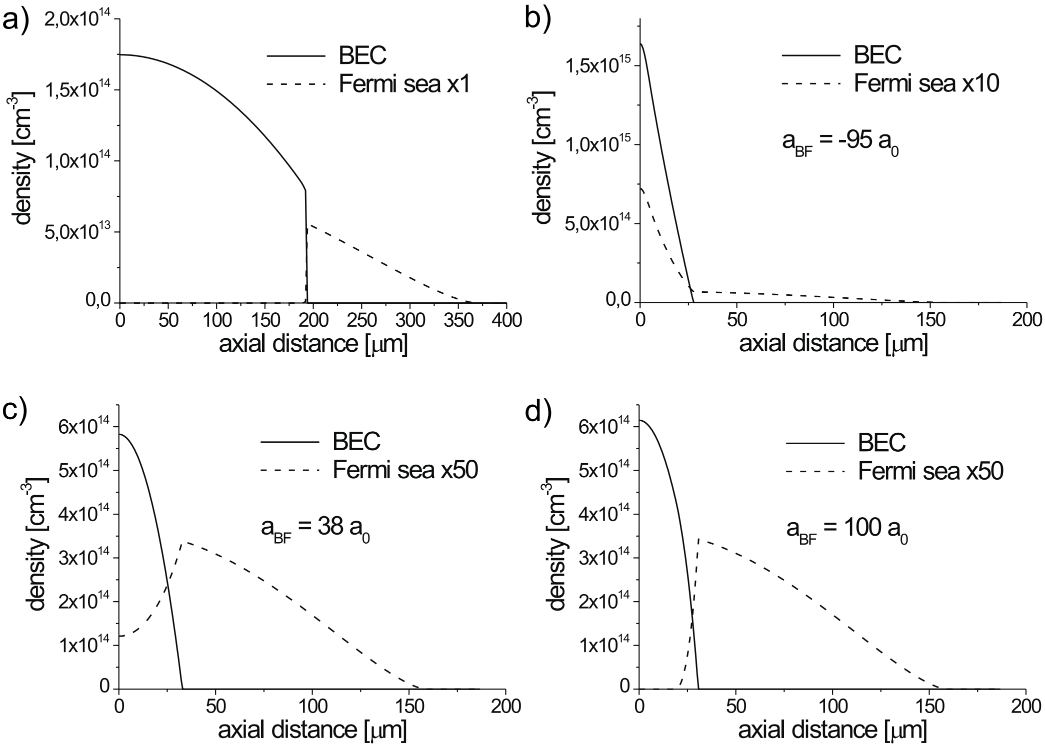

Figure 1.7: *Density profiles of boson-fermion mixtures in our magnetic trap* ($\omega_{ax} = 2\pi \times 80\,Hz$, $\omega_{rad} = 2\pi \times 5000\,Hz$ *for* ^7Li)*. a) A phase separation occurs for the extreme parameters* $a_{BF} = 2000\ a_0$, $a_{BB} = 1000\ a_0$, $N_F = N_B = 10^6$*. The fermionic component forms a shell outside a bosonic core. The fermionic mean field strongly affects the shape of the condensate. b,c,d) The experimentally reached atom numbers* $N_F = N_B = 10^4$ *and bosonic scattering length* $a_{BB} = 5.1\ a_0$ *are used. The interspecies scattering is varied. b)* $a_{BF} = -95\ a_0$*. For a slightly smaller interspecies scattering a collapse would occur. The profiles are already strongly modified by the attraction. c)* $a_{BF} = 38\ a_0$*. This is the experimental situation. The fermionic density is slightly diminished in presence of the condensate. The bosonic component is not changed noticeably. d)* $a_{BF} = 100\ a_0$*. The repulsion is strong enough to expulse nearly all fermions from the region of the condensate. Note that the experimental signal does not actually consist of the density profiles shown here, but the one- or two-times integrated density profile, thus decreasing the measurable effect.*

To reach these conditions it is favorable to use a small number of fermions and a large number of bosons at low temperature and if possible, a strong boson-fermion coupling constant. In figure (1.7d) this is demonstrated by increasing the interspecies scattering length to $a_{BF} = 100\ a_0$, while holding the other parameters fix.

Another effect, a collapse of the gas, can occur for negative interspecies scattering length. The distributions at the border to a collapse are shown in (1.7b).

1.1.14 The BCS transition

At low temperatures, degenerate Fermi gases can undergo a phase transition and build up a superfluid phase, *i.e.*, frictionless flow. This is well known for metals, where superconductivity is the consequence, or for ^{3}He. One of the goals of our experiment is to search for this Bardeen-Cooper-Schrieffer (BCS) transition [50]. The fundamental idea explaining this observation was introduced in 1956 by Cooper [49]. For an ideal Fermi gas in a box, the ground state is the Fermi sea and all states up to the Fermi energy are occupied. In momentum space this corresponds to the Fermi sphere, with all states up to $k = k_F$ occupied. However, if an attractive interaction exists between the fermions it is energetically favorable to form bound pairs which have momentum $\overrightarrow{k_F}$ and $-\overrightarrow{k_F}$. This pairing occurs for arbitrarily weak interactions which is a consequence of the presence of the degenerate Fermi sea. Such pairs, called Cooper pairs, have a bosonic character, since their spin is integer, and can Bose condense. They have long range correlations and show superfluidity.

Cooper pairing

The principle of Cooper pairing can be understood with a simple model [6, 100]. Consider a Fermi sphere and add two fermions with opposite momentum of equal magnitude. The Fermi sphere blocks access to all states having a momentum lower than k_F. Interactions with fermions outside the Fermi surface may be neglected. The wavefunction of any pair of fermions is a superposition of all possible plane waves with opposite momenta,

$$\Psi(\overrightarrow{r_1}, \overrightarrow{r_2}) = \sum_{\overrightarrow{k}} g(\overrightarrow{k}) e^{i\overrightarrow{k}\cdot\overrightarrow{r_1}} e^{-i\overrightarrow{k}\cdot\overrightarrow{r_2}}\,, \tag{1.60}$$

where all probability amplitudes $g(\overrightarrow{k})$ with $k < k_F$ are equal to zero because of the Pauli exclusion principle. The Schrödinger equation for the two fermions is

$$-\frac{\hbar^2}{2m}(\nabla_1^2 + \nabla_2^2)\Psi(\overrightarrow{r_1}, \overrightarrow{r_2}) + V(\overrightarrow{r_1}, \overrightarrow{r_2})\Psi(\overrightarrow{r_1}, \overrightarrow{r_2}) = \left(E + \frac{\hbar^2 k_F^2}{m}\right)\Psi(\overrightarrow{r_1}, \overrightarrow{r_2})\,, \tag{1.61}$$

where E is the energy shift of the fermions relative to two fermions at the surface of the Fermi sphere. By inserting (1.60) into (1.61) one obtains an equation for the $g(\overrightarrow{k})$

$$\frac{\hbar^2 k^2}{m} g(\overrightarrow{k}) + \sum_{\overrightarrow{k}'} g(\overrightarrow{k}') V_{\overrightarrow{k}\overrightarrow{k}'} = (E + 2E_F) g(\overrightarrow{k})\,, \tag{1.62}$$

where

$$V_{\vec{k}\vec{k}'} = \frac{1}{L^3}\int V(\vec{r})e^{-i(\vec{k}-\vec{k}')\vec{r}}\,d\vec{r} \tag{1.63}$$

is the matrix element of the interaction between the fermions. L^3 is the volume of the system. In order to simplify the calculation, an attractive constant interaction $V_{\vec{k}\vec{k}'} = -V/L^3$ between $\vec{k}$ states in an energy band between E_F and $E_F + \hbar\omega_D$ and no interaction for other momentum states is assumed

$$V_{\vec{k}\vec{k}'} = \begin{cases} -V/L^3 & \text{for} \quad \hbar^2k^2/(2m)\,,\, \hbar^2k'^2/(2m) < E_F + \hbar\omega_D \\ 0 & \text{otherwise}\,. \end{cases} \tag{1.64}$$

Then equation (1.62) becomes

$$\left(-\frac{\hbar^2k^2}{m} + E + 2E_F\right) g(\vec{k}) = -\frac{V}{L^3}\sum_{\vec{k}'} g(\vec{k}')\,,$$

$$\text{with} \quad E_F < \frac{\hbar^2k'^2}{2m} < E_F + \hbar\omega_D\,. \tag{1.65}$$

By dividing both sides by the term in parenthesis, summing over all $\vec{k}$ with $E_F < \hbar^2k^2/2m < E_F + \hbar\omega_D$ and canceling $\sum g(\vec{k})$ with $\sum g(\vec{k}')$ one obtains

$$1 = \frac{V}{L^3}\sum_{\vec{k}} \frac{1}{-E + \frac{\hbar^2k^2}{m} - 2E_F}\,, \tag{1.66}$$

with $E_F < \hbar^2k^2/2m < E_F + \hbar\omega_D$. This sum can be calculated by approximating it as an integral. To do so, the density of states $N(\xi) = (2\pi)^{-3}4\pi k^2 dk/d\xi$ is introduced, where $\xi = \hbar^2k^2/2m - E_F$. Then equation (1.66) becomes

$$1 = V\int_0^{\hbar\omega_D} N(\xi)\frac{1}{2\xi - E}\,d\xi\,. \tag{1.67}$$

If $\hbar\omega_D \ll E_F$, $N(\xi)$ can be considered constant and replaced by its value $N(0)$ at the Fermi energy. The integration can be performed analytically and yields

$$1 = \frac{N(0)V}{2}\ln\frac{E - 2\hbar\omega_D}{E}\,. \tag{1.68}$$

For weak interactions,*i.e.*, $N(0)V \ll 1$ this equation has the solution

$$E = -2\hbar\omega_D e^{-2/N(0)V}\,. \tag{1.69}$$

E was defined as the energy that the two fermions added to the Fermi sphere acquire in addition to the $2E_F$ that would be expected in the case of no interactions. When this energy is negative it follows that a bound state of the two fermions exists, mediated by the interaction. This is a Cooper pair.

In this simple model only two fermions were added to a Fermi sphere. In general many Cooper pairs can be formed. It can be shown that the size of a Cooper pair is much larger than the average distance between nearest neighbor particles, giving rise to correlations between them. The energy spectrum of a Cooper paired gas shows a gap above the ground state of the system, which corresponds to the energy E needed to break up a Cooper pair.

BCS state in a gas of neutral atoms

The principle of Cooper pairing was explained in the case of a zero temperature Fermi gas and an idealized interaction. Cooper pairing can also occur for finite temperatures and scattering between neutral atoms. A BCS phase transition between a normal degenerate Fermi gas and a Fermi gas with a Cooper paired phase is predicted to occur when the temperature decreases below a critical temperature T_{BCS}. The critical temperature depends on the nature of the attractive interaction. Several coupling mechanisms can be considered, such as p-wave scattering [101, 102], exchange of phonons (density fluctuations) and s-wave collisions [103, 71, 104, 105]. Of all these, s-wave collisions are the most promising since the predicted critical temperature is the highest. The critical temperature can be calculated and is [105, 101]

$$T_C \simeq T_F \exp(-\pi/2k_F|a|)\,, \tag{1.70}$$

where a is the s-wave scattering length. Although this equation is only valid for $k_F|a| \ll 1$. In the extreme case $k_F|a| = 1$, $T_{BCS} \simeq 0.2\,T_F$, which suggests what the upper bound might be for the transition temperature.

Consider how the necessary attractive interaction can be obtained for ^{6}Li. A consequence of the anti-symmetrization postulate for the wavefunction of identical fermions is that s-wave collisions are suppressed (see section 1.3). By using fermionic atoms in different internal states, the fermions become distinguishable and s-wave collisions are possible. In ^{6}Li the states $|F = 1/2, m_F = 1/2\rangle$ and $|F = 1/2, m_F = -1/2\rangle$ are especially well suited for this task. Since they are the states with the lowest energy, their mixture should be more stable against inelastic collisions than any other mixture. Even more important is the s-wave scattering length in collisions between these states. For magnetic fields higher than $\sim 1000\,$G the electronic and nuclear spins are decoupled. In the case of the two states mentioned above, both electronic spins are parallel. The states are distinguished by different orientations of the nuclear spin. It follows that the scattering length is the triplet scattering length of ^{6}Li, $a_T = -2160\,a_0$, which is large and attractive. Furthermore, a pronounced and wide Feshbach resonance exists around 800 G, making it possible to tune to even more extreme values (see section 1.3.3). This makes it easy to enter the regime of strong coupling, $k_F|a| \simeq 1$.

A new question arises in this strong coupling regime: is the gas still stable against collapse? As we have seen in section (1.1.3), for a strong attractive interaction a collapse of the gas can occur. The subject was treated in greater detail in [71]. In the vicinity of the collapse, density fluctuations occur easily. This can lead to an additional attractive interaction due to phonon exchange, as it is the case in low T_C superconductors. Including this effect, the critical temperature T_{BCS} has a more complicated dependence on the experimental parameters as given by equation (1.70). It has been calculated numerically in [71]. The maximum value $T_{BCS} = 0.025 T_F$ is reached for $\lambda = 0.98$, shortly before the collapse.

A different type of BCS transition was proposed by M. Holland *et al.* in [72]. A pairing transition in the vicinity of a Feshbach resonance is considered (see section1.3.3). Near a Feshbach resonance, the scattering length becomes very large, because the colliding atoms can enter a quasibound molecular state during their collision, in which they can remain for a long time compared to the time a normal collision takes. Instead of calculating an effective scattering length and developing BCS theory with this, Holland treated the quasibound state separately. Cooper pairs appear as a population of this state. The calculation was performed for the case of ^{40}K. A high critical temperature of $T_C = 0.5\, T_F$ is found. A maximum of 1.5% of the atoms form quasibound molecules, which here play the role of Cooper pairs.

Detection of the BCS state

In superconductors the BCS phase transition is evident in several macroscopic properties. The resistance drops to zero due to the frictionless flow of the superfluid. The material becomes a perfect diamagnet, which is the basis for the striking experiment of floating a superconductor over a magnet. The heat capacity has a discontinuity at the phase transition.

In neutral atomic gases, the detection of a Cooper paired phase is more difficult. The fermions are neutral, which means that measurements of electric or magnetic properties can not show signs for Cooper pairing. The spatial and momentum distributions are only slightly modified in comparison with a degenerate Fermi gas, since only a small fraction of atoms in momentum states around k_F are involved in the pairing.

Over the last few years several methods of detecting the BCS state have been suggested. The following types of experiments have been proposed: the detection of the correlated Cooper pairs; to measure the energy gap or, more generally, the excitation spectrum; to measure the heat capacity [106]; and finally, to measure changes in the density profile due to the superfluidity.

The first set of proposed experiments considers the scattering of light off a normal versus a BCS phase. The spatial distribution of off-resonance light scattered from a BCS state is calculated in [107]. It is found that light is scattered into a large angle by the Cooper pairs, due to their small spatial extension. This angle is larger than the angle in which light from a degenerate Fermi gas without pairing is scattered. In [108] an increase in the intensity of off-resonance light scattered at small angles is calculated. Line shift and increase in the line width of a resonant transition is predicted in [109, 110].

The energy gap can be measured by spectroscopic means [111]. One of the atoms forming a Cooper pair is transferred to an different internal state *via* a Raman transition. This process breaks up the Cooper pair and therefore the laser must provide the pairing energy. This can be seen as a shift in the transition in comparison with a normal phase.

The excitation spectrum can be measured with Bragg spectroscopy [112] or by scattering of test particles [113, 65]. The dynamic structure factor which describes the outcome of these experiments has been calculated for a normal Fermi gas and a BCS gas in [114] and it has been shown that clear signatures of the superfluid phase exist.

Several proposals have been made to study the response of the superfluid phase on collective excitations. These can be density oscillations under periodic modulations of the trap frequency [115, 106]. For scissor modes, where one axis of the trap is rotated, transverse modes of excitation are suppressed for the superfluid but not for a collisionless normal fluid [116]. These modes have already been studied theoretically [117] and experimentally [19] for Bose-Einstein condensates of bosonic atoms. The moment of inertia is predicted to change with the appearance of a superfluid phase [118].

Lastly, for a BCS transition induced by a Feshbach resonance the density near the trap center should increase [119], which could be an experimentally observable signature.

1.2 Evaporative cooling

Evaporative cooling is to date the only cooling method by which quantum degeneracy can be reached. It was originally proposed by Hess for the cooling of magnetically trapped hydrogen [120] and soon afterwards experimentally implemented [121, 122]. Later it was used to cool alkalis and led to the first BECs in dilute vapors of alkali metals [7, 123, 8].

The mechanism of evaporative cooling is the following (figure 1.8a): particles with an energy higher than the mean energy are removed from the system. The remaining particles rethermalize by elastic collisions and the system thereby acquires a lower temperature. This principle occurs commonly in nature, *e.g.*, during evaporative cooling of water or during the cooling down of an excited nucleus by the ejection of neutrons.

In a typical BEC experiment evaporative cooling is implemented in the following manner (figure 1.8b): The atoms are in a low magnetic field seeking internal state. They are kept in a magnetic field which has a minimum at the center and increases in all directions. For small enough temperature this potential can be well approximated by an anisotropic harmonic potential. Neglecting gravity, surfaces of equal magnetic field modulus correspond to the potential energy $U = m_F g_F \mu_B |\overrightarrow{B}|$ (where m_F is the magnetic sublevel, g_F the Landé factor and μ_B the Bohr magneton). Selective removal of high energy atoms is achieved by driving transitions to high field seeking states ($m_F g_F < 0$) which are ejected from the trap, using Zeeman or hyperfine radio frequency transitions. The selectivity comes from the fact that these transitions are frequency shifted proportional to $|B|$ due to the Zeeman effect. For a given radio frequency ν, atoms at a spatial position corresponding to a given potential energy E_{cut} are removed. One commonly speaks of a *radio frequency knife* which "cuts" atoms out of the trap at the *cut energy* E_{cut}.

Because of the motion of the atoms this means that after a time which is long in comparison with the trap frequencies all atoms with a total energy higher than E_{cut} are lost. To characterize the cut energy one introduces the cut parameter η, which links E_{cut} and the temperature: $E_{cut} = \eta k_B T$. Typical values for η range from 5 to 10.

This simple picture breaks down when the earth's gravitational potential energy becomes comparable to the intended cut energy. In this case the confining potential can be shifted so strongly with respect to the $|B|$ field equipotential surfaces that only atoms in the lower part of the trap are removed. This effect can be harmful, since removal takes longer. However, it can also be helpful, for example if only atoms with low horizontal angular momentum should be removed, in which case the average angular momentum per particle increases [124].

The evaporation cooling process decreases temperature and thus, for constant elastic collision rate, decreases the rate of atoms generated by collisions with an energy above the cut energy. This effect slows down the cooling process and must be counterbalanced by a continuous decrease in the cut energy such that η is kept approximately constant.

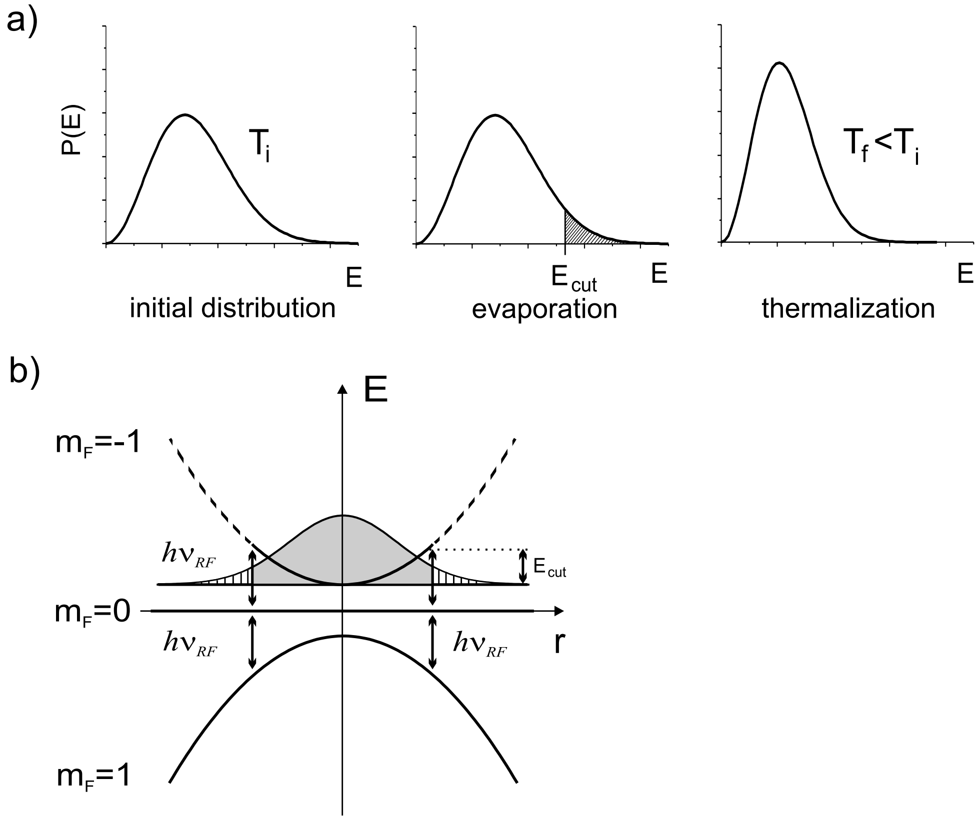

Figure 1.8: *The principle of evaporative cooling. a) Particles with an energy above* E_{cut} *are removed from the initial distribution, which has a temperature* T_i*. After thermalization due to elastic collisions the temperature has decreased to* T_f*. b) Implementation of the selective removal of high energy atoms. Shown is the energy of the hyperfine ground state triplet* $|F=1, m_F=-1,0,1\rangle$ *of* ^7Li *versus the distance from the magnetic trap center. Atoms in the* $m_F=-1$ *state are trapped, while in the* $m_F=0,\,1$ *states they are untrapped. A radio frequency wave is resonant with atoms having the potential energy* E_{cut}*. These atoms are transferred to nontrapped states and thus removed from the trap. After several trap oscillation periods, all atoms with a total energy superior to* E_{cut} *have been removed due to motion in the trap.*

This kind of evaporative cooling is called forced evaporative cooling.

Evaporative cooling relies on elastic collisions. The elastic collision rate $\Gamma = \bar{n}\sigma v$, where $\bar{n}$ is the mean density , σ the elastic scattering cross section and v the mean velocity, depends on the atom number N and on the temperature: $\Gamma \propto N/T$. This means that the temperature has to decrease at a rate at least proportional to the atom number, in order for the evaporative cooling not to slow down. This regime is called runaway evaporation. The quantity of interest in evaporative cooling is the phase-space density $\rho = n\lambda^3 \propto N/T^3 \propto \Gamma/T^2$, which can increase even if Γ decreases due to its stronger dependence on temperature. But under these conditions the evaporation process will slow down drastically. At the border to runaway evaporation the elastic collision rate stays constant and $\rho \propto T^{-2}$. This is exactly the case in our experiment (see section 3.3.1). It can be shown that the number of elastic collisions must exceed the number of inelastic collisions by a factor of about 200 ($\Gamma_{el}/\Gamma_{in} > 200$) to be in the runaway regime [125].

A further complication to evaporative cooling are loss processes. They hinder the cooling by removing atoms which have an energy below E_{cut}. If atoms with an energy below $k_B T$ are removed the sample is even heated. In addition some loss processes lead to the conversion of internal energy to kinetic energy.

There are five types of loss processes:

- **Collisions with the background gas.** During a collision an atom can acquire an energy higher than the depth of the trapping potential. This leads to loss of the atom. During a glancing incidence collision, only a fraction of the total collision energy is transferred to the atom. The atom stays trapped, rethermalizes and thus heats the sample. Loss due to background gas collisions does not depend on the density of the cloud. It can be reduced by reducing the residual gas pressure in the vacuum chamber.

- **Spin-exchange collisions.** Atoms can exchange angular momentum during a collision. For example, two atoms in the $|2,1\rangle$ state can produce one atom in the $|2,2\rangle$ state and one in the untrapped $|2,0\rangle$ or $|1,0\rangle$ state. In the latter case the hyperfine energy is released, which leads to heating. Fortunately these collisions are subject to strict selection rules: the orbital angular momentum quantum numbers l and m_l, as well as the total spin projection $M_F = m_{F_1} + m_{F_2}$ must be conserved. Thus it is easy to avoid this kind of loss by making the proper choice of internal state. Stretched states (states of maximum F and m_F), for example, are always stable.

- **Dipolar collisions.** The magnetic dipole-dipole interaction has less severe selection rules: only $m_l + M_F$ is conserved and $|\Delta l|$ is required to be 0 or 2. Thus atoms that would be stable against spin relaxation can end in an untrapped state. The dipole-dipole interaction strength depends on the internal state. According to the Fermi golden rule, the transition probability also depends on the number of accessible internal and momentum endstates and thus on the internal energy converted to kinetic energy during the collision. For this reason, states in the lower hyperfine multiplet are potentially less vulnerable to dipolar decay. Dipolar collisions can eventually be reduced by tuning the magnetic field. Although they depend on density $\Gamma_{in} \propto \beta n$, a decrease in trap confinement is useless since the important parameter Γ_{el}/Γ_{in} is proportional to $\sqrt{T}$. Instead, the confinement must be increased to adiabatically increase the temperature.

- **Three body recombination.** The absolute ground state of an ultracold gas is a solid. However, the gas is metastable because of energy and momentum conservation which prevents the formation of a molecule during a simple two-body collision. Only in a three-body collision can a molecule be formed and excess energy and momentum absorbed by the third atom. This type of collisions leads to loss and heating. But since it is proportional to n^2 it can be reduced by lowering the density by an adiabatic expansion of the gas.

- **Majorana spin flip.** Atoms are trapped in a magnetic field minimum if their magnetic moment is antiparallel to the local magnetic field line, since then their energy increases with higher B-field modulus. While the atom is moving in the trap the direction of the local B-field vector changes. Normally an atom's spin follows the field adiabatically. But if the rate of change of the direction of the B-field vector $\frac{\partial\Theta}{\partial t}$ is greater than the Larmor frequency $\omega_l = 2\pi\, 1.4\frac{\mathrm{MHz}}{\mathrm{G}}|B|$, then the spin can not respond adiabatically and transitions to other states occur. If these states are trapped, further loss is induced by spin relaxation collisions; if not, the atom is simply lost. This loss mechanism is important for quadrupole traps which have a B-field zero at the center. Its rate is $\Gamma = \hbar/(ml^2)$. It can be prevented by using a trap type which has a nonzero and high enough B-field minimum, *e.g.*, a Ioffe-Pritchard trap.

In all of the above cases, when the gas is near the hydrodynamic regime, *i.e.*, when the mean free path is shorter than the trap diameter, or equivalently, when the collision rate is higher than the trap oscillation frequency, further heating and loss are induced. In this case an atom in an untrapped state will gain energy while escaping the trap and distribute this energy to other trapped atoms in collisions or expel other atoms. This can even have the character of an avalanche [126].

1.2.1 Sympathetic cooling

Evaporative cooling relies on the existence of elastic collisions. If the atomic species of interest does not have a sufficiently high elastic collision cross section to allow evaporative cooling, it may still be possible to cool it by bringing it in contact with a thermal bath that is actively cooled. This *sympathetic cooling* was originally implemented with two species ion traps, where sideband cooling was performed on one ion species [127, 53]. Due to the electrostatic interaction between the ions, the ions of the other species were also cooled. This could be an interesting cooling scheme for quantum computation or optical clocks, since it leaves the internal state of the Q-bits or clock ions untouched but cools them all the same. Neutral atoms and molecules such as europium, chromium, and lead monoxide have been cooled sympathetically by thermal contact due to collisions with a cryogenically cooled Helium buffer gas [54, 55, 56]. Sympathetic cooling in combination with evaporative cooling was first demonstrated using two different internal states of ^{87}Rb and produced two overlapping Bose-Einstein condensates [57].

The importance of sympathetic cooling for Fermi gases is that s-wave collisions are forbidden in a polarized sample of fermions, due to the necessary antisymmetry of the wavefunction. Higher order partial angular momentum waves freeze out with decreasing temperature if the interatomic potential decreases faster than $1/r^3$ ($n > 3$ for $1/r^n$), which is the case for the usual long-range Van der Waals interaction ($n = 6$) (see section 1.3). The p-wave cross section, for example, decreases as T^{-2} and is by far too small to sustain evaporative cooling in the temperature region of interest for degeneracy. An exception to this is the magnetic or electric dipole-dipole interaction which has an $1/r^3$ dependence and thus allows p-wave collisions also at $T = 0$. This might be important in chromium, which has a high magnetic momentum [128]. An electric dipole moment could be induced in lithium by applying an electric field, giving rise to collisions [129]. Another exception are p-wave shape resonances, which are discussed in section 1.3.3.

The most straightforward approach to overcome this lack in elastic collisions is to mix the fermions with distinguishable atoms. Then s-wave collisions are allowed and evaporative cooling is possible. The first implementation of this was done by mixing equal amounts of two internal states of fermionic ^{40}K. Evaporative cooling was performed on both states simultaneously resulting in two degenerate Fermi seas with a maximum degeneracy of $T/T_F = 0.5$ [60]. At high degeneracies this cooling scheme slows down, because of Pauli blocking of the collisions.

This approach is impossible for lithium, since spin relaxation between two different internal states has a particularly large cross section. Our method consists of mixing the fermionic with the bosonic isotope in about a 1:1000 ratio. Evaporative cooling is performed only on the bosonic isotope, and s-wave collisions between the isotopes mediate sympathetic cooling of the fermionic isotope. In our experiment this results in a Fermi gas with a degeneracy of $T/T_F = 0.2(1)$ (see section 3.4.5). One advantage of this method is that Pauli blocking occurs only for the fermionic component.

Sympathetic cooling is a general scheme and appears several times in different flavors in our experiment. In a preparation stage for evaporative cooling, the bosonic component is cooled optically in the magnetic trap, which sympathetically cools the fermions due to collisions (see section 3.1.5). For the production of a condensate in the $|F = 1, m_F = -1\rangle$ state we can evaporatively cool the fermionic component and allow the bosons to be cooled sympathetically. For a faster evaporation, both components can be evaporatively cooled, using mainly the collisions between the components for rethermalization (see section 3.4.4).

Several other groups plan to sympathetically cool fermions, *e.g.*, ^{40}K by ^{87}Rb [43, 130, 131] or the fermionic by the bosonic isotope of Ytterbium [132] (see discussion in section 2.3). The group of W. Ketterle recently produced a ^{6}Li Fermi sea by sympathetically cooling with ^{23}Na [63] and J.E. Thomas at Duke university cooled a mixture of the two lowest states of ^{6}Li in a dipole trap to degeneracy [64]. Sympathetic cooling of bosonic ^{7}Li by ^{133}Cs in a CO_2 optical trap was also shown [62].

1.2.2 The Limits of sympathetic cooling

The goal of sympathetic cooling of fermions by bosons is to reach the highest possible degeneracy T/T_F of the fermionic component. Several limits hinder the achievement of arbitrary high degeneracies. In the following we will discuss some of these limits.

Heat capacities

The first limit involves the heat capacities of the actively cooled component A, C_A, and the sympathetically cooled component S, C_S. During sympathetic cooling, the heat capacity of A is continuously lowered since atoms are evaporated. Shortly after the heat capacities of both components become equal ($C_A = C_S$), the cooling stops. Once C_A is smaller than C_S, an initial reduction in the temperature of A due to evaporation over an imposed cut energy does not cool S. On the contrary, S will heat A up to nearly the same initial temperature. Thus, still more atoms of A will be evaporated with the same cut energy, which reduces the heat capacity of A and amplifies the effect. At the end, all atoms of A are lost, with only a minor temperature reduction of S.

For classical gases the heat capacity is $C_{cl} = 3Nk_B$ and the condition of equal heat capacity becomes a condition of equal atom number. To lower the temperature at which the decoupling occurs, the number of sympathetically cooled atoms has to be reduced.

In the quantum regime the heat capacities behave differently. The heat capacity of a bosonic (fermionic) gas with $T < T_C$ ($T < T_F$) is [133, 134]

$$C_B = 12\frac{\zeta(4)}{\zeta(3)}N_B k_B \left(\frac{T}{T_C}\right)^3 , \tag{1.71}$$

$$C_F = \pi^2 N_F k_B T/T_F \, . \tag{1.72}$$

To check if the sympathetic cooling breaks down, one has to compare the heat capacities during the whole evaporative cooling process. In the following we will limit the discussion to the interesting regime $T \leq T_C$, T_F. Other cases can be checked along the same lines.

In our experiment we can enter the region of quantum degeneracy with two different schemes, for each of which we have to continue the discussion separately.

In the first scheme, the fermions (component S) are sympathetically cooled by evaporative cooling of the bosons (component A) (see section 3.3.2). The number of fermions stays nearly constant during the evaporation. The condensate produced in this scheme is unstable, which means it can not exceed a maximum number of atoms N_{max}. Thus the temperature must remain high enough that less than N_{max} atoms are in the condensate, in practice not much lower than T_C. Below this temperature the condensate collapses, leading to a reduction in T_C because of the reduced number of bosons (see section 1.1.8 and 3.3.1). The heat capacity of the bosons at $T = T_C$ is $C_B = 10.805\, N_B k_B$. By equating this quantity to the fermionic heat capacity eq. (1.72), expressing N_B and N_F in terms of T_C and T_F, and setting $T = T_C$, the limit in the achievable fermionic degeneracy $T/T_F = 0.3$ is found [61]. In the experiment we could obtain $T/T_F = 0.25(5)$, in good agreement with this prediction.

The second scheme uses the atoms in their lower hyperfine states (^{7}Li : $|F = 1, m_F = -1\rangle$, ^{6}Li : $|F = 1/2, m_F = -1/2\rangle$). The bosons (now component S) are sympathetically cooled by evaporation cooling of the fermions (now component A). As explained in section 3.4.3, only inter-isotope collisions are used to rethermalize the system. To optimize the collision ratio, a 1:1 boson-to-fermion number ratio is kept during the entire evaporation. The condensate is stable for arbitrary atom numbers because of the positive boson-boson scattering length, giving access to temperatures below T_C. This cooling scheme would break down if the heat capacity of the bosons exceeded by far the heat capacity of the fermions. To check if a fundamental limit exists, we can calculate the ratio of these two heat capacities below T_C and T_F. With the expressions (1.71) and (1.72) for the heat capacities and the expressions for T_C and T_F we obtain

$$\frac{C_B}{C_F} = \frac{4}{5}\pi^2 \left(\frac{\omega_B}{\omega_F}\right)^3 \frac{N_B}{N_F} \left(\frac{T}{T_F}\right)^2 = 5.4 \frac{N_B}{N_F} \left(\frac{T}{T_F}\right)^2 , \tag{1.73}$$

where ω_F and ω_B are the mean trap oscillation frequencies for the fermions and the bosons. To calculate the prefactor 5.4, the masses and magnetic moments of lithium in the used hyperfine states were taken into account. As we can see, the ratio of the heat capacities becomes lower for higher degeneracy, and thus there is no fundamental limit. The worst ratio is obtained at $T = T_C$ when the bosonic heat capacity reaches its maximum. At this point $T/T_F = T_C/T_F = 0.59$ which yields $C_B/C_F = 1.86\, N_B/N_F$ which is too small to provoke a breakdown of sympathetic cooling for $N_B = N_F$, a fact that we also observe experimentally.

The relative heat capacities will not give a limit in the degeneracy for this case, but there are other considerations which have to be taken into account. Sympathetic cooling is governed by three different types of timescales: the rethermalization of the thermal bath component(s) on which evaporation is performed, the rethermalization between the components, and the lifetimes of the different components. For successful sympathetic cooling the rethermalization timescales should be at least a factor 200 shorter than the lifetime. This can be a problem, especially at high degeneracies. First of all the density in the Bose condensate becomes big, thus giving rise to increased two- and three-body loss, and limiting the lifetime.

Pauli blocking

Next there are three processes reducing the inter-component collisions. The Pauli blocking will lower the number of possible scattering processes. This is unavoidable, since we are interested in producing a degenerate Fermi sea.

Phase separation

Next, the mean field interaction between the components can lead to a spatial phase separation. Collisions can occur only in the overlap of the clouds, which might be small and thus reduce thermal contact. As discussed in section (1.1.13), phase separation does not play a role for our current experimental parameters.

Superfluidity

Finally the Bose-Einstein condensate is superfluid for impurity atoms moving at a speed less than the speed of sound. If the Fermi velocity is below the sound velocity only the thermal component contributes to the collisions, leading to a slowdown in rethermalization [135]. For our experimental parameters this effect does not play a role.

Hole heating

A different kind of limit comes from the creation of holes in the degenerate Fermi gas by particle loss [136]. Consider a Fermi gas with N atoms at zero temperature, having a total energy $E(N)$. All energy states up to the Fermi energy E_F are occupied. A loss process would create a hole in the Fermi distribution with an energy $E_{loss} < E_F$. The energy of a zero temperature Fermi gas with $N-1$ atoms is $E(N-1) = E(N) - E_F$, since one atom is removed from the surface of the Fermi sphere. But with the loss process, the gas would have an energy $E' = E(N) - E_{loss} = E(N-1) + E_F - E_{loss} > E(N-1)$, greater than the energy of a zero temperature gas with $N-1$ atoms. Thus the gas has been heated by the hole creation. By similar considerations at finite temperature, and by converting the energy gain to a temperature increase using the heat capacity of the gas, a differential equation for the increase in temperature is obtained [136]. The solution of this equation is

$$T = T_0 \sqrt{1 + \frac{3t}{\tau_2}} \;\; ; \;\; \tau_2 = \frac{15\pi^2}{8} \left[\frac{T_0}{T_F} \right]^2 \tau_L \, , \tag{1.74}$$

where T_0 is the initial temperature, T_F the Fermi temperature of the initial cloud and τ_L the lifetime of the system due to losses. The system doubles its temperature after a time τ_2, which is proportional to the square of the ratio between initial and Fermi temperature. The more degenerate the gas is, the faster hole creation will heat. For our system the initial degeneracy is $T/T_F = 0.2$ resulting in $\tau_2 = 0.8\tau_L$. The system doubles its temperature in 0.8 lifetimes.

This effect becomes important at the end of the evaporation. When degeneracy is highest, *hole heating* is strongest and cooling by rethermalization is most prohibited by Pauli blocking. This has been simulated by T. Bourdel using a simulation analogous the one described in section (1.2.3). The equilibrium temperature of a Fermi gas in presence of losses was calculated with a Bose condensed gas at zero temperature as heatsink. The result is shown in figure 1.9.

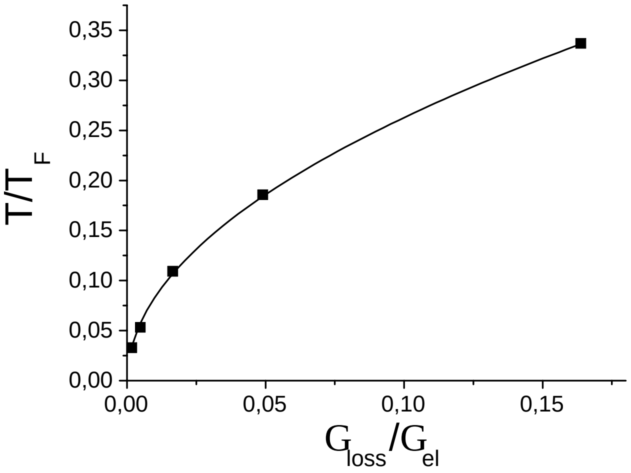

Figure 1.9: *The equilibrium degeneracy of a fermionic gas, heated by trap loss and cooled by a condensate at zero temperature versus the ratio of loss rate and elastic collision rate (figure courtesy of T. Bourdel).*

Degeneracy can also be limited by more trivial effects, such as heating by a trap with fluctuating potential due to technical noise or other technical imperfections such as a fluctuating cut energy. In the experiment we could measure degeneracies down to $T/T_F = 0.2(1)$. The exact determination of the degeneracy requires a more sophisticated method of determination of temperature (see section 3.4.5).

1.2.3 The Boltzmann equation

To understand quantitatively the evolution of temperature and atom number during processes such as sympathetic cooling, a simulation was written. The simulation is based on the numerical solution of two coupled Boltzmann equations describing the bosonic and fermionic distributions and is a generalization of the method proposed in [137]. The Boltzmann equation describes the evolution of the phase-space density distribution due to the motion of the particles in the potential and due to collisions. To simplify the calculation, the assumption of ergodicity is applied. It states that volumes in phase-space belonging to the same total energy have the same occupation. The validity of this assumption depends on the mixing of trajectories and thus on the potential shape and the collision rate. Even if this mixing is not fast enough, the ergodicity assumption is still valid if all processes bringing the cloud out of equilibrium are symmetric in energy. Under the ergodicity condition no information is lost when integrating the Boltzmann equation over equi-energy surfaces in phase-space. Furthermore, the assumption is made that bosons and fermions have the same mass m and thus the same energy density of state $\rho(E)$ in the trap (for justification see section 1.2.4). For the numerical solution of the differential equation the energy scale is discretised in steps of width ΔE up to a maximum energy E_{max}. The bosonic and fermionic energy distributions are given by b_i and f_i, where i indicates the energy interval $E_i = i\,\Delta E$. The resulting set of coupled equations is the following.

$$\begin{aligned}\rho_i \dot{b}_i = \frac{m\sigma_{BB}}{\pi^2\hbar^3}(\Delta E)^2 \sum_{k,l} \rho_h \left[b_k b_l (1+b_i)(1+b_j) - b_i b_j (1+b_k)(1+b_l)\right] + \\ \frac{m\sigma_{BF}}{\pi^2\hbar^3}(\Delta E)^2 \sum_{k,l} \rho_h \left[b_k f_l (1+b_i)(1-f_j) - b_i f_j (1+b_k)(1-f_l)\right] \,, \qquad (1.75)\end{aligned}$$

$$\rho_i \dot{f}_i = \frac{m\sigma_{BF}}{\pi^2\hbar^3}(\Delta E)^2 \sum_{k,l} \rho_h \left[f_k b_l (1-f_i)(1+b_j) - f_i b_j (1-f_k)(1+b_l)\right] \,, \qquad (1.76)$$

where $\rho_i = \rho(E_i)$, $j = k + l - i$ and $h = min(i, j, k, l)$. These equations are easy to understand. Change in the occupation of an energy interval E_i comes only from collisions, since motion in the trap conserves total energy. Collisions can happen between bosons with the scattering cross section σ_{BB} and between bosons and fermions with the cross section σ_{BF}. No collisions are allowed between fermions. This gives rise to the two collision sums for the change in the bosonic distribution and one sum for the fermionic distribution. To calculate the change in occupation of an energy interval E_i, each sum goes over all possible energies of the collision partners, observing energy conservation. Now the probability of collisions that scatter particles into and out of the considered energy interval are calculated. Here the energetic density of state of the lowest energy collision partner, which is limiting the collision probability, is multiplied with the occupations of the initial states and terms involving the occupations of the final states. The latter depend on statistics, and describe Bose enhancement with $1+b_i$ and Pauli blocking with $1-f_i$ instead of 1. This amplifies for bosons the scattering into already occupied states, ultimately giving rise to Bose-Einstein condensation in the ground state. For fermions, it prevents the occupation to exceed one atom per state. When solving the equations for the equilibrium distributions, these terms give rise to the Bose-Einstein and Fermi-Dirac distributions. Without them the classical Boltzmann distribution is obtained.

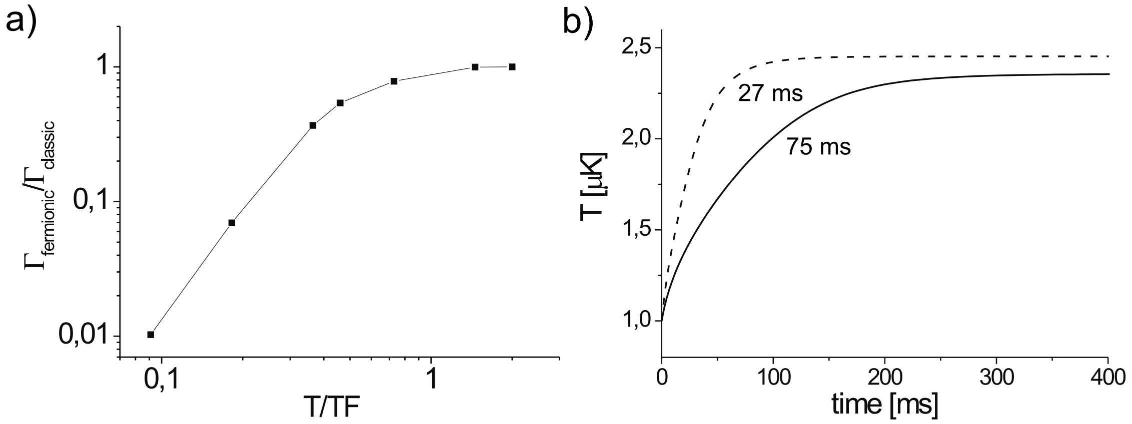

Figure 1.10: *Suppression of collisions due to Pauli blocking. a) The elastic collision rate of a zero-energy test particle in a Fermi gas versus degeneracy, normalized by the classical expectation. b) Rethermalization of a* ^7Li *cloud with* 5×10^3 *atoms and an initial temperature of* $1\mu K$ *with a Fermi gas of* 5×10^5 *atoms at* $2.5\mu K$ *corresponding to a degeneracy of* $T/T_F = 0.3$ *(solid line). An exponential fit gives a timescale of 75 ms. The same calculation assuming classical particles shows a rethermalization on a timescale of 27 ms (dashed line). The final temperatures differ because of the different heat capacities of a fermionic and a classical gas. The trap oscillation frequencies are* $\omega_{ax} = 2\pi \times 82\,Hz$ *and* $\omega_{rad} = 2\pi \times 4340\,Hz$*.*

1.2.4 Simulation of rethermalization including Pauli blocking

We first calculate the collision rate of a zero energy test particle in presence of a Fermi sea with varying degeneracy. The result is normalized by the collision rate of such a test particle in presence of a classical gas of the same temperature. The result is shown in figure (1.10a). For a degeneracy of $T/T_F = 0.2$ the collision rate is suppressed by a factor 10. The result of this calculation is the same as the result of the calculation involving the phase-space Boltzmann equation done in [65]. This justifies the assumptions of ergodicity and equal mass.

In the experiment, the zero energy test particle is replaced by a finite temperature bosonic cloud with an initial temperature below the temperature of the fermionic gas. The change in temperature with the rethermalization time of the bosonic cloud is observed. The fact that the initial temperature is finite reduces the suppression of collisions, since there are more collisions for which the final energy of the fermion is well above the Fermi energy, where Pauli blocking plays no role. Since the temperature of the bosonic test cloud increases with time, the suppression of collisions decreases continuously. Because of these two facts, the observable change in the timescale of the rethermalization is smaller than the change in the collision rate of a zero energy test particle. For this reason, a dynamic simulation was also done, using the experimental parameters achievable with our setup ($N_F = 5 \times 10^5$, $T = 2.5\mu\mathrm{K}$, $T/T_F = 0.3$, $N_B = 5 \times 10^3$, $T_{B_{init}} = 1\mu\mathrm{K}$, $\omega_{ax} = 2\pi \times 82\,\mathrm{Hz}$ and $\omega_{rad} = 2\pi \times 4340\,\mathrm{Hz}$). The temperature at each time step was determined by fitting a Boltzmann distribution to the bosonic energy distribution. The result is shown in figure (1.10b) for a fermionic degeneracy of $T/T_F = 0.3$ and compared to a calculation assuming classical particles. As expected, the rethermalization takes longer for a fermionic than for a classical gas. Exponential fits give rethermalization times of 75 ms and 27 ms respectively. This suppression of a factor 2.8 is lower than the suppression of the collision rate of 5 for a zero energy test particle under the same conditions because of the reasons explained above.

In the experiment a measurement has been performed for a degeneracy of $T/T_F = 0.5$, where in the simulation a factor 1.7 change in the rethermalization timescale is found. This change was unfortunately smaller than the measurement uncertainty, so that the effect of Pauli blocking could not be verified experimentally. But the measurement determined the rethermalization timescale and gave an estimate for the elastic scattering cross section (see section 3.3.5).

1.2.5 Simulation of sympathetic cooling

The same simulation has been used to simulate the sympathetic cooling process. After each time step in the evaluation of the Boltzmann equation, other effects are taken into account by modifying the energy distributions. Particle loss due to background gas, and two- and three-body collisions are simulated by removing atoms independent of energy. The evaporation is performed by putting the occupation of all states above the cut energy to zero for the component(s) on which evaporation is performed. From time to time the energy interval size ΔE and the maximum energy are reduced by a factor two to take into account the reduced energy spread of the clouds due to the cooling process. The result of this simulation for our experimental parameters is shown in figure (1.11).

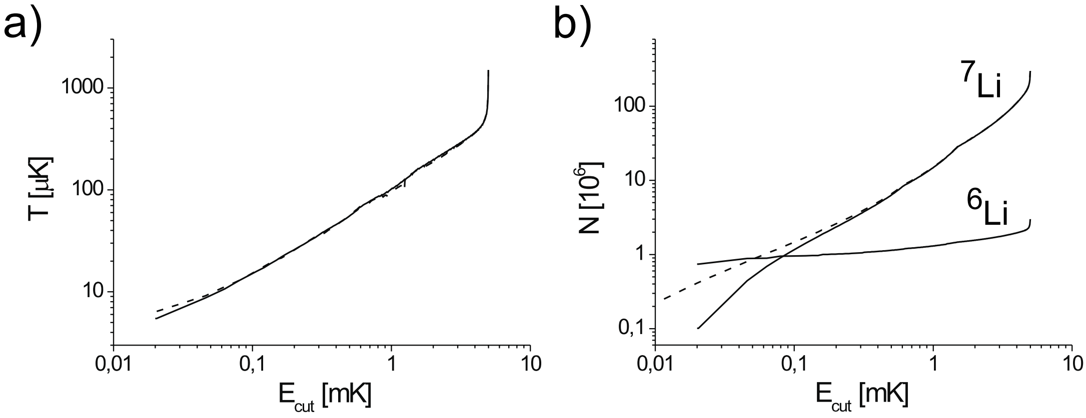

Figure 1.11: *Simulation of evaporative cooling. The development of temperature (a) and atom number (b) during sympathetic and evaporative cooling is shown. The solid lines describe sympathetic cooling of* 3×10^6 ^6Li *fermions by evaporative cooling of* 3×10^8 ^7Li *bosons. The number of fermions stays nearly constant during sympathetic cooling. The dashed line shows the behavior of* ^7Li *without* ^6Li*. It differs from the behavior with* ^6Li *present mainly in the region where the* ^6Li *and* ^7Li *atom numbers are comparable. The parameters for the simulation are* $\omega_{ax} = 2\pi \times 81\,Hz$*,* $\omega_{rad} = 2\pi \times 2.8\,kHz$*, an initial temperature of* $1.5\,mK$ *and a dipolar loss rate of* $\beta = 5 \times 10^{-19}\ cm^3 s^{-1}$*. The qualitative features are the same as in the experiment. Only when the heat capacities of* ^6Li *and* ^7Li *become of the same order of magnitude, the evaporation of* ^7Li *is affected by* ^6Li*.* ^6Li *and* ^7Li *always stay in thermal equilibrium. The experimental behavior could not be quantitatively reproduced.*

1.3 Collisions

Elastic collisions drive evaporative and sympathetic cooling, give rise to the mean field potential which determines the properties of the condensate, and lie behind phenomena such as bright solitons. The theory of elastic collisions is well documented in textbooks [138]. For this reason only a brief summary will be given.

The scattering problem of two atoms can be reduced to the scattering of a particle with reduced mass in the molecular potential between the two atoms. The corresponding Schrödinger equation can be solved by the ansatz

$$\Psi_k(\vec{r}) = e^{i\vec{k}\vec{r}} + f(k, \vec{n}, \vec{n}')\frac{e^{ikr}}{r}\,. \tag{1.77}$$

The first term describes an incoming plane wave with momentum $\vec{k}$ and the second term a scattered outgoing spherical wave. The scattering amplitude is $f(k, \vec{n}, \vec{n}')$, where $\vec{n}$ and $\vec{n}'$ are the directions of $\vec{k}$ and $\vec{r}'$. The measurable quantities are the differential and total scattering cross section, defined as the flux of particles going into the spherical angle $d\Omega$ or the total flux of scattered particles, both normalized on the incoming flux. Their relation with the scattering amplitude is

$$\frac{d\sigma}{d\Omega} = |f(k, \vec{n}, \vec{n}')|^2\,, \tag{1.78}$$

$$\sigma(k, \vec{n}) = \int |f(k, \vec{n}, \vec{n}')|^2\, d^2n'\,. \tag{1.79}$$

The scattering amplitude is to first order given by the Fourier transform of the potential (Born approximation).

The solution of the scattering problem is simplified considerably if the scattering potential is isotropic. In this case the scattered wave is also isotropic around the direction of the incident wave. The wavefunction can be expanded in terms of angular momentum partial waves (named s, p, d, f for $L = 0, 1, 2, 3\hbar$). The scattering amplitude acquires a phase factor $e^{i\delta_l}$ for each angular momentum order l. When plugging this ansatz into the Schrödinger equation, a one dimensional Schrödinger equation for the radial wavefunction is obtained. In addition to the scattering potential, a centrifugal potential $\hbar^2 l(l+1)/(mr^2)$ depending on the angular momentum appears. Solutions of this Schrödinger equation, giving the dephasing δ_l and thus the scattering properties, can easily be obtained numerically.

The centrifugal potential has far-reaching consequences. For angular momenta $l > 0$ it leads to the formation of a centrifugal barrier if the molecular potential decreases faster than r^{-3} (see figure 1.13). If the collisional energy E is less than the height of the barrier E_c, the wavefunction will mainly probe the adiabatically varying outside of the potential hill and is thus reflected without phaseshift. This means that scattering at nonzero angular momentum becomes suppressed for sufficiently low energies. This can

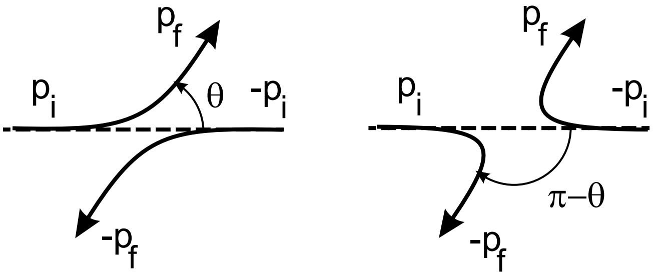

Figure 1.12: *Two scattering processes leading to the same final state for indistinguishable particles.*

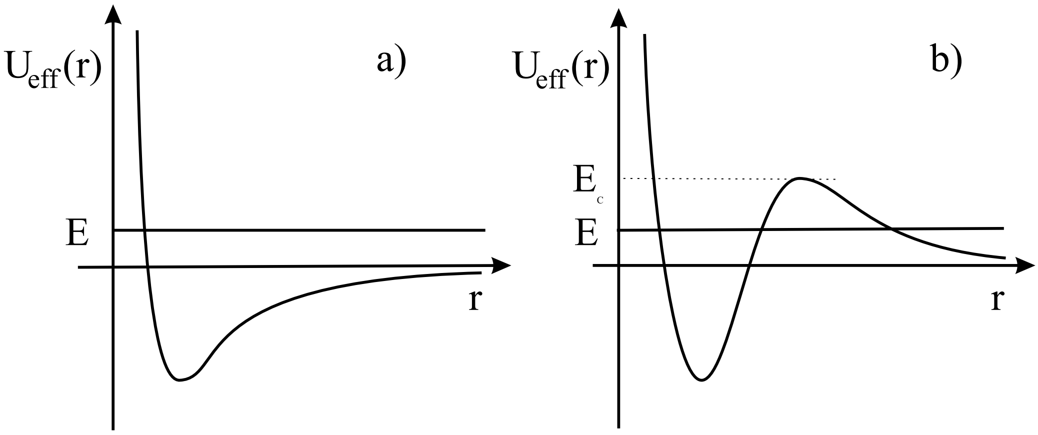

Figure 1.13: *The potential entering the 1D Schrödinger equation. a) s-wave scattering b) p-wave scattering, a centrifugal term is added to the interatomic interaction and leads to a centrifugal barrier with height E_c.*

also be understood in the particle picture. Angular momentum for very slow atoms requires a large distance between the two atoms even at their closest point to each other (since $\overrightarrow{L} = \overrightarrow{p} \times \overrightarrow{r}$). But at large distances the interatomic potential is weak and does not scatter. Only isotropic s-wave scattering is possible at low energies. It can be described by a single quantity, the s-wave scattering length a. The cross section can be written as

$$\lim_{k\to 0} \sigma_{l=0}(k) = 4\pi a^2 \quad \text{(distinguishable particles)}\,, \tag{1.80}$$

where the scattering length is defined as

$$a = -\lim_{k\to 0} \frac{\tan \delta_0(k)}{k}\,. \tag{1.81}$$

It can be shown that the cross sections for scattering with angular momentum go to 0 with decreasing k as

$$\sigma_{l\neq 0}(k) \propto k^{4l}\,. \tag{1.82}$$

Until now, we have considered the scattering of distinguishable particles. The two scattering processes shown in figure (1.12), corresponding to $f(k,\Theta)$ and $f(k,\pi-\Theta)$, can then be distinguished in principle. For identical particles, this is not the case and the two scattering amplitudes interfere. It can be shown that for bosons (fermions) this interference doubles the contribution for even (odd) angular momentum waves and cancels the contribution of odd (even) waves to the total scattering cross section. This implies that fermions do not scatter at low energies, where only s-waves can contribute, whereas the bosonic scattering cross section doubles in comparison with distinguishable particles. The suppression of collisions for identical fermions at low temperature is the principal obstacle for evaporative cooling of fermions. Remedies for this have been discussed in section (1.2.1).

1.3.1 Energy dependence of the cross section

The scattering cross section depends on the collision energy. Taking as a simple model potential the delta potential, the s-wave cross section can be obtained analytically and yields

$$\sigma(k) = \frac{8\pi a^2}{1+k^2a^2}\,. \tag{1.83}$$

For large k the scattering saturates at the so called *unitary limit* $\sigma = 8\pi^2/k^2$.

To obtain a more realistic idea of this dependence the Schrödinger equation is solved numerically. As model potential a Van der Waals potential with hard sphere core is chosen

$$\left\{\begin{array}{ll} V(r) = +\infty\,, & \text{for}\, r < r_c\,, \\ -C_6/r^6 & , \text{for}\, r \geq r_c\,. \end{array}\right. \tag{1.84}$$

The C_6 coefficient is often known from photoassociation measurements [139]. The hard core radius r_c is chosen to produce the scattering length a at zero energy. It is convenient to introduce the range of the Van der Waals potential $a_c = (2m_rC_6/\hbar^2)^{1/4}$. Using this potential, the radial Schrödinger equation is solved numerically for different momenta of k, which delivers the phase shift δ_0 and thus the scattering cross section. For $a > 0$ the result of this calculation is well approximated by the analytic result obtained for the delta function (1.83). For $a < 0$ by contrast, the scattering cross section goes to zero for $ka_c \approx 1$. The explanation for this is found in [140] by calculating the first order correction to the phase shift which yields

$$\tan\delta_0(k) \approx -ak - \frac{1}{2}a_ca^2k^3\,. \tag{1.85}$$

For negative a, the first term (which dominates at low momenta k) is positive, while the second (dominating at high momenta) is negative. There is a momentum k at which the phase shift is zero and thus no scattering is possible.

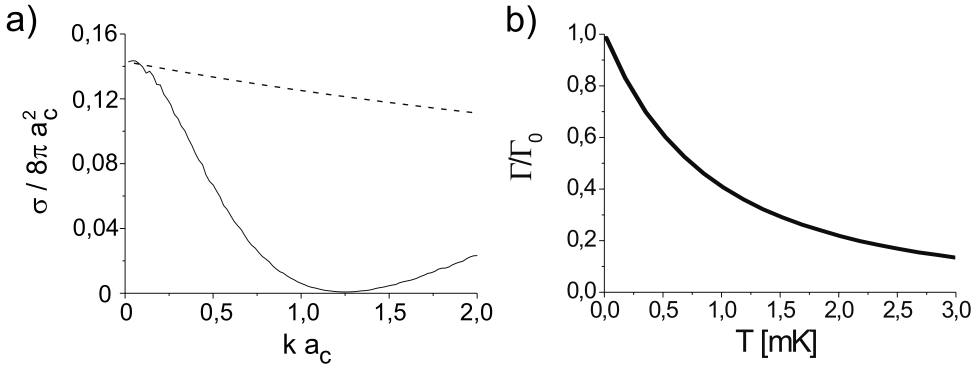

Figure 1.14: *Energy dependence of the scattering cross section of the* $^7Li\,|F=2, m_F=2\rangle$ *state, which has the negative scattering length* $a=-1.4\,nm$ *(*$a/a_c=-0.38$*). a) The scattering cross section (solid line) has a zero crossing at* $ka_c=1.25$ *corresponding to* $6.6\,mK$*. For a positive scattering length with the same magnitude* $a=+1.4\,nm$ *the cross section decreases only slightly with energy (dashed). b) Effective scattering cross section normalized by the cross section at zero temperature versus the temperature, calculated by averaging curve a) over the occurring collisions.*

This absence of interaction plays an important role in lithium and was the main obstacle to overcome before evaporative cooling could start (see section 3.1.5). The result of a calculation done by J. Dalibard is shown in figure (1.14a). It uses the C_6 coefficient of lithium $C_6 = 1.328 \times 10^{-76}\mathrm{Jm}^{-6}$ [139] and the scattering length of the $^7\mathrm{Li}\,|F=2, m_F=2\rangle$ state ($a=-27\,a_0=-1.4\,\mathrm{nm}$ from [141] where $a_0=0.5\,\mathrm{nm}$). The zero crossing appears at an energy of $k_B \times 6\,\mathrm{mK}$, which corresponds to the temperature of our atoms in the magnetic trap. For comparison, the result for a positive scattering length of same magnitude is plotted after equation (1.83). The cross section decreases only slightly for the considered energy region.

To calculate the suppression of collisions in a cloud of temperature T, an average over the occurring collision energies has to be taken. The reduction in collision rate in comparison with a constant cross section σ_0 is given by

$$\frac{\gamma}{\gamma_0} = \frac{1}{8\sigma_0 v_0^4}\int_0^\infty dv_r\, v_r^3 \sigma_{el}(v_r)\exp\left(\frac{v_r^2}{4v_0^2}\right)\,, \tag{1.86}$$

where $v_0=\sqrt{k_B T/m}$. This is plotted in figure (1.14b). For a temperature of 2 mK the collisions are suppressed by a factor 5. This effect was a significant obstacle for us to start the evaporative cooling and could finally be overcome by Doppler cooling in the magnetic trap.

1.3.2 Mean field potential

An atom submerged in a cloud of scatterers experiences an effective potential, resulting from the scattering with all other particles. For low temperatures this *mean field* potential depends only on the scattering length and not on the exact shape of the scattering potential. It can be shown that the mean field potential in 3D for distinguishable particles has the magnitude

$$U = \frac{4\pi\hbar^2 an}{m} \tag{1.87}$$

and takes twice this value for identical bosons in a thermal cloud. For a positive value of the scattering length, the mean field leads to a repulsion of the atoms in the cloud, leading to a growth in size. If the mean field exists between two different components, a phase separation can be the consequence (see section 1.1.13). For a negative scattering length, the mean field is attractive and leads to a shrinking of the cloud size. This can lead to the collapse of the cloud or to the formation of a bright soliton (see section 3.3.1 and 3.6.5).

1.3.3 Resonance enhanced scattering

The scattering cross section depends on the phase shift between the incoming and outgoing wavefunction of the interatomic potential. If a bound state lies close to the energy of the colliding atoms, then the atoms can enter this bound state during the collision, which corresponds to the formation of an excited molecule. The molecule decays back into the free atoms, which will have accumulated a phaseshift, that can be large. Thus the scattering cross section is resonantly enhanced.

Feshbach resonances in collisions of ultracold atoms have been first predicted in [70]. They have been first observed in a Na BEC by the group of Ketterle [142] and shortly afterwards in ^{85}Rb by Cornell and Wieman [143, 144]. This resonance was used to condense ^{85}Rb [145]. Many resonances have been measured in ^{133}Cs and lead to better knowledge of the scattering potential, which in turn was useful to determine the collisional frequency shift of Cs fountain clocks [146, 147, 148].

Several different situations can lead to a bound state at the collision energy (see figure 1.15). The simplest is a bound state of the s-wave scattering potential at zero energy, a zero-energy resonance as it exists in Cesium.

For a polarized fermionic sample, s-wave collisions are forbidden, but p-wave scattering plays a role. At collision energies below the centrifugal potential hills height, a quasi bound state with the collision energy can exist confined by the potential hill.

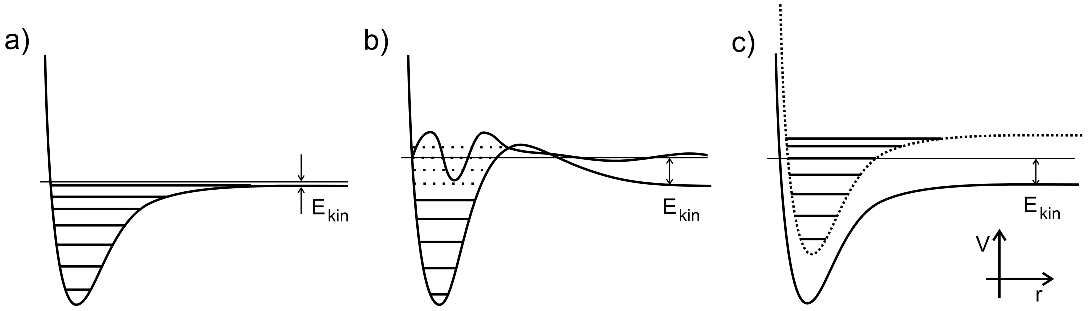

Figure 1.15: *Different types of resonance enhanced scattering. Shown are molecular potentials playing a role for the scattering process. Energy levels are marked with solid lines. The collision energy is E_{kin}. a) Zero-energy resonance. A (real or virtual) bound state lies near the dissociation limit. During a collision the atoms can enter this bound state and accumulate a phase shift. b) p-wave shape-resonance. The scattering potential has a centrifugal barrier. For some energies, the wavefunction is resonantly enhanced in the potential well (symbolized by dotted lines and the wavefunction for E_{kin}). Again, this leads to an increase in the time the atoms stay together and thus to an increased phaseshift. c) Feshbach resonance. The collision energy coincides with the boundstate of a molecular potential different from the scattering potential. The atoms can form a molecule in this state for some time and accumulate a phase shift. If the magnetic moments of the two molecular potentials are different, there relative energy can be shifted by applying a magnetic field and a bound state can be brought into resonance.*

Under these conditions the wavefunction has a large amplitude inside the potential hill, due to tunnelling.

Experimentally, the most useful type of resonance is a Feshbach resonance. Here the atoms are coupled to a bound state of a molecular potential belonging to different internal states of the atoms and having a higher dissociation energy (see figure 1.15c). An example of this situation are two colliding atoms in their lower hyperfine states. The Feshbach state could be a bound state of the molecular potential belonging to both atoms in the higher hyperfine state. This molecular potential may also have different angular momentum to conserve angular momentum during the coupling. The bound state is normally an excited state of the corresponding molecule. The importance of Feshbach resonances lies in the fact that the energy of the bound states can be shifted relative to that of the incoming atoms if the two molecular states have different magnetic moment, simply by applying a magnetic field. Even if at zero magnetic field the resonance condition is not fulfilled for any bound state, it is often possible to shift a bound state to resonance by applying a magnetic field with a reasonable strength. Thus the scattering length can be tuned experimentally to high positive and negative values. These big scattering length can give rise to fascinating phenomena such as phase separation, collapse or possibly Cooper pairing. Inelastic collisions usually accompany a Feshbach resonance, since their probability increases with the elastic scattering length a [149]. For three-body recombination the scaling is $\Gamma_{in} \propto a^4$ [150, 151]. This can limit the available time to perform experiments or the accessible densities. Furthermore, the Feshbach resonance has a finite width, both in magnetic field strength and collision energy. For a Feshbach resonance to be experimentally useful, this width has to be bigger than the achievable stability of the magnetic field. And to affect all atoms equally, the width should be much larger than the kinetic energy spread of the cloud.

For lithium several Feshbach resonances are predicted for different mixtures in our experimentally attainable magnetic field range from 0 to 1200 Gauss [152, 153]. In the experiment, we use a resonance in the ^{7}Li $|F = 1, m_F = 1\rangle$ state to produce a condensate by evaporative cooling in the optical trap. Another resonance between a ^{6}Li $|F = 1/2, m_F = 1/2\rangle$ and a $|F = 1/2, m_F = -1/2\rangle$ atom could be useful to obtain a Cooper paired gas. The dependence of the scattering length with magnetic field is given in figure (1.16).

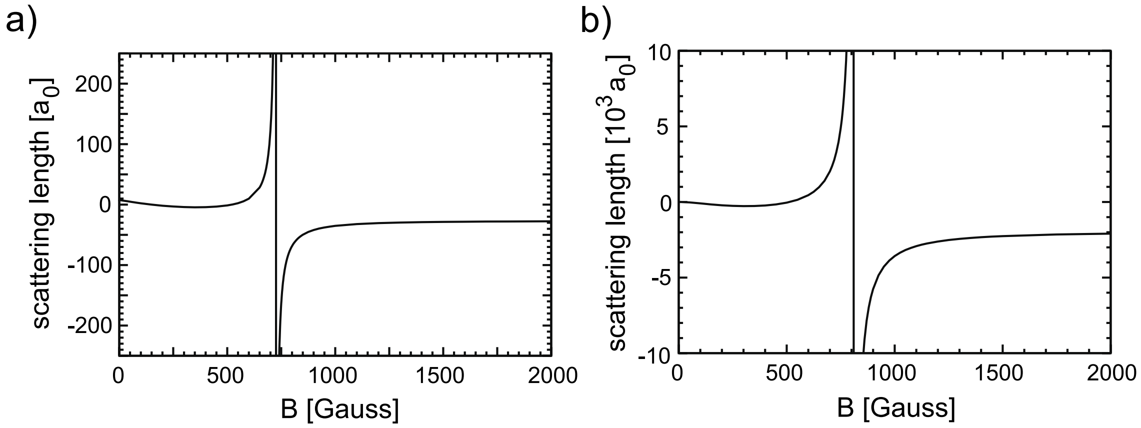

Figure 1.16: *Feshbach resonances in lithium (courtesy of V. Venturi and C. Williams). Shown is the scattering length versus the magnetic field. a) Feshbach resonance in the* ^{7}*Li* $|F = 1, m_F = 1\rangle$ *state. b) Feshbach resonance between the* ^{6}*Li* $|F = 1/2, m_F = 1/2\rangle + |F = 1/2, m_F = -1/2\rangle$ *states.*

Chapter 2

The experimental setup

In this chapter I will describe our experimental setup and compare it to other machines built with the goal to produce a degenerate Fermi gas. The thesis of my predecessor, G. Ferrari, describes the setup in its form as of spring 2000 [154]. In the following, I will give an overview of the machine and explain in detail especially the subsystems that have been added or modified. I will leave out the detailed description of the construction of the magnetic trap and the performance of the Laser system, which may be found in [154].

2.1 Overview of the experiment

The layout of the machine is similar to many machines used to produce Bose-Einstein condensates of alkali metal gases. A lithium gas jet is produced in a vacuum chamber by heating lithium in an oven and letting the gas escape through a tube. The beam is slowed down by a counter-propagating laser beam in a Zeeman slower configuration. Slow atoms are collected and cooled in a magneto-optical trap (MOT). After transfer of the atoms to a strongly confining magnetic trap, sympathetic cooling is applied. Fermionic lithium is cooled by thermal contact with an evaporatively cooled bosonic cloud. Measurements are performed by recording absorption images of the resulting clouds on a CCD camera. An optical dipole trap is used to explore the properties of gases and mixtures of gases in states that cannot be trapped in a magnetic trap. The dipole trap is used especially to study and use Feshbach resonances in lithium.

The whole system was designed to obtain a reliable and performant research tool. New concepts were introduced especially in the laser system and the magnetic trap. In the following sections I will first describe the properties of lithium and explain our decision to use this atom. Our approach will be compared to other machines which have the goal of producing degenerate Fermi gases. The rest of the chapter is dedicated to the description of every subsystem.

2.2 Properties of lithium

The first step in the construction of an experiment, which has the goal to study degenerate atomic Fermi gases, is the choice of the element. Several fermionic isotopes can be laser cooled and have stable fermionic isotopes, including ^{3}He, ^{6}Li, ^{40}K, ^{171}Yb, ^{43}Ca, ^{87}Sr, ^{25}Mg and ^{53}Cr and the artificial ^{88}Rb. We choose lithium for reasons explained later. In the following its properties are presented and their consequences for the experimental setup are discussed.

2.2.1 Basic properties

There are two stable lithium isotopes, the bosonic ^{7}Li and the fermionic ^{6}Li. The natural abundance of ^{6}Li is rather high, 7.5%. A natural source is sufficient to deliver a fermion and a boson, which is very useful for sympathetic cooling. In addition it is easy to obtain enriched ^{6}Li, probably because of the high 16% mass difference between ^{6}Li and ^{7}Li (and also because it is used in hydrogen bombs to breed tritium [155]).

For laser cooling it is important to have an optical transition frequency that is easy to produce. With 671 nm, this is the case for lithium. Diode lasers are reliable light sources at this wavelength. The bright red color helps when it comes to aligning beams or optimizing the shape of the MOT.

Lithium becomes liquid at 180.54 °C. To capture atoms in a MOT, their velocity must be below the capture velocity $v_{cap} \sim 50\,\mathrm{m/s}$. The high liquification temperature together with the small mass of $6\,m_p$ (^{6}Li) or $7\,m_p$ (^{7}Li) makes the relative population of slow atoms ($v < v_{cap}$) in the Boltzmann distribution small. This makes loading from a vapor pressure cell extremely difficult and demands the construction of a Zeeman slower.

2.2.2 Confinement in a magnetic trap

Trapping in a static magnetic field confines atoms in a magnetic field minimum. For this, the magnetic field dependence of the internal energy is important. Only states for which energy grows with increasing magnetic field, *low field seekers*, can be trapped. The energy of the lowest atomic states versus the magnetic field is plotted in figure (2.1). For low magnetic fields, the electronic and the nuclear magnetic moment are coupled and give rise to the two hyperfine levels, depending on their relative orientation. The resulting magnetic moments can take a finite number of angles relative to an external magnetic field. Depending on this orientation, the state is high- or low-field-seeking for weak magnetic fields. If the magnetic field energy becomes larger than the hyperfine splitting, the electronic and nuclear magnetic moments decouple and take individual orientations relative to the external magnetic field. For even stronger fields, the stronger electronic magnetic moment dominates the interaction energy, and some of the initially low-field-seeking states become high-field-seeking and vice versa. This is especially important for the $|F = 1, m_F = -1\rangle$ and the $|F = 1/2, m_F = -1/2\rangle$ states of ^{7}Li and ^{6}Li. They are only trappable to 140 G and 27 G, respectively. The energy difference between zero magnetic field and the turning point is a limit for the maximum trap depth. They are 2.4 mK and 0.2 mK in the considered cases, which is not deep enough to confine the atoms of the magneto optical trap (for which a typical temperature is 1 mK).

Therefore states from the higher hyperfine state have been used for initial magnetic trapping. Spin-relaxation (see section 1.2) further limits the choice of possible states. Consider a collision of two atoms in the ^{6}Li($F = 3/2, m_F = 1/2$) state. During a spin-relaxation collision only the total $M_F = m_{F1} + m_{F2}$ is conserved. This means that the atoms can change their state and be after the collision for example in the ^{6}Li(3/2,3/2) and the ^{6}Li(3/2,-1/2) state. The latter is lost from the trap. In testing all combinations one realizes that only the highest states of each hyperfine manifold (^{6}Li(3/2,3/2), ^{6}Li(1/2,-1/2), ^{7}Li(2,2), ^{7}Li(1,-1)) are immune against spin-relaxation collisions. We can also consider mixtures of ^{6}Li and ^{7}Li. Only mixtures with both atoms in the upper or both in the lower hyperfine state can avoid spin-relaxation collisions (^{6}Li(3/2,3/2)+^{7}Li(2,2) or ^{6}Li(1/2,-1/2)+^{7}Li(1,-1)). As a counterexample, consider a collision of a ^{6}Li(3/2,3/2) fermion with a ^{7}Li(1,-1) boson, which can produce a ^{6}Li(3/2,1/2) fermion and a ^{7}Li(1,0) boson, which is lost. The spin-exchange decay

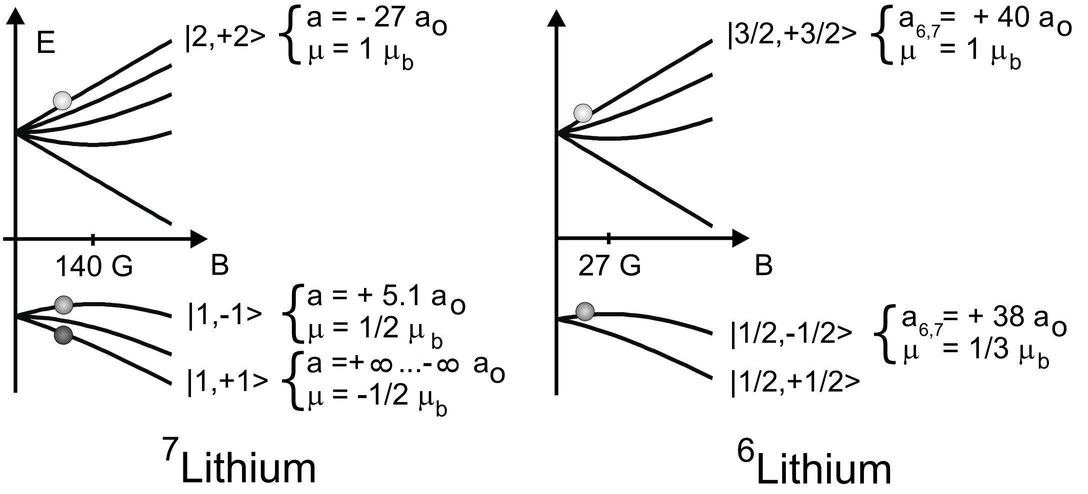

Figure 2.1: *Energy levels of the* ^{7}*Li and* ^{6}*Li ground states in a magnetic field. Relevant scattering lengths, a, and magnetic moments,* μ*, are given.* μ_b *is the Bohr magneton and* $a_0 = 0.53 \times 10^{-10}\,m$ *is the Bohr radius. The* $|1,-1\rangle$ *state (*$|1/2,-1/2\rangle$*) is only trapped in fields weaker than 140 G (27 G). Light balls: states used in first sympathetic cooling stage, the condensate will collapse for too high atomnumbers. Dark balls: states used in second cooling stage, enabling the production of a condensate which does not collapse for any atomnumber. Black ball: state used for evaporation in the optical trap, resulting in a condensate with tunable scattering length and a bright soliton due to a Feshbach resonance.*

rates were calculated in [153] and are reproduced in table (2.1). They are in the range of $10^{-11}\,\mathrm{cm}^{-3}/\mathrm{s}$. To evaluate if these losses are too high to permit evaporative cooling, the inelastic collision rate $\Gamma_{in} = G\,n$ has to be compared to the elastic collision rate $\Gamma_{el} = n_0\,\sigma\,v$, where n_0 is the peak density, $v = \sqrt{k_B T/m}$ and $\sigma = 4\pi\,a^2$ the scattering cross section. To be in the runaway regime, the rate of elastic collisions has to exceed the rate of inelastic collisions by at least a factor 200, *i.e.*, $\Gamma_{el}/\Gamma_{in} = \sigma v/G \gtrsim 200$ (see section 1.2). The temperature at the beginning of evaporative cooling is about 1 mK, corresponding to $v = 1\,\mathrm{m/s}$ for lithium. Taking the best values for a and G for unstable mixtures from table (2.1), a scattering length of $a = 40\,a_0$ and $G = 0.1 \times 10^{-11}\,\mathrm{cm}^{-3}/\mathrm{s}$ the ratio is $\Gamma_{el}/\Gamma_{in} = 50$. For these conditions evaporative cooling will not work. The case of a ^{6}Li(3/2, 3/2)+^{6}Li(1/2, -1/2) mixture is special since a and G depend on magnetic field and temperature and have more extreme values, but an analysis analog to the example given shows, that runaway evaporation can not be reached. Thus evaporation has to be performed with mixtures which are inherently immune against spin relaxation (^{6}Li(3/2,3/2)+^{7}Li(2,2) or ^{6}Li(1/2,-1/2)+^{7}Li(1,-1)).

All these considerations place severe constraints on the possible mixtures for sympathetic cooling in the magnetic trap. Since it is not possible to trap two different

Channel	$a\,(a_0)$	$G\,(10^{-11}\,\mathrm{cm}^3/\mathrm{s})$
^{7}Li (2, 2)+^{6}Li (3/2, 3/2)	40.8 ± 0.2	stable
^{7}Li (1, -1)+^{6}Li (1/2, -1/2)	38.0 ± 0.2	stable
^{7}Li (2, 2)+^{6}Li (1/2, -1/2)	34.9 ± 0.4	2.7 ± 0.3
^{7}Li (1, -1)+^{6}Li (3/2, 3/2)	38.5 ± 0.2	0.15 ± 0.01
^{6}Li (3/2, 3/2)+^{6}Li (1/2, -1/2)	$-(17 \pm 6) \times 10^2$	$\rightarrow 0$
^{7}Li (2, 2)+^{7}Li (1, -1)	$-(14 \pm 1)$	2.4 ± 0.2

Table 2.1: *Scattering length a at zero temperature and zero magnetic field and spin-exchange decay rate constant G for several different magnetically trappable mixtures of lithium. For* ^{6}*Li(3/2, 3/2)+*^{6}*Li(1/2, -1/2), G rises to* $10^{-8}\,\mathrm{cm}^{-3}\mathrm{s}^{-1}$ *for* 100 *mG or to* $10^{-10}\,\mathrm{cm}^{-3}\mathrm{s}^{-1}$ *at* 10 *nK. These values are taken from [153].*

fermionic states, the thermalizing s-wave collisions must be inter-isotope collisions. Initially the atoms have to be in the $|F = 2, m_F = 2\rangle$ and $|F = 3/2, m_F = 3/2\rangle$ states, called *stretched states* because electron and nuclear spin are aligned. At temperatures of a few micro Kelvin a passage to a $|F = 1, m_F = -1\rangle$, $|F = 1/2, m_F = -1/2\rangle$ mixture becomes possible. To study different states or mixtures beyond these few, the atoms must be confined in an optical trap.

2.2.3 Elastic scattering cross sections

The scattering length plays an essential role in ultracold atom experiments. A high enough absolute value of the scattering length is required for successful evaporative and sympathetic cooling (section 1.2). The sign of the scattering length decides of the stability of a condensate (section 1.1.8). The mean field due to the interaction can lead to phase separation or the formation of bright solitons. Finally, an attractive interaction between fermions is required for Cooper pairing. In table (2.2) the singlet and triplet scattering length for both isotopes and the inter-isotope scattering length is given. Here singlet and triplet refers to the electronic spin wavefunction of the combined state of the colliding atoms. The scattering length in the stretched state ($|F = 2, m_F = 2\rangle$ for ^{7}Li or $|F = 3/2, m_F = 3/2\rangle$ for ^{6}Li) is the triplet scattering length since both electronic spins are parallel. For the other states, the electronic spin wavefunction has to be decomposed into its singlet and triplet components. To calculate the scattering length the dephasing of each of these components is calculated separately. The resulting wavefunction is projected on the initial state, giving the effective dephasing. The resulting scattering length for the states used in the experiment are given in figure (2.1).

The triplet scattering length for the bosons of $-27\,a_0$ ($a_0 = 0.53 \times 10^{-10}\,\mathrm{m}$ is the

	^{6}Li	^{7}Li	^{6}Li /^{7}Li
a_T	-2160 ± 250	-27.6 ± 0.5	40.9 ± 0.2
a_S	45.5 ± 2.5	33 ± 2	-20 ± 10

Table 2.2: *Triplet and singlet scattering length for the two isotopes of lithium after [141]. The scattering length are given in units of the Bohr radius* $a_0 = 0.53 \times 10^{-10}$ *m.*

Bohr radius) is not very high in absolute value, ^{87}Rb for instance has a four times longer triplet scattering length. To obtain the required ratio of $\Gamma_{el}/\Gamma_{in} \gtrsim 200$ for runaway evaporative cooling, one can use a steeply confining trap to provide a high elastic collision rate, as it is the case in our experiment. An alternative is to reduce the background gas pressure in the vacuum chamber to obtain long lifetimes ($> 600\,$s), as it is the case for the experiment of R. Hulet, who observed the condensation of lithium in 1995 [123]. Since the sign of the scattering length is negative, the condensate is unstable above a critical number of atoms. The scattering cross section has a zero point at 6.6 mK collision energy (see section 1.3.1), which means attention has to be paid not to start the evaporative cooling at temperatures above $\sim 1\,$mK. The scattering length between the two isotopes in the stretched states has a higher magnitude of $41\,a_0$. But because of the Bose enhancement in the scattering cross section between ^{7}Li atoms ($\sigma = 8\pi a^2$ instead of $\sigma = 4\pi a^2$), the scattering cross sections are nearly the same ($\sigma_{67}/\sigma_{77} = 1.1$). This guarantees that the thermalization between isotopes is as fast as the thermalization of the bosonic thermal bath, a favorable condition for sympathetic cooling.

The scattering length in the ^{7}Li $|F = 1, m_F = -1\rangle$ state is $a = 5.1\,a_0$: very small, but positive [73]. Condensates formed in this state are stable and have a very small mean field (see section 3.4.4). But we could never achieve evaporative cooling with this state alone because of the small scattering length. Instead we used the ^{6}Li-^{7}Li scattering length of $a = 38\,a_0$ with the ^{6}Li $|F = 1/2, m_F = -1/2\rangle$ state, which is nearly the same value as in the higher hyperfine states, to thermalize the gas during the cooling process.

Interesting possibilities are opened when working in an optical trap. Then Feshbach resonances can be used to tune the scattering length (see figure 1.16). Several resonances have been predicted in lithium [152, 141, 156]. For a $|F = 1/2, m_F = \pm 1/2\rangle$ spin-mixed fermionic gas a Feshbach resonance is predicted for 800 G, which could possibly be used for the observation of a BCS transition (see section 1.1.14). Another experiment using these states would be the observation of a phase separation between them using the Feshbach resonance enhanced coupling. We measured a resonance in the bosonic $|F = 1, m_F = 1\rangle$ state and used it to perform evaporative cooling in an optical trap, which resulted in the production of a Bose-Einstein condensate with tunable scattering length and a bright soliton. A Feshbach resonance is also predicted between

^{7}Li $|F=1, m_F=-1\rangle$ and ^{6}Li $|F=1/2, m_F=-1/2\rangle$, which could be used to observe a phase separation between a BEC and a Fermi sea.

2.3 Other strategies to a degenerate Fermi gas

Several other groups are building or have built experiments to study degenerate Fermi gases. They distinguish themselves mainly in the mixture of atoms or atomic states used to make sympathetic cooling work.

- **^{6}Li + ^{7}Li:** Besides our group, the group of R. Hulet has built a lithium machine with the same sympathetic cooling approach and the same goals as ours [61]. The main technical differences between our machines are that they use a dye laser system in contrast to our all-diode laser system, and that their magnetic trap is not as strongly confining as ours, but they have a longer lifetime. Both groups achieved the production of degenerate Fermi gases in the year 2000.

- **^{6}Li:** The group of J.E. Thomas has confined the ^{6}Li $|F=1/2, m_F=\pm 1/2\rangle$ states in a CO$_2$ dipole trap. They tuned the scattering length to $a \approx -100\,a_0$ using a magnetic field of 130 G (see figure 1.16). They could perform evaporative cooling by lowering the confinement and reach a degeneracy of $T/T_F=0.5$ [64]. A somewhat similar approach is undertaken by the group of R. Grimm. They can capture lithium in a resonator enhanced optical trap and intend to use the Feshbach resonance to perform evaporative cooling [157].

- **^{40}K:** The first experiment to obtain evidence for a degenerate Fermi gas was the experiment of B. de Marco and D. Jin [60]. They use ^{40}K for which the hyperfine state with the greater spin has a lower energy (inverted hyperfine structure). For this reason it is possible to trap two different internal states without spin relaxation, the $|F=9/2, m_F=9/2\rangle$ state together with the $|F=9/2, m_F=7/2\rangle$ state. This means only one isotope has to be laser cooled. Potassium has a low melting point of 63.38 °C and can be loaded into a MOT from a vapor cell. These two points simplify the experimental setup. A Feshbach resonance is also predicted, which gives hope for the detection of Cooper pairing. One disadvantage of this approach is, that by sympathetically cooling one fermion by another, the effect of Pauli blocking at the end of evaporation is doubled.

- **^{40}K + ^{87}Rb:** To overcome this problem, to my knowledge at least three groups are building mixed ^{40}K/^{87}Rb machines: the group of M. Inguscio [43], D. Jin's group [130] and J. Close's group [131]. This mixture has the advantage, that both atoms have very similar properties. For example the cooling and trapping transitions are only 13 nm apart. This makes an amplification of both frequencies in one tapered amplifier possible (see section 2.6). These machines can also be used to study condensates of ^{41}K as has been recently demonstrated [43].

- **^{6}Li + ^{23}Na:** Another mixture being tested is ^{6}Li with ^{23}Na. The effort for such a machine is somewhat bigger than for the machines discussed until now, since the trapping transitions are at frequencies far apart (red for Li and yellow for Na), requiring two different laser systems, one of them a dye laser. As in our system a Zeeman slower has to be used to load the MOT. It is a logical extension to an existing ^{23}Na machine and pursued in the group of W. Ketterle. They were able to sympathetically cool ^{6}Li to quantum degeneracy recently [63].

- **^{3}He + ^{4}He:** The next possibility is to perform sympathetic cooling on a mixture of metastable ^{3}He* and ^{4}He*. ^{4}He* machines have been built by our colleagues at LKB and by the group of A. Aspect. Both recently produced BECs of metastable ^{4}He* [41, 42]. For the moment, at least, the group at LKB does not plan to pursue the direction of fermions, but rather to study the properties of the condensate.

- **^{53}Cr:** An effort to produce a degenerate Fermi gas of ^{53}Cr is pursued by the group of T. Pfau in Stuttgart [128]. They plan to use the high magnetic dipole-dipole interaction to overcome the suppressed s-wave problem (see section 1.3). A disadvantage with Cr is its trapping transition in the blue. The loading of the magnetic trap from the MOT can be done continuously by using intercombination transitions to magnetically trappable metastable states [128].

- **^{171}Yb + ^{172}Yb:** T.W. Mossberg in Oregon has demonstrated simultaneous multi-isotope trapping of ytterbium in a MOT [132]. One of the trapped mixtures contains ^{171}Yb, a fermionic isotope.

- **He cryostat:** Neutral atoms and molecules such as europium, chromium, and lead monoxide have been cooled sympathetically by thermal contact due to collisions with a cryogenically cooled Helium buffer gas and loaded into a magnetic trap [54, 55, 56]. In combination with evaporative cooling this technique could lead to degenerate quantum gases of atomic or molecular bosons and fermions.

Of all these approaches we choose a mixture of fermionic and bosonic lithium. One reason was that at the time of our decision the scattering lengths were well known and it had been shown that bosonic lithium can be condensed. This was a difference especially to ^{40}K. And the predicted Feshbach resonance in ^{6}Li gave a good perspective for the observation of a BCS transition. A machine mixing two different atoms seemed more complicated than a machine based only on lithium.

2.4 The vacuum system

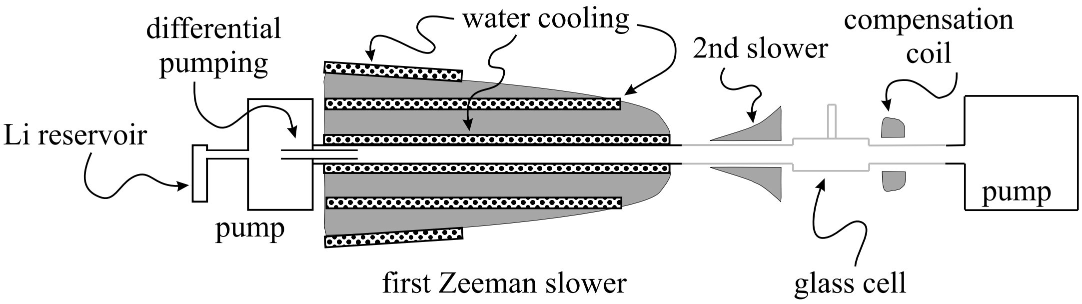

Figure 2.2: *Scheme of the vacuum chamber. To the left the oven is shown. The atomic beam passes through collimation and differential pumping tubes and is slowed down in a Zeeman slower of which the coils are shown. The MOT and the magnetic trap reside in a glass cell. Ion pumps are used in the oven chamber and at the end of the main chamber.*

After the decision which strategy we would apply to produce a degenerate Fermi gas, a machine was designed appropriate for lithium. In this section we will discuss the different subsystems of the setup. We start with the vacuum chamber, a scheme of which is shown in figure (2.2). It consists of two chambers, the oven chamber and the main chamber, that are separated by a differential pumping tube of 3.5 mm inner diameter and 12 cm length. Each chamber is pumped by an ion pump, the oven chamber by a 50 l/s pump (MECA 2000 PID 50 N) the main chamber by a 100 l/s pump (MECA 2000 PID 100 N, both with noble gas electrodes). In addition a titanium sublimation pump is installed in each chamber, though the pumps are not used at the moment. To improve further the vacuum, graphite disks (5 cm diameter, 5 mm thickness) are placed in the main chamber. The disks are outgassed during the bake-out procedure and work afterwards as a getter. As discussed before, a vapor cell can not be used as source for the lithium MOT. So an oven plus Zeeman slower was constructed.

2.4.1 The atomic beam source

A sketch of the oven is shown in figure (2.3a). Its design is modified from the oven used a year ago. It consists of a reservoir chamber made of a vertically oriented steel tube with 2 cm diameter and 12 cm length. The tube was closed at the lower side by soldering a steel disk into the opening. In the old oven, this side was used to fill the reservoir and closed only by a vacuum flange with a nickel gasket. After one year of operation the oven developed a leak, probably because liquid lithium corroded through the gasket. This already happened before when a copper gasket was used. With copper, the gasket held only about one month. Now the reservoir chamber is filled from the top, where no liquid lithium can come into contact with the nickel gasket. Around the reservoir a heating element (Thermocoax) and a temperature sensor (Omega XICB-K-1-1-3) is soldered. At the midpoint of the reservoir, a collimation tube with 4.5 mm inner diameter and 7.5 cm length is attached. Atoms hitting the walls of the collimation tube are transported back into the reservoir by capillary forces, driven by the temperature gradient along the tube. This process is improved by increasing the inner surface of the tube by sliding a tube formed out of a steel mesh (Alfa Nō 13477) into it. The diameter of the collimation tube was thus decreased to 3.5 mm. The other end of the collimation tube is soldered to a flange (Caburn CFB114) which is attached to a cubic chamber with openings to all six faces. In the chamber, a mechanical shutter moved by a stepper motor through a mechanical feedthrough (MDC HTBRM-275) can block the atomic beam. The titanium and ion pumps, a surveillance window, and a valve through which pumpdown is performed are also attached to the cubic chamber. The connection to the main chamber can be blocked by a linear feedthrough valve (MECA 2000 VUVD 6) that is a constant source of problems since it does not close completely and since the mechanical CF16 connection to the oven chamber is too weak to withstand the torque necessary to close the valve. The next time the main chamber is under pressure, it will be exchanged against a stronger CF40 valve.

The oven chamber and the Zeeman slower are connected by a differential pumping tube. In its initial design it had an inner diameter of 4.5 mm and a length of 10 cm, corresponding to a differential pressure of 100. As it turned out, this was not sufficient: the lifetimes obtained in the magnetic trap were only about 30 s. As a first solution, the diameter of the differential pumping tube was reduced to 2.3 mm and its length extended to 12 cm. This reduced the flux of atoms captured in the MOT by a factor five (to 5×10^8 atoms/second), but since the MOT lifetime increased to over 2 minutes, a longer charging time permitted us to obtain the same number of atoms in the MOT. This decreased background pressure was an essential step to make evaporative cooling work.

2.4.2 Oven bake-out procedure

Mass spectroscopic studies of the oven chamber pressure have lead to an understanding of our initial background pressure problems. The background gas in the oven chamber consists only of hydrogen. During operation of the beam, we found the partial pressure of H dominated by the oven: at 500 °C it was 1.3×10^{-8} mbar, and when the oven was colder than 300 °C the pressure dropped to 1.2×10^{-9} mbar and saturated there. Our interpretation of this was that LiH is present in our lithium sample. Since the collimation tube has a conductivity of only 1 l/s the lithium is never well outgased and the LiH stays there. This LiH dissociates at the operation temperature of the oven, about 500 °C.

The next time we had to replace the oven because of the leak, we baked out the

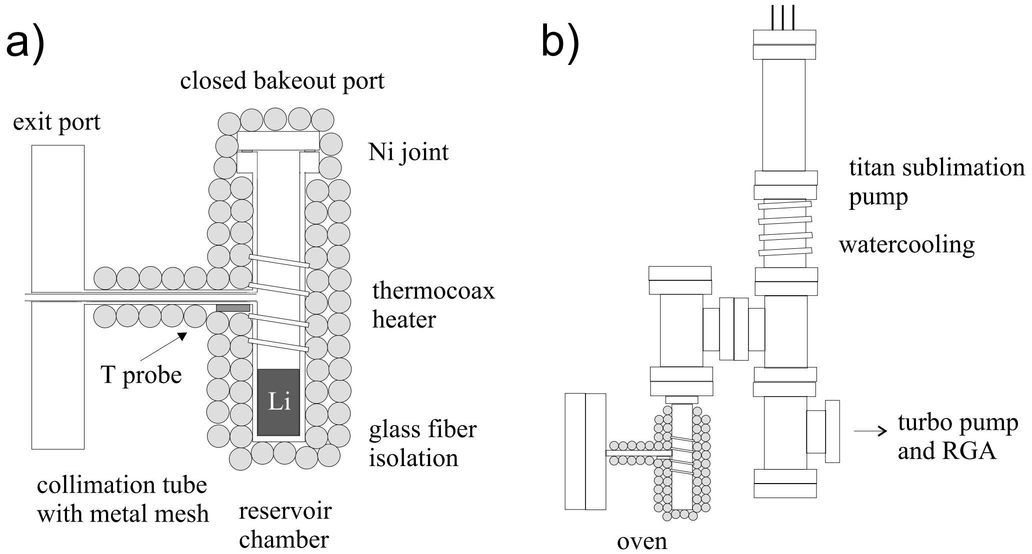

Figure 2.3: *The atomic beam source. a) Lithium vapor is produced by heating a sample in the reservoir chamber using a thermocoax heater. The temperature is controlled using the temperature probe. The reservoir is isolated by glass fiber ribbon and aluminium foil. The gas escapes through a collimation tube and forms the atomic beam. A metallic mesh increases the inner surface of the collimation tube and helps transporting collected lithium back into the reservoir by capillary action. b) To remove LiH, the lithium sample is baked out before use. The vacuum chamber for this process is shown. Between the heated reservoir and the pumps a cooler part of the vacuum chamber collects all evaporated lithium.*

lithium in the reservoir chamber. The apparatus used for this is shown in figure (2.3b). In an argon environment, the reservoir was loaded (up to the collimation tube) with lithium. A mixture of 80% natural lithium and 20% enriched ^{6}Li was used. To work under argon atmosphere, the vacuum chamber was placed in a transparent plastic bag, which had two gloves attached, showing to the inside. After attaching the oven to the bake-out chamber the reservoir was heated for one night to 600 °C, 70 °C above the normal operation temperature and 80 °C below the melting point of the solder used to construct the oven. The temperature was regulated by a thermostat (Newport-Omega ref. CN76133) in the same way as done in the experiment. To pump the hydrogen a titanium sublimation pump and a 25 l/s turbo pump were used. After the bake-out, about half of the lithium was deposited at the walls of the vacuum chamber above the reservoir. The remainder of the lithium stayed in the lower half of the oven, filling the reservoir up to a height of 1.5 cm. The top of the reservoir was closed using a CF16 flange with a nickel gasket. The oven was installed onto the oven chamber of the experiment, again inside an argon filled glovebag. During the same operation, the diameter of the differential pumping tube was increased to 3.5 mm. Unfortunately the valve between the oven and the main chamber could not be completely closed, so that a 10^{-6} mbar argon pressure existed during one hour in the main chamber. This provoked an argon instability in the ion pump of the main chamber, which could luckily be solved by baking the pump out at 150 °C for one day and pumping with a 25 l/s Turbo pump on the main chamber. After this bake-out procedure, we no longer saw an increase in the hydrogen pressure of the oven chamber, when heating the oven to 500 °C. The lifetime of magnetically trapped atoms is about 70 s as before the leak in the oven, and this with an in. But we could not measure any increase in the flux of captured atoms, which we expected from the increase in diameter of the differential pumping tube. This could be explained, if the collimation tube and the differential pumping tube are slightly misaligned. The next time the oven chamber is opened, the diameter of the differential pumping tube should be increased back to its initial value of 4.5 mm. One additional positive result is that the flux of the oven is more stable than before the changes.

2.4.3 The main chamber

Now we take a look at the main chamber. The atomic beam first travels through the tube of the Zeeman slower, which will be described in the next section. The Zeeman slower opens onto a glass vacuum chamber that is the central part of the experiment. The glass chamber has two components: a MOT chamber (4 cm×4 cm×10 cm, Width × Heights × Length) and a smaller appendage chamber (20 mm×40 mm×7 mm), used for magnetic trapping. The wall thickness is 5 mm for the lower chamber and 2 mm for the upper chamber (see figure 2.7). Around the appendage the Ioffe-Pritchard magnetic trap is constructed (see section 2.7). The glass chamber is connected at both sides with the steel chamber using glass-metal connections and bellows to reduce stress. At the far side of the vacuum chamber a T-shaped end chamber is attached. It is closed at the end by a window, through which the Zeeman slowing laser beams enter. The non-slowed lithium atoms of the atomic beam hit this window. Since lithium and glass react and form an opaque substance, the window is heated to 40 °C which helps prevent this reaction. To prevent heating of the end chamber, which increases the pressure, it is watercooled right at the side of the end window. To orthogonal ports, the 100 l/s ion pump and the titanium sublimation pump are attached. The graphite getters are placed in the end chamber.

2.5 The Zeeman slower

A thermal beam with a mean velocity of about 1000 m/s is produced by the oven. The MOT can capture only atoms with speeds less than the capture velocity of about 50 m/s. To bridge the gap, we use a slowing stage that employs the radiation pressure of a laser beam counter-propagating to the atomic beam [158]. Each absorption event reduces the momentum of an atom by the photons momentum $\hbar k$. The maximum achievable deceleration is

$$a_{max} = \frac{\hbar k}{2m\tau}\,, \tag{2.1}$$

where τ is the lifetime of the excited level and m the mass of the atom. For finite intensities of the laser beam, the maximum acceleration is lower than a_{max}. For lithium at $a = 0.5\,a_{max}$, $I = 2.5\,\mathrm{mW/cm^2}$. Since the resonance frequency of the atoms depends on their velocity by the Doppler shift ($\Delta\nu = \nu_0 v/c$) the resonance condition is only fulfilled for one velocity. To slow down a thermal beam, each velocity class has to be addressed. This can be done by changing the laser frequency to stay in resonance with atoms as they are slowed (chirped slower), or it can be done by applying a magnetic field and using the Zeeman effect ($\Delta\nu = \mu_B B$ where μ_B is the Bohr magneton), hence the name Zeeman slower. The magnetic field is changed spatially. At the entrance of the Zeeman slower, the laser frequency and the field are chosen such that atoms with the high *capture velocity* v_c are in resonance. After a certain flight distance the atoms have slowed down. At this point the field strength is chosen to put these slower atoms in resonance. In this way the atoms can be slowed from v_c to an arbitrary velocity which is chosen to be below the capture velocity of the MOT. Atoms with an initial speed lower than the capture velocity travel undisturbed down the Zeeman slower, until their velocity class comes in resonance. This means that the whole thermal distribution below v_c can be slowed down. The necessary magnetic field dependence is given by

$$B(z) = \frac{\hbar k v(z)}{\mu_B} + B_0 = \frac{\hbar k\sqrt{v_c^2 - 2az}}{\mu_B} + B_0\,, \tag{2.2}$$

where B_0 is an arbitrary offset field depending on the laser detuning. We choose to implement this field using two field coils one after the other, producing fields parallel to the atomic beam but with opposite directions. This approach, called a *spin-flip Zeeman slower* has several advantages.

- The difference between capture and end velocity is proportional to the difference in magnetic field. By choosing opposite field directions the maximum absolute field strength necessary is reduced and thus the power consumption of the coils.
- The second magnetic field coil is rather small and can be placed very near the MOT. It is only here that slow atoms are produced. This reduces the total time of travel, and consequently reduces the spatial spread of the atomic beam due to the transverse velocity.
- The laser is resonant with atoms all along the Zeeman slower, also in the weak field region between the coils. Here the atoms have in our case a velocity of 285 m/s. This guarantees that the laser is far off resonance for the slow atoms in the MOT, where the magnetic field is also weak.

The atomic spin has to be antiparallel to the direction of the first magnetic field and parallel to the second. This is the reason for the name spin-flip Zeeman slower. Of course spatially the spin stays oriented in the same direction. In the region between the two field coils, the direction of the magnetic field changes and the atomic spin will either follow this change or, if the absolute magnetic field value gets too small to allow adiabatic following, the spin orientation will get mixed up. The spin is again pumped to the correct orientation by the σ polarized slowing laser beam. To prevent loss of atoms which get transferred to the lower hyperfine state, a repumping beam is superimposed with the slowing beam. This beam helps also for the initial preparation of the atoms in a cycling transition. Since the excited state hyperfine structure of lithium is small, the transition is not perfectly cycling and the repumper is also important during the slowing process.

The construction of the coils has to fulfill several requirements. It has to be possible to heat the vacuum tube of the slower to 300 °C during the bake-out of the vacuum chamber. The power dissipated in the coils during normal operation has to be removed. And it is very convenient if the winding of the coils can be done on a lathe. Our construction fulfills these requirements. The first coil with a length of 80 cm and a maximum field strength of 800 G is made out of glassfiber isolated heater wire (Newport-Omega HTMG-ICU-3145) which resists easily the temperatures during bake-out. The wire is wound around a steel tube and held in place using cement (Sauereisen Nō 10) which also serves as heat conductor. To remove heat, water cooling is used. The vacuum tube has a slightly smaller diameter than the tube around which the coil is wound. Between these tubes cooling water is flowing. In addition after seven and after fifteen layers of wire, a layer of copper tubes is wound. Cooling water is also circulating in these copper tubes.

The second coil is much smaller and can be wound around the vacuum chamber after bake-out. It is placed on a watercooled copper tube around the glass-metal transition of the glass cell. A third coil of the same construction type is placed around the glass-metal transition at the end of the glass cell in direction of the atomic beam. It is put in a quadrupole configuration with the second slower coil and subtracts the offset magnetic field of the Zeeman slower at the place of the MOT. Only a gradient of $\sim 10\,\mathrm{G/cm}$ is left over.

The operation parameters of the Zeeman slower, as the laser detuning and the coil currents, are optimized on the loading of the MOT. Of course these parameters depend on the MOT parameters. This means the optimization has to be done iteratively for both. We could obtain a maximum flux of 5×10^8 at/s. Out of unknown reasons, this flux was sometimes increased by a factor ~ 5 for some days before falling back to its normal value. This behavior was attributed to the oven and did not appear anymore after the oven had been changed.

In the laboratory of R. Hulet an increasing-field slower with a length of only 30 cm is used. They reach loading times of the MOT about 10 times faster than we, with the same number of atoms in the MOT. Since the construction of the oven and the parameters of the MOT are similar in both machines, this large flux could be due to the construction of the slower or due to the fact that Hulet's group uses higher laser intensities for the slowing beams than we have at our disposal. In the latter case the construction of a final amplifier stage for the slowing beam using a tapered amplifier could increase our flux.

2.6 The laser system

The next subsystem at which we will take a closer look is the laser system. Near-resonant laser beams are used in five phases of a typical experimental sequence: the Zeeman slowing, the trapping and cooling in the MOT, the optical pumping to a magnetically trappable state, the Doppler cooling in the magnetic trap and the detection using absorption images. In addition, near-resonant light can be used to detect effects of quantum degeneracy, *e.g.*, by studying the suppression of light scattering (see section 1.1.4) and is in general a very useful tool to manipulate the atoms. This wide field of applications makes it clear that a reliable source of near resonant light is needed.

The wavelength of the lithium transition is 671 nm, in the red part of the spectrum. Different types of lasers can produce this wavelength: dye lasers, argon ion pumped titanium sapphire lasers and diode lasers. The first two types produce high power beams but are expensive and need a lot of maintenance. Diode lasers are cheap and reliable but have at our wavelength only typically 30 mW of power, which is barely sufficient for the operation of a MOT. However, in combination with a diode amplifier, such as a tapered amplifier or a broad area diode, powers of up to $\sim$ 500 mW can be achieved. We choose this option for our laser system.

Let us consider now which frequencies are necessary for our experiment. In figure (2.4) the lowest S and P states of both lithium isotopes are shown. Each isotope needs a trapping and cooling laser on the D2 line, the $2^2S_{1/2} \Rightarrow 2^2P_{3/2}$ transition. For ^{7}Li (^{6}Li) the transition from the $F = 2$ ($F = 3/2$) to the excited $F' = 3$ ($F' = 5/2$) state is used. Since the excited hyperfine structure has a splitting of the same order as the natural linewidth (6 MHz), also higher lying states (*e.g.* $2^2P_{3/2}$ $F' = 2$ for ^{7}Li) can be excited. These states can decay to the lower hyperfine state ($F = 1$ or $F = 1/2$). For this reason, a repumping laser from the lower state is essential. For ^{7}Li the repumping is done on the D2 line from $F = 1$ to $F' = 2$. In a first version of the laser setup the repumping for ^{6}Li was also done on the D2 line using the $F = 1/2$ to $F' = 3/2$ transition. This transition is by coincidence resonant with the D1 line of ^{7}Li at the $F = 2 \rightarrow F' = 1$ transition. This is a non-trapping transition and adding light at this frequency to a ^{7}Li MOT can completely destroy the MOT. That is why we choose to repump ^{6}Li on the D1 transition, the $2^2S_{1/2} \Rightarrow 2^2P_{1/2}$ transition, using the $F = 1/2 \rightarrow F' = 3/2$ hyperfine states.

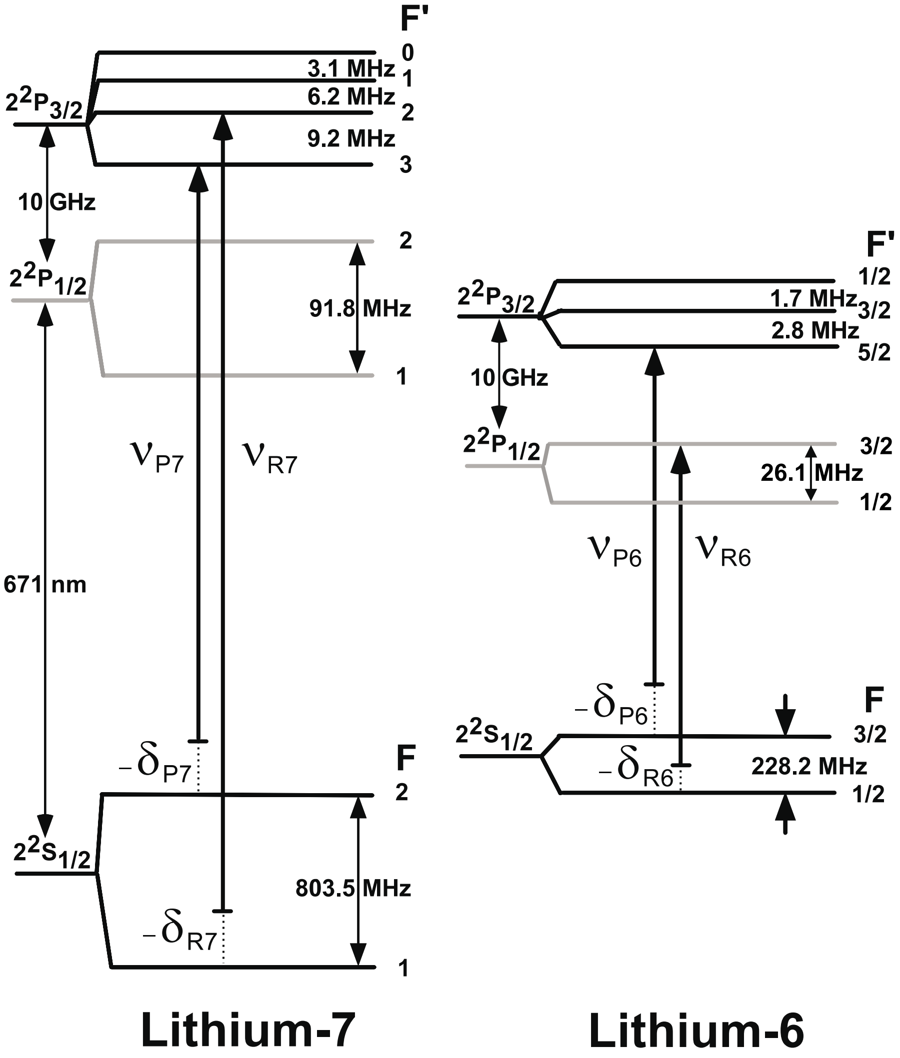

Figure 2.4: *Energy level diagram for the lower S and P levels of* ^{7}*Li and* ^{6}*Li. The transitions used for the MOT are shown, the index P referring to the principal transition and the index R to the repumping transition. Note that* ^{6}*Li is repumped on the D1 (*$2^2S_{1/2} \Rightarrow 2^2P_{1/2}$*) transition since the D2 (*$2^2S_{1/2} \Rightarrow 2^2P_{3/2}$*) repumping transition coincides with the D1 transition of* ^{7}*Li.*

The isotopic shift as well as the shift between D1 and D2 lines is 10 GHz. This frequency gap could be spanned by creating sidebands on the light using an EOM, or by a series of AOMs, but the latter has poor efficiency. In practice it is simpler to use a separate master laser for each one of these lines. Since the ^{7}Li D1 and the ^{6}Li D2 lines coincide, only one master laser is necessary for both. From these three basis frequencies, all other frequencies can easily be derived using AOMs, the biggest frequency gap being the 803.5 MHz between the hyperfine ground states of ^{7}Li.

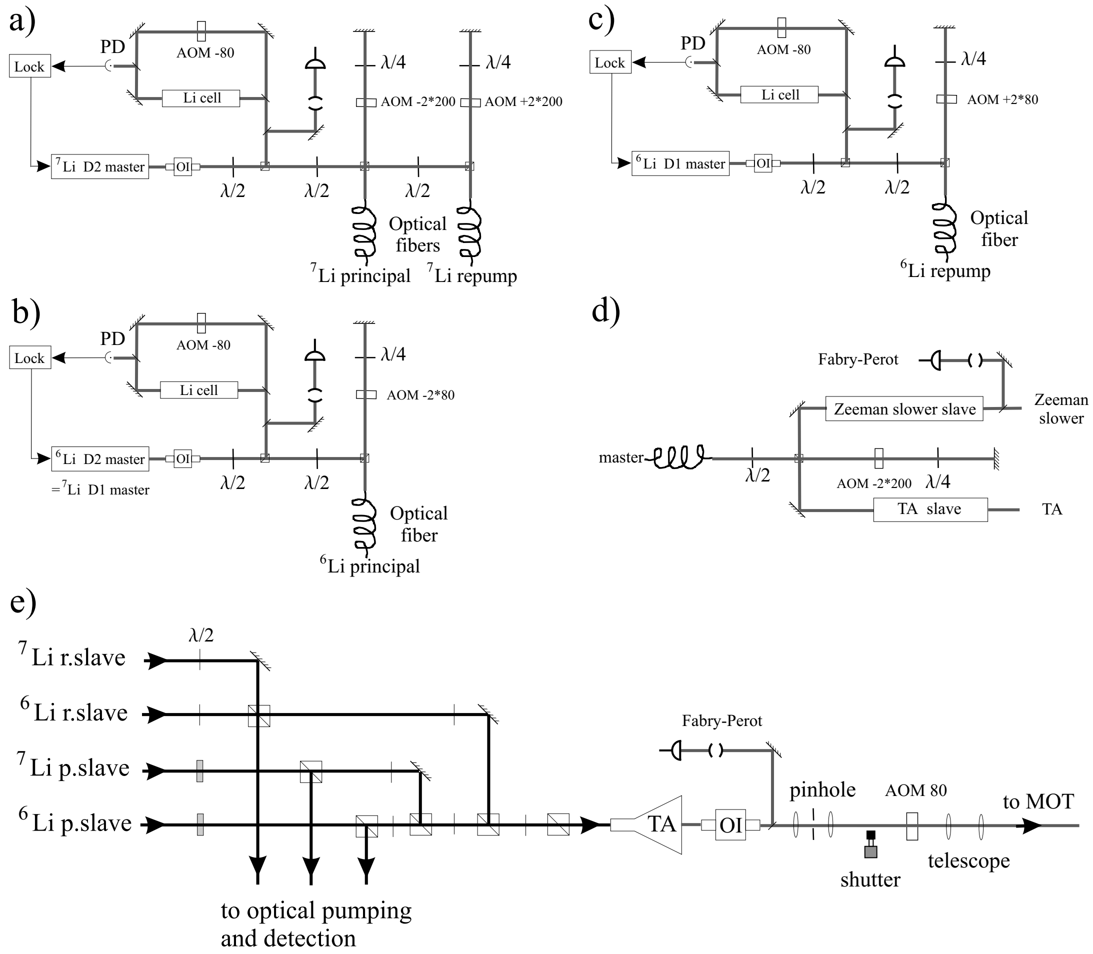

Figure 2.5: *The laser system. Grating stabilized external cavity master lasers are locked using Doppler free saturation spectroscopy. Three systems have been set up giving access to the ^{7}Li D2 transition (a), the ^{6}Li D2 transition (coinciding with the ^{7}Li D1 transition) (b) and the ^{6}Li D1 transition (c). Required frequencies are derived using AOMs. After transfer through optical fibers to the main optical table, each beam is amplified with injection locked lasers. The beam for Zeeman slowing is frequency shifted before amplification (d). All four MOT frequencies are mixed and further amplified in a tapered amplifier (TA) (e). Fabry-Perot cavities are used to verify the mono mode operation of the master lasers and to check the injection of the slave lasers.*

Figure (2.5) shows the setup of the laser system. The optical system is split in two parts. The master lasers with the necessary optics for locking their frequencies and AOMs to derive the principal and the repumping light for both isotopes is placed on an optical table of its own. This reduces the influence of electromagnetic radiation, air currents and noise resulting from the use of radio frequency radiation and high current power supplies placed near the vacuum chamber of the experiment. The four resulting frequencies are sent to the main optical table, on which the vacuum chamber is placed, *via* polarization maintaining optical fibers. There, frequencies for the MOT and the Zeeman slower are derived and finally amplified in one or two stages.

The master lasers are external cavity stabilized diode lasers in Littrow configuration (Spectra Diode Laboratories SDL-7311-G1). Their frequency is stabilized using Doppler free spectroscopy on lithium gas samples prepared in heated Li vapor cells.

These spectroscopy cells consist of a $\sim 30\,\mathrm{cm}$ long metal tube. They are heated in the middle to about $300\,^{\circ}\mathrm{C}$ by a two-wire thermocoax soldered on the pipe. The current in the wires flow in opposite directions to avoid magnetic fields. At the ends the pipe is water cooled and closed by windows (BK7). The pipe is filled with a sample of lithium and argon. Argon is necessary to reduce the mean free path of lithium so that no direct path to the windows is possible, to avoid that lithium covers the windows and makes them opaque. The argon pressure was regulated by observing the spectral linewidth and choosing a low enough value that no pressure broadening is apparent. Lithium condenses on the walls at the end of the pipe and is transported back to the center by capillary action. To increase the transport speed, a steel mesh covers the inside of the pipe (Alfa type 304).

The Doppler free spectroscopy is done in a counter-propagating pump-probe configuration. The pump frequency is modulated with an AOM and the probe intensity observed at that frequency using a lock-in amplifier. The low frequency part of the error signal is used to adapt the external cavity length by displacing the grating using a piezo. The high frequency part is added to the diode laser current.

Three master laser systems exist which give access to the D1 and D2 lines of the two isotopes. Using AOMs, frequencies about 120 MHz below the principal and repumping transitions are derived and sent to the main optical table using fibers. Here each beam is separated in two, for the Zeeman slower and for the MOT.

The Zeeman slowing beams are further frequency shifted to the red by a set of four 200 MHz double pass AOMs. The eight resulting beams are amplified using slave lasers. The slave lasers consist of temperature stabilized 30 mW laser diodes of the same type as the diodes used in the master lasers. The injection is done through the sideport of isolators placed after each slave laser. The four beams for the Zeeman slower are geometrically superimposed under a slight angle. A telescope expands the beam size and a converging beam is sent through the vacuum chamber against the atomic beam, and focused on the ovens collimation tube. The power in each frequency component is about 20 mW and at the entrance window the beam size is about 4 cm.

The MOT beams are also amplified in a set of four slave lasers. The four beams are carefully superimposed using polarizing beam splitters and halfwave plates. The resulting four frequency component beam injects a tapered amplifier delivering typically 300 mW of light (Spectra Diode Laboratories SDL-8630). This method is described in detail in [159], which is reproduced in appendix (A). A tapered amplifier consists of a waveguide with attached diode gain medium. The gain region has a tapered form, hence the name. The beam expands and coherently fills the whole gain region, while increasing in power. The frequency composition of the outgoing beam closely follows that of the injecting beam. The nonlinearity of the amplification produces sidebands at the frequency of the beatnote between the injecting frequency components. About 20% of the total output power is lost in these unwanted sidebands in our case. Luckily, the frequencies of the sidebands do not disturb the working of the MOT or the Zeeman slower. The 20% loss is not important since the total output power is high enough for our needs. The outgoing beam is corrected for astigmatism by a cylindrical lens and cleaned in a $30\,\mu$m pinhole. After this procedure we are left with 180 mW of light in a nearly gaussian beam, containing all four frequency components necessary for the two isotope MOT. This approach simplifies the optical system a lot in comparison with a system using superimposed slave laser beams. In the latter, the beam profile of each frequency component would be different, making the optimization of the MOT very difficult. The trick of using a tapered amplifier for several frequencies is very general and is also used in the Rb/K experiments. Even with the wavelength difference of 13 nm between the two atoms it works well [43].

The beam passes a final AOM (used to switch-off quickly the light of the MOT), is expanded in a telescope, and distributed to the six arms of the MOT using polarizing beam cubes and halfwave plates. The MOT beams have a diameter of 2.2 cm an intensity of $7\,\mathrm{mW/cm^2}$ at center, and an intensity of $4\,\mathrm{mW/cm^2}$ at the border.

The laser beams necessary for the imaging system are derived from the slave lasers injecting the tapered amplifier (see figure 2.12). The power distribution between the tapered amplifier and the imaging system can be changed during the experimental sequence using electronic waveplates. In this way it is possible to use nearly all power to inject the amplifier during the MOT phase and later on use all the power for absorption imaging. Since the waveplates have a characteristic response time of $1 - 10\,$ms, this works only for images taken more than this delay after the MOT phase. This is the case for images taken from atoms in the Ioffe-Pritchard trap, but not for images of the MOT itself. Thus a small but sufficient part of the slave laser power is always directed to the imaging system. The repumping beam for the imaging system is identical to the optical pumping beam. A beam exiting one of the two exit ports of the repump laser mixing cube is used for this. The beam used for Doppler cooling in the Ioffe-Pritchard trap is derived from the second order beam exiting the final AOM. The production of these beams will be described in detail in the sections explaining the respective systems.

During evaporative cooling, the atoms are trapped in a magnetic trap. This trap works only for some internal states. Resonant stray light from the laser system could induce transitions to untrapped states. To prevent this, the slave lasers and the tapered amplifier are enclosed in boxes of card board. During the magnetic trapping phase, shutters block all beams leaving these boxes. The other advantages of the boxes is the reduction of air currents, which leads to a more stabel injection of the slave lasers and the protection of the optics from dust.

2.7 The magnetic trap

For alkali atoms, it is difficult to exceed phase-space densities of about 10^{-6} in a magneto optical trap. The scattering of light imposes a limit on temperature and density. This limit depends on the linewidth of the cooling transition. The highest phase-space density obtained in a MOT could be achieved in strontium by cooling on a narrow, spin-forbidden transition [160]. But it is still a factor 100 away from the phase-space density necessary for condensation. In our experiment, the gap is bridged by evaporative cooling. To use this technique, the atoms have to be trapped without using resonant light. One method is to employ an optical dipole trap. The group of M. S. Chapman recently achieved condensation of rubidium by evaporation in such a trap [34]. We also produced a condensate by using a final evaporation stage in an optical trap (see section 3.6.3). The more common approach is evaporative cooling in a magnetic trap.

2.7.1 Theory of magnetic trapping

This kind of trap forms a potential well for atoms by the coupling energy between the magnetic moment of the atom and a magnetic field

$$U(\overrightarrow{r}) = m_F g_F \mu_B B(\overrightarrow{r}) \,, \tag{2.3}$$

where m_F is the magnetic quantum number, g_F the Landé factor and μ_B the Bohr magneton. To be a trap, the magnetic field has to possess an extremum of field amplitude in which the atoms will be trapped. Maxwell's equations forbid the formation of a static field maximum, so field minima are used (see S. Chu in [161]). Only atoms in states with the magnetic moment antiparallel to the field direction (low field seekers) can be trapped with static fields. The direction of the magnetic field may vary around the trap. The atom is moving in the trap, and sees the magnetic field direction change. As long as the rate of change of the field direction $\frac{\partial \Theta}{\partial t}$ is smaller than the Lamor frequency $\omega_L = 2\pi \times 1.4 \, \frac{\mathrm{MHz}}{\mathrm{G}} |B|$ the magnetic moment follows adiabatically the magnetic field direction. Thus only the field magnitude is important for the potential. If the adiabaticity condition is not fulfilled, the magnetic moment changes its orientation and the atom is eventually lost from the trap. Such *Majorana* spin flips occur in regions with weak magnetic field and/or a fast rate of change of the field direction.

We use two types of field geometry to trap our atoms: a quadrupole field and a

Ioffe-Pritchard field. The quadrupole field has the field geometry

$$\overrightarrow{B}(x,y,z) = \begin{pmatrix} -0.5Gx \\ -0.5Gy \\ Gz \end{pmatrix}, \tag{2.4}$$

where G is the gradient of the magnetic field in z direction. The resulting adiabatic potential is

$$U(\overrightarrow{r}) = m_F g_F \mu_B G \sqrt{x^2 + y^2 + 4z^2}/2\,. \tag{2.5}$$

Since the potential is linear, the oscillation frequency depends on the energy E (and is given by $\nu = m_F g_F \mu_B G/\sqrt{32Em}$). Such a magnetic field can be created by two field coils with currents in opposite directions (anti-Helmholtz configuration). Around the center of this trap the magnetic field is low and changes its direction quickly. This means that atoms can be lost by Majorana flips [162]. The rate of loss is given by $\Gamma = \hbar/(ml^2)$, where m is the atomic mass and l the trap width. Remedies for this are plugging the central region with a blue detuned repulsive light beam [8] or spinning the central region faster around the cloud of atoms than the atoms can follow (time orbiting potential (TOP) trap) [162]. This results in average in a harmonic potential.

Another approach is to trap the atoms with a 2D quadrupole field in two *radial* directions. The magnetic field lines are all in the radial plane. The field zero, which is in this case a line, can be plugged with an offset magnetic field B_0 with a field direction parallel to the line, in the *longitudinal* direction. Trapping along the axis of the field is done by giving this longitudinal field a curvature C_{ax}, creating a magnetic field minimum. This kind of trap is called a *Ioffe-Pritchard trap* [163]. The total magnetic field is then given by

$$\overrightarrow{B}(\overrightarrow{r}) = \begin{pmatrix} Gx \\ -Gy \\ 0 \end{pmatrix} + \begin{pmatrix} -C_{ax}xz \\ -C_{ax}yz \\ B_0 + \frac{1}{2}C_{ax}\left(z^2 - (x^2+y^2)/2\right) \end{pmatrix}, \tag{2.6}$$

where the first term describes the 2D quadrupole field and the second term the longitudinal offset field with curvature. The magnitude of the field is

$$\begin{aligned} B(\overrightarrow{r}) &= \sqrt{\left(B_0 + \frac{1}{2}C_{ax}\left(z^2 - (x^2+y^2)/2\right)\right)^2 + G^2\left(x^2+y^2\right)} && (2.7) \\ &\simeq B_0 + \frac{1}{2}C_{ax}z^2 + \frac{1}{2}C_{rad}(x^2+y^2)\,, && (2.8) \end{aligned}$$

where the second equation is the harmonic approximation, valid for excursions in the potential smaller than $x, y \lesssim B_0/G$. In this case the radial confinement is harmonic with curvature

$$C_{rad} = \frac{G^2}{B_0} - \frac{C_{ax}}{2}\,. \tag{2.9}$$

For greater excursions the radial potential is linear with gradient G. The trapping frequency for an atom with mass m in a harmonic potential is

$$\nu = \frac{1}{2\pi}\sqrt{\frac{m_F g_F \mu_B C}{m}}\,. \tag{2.10}$$

2.7.2 Design parameters of the magnetic trap

The Ioffe-Pritchard type potential is used by most BEC experiments, including ours. There are different implementations of this field geometry: the cloverleaf trap [38], the QUIC trap [164], microtraps [36], permanent magnet traps [165], iron core magnets [166] or the classical Ioffe-Pritchard trap after which the field geometry is named. The Ioffe-Pritchard trap (see figure 2.6) uses four parallel conductors placed vertically on the corners of a square. The currents flow in alternate directions through these *Ioffe bars* and create a two dimensional quadrupole field. Two field coils, called pinch coils, are oriented with their axes parallel to the bars and create the offset field. Their distance is chosen greater than it would be in a Helmholtz configuration. The field has a minimum between the coils and two maxima at the center of the coils, confining the atoms in the longitudinal direction.

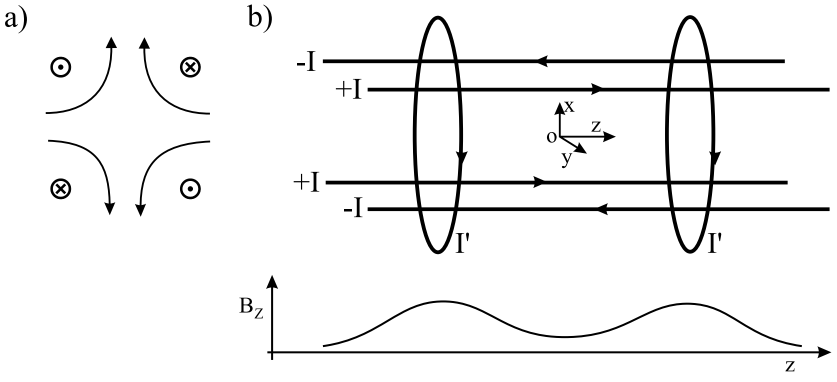

Figure 2.6: *Principle of the Ioffe-Pritchard magnetic trap. a) The radial confinement is achieved by a two dimensional quadrupole field produced by four parallel electric conductors, the Ioffe bars. b) Axial confinement is provided by a pair of pinch coils, producing a field mainly orthogonal to the quadrupole field and having a field minimum at mid-distance between the coils. These coils also provide a bias field, removing the zero field region in the center of the quadrupole. A pair of Helmholtz coils (not shown) compensates most of the uniform field of the pinch coils, thus increasing the radial confinement (see formula 2.9).*

When we choose the design of our magnetic trap we payed attention to four points.

- **Rapid switch-off.** After a sudden release of the atoms from the trap, the cloud will expand. In absence of collisions, each atom will follow a trajectory given by its momentum at the instance of the switch-off. After a time of flight sufficiently large to permit the atomic distribution to grow much bigger than the initial distribution in the trap, the initial conditions can be neglected and the spatial distribution corresponds to the momentum distribution. From this, the temperature of the cloud is derived (see section 3.2.2). This *time-of-flight* (TOF) technique is also very useful to measure the presence or properties of a condensate. Due to the release of mean field energy, spatial distribution of a BEC after a time-of-flight can be anisotropic, in contrast to the isotropic velocity distribution of a classical gas, providing a clear signature for degeneracy (see section 1.1.7). It is important that the atomic distribution not be modified during the switch-off of the trap. This means that the switch-off has to be non-adiabatic with respect to the oscillation frequencies of the trap ($\tau_{switch-off} \ll \tau_{osc} = 2\pi/\omega_{osc}$). We wanted to be able to use the TOF technique and thus opted for an electromagnetic trap. This stays in contrast to the permanent magnet trap used in the first experiment to condense lithium [123]. Because it was not possible to switch off the trap, the cloud had to be imaged *in situ*. The small size and high density made observations sensitive to the aberations of the imaging system [39].

- **Good optical access.** Optical access to the trapped atoms has to be provided for various reasons. The cloud is absorption imaged using a microscope. The resolution depends on the open view angle to the atoms. Access is also needed for the imaging probe beam, a repumping beam, the crossed dipole trap, and the Doppler cooling beam. In the future, various other laser beams will be used to manipulate the atoms.

- **Tight confinement.** The scattering length of ^{7}Li is with $a = -27\,a_0$ not very high. We compensated for this fact by constructing a tightly confining magnetic trap ($\omega_{rad} = 2\pi \times 8000\,\mathrm{Hz}$, $\omega_{ax} = 2\pi \times 130\,\mathrm{Hz}$ for ^{7}Li). Thus after capture of the atoms in the magnetic trap, the cloud can be adiabatically compressed, increasing the density and temperature and thus elastic collision rate. It is a bit unfortunate, that the increase in temperature leads for ^{7}Li to a drastic decrease in the elastic scattering cross section. But we could compensate this by implementing an optical cooling stage in the Ioffe trap (see section 3.1.5). Another advantage of a steep confinement is that we can obtain high Fermi energies in the degenerate Fermi gas. This can simplify experiments detecting the degeneracy, for example with light scattering. And the high oscillation frequencies together with the high anisotropy of our trap made it possible to create one dimensional condensates.

- **High atom number.** The elastic scattering rate scales linear with the atom number, and thus it is good for evaporative cooling to start with a high number of atoms. And of course having a high number of atoms at the end of the cooling process in the degenerate quantum gas, simplifies every study of its properties, and is sometimes essential for its formation.

2.7.3 Realization of the magnetic trap

Layout, transfer of atoms from the MOT to the Ioffe trap

Our magnetic trap is a Ioffe-Pritchard trap, following the design explained above (figure 2.6). It uses high current electromagnets positioned outside a glass vacuum chamber. One problem encountered when designing the trap was, that the design parameter *high atom number* contradicts the design parameter *steep confinement*. The magnetic trap is loaded from a MOT. To obtain a large number of atoms in the MOT, large diameter laser beams are advantageous. This means, that the glass cell should be big to permit the entrance of the beams. To obtain a steeply confining magnetic trap the conductors should be placed as close as possible to the atoms. Because the conductors remain outside the vacuum chamber, the class cell should be small. To resolve this contradiction without compromise, we separated the MOT and the Ioffe-Pritchard trap regions spatially (see figure 2.7). The glass vacuum chamber consists of a $4\,\text{cm}\times 4\,\text{cm}\times 10\,\text{cm}$ MOT cell with a $2\,\text{cm}\times 4\,\text{cm}\times 0.7\,\text{cm}$ appendage for the Ioffe-Pritchard trap projecting from the top of it. The transfer between the two regions is done magnetically. The MOT atoms are captured after optical pumping in a quadrupole trap centered on the MOT. The coils for this quadrupole trap are identical to the coils of the MOT (LQ). After compression of the quadrupole trap, a second pair of quadrupole coils, the transfer coils (HQ), centered in the Ioffe-Pritchard trap region, is ramped on. The center position of the resulting quadrupole field depends on the current ratio in the two coil pairs. At equal current the atoms are approximately midway between the two coil centers. Next the current in the MOT coils is ramped off, transferring the atoms to the center of the Ioffe trap.

Since the appendage has an internal dimension of only 3 mm, it is very important that the center of the quadrupole coil pairs corresponds to the center of the appendage. To achieve this, the position of the MOT and the transfer coils has to be adjusted to the glass cell with a precision of 0.1 mm, which is not easy. The position of the center of the quadrupole field relative to the small dimension of the appendage can be moved by applying a magnetic field orthogonal to this direction. We do so using the compensation coil of the Zeeman slower. The transfer efficiency is optimized by varying the orthogonal field applied during the transfer. If the optimum orthogonal field at the end of transfer is found to be different from zero, the transfer coils are mechanically moved in the direction indicated by the orthogonal field. It is mechanically impossible to move the MOT coils. Thus a ramp with the orthogonal field is always applied during the transfer to compensate for the misalignment of the MOT coils.

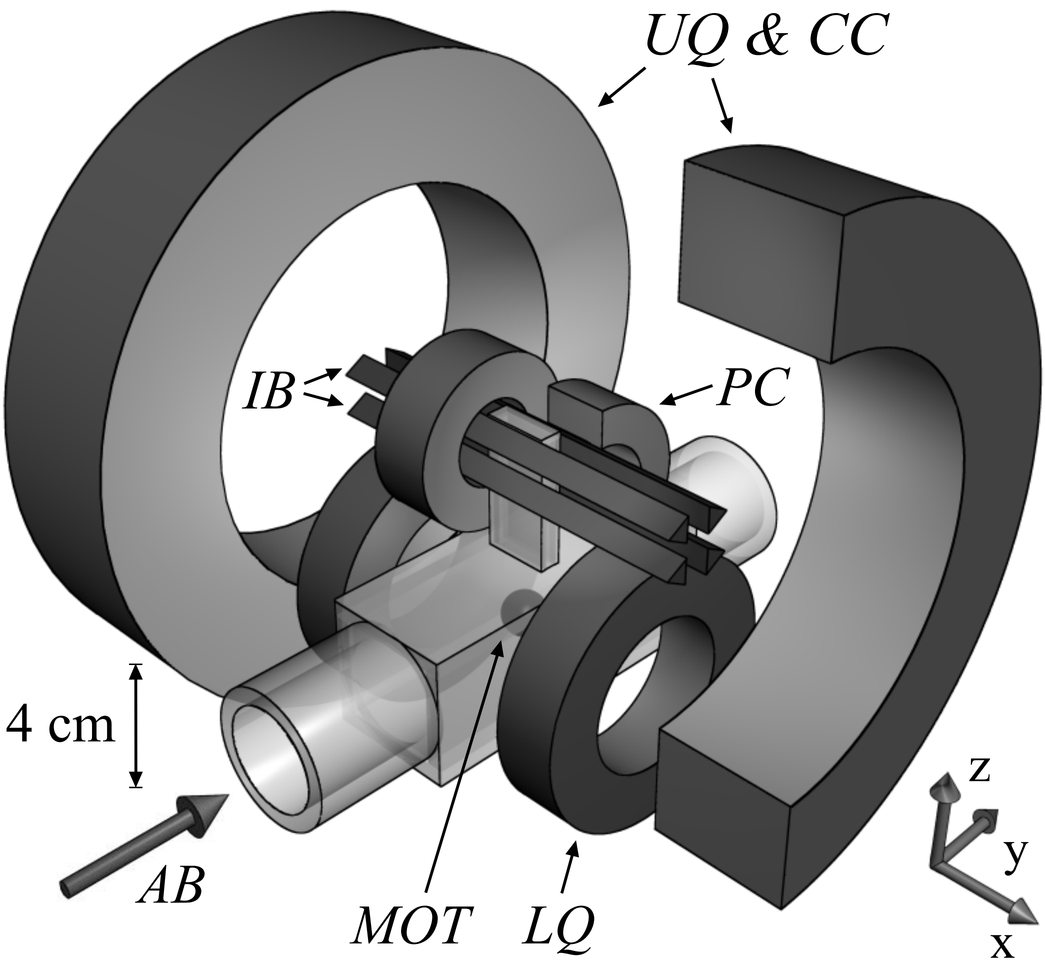

Figure 2.7: *The magnetic trap. Both lithium isotopes are collected from a slow atomic beam (AB) in a magneto-optical trap (MOT) at the center of a glass cell. Atoms are magnetically elevated using lower quadrupole (LQ) and upper quadrupole (UQ) coils into a small appendage. At this site, a strongly confining Ioffe-Pritchard trap consisting of 4 Ioffe bars (IB), two pinch coils (PC) and two compensation coils (CC) allows evaporative cooling of* ^7Li *to quantum degeneracy and sympathetic cooling of* ^6Li-^7Li *mixtures.*

The loading of the Ioffe trap is done in two steps. First, only the Ioffe bars are switched on with a gradient twice the radial gradient of the quadrupole coils. This inverts the direction of the magnetic field in the vertical direction, taking already the direction it will have in the Ioffe trap. Now the cloud is compressed adiabatically in the radial directions while the axial confinement is weakened by increasing the current in the Ioffe bars and decreasing the current in the transfer coils. Finally the transfer coils are switched off and the pinch coils are switched on, taking over the axial confinement and creating an offset field to hinder Majorana spin flips. The offset field produced by the pinch coils is bigger than necessary. Since the radial curvature increases with decreasing offset field (see formula 2.9), the offset field is compensated by reusing the transfer coils in a Helmholtz configuration with the magnetic field direction opposite to the field direction of the pinch coils. An additional pair of Helmholtz coils is used to finetune the offset field. This compensation of the offset field is done adiabatically. The oscillation frequencies obtained with this trap are very high, 7 kHz in the radial direction and 120 Hz in the axial direction for an offset field of 2 G and for ^{7}Li. These frequencies would be extremely difficult to obtain when building the magnetic trap around a big glass cell, suitable for a MOT.

This approach however also has a drawback, as we will see in the result section. Because of the relatively high temperature of the MOT sample, 90% of the atoms trapped in the initial quadrupole trap are lost during the transfer. The spatial extent of the cloud is larger than the inner size of the appendage. Second, the compression of the cloud to these high oscillation frequencies leads to adiabatic heating of the cloud. After the compression the cloud is at temperatures of 3 to 9 mK, exactly the temperature range, in which elastic collisions are suppressed for lithium. Remedies for this problem are explained in the section on Doppler cooling (3.1.5).

Construction of the trap

The coils are constructed out of rectangular copper tubes. The tubes are isolated by a layer of glass fiber ribbon and held together in the shape of a coil with epoxy glue. Each coil can carry a current of up to 500 A. The coils are cooled by water flowing inside the tubes. For the Ioffe bars and the compensation coils water pressurized by a pump (Sinatec HVX 2/18) to 15 bar is used, while for the other coils 3 bar is sufficient. The construction of the Ioffe bars is different from the other coils. The shape of each bar is given by the requirement that the bar has to fit into the space between the pinch coil and the appendage, and that a large optical access to the trapped atoms is required for imaging and optically manipulating the cold atoms (see figure 2.8). Each bar consists of three tubes, specially deformed to give the required triangular shape, when put together. To interconnect the bars, the ends of each tube is wound to a neighboring bar. These *end caps* give rise to an offset magnetic field in the longitudinal direction. To minimize this field one tube is connected to the left hand neighbor and the next to the righthand neighbor. The two resulting end caps compensate their offset fields. The connection of the third tube is not compensated. To minimize its effect, its end cap has a greater distance from the trap center. The current in the bars can be 700 A in continuous operation and up to 1000 A for a few seconds.

It is extremely important that the magnetic trap and especially the magnetic trap's offset field is stable. To achieve this, first of all the coils and the conductors supplying the coils have to be very well fixed mechanically. To stabilize the offset field further,

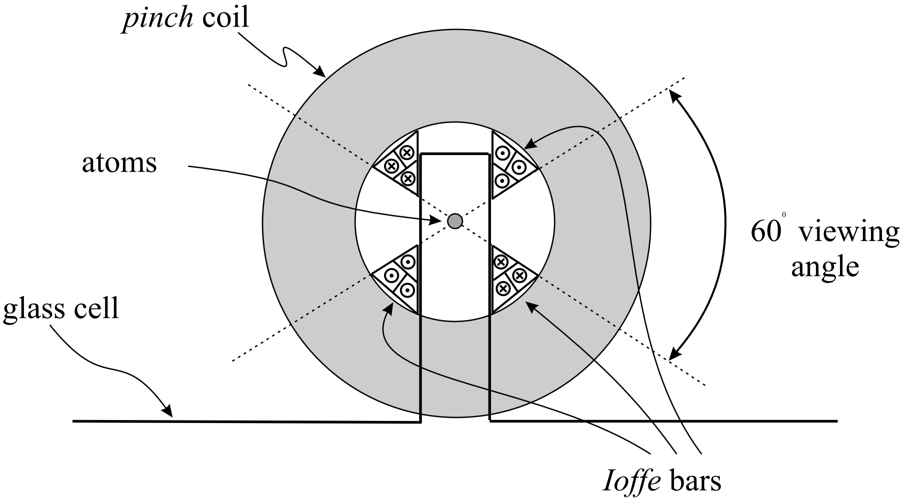

Figure 2.8: *Each Ioffe bar consists of three copper tubes. The tubes are deformed to fit in the space between the appendage and the inner surface of the pinch coils, leaving a 60° viewing angle to the atoms.*

some tricks have to be applied. The main contribution to the offset field comes from the pinch coils. This offset field is nearly completely subtracted by the transfer coils operated in Helmholtz configuration, the *compensation coils*. The current flowing in these coil pairs may fluctuate, since not very stable high power current supplies are used. Independent fluctuations would provoke a fluctuating offset field. Thus the pinch and compensation coils are installed in series in one electric circuit. The same current passes through both coil pairs. Fluctuations in this current do not affect the offset field, if the mutual compensation is perfect. In reality the compensation is not perfect and an offset field of 23 mG/A is produced by these coils. The offset field produced by the Ioffe bars is reduced to 3.1 mG/A, using the tricks described above. Fluctuations in the Ioffe bars current thus do not affect the offset field much. To regulate the exact value of the offset field a small field up to 26 G is added with a separate Helmholtz coil pair. The power supply for this coil pair is a high precision low noise power supply (Delta Elektronika SM 70-45 D).

The total power dissipated in this system can be as high as 45 kW. A failure of the cooling system would have disastrous consequences, destroying at least the coils and the glass cell. To exclude this as well as possible, a security system has been installed. It compares the temperatures at the water exit of each coil with preset maximum temperatures and it compares the waterflow through each coil with a minimum waterflow. If one of these conditions is not fulfilled, the security system switches off the electric currents. This system proved already very useful several times, and spared us many tears.

The electronic circuit

The electronic circuit used for the magnetic trap is shown in figure 2.9. The power supplies are high current power supplies (Lambda EMI, Electronic Measurements Inc., ESS-30-500-10-D-TC-CE-0806 and similar). For the MOT a 500 A, 30 V supply is used, for the transfer circuit two 500 A, 20 V supplies in series and for the Ioffe bars a 1000 A, 10 V supply. A MOSFET in parallel with each power supply can discharge the internal capacitors and prepare the power supplies for a switch-on without current peak from the capacitors. Varistors protect the power supplies against overvoltage. To configure the circuit and switch the currents off quickly, IGBT switches are used. Each consists of several 600 A, 1200 V voltage selected IGBTs in parallel (Powerex CM600HA-24H). Since a 600 A IGBT module can only be used at currents up to 300 A in continuous mode, two of them have to be used in parallel for 500 A and four of them for 1000 A. The IGBTs are mounted for cooling on a water circulated copper box. To switch the IGBTs, opto-isolated drivers have been constructed, giving peak currents of 20 A to charge and discharge the IGBTs gate capacity in less than $10\,\mu$s (see manuals [167, 168]). This fast switching time is important, since the IGBT junction will behave as a load for the current when the IGBT gate is not saturated, and heat up until destruction. IGBTs block current in only one direction. A diode integrated in the IGBT module bypasses current in the opposite direction. For some configurations of the electronic circuit this is not wanted. Especially during the switch-off of the circuit, closed loops are formed with induction current flowing for some milliseconds. For this reason the diodes D1, D2, and D3 were added in series with IGBTs to the circuit. They are conducting in the sense of operation of the IGBT and block current in the opposite direction. Diodes D1 and D2 also protect the transfer and the MOT power supplies against currents in counter direction. Each diode module consists of three voltage selected 250 A diodes which are watercooled and can withstand up to 1200 V before breaking. To protect the diodes against higher overvoltages, a 800 V varistor is put in series with them.

The electronic circuit can be operated in several configurations. During the MOT and transfer phase IGBT 6, 3 and 1 are closed. Current in the MOT coil is applied using the MOT power supply. The transfer coils are in a quadrupolar configuration and supplied by the transfer power supply. Also during the MOT phase a small current of 3 A is passed through the transfer coils to center the quadrupole field with the laser beams in the vertical direction. After the transfer to the Ioffe-Pritchard trap region, the MOT coils are completely switched off and IGBT 6 is opened. The Ioffe bars are activated by closing IGBT 8 and switching on the Ioffe bar power supply. After the adiabatic deformation, the transfer coils are switched off by opening IGBT 1 and 3. Next IGBT 4 and 5 are closed simultaneously and the MOT power supply is used to pass current through the pinch coils. For the compensation of the offset field, IGBT 2 is closed and current is put through the compensation and pinch coils in series, while the current added to the pinch coils using the MOT supply is reduced. When this current reaches zero IGBT 5 is opened. The pinch and compensation coils are not switched on simultaneously because the resulting inductance is so high that the switch-on time would be several milliseconds. During this time, the atom cloud would expand freely in the axial direction resulting in a loss of phase-space density. This is also one of the reasons why it is difficult to start with the atoms in the lower hyperfine state, where the maximum field may not exceed 140 G (27 G) for ^{7}Li (^{6}Li).

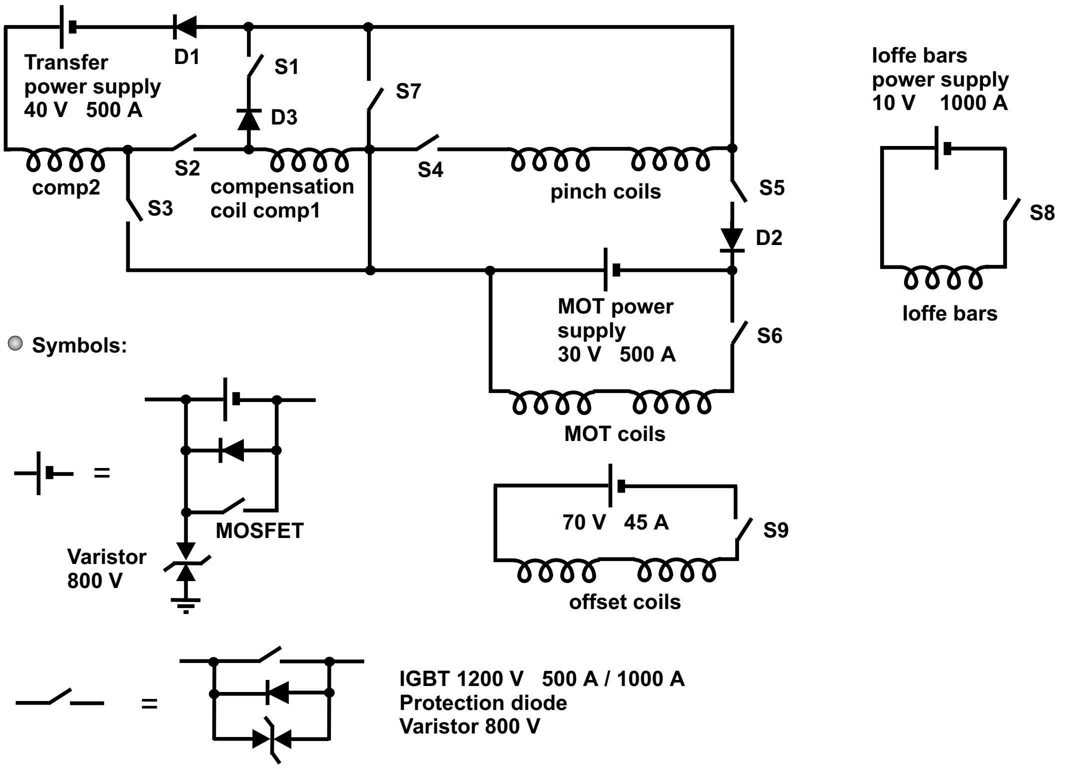

Figure 2.9: *The electric circuit used for the magnetic trap. The power supplies deliver up to* 1000 *A to the field coils. Different configurations can be achieved using IGBT switches, thus enabling the magnetic transfer of the atoms from the MOT to the appendage region, the reuse of the transfer coils as compensation coils and the use of the pinch or the compensation coils to produce the field necessary for Feshbach resonances. The circuit is explained in detail in the text.*

The offset field for the Feshbach resonance

An offset field up to 1200 G can be applied by either using the pinch or the compensation coils. When using the pinch coils, IGBT 4 and 5 are closed and current is provided by the MOT power supply. The compensation coils are active when IGBT's 2 and 7 are closed and the "transfer" power supplies are on. The advantage of the pinch coils is their smaller inductance and thus a faster response time than the compensation coils. Their eventual disadvantage is the inhomogeneity of the field. The compensation coils provide a homogeneous field at the expense of a higher inductance. Their field is oriented in the opposite direction of the offset field used in the magnetic trap. The field direction has to be reversed adiabatically in order not to loose the polarization of the atoms. For this a field orthogonal to the trap axis (which can be the earth magnetic field, or the field of the Zeeman slower compensation coil) is applied during the time when the offset field changes its direction. For the Feshbach field, the power supplies are used in control current mode. The slope of the current increase has to be changed smoothly. Otherwise the power supplies will not closely follow the programmed current. This can result in uncontrolled loss of atoms due to inelastic collisions if the offset field gets too close to the Feshbach resonance. In practice, the current is increased after $I(t) = I_{final}(1 - \exp(-t/\tau))/(1 - \exp(-\eta))$ for $t < \eta\,\tau$ and $I(t) = I_{final}$ for later times. τ is about 10 ms and $\eta \sim 5$.

Switch-off

In order to avoid disturbing the atomic momentum distribution, the switch-off of the confining potential has to be much faster than the oscillation frequencies. The switch-off time depends on the allowed induction voltage since $U_{ind} = -L\dot{I}$ where L is the coils inductivity. The induction voltage falls off at the junction of the switch. We choose IGBTs which can support 1200 V before breaking down. Varistors are connected in parallel with the IGBTs. They are chosen to become conducting at a voltage of 800 V and thus protect the IGBTs. The magnetic field's energy is dissipated in the varistors during switch-off. Attention has to be payed not to switch off several IGBTs which are in series. The sum of the induction voltages can be greater than the isolation provided by the opto-couplers that decouple the magnetic trap system from the computer control. This effect already once destroyed part of the computer. After the accident, additional 800 V varistors were connected between different points of the circuit and the ground to prevent further accidental overvoltages.

Detection of magnetic sublevels

To separate the different magnetic momentum states during the time of flight, a magnetic field gradient can be applied. The coil used to produce the field is made out of thin, isolated copper wire and has 70 turn with a diameter of 1 cm. The coil is places about 2 cm above the atoms and produces a gradient of 300 G/cm at a current of 150 A. The current source are capacitors inside a power supply, charged to 80 V. The current is switched by a MOSFET and typically left on for less than 1 ms after switch-off of the trap.

2.8 The optical dipole trap

As we have seen above, only low-field seeking states can be trapped in a magnetic trap (section 2.7.1). It can be of great interest to also trap other states in a conservative potential. For instance, a Feshbach resonance exists for the ^{7}Li $|F = 1, m_F = 1\rangle$ state, which is a high-field seeking state (section 1.3.3). An optical dipole trap is capable of trapping atoms regardless of their internal state, making it possible to explore properties of states and mixtures of states which are not trappable in a magnetic trap [169, 170]. A homogenous magnetic field can be applied without changing the properties of the optical trap. This field can serve to tune the scattering length near a Feshbach resonance. In a magnetic trap, the trapping frequencies depend on the offset magnetic field. The Feshbach resonances in lithium require fields of several 100 G, which would result in a much weaker confinement than that obtained for the usual offset field of 1.5 G (see formula 2.9). Despite all these useful properties of the optical trap, it does not make the magnetic trap obsolete, since the latter provides a deeper and more spatially extended potential, capable of retrapping all the atoms from the lithium MOT. In addition, the magnetic trap allows forced evaporative cooling to be implemented by the use of radio frequency transitions to untrapped states. This allows the tuning of the cut energy, essential for forced evaporative cooling. However, in typical optical traps, the cut energy is equivalent to the potential depth. As we will see below, the trap becomes weaker, when lowering the potential depth. This reduces the elastic collision rate, which may stop evaporative cooling if the initial elastic collision rate was to low. However, radio frequency evaporation can still be implemented in an optical trap, *e.g.*, by using a magnetic field gradient to tilt the potential in dependence of the magnetic moment and thus creating untrapped states, see also section 3.6.3. In the following the principle and the properties of an optical trap will be discussed. At the end our implementation of the optical trap is presented.

2.8.1 Principle of an optical dipole trap

The simplest implementation of an optical trap is a focused gaussian laser beam, with a frequency below the frequency of the atomic transition [169]. In this case the atoms experience an attractive potential proportional to the laser intensity and are kept in the focus of the laser beam. The origin of the potential can be thought of in a number of different ways (see lectures of C. Cohen-Tannoudji, S. Chu, and B. Phillips in [161]). In the dressed atom picture, the eigenstates of the combined atom, electromagnetic field system are shifted in comparison to the energy states of the atom alone. This energy shift is called the *a.c.-Stark shift* or *light shift*. Another way of thinking is to consider the atom as a driven harmonic oscillator. The oscillating electric field $\overrightarrow{E}$ induces an oscillating dipole moment $\overrightarrow{m} \propto \overrightarrow{E}$ which is in phase with the driving field when driven below resonance and out of phase when driven above resonance. The interaction energy between dipole and field is $U \propto \overrightarrow{m}\overrightarrow{E} \propto E^2 \propto I$. The energy shift depends on the intensity I of the light. Below resonance the energy is negative and the oscillator will be drawn toward a more intense field, while above resonance it will be pushed to regions of weaker field. Thus an atom can be trapped in the focus of a gaussian beam with a frequency below the atomic resonance. This method of creating a potential works with any particle possessing electric polarizability, not only atoms, but also molecules or even cells and dust particles.

2.8.2 Trapping of an alkali atom in a dipole trap

Trapping potential

Now we will specialize our discussion to the case of an alkali atom, trapped in a focused gaussian laser beam. The trapping potential is given by the gaussian shape of the laser beam

$$U(r,z) = U_0 \frac{\exp\left[-2r^2/w(z)^2\right]}{1+(z/z_R)^2}\,, \tag{2.11}$$

where r and z are the radial and longitudinal coordinates, $w(z) = w_0\sqrt{1+(z/z_R)^2}$ the beam radius as a function of longitudinal position, where $z_R = \omega_0^2\pi/\lambda$ is the beam Rayleigh range, with λ being the wavelength. The depth of the potential is given for an alkali atom by [171]

$$U_0 = \frac{\hbar\gamma I_0}{24 I_S}\left[\left(\frac{1}{\delta_{\frac{1}{2}}}+\frac{2}{\delta_{\frac{3}{2}}}\right) - g_F m_F\sqrt{1-\epsilon^2}\left(\frac{1}{\delta_{\frac{1}{2}}}-\frac{1}{\delta_{\frac{3}{2}}}\right)\right]\,, \tag{2.12}$$

where γ is the natural line width, m_F the Zeeman sub level of the atoms, g_F the Landé factor, I_S the saturation intensity, defined as $I_S = 2\pi^2\hbar c\gamma/(3\lambda^3)$, I_0 is the peak intensity $2P/(\pi\omega_0^2)$ in terms of the laser power P [172, 173]. The detunings $\delta_{\frac{1}{2}}$ and $\delta_{\frac{3}{2}}$ are in units of γ and represent the difference between the laser frequency and the D1 ($2^2S_{1/2} \Rightarrow 2^2P_{1/2}$) and D2 ($2^2S_{1/2} \Rightarrow 2^2P_{3/2}$) transition frequencies, respectively ($\delta = 2\pi c(1/\lambda_{trap} - 1/\lambda_{atom})/\Gamma$). The parameter ϵ depends on the polarization of the laser beam. It is defined by writing the polarization vector of the light as $\hat{\epsilon} = (\hat{x}\sqrt{1+\epsilon} + i\hat{y}\sqrt{1-\epsilon})/\sqrt{2}$. For linearly polarized light $\epsilon = 1$ and all Zeeman sub levels experience the same potential.

Photon scattering

Even if the laser frequency is far from the atomic transition, photons can be scattered. As a result the trapped gas is heated and atoms can be lost. The scattering rate is proportional to the laser intensity and can be expressed in terms of the optical potential

$$\Gamma_{scat} = \frac{U(r,z)}{\hbar|\delta|}\,, \tag{2.13}$$

where the detuning δ (in units of γ) has been assumed to be far from the D1 and the D2 transition $\delta = \delta_{\frac{1}{2}}$ with $|(\delta_{\frac{3}{2}} - \delta_{\frac{1}{2}})/\delta_{\frac{3}{2}}| \ll 1$. Keeping the potential U constant (by changing the laser power) the scattering rate decreases as $1/\delta$ with the detuning. To achieve a low scattering rate it is good to use a far detuned laser. The momentum $\hbar k = h/\lambda$ is transferred to the atom, giving it a recoil energy of $E_{rec} = (\hbar k)^2/2m$. The heating rate in K/s resulting from this is $h_{scat} = \Gamma_{scat} E_{rec}/k_B$.

Oscillation frequencies

For small excursions of the atoms from the trap center, the gaussian trapping potential (2.12) can be approximated by a harmonic oscillator potential,

$$U(r,z) \simeq U_0 \left(1 - \frac{z^2}{z_R^2} - \frac{2r^2}{w(0)^2}\right)\,. \tag{2.14}$$

For $U_0 < 0$ the oscillation frequencies are obtained from this.

$$\omega_{rad} = \sqrt{\frac{4|U_0|}{m w_0^2}}\,, \tag{2.15}$$

$$\omega_{ax} = \sqrt{\frac{2|U_0|}{m z_R^2}} = \frac{\lambda}{\sqrt{2}\pi w_0}\omega_{rad}\,. \tag{2.16}$$

Both frequencies increase for a tighter waist w_0. The axial frequency is usually much smaller than the radial, since $\lambda \ll w_0$. For that reason, often two focused gaussian laser beams propagating in orthogonal directions are superposed, with their focuses coinciding. In comparison with a single beam, the potential depth U_0 is doubled for equal intensity in the two beams. The new potential has oscillation frequencies $\omega_{ax}^{crossed} = \sqrt{2}\omega_{rad}$ and $\omega_{rad}^{crossed} = \sqrt{\omega_{rad}^2 + \omega_{ax}^2} \simeq \omega_{rad}$, where the last equality is true for $\omega_{ax} \ll \omega_{rad}$. A gas trapped in a crossed dipole trap potential has a pancake shape.

2.8.3 Setup of the optical trap

Our optical dipole trap is a crossed dipole trap, consisting of two focused Nd:YAG laser beams, with a wavelength of 1.064 μm and a power of about 3 W each. The focus is about $w_0 = 40\,\mu$m. The transition frequency of lithium is 671 nm. The D1 and D2 lines are separated by 10 GHz, making $\delta_{\frac{1}{2}}$ and $\delta_{\frac{3}{2}}$ nearly identical. The linewidth is $\Gamma = 2\pi \times 6$ MHz. For these parameters the potential depth of the crossed beam trap is

$U_0 = 120\,\mu$K, the oscillation frequencies are $\omega_{ax}^{single} = 2\pi \times 11$Hz, $\omega_{rad}^{single} = 2\pi \times 2100$Hz, resulting in $\omega_{ax}^{crossed} = 2\pi \times 3000$Hz, $\omega_{rad}^{crossed} = 2\pi \times 2100$Hz and the scattering rate at the center of the trap is 0.3 photons per second per atom.

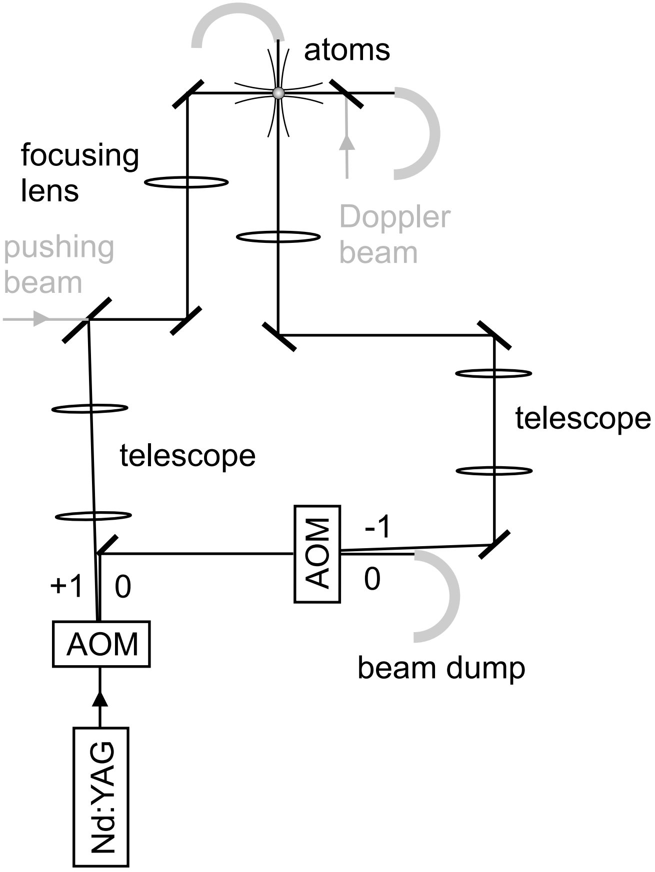

Figure 2.10: *Setup of the crossed optical dipole trap. A 9.5 W Nd:YAG laser beam is split in two beams. They pass through AOMs which are used to control the beam intensities. Both beams are expanded using telescopes and focused under orthogonal directions on the atoms in the Ioffe-Pritchard trap region. The* 671 *nm pushing beam and the Doppler cooling beam are coupled into the horizontal dipole trap beam by using dichroic mirrors.*

The setup is shown in figure (2.10). A 9.5 W Nd:YAG laser beam (Spectra-Physics T40-8SS(08T)) is passed through an AOM, which serves to control the intensity ratio of the horizontal and the vertical dipole trap. The light in the first diffraction order serves for the horizontal dipole trap. The light passing undiffracted through the AOM is used for the vertical dipole trap. It passes a second AOM, used to control the vertical beam intensity. Different diffraction orders are used for the two AOMs to avoid interference between the two beams in the optical trap. The first AOM is not optimized for maximum intensity in the diffracted beam, as is usually the case. Such an optimization would result in a zero order beam with intensity dip in the center. But a nice gaussian zero order beam is needed for the vertical dipole trap. We operate this AOM at 100 MHz instead of the frequency it is specified for of 80 MHz, which reduces its efficiency and leaves the zero order beam gaussian. The beams for the horizontal and vertical dipole traps are expanded using telescopes and focused along orthogonal directions onto the atoms in the Ioffe-Pritchard trap region. The construction of this optical system has to be done with great care. The mechanics have to be stable to prevent trap vibrations. High quality achromatic lenses should be used to reduce spherical abberation. For the same reason the laser beam should pass the lenses orthogonal in their center. Mirrors are anti-reflection coated at $1.064\,\mu$m for high intensity beams. If not, the laser will locally heat up the mirror, leading to a deformation. This can change the position of the focus. After passage through the trapping region, the beams are dumped in curved copper tubes, which are closed at one end. Two 671 nm beams are coupled into the horizontal beam using dichroic mirrors. One is used for Doppler cooling in the Ioffe trap and counter-propagates with the dipole trap beam. The other, the *pushing beam* is carefully superposed with the horizontal Nd:YAG laser, so that the focus of the 671 nm and the 1064 nm beams coincide. The pushing beam is derived from the probe beam for the MOT detection system.

Alignment of the optical trap

The alignment of the optical dipole trap is done using the following method. The horizontal beam is extracted from the optical system after the focusing lens. Now the position and the waist of the horizontal beam focus can be measured by blocking the beam partially with a knife edge mounted on a two axis translation stage. By changing the expansion of the telescope, the waist can be adjusted to the desired size. The size of the waist is measured along two orthogonal axis to detect possible astigmatism of the beam. The additional mirror is removed and the position of the last lens is adjusted along the axis of the beam so that the longitudinal position of the focus coincides approximately with the magnetic trap center. The beam is superposed with the Doppler cooling beam, which we know to be superposed with the magnetic trap with an accuracy of 1 mm.

Next, a cold cloud is prepared in the magnetic trap using evaporative cooling. The pushing beam, which is resonant with the atomic transition, is switched on for ~ 10 ms. This pumps atoms to non trapped states and thus creates a loss of atoms. The loss is the highest if the focus of the pushing beam coincides with the center of the magnetic trap. The pushing beam together with the superposed horizontal Nd:YAG laser beam are moved laterally to optimize this loss of atoms. Once an optimum has been found, the pushing beam is blocked for all further experiments. Normally the effect of the potential of the horizontal dipole beam can now be seen in the behavior of the atoms. For this, the beam is ramped on after an evaporation. The magnetic trap is switched off and 10 ms later an absorption image of the atoms is taken. Some atoms will be guided in the optical potential. Now the position of the focus in all three directions is adjusted to trap as many atoms as possible.

The alignment of the vertical beam follows the same scheme. By shifting the beam orthogonally to the axis of the magnetic trap, a position can be found where an influence of the beam on the atoms is visible. For this only one degree of freedom has to be scanned. Hence a pushing beam is not necessary for the alignment of the vertical optical trap. As soon as a signal has been found, the lateral position and the longitudinal position of the focus can be optimized on the position of the optical trap with respect to the magnetic trap and on the number of trapped atoms.

Finally, the intensity of the Nd:YAG beams was calibrated, making it possible to perform controlled intensity sweeps, despite the strongly nonlinear response of the AOMs.

2.9 The radio frequency system

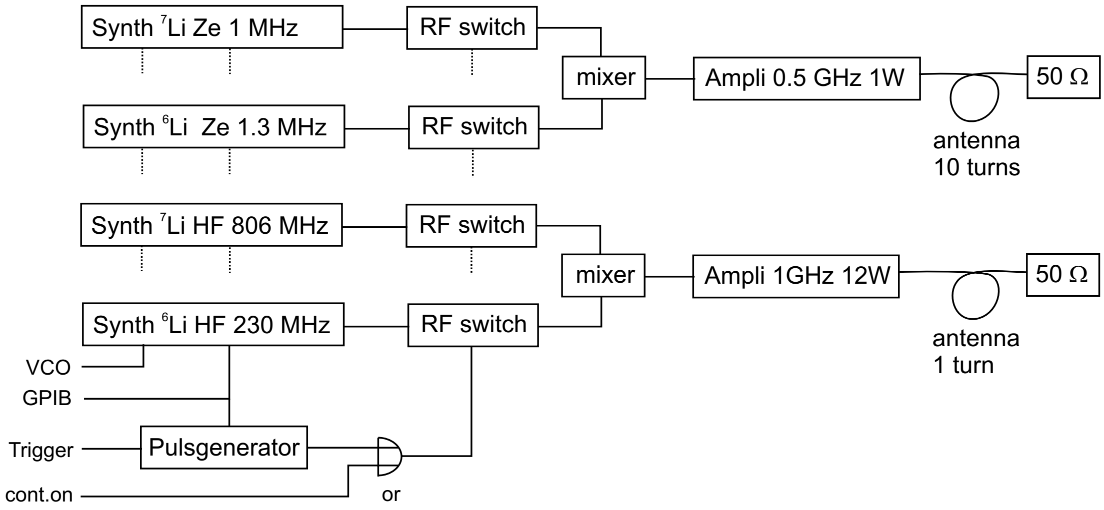

Figure 2.11: *Scheme of the radio frequency system. For each isotope two synthesizers produce frequencies resonant with the hyperfine or the Zeeman transition. The frequencies given are for an offset field of 1.4 G. The output of each synthesizer is transmitted to an amplifier and the antenna via a radio frequency switch. The switch can be operated either in continuous mode (cont. on) or using a pulse generator. The synthesizer is programmed via GPIB. For the adiabatic passage, it is put in the voltage controlled oscillator (VCO) mode and programmed by an external voltage. The outputs are grouped after the frequency range and transmitted after mixing to adapted amplifiers and antennas.*

The radio frequency system is used for the evaporation, for measuring the energy distribution of a cloud, for state transfer, and to put a cloud out of thermal equilibrium. To achieve all these different tasks, the system has to be versatile. A scheme of it is shown in picture (2.11). Four frequency synthesizer are used to produce frequencies for the intervening four transitions: the hyperfine transition at 803.5 MHz (228.2 MHz) and the Zeeman transition at 1 MHz (1.3 MHz) for 1.4 G offset field for ^{7}Li (^{6}Li). (The synthesizers are: Rohde & Schwartz SMT03, Marconi Instruments 2030 and Stanford Research SRS DS345) The two hyperfine frequencies are combined on a mixer (Mini-circuits ZFRSC 2050) and put on a common amplifier (Mini-circuits TIA 1000-4) and antenna, adapted for this frequency range. The same is done independently for the two Zeeman frequencies (amplifier: Mini-circuits ZHL-1-2W). The antennas consist of one (ten for the Zeeman frequencies) sphere of isolated 0.5 mm diameter copper wire. The antennas have one centimeter diameter and are placed at a distance of 1.5 cm from the atoms. They are terminated by a 50 Ω 1 W resistance with a frequency range up to 1 GHz. Each synthesizer has a radio frequency (RF) switch between them and the amplifier. The RF switch consists of two RF switches (Mini-circuits ZYSWA-2-50DR) in series to improve the attenuation. The switches are controlled both directly by a TTL signal or, for very fast pulses, through an externally triggered, GPIB programmed pulse generator (Quantum Composers 9300).

The system is used in different modes. For the evaporative cooling frequency ramps, the switches are continuously on and the synthesizers frequency is reprogrammed every 70 ms *via* GPIB. For the state transfer using Rabi oscillations (see section 3.4.1), the synthesizers are programmed to the desired frequencies and intensities and the pulse generator to the desired pulse duration. Then the pulses are emitted by triggering the pulse generator. For the state transfer using an adiabatic passage (see section 3.6.1), the synthesizers are put into voltage controlled oscillator (VCO) mode and the VCO frequency range is programmed. Then the sweep is performed by switching the RF switches continuously on and performing a voltage sweep on the VCO entry of the synthesizers.

To verify the correct operation of the radio frequency system, it is very useful to install a single loop pickup coil directly above the antennas and look at its signal on a fast oscilloscope. Even if the oscilloscope is not fast enough to resolve the waveperiod, a clearly visible signal will be available. If the exact behavior of a high frequency signal has to be verified, a beat measurement is performed, by mixing the pick-up coil voltage to a reference frequency near the frequency of the signal of interest on a mixing diode and looking at the beat signal.

2.10 Detection of the atoms

Cold atomic gases or atomic beams can be detected in various ways.

- An atomic beam can be detected by using a hot wire in combination with an electric field. The atoms which come in contact with the wire get ionized and the resulting flux of electrons is measured [174].
- Rydberg atoms can be detected one by one by ionization in an electric field and measuring the flux of electrons (important for the experiment described in [175]).
- The atoms can be resonantly ionized using lasers and the flux of produced ions measured (see for instance [176]).
- Metastable atoms, such as $^4\text{He}^*$, release their internal energy when they come into contact with a surface. In a multi channel plate this is used to produce a detectable signal. This was used to detect the He condensate in the group of A. Aspect [41].
- The fluorescence of atoms in a resonant light field can be captured on a photo detector or a camera.
- The absorption of light from a near resonant probe beam passing through the atomic cloud can be measured using a photodiode or a camera.
- The phase-shift induced by the atoms in a far-resonant probe beam can be detected using phase-contrast or dark field imaging techniques [177].

2.10.1 Principle of absorption imaging

The method we choose for its flexibility is a camera system for absorption images of the cloud, which will now be discussed in detail. A laser beam is sent through the region of the cloud. The width of the beam has to be as least as large as the spatial region of interest. The beam is near resonant so that the atoms absorb light from it. A lens system images the plane of the atomic cloud on a CCD chip. The resulting image shows the shadow of the atoms in the laser beam. Since the laser beam profile is never perfectly flat one has to normalize the picture to a reference picture without atoms present. To subtract an eventual offset from background ambient light, a third image without laser beam is taken and subtracted from the first two before further treatment. The link between the images and the atomic density comes from the absorption law

$$A(x,y) = \frac{I(x,y)}{I_0(x,y)} = \exp\left(-\sigma \int dz\, n(x,y,z)\right) , \tag{2.17}$$

where $n(x,y,z)$ is the atomic density distribution, σ the absorption cross-section, $I_0(x,y)$ the laser profile and $I(x,y)$ the laser profile after passage through the atomic cloud. The integration is done in the direction of the laser axis. It is convenient to work with the optical density, which is proportional to the integrated atomic density and defined as

$$D_{opt}(x,y) = -\ln\left(\frac{I(x,y)}{I_0(x,y)}\right) = \sigma \int dz\, n(x,y,z)\,. \tag{2.18}$$

This quantity is readily calculated from the recorded images.

2.10.2 Imaging optics

In our system we installed two camera systems working with this principle. The first allows us to take images in the MOT region, whereas the second is used for images of the Ioffe-Pritchard trap region. The MOT cameras optical system consists of a single lens producing an image with a magnification of 0.4. The camera (i2S iMC500) uses a video CCD chip working in interlaced mode. It can be externally triggered. To remove stripes due to the interlacing, only the even lines are used, giving an image size of 384×256 pixels (horizontal × vertical) with a calibration of $33\,\mu$m x $48\,\mu$m per pixel. The image is digitized with a dynamics of 8 bit. This very simple camera system is sufficient to optimize the MOT, the optical pumping, and the capture in the magnetic trap.

The "scientific" camera system centered on the Ioffe-Pritchard trap region is much more sophisticated. It consists of a pair of achromatic 160 mm lenses, used to transport the image and an exchangeable third lens, defining the magnification (see image 2.12). Usually either a 50 mm lens or a 4× microscope objective is used, providing a magnification of 0.4 and 4 respectively. The camera is a 16 bit slowscan camera with 512 pixels horizontally and 1024 pixels vertically (Andor Technologies V437-BV). The CCD chip is back-illuminated giving a quantum efficiency of 90%. The pixels have a size of $13\,\mu$m × $13\,\mu$m. The resolution of the imaging optics has been measured under ideal conditions outside the experimental apparatus to be about $3.5\,\mu$m. This value has not yet been reached in the experiment. The resolution for most of the data I will present in the result section was about $10\,\mu$m.

2.10.3 Probe beam preparation

The optics for the preparation of the probe beam is sketched in figure 2.12. The beams are derived from the slave lasers injecting the tapered amplifier. Using electronic retardation plates, the light of these lasers can either inject the amplifier or be directed to the camera system. Before the ^{6}Li and ^{7}Li probe beams are mixed, each beam passes an AOM which serves to switch the beams selectively on and off. After being mixed on a polarizing beam cube, the light passes through an optical fiber. This serves to clean the mode and give the same spatial mode to both beams. A shutter is installed directly before the fiber, to completely block the light during the evaporation. After the fiber

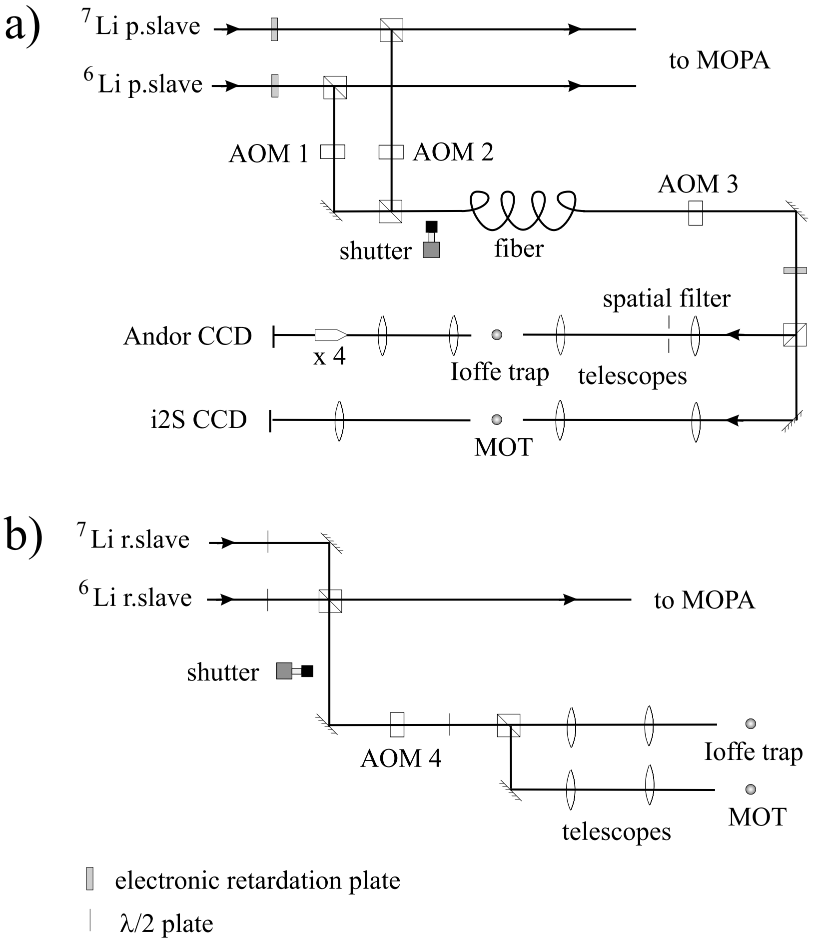

Figure 2.12: *The optical system for detection of the atomic cloud. (a) ^{6}Li and ^{7}Li probe beams are derived from the slave lasers injecting the tapered amplifier. Electronic retardation plates are used to switch the light from the tapered amplifier to the detection system. The beams are superposed and cleaned in a fiber. Both beams can be used independently and in fast sequences using AOMs. Two AOMs in series are used to achieve a high attenuation. The absorption of the atoms is detected by imaging their shadow on a CCD chip. (b) Beams on the repumping transition are used to optically pump the atoms to the higher hyperfine state. They are used before capture in the magnetic trap and during absorption imaging.*

another AOM shifts the light to resonance. This AOM is also important to give a higher attenuation when the beams are switched off since the slow scan camera is very sensitive. Next the beams are split on a polarizing beam cube and are directed to the two different camera systems. An electronic retardation plate chooses which frequency component is directed to which system, or can be put to a state where equal ratios of both beams are sent to both systems. Finally the beams are expanded and sent through the glass cell to the cameras. The slow scan camera beam is further cleaned by a pinhole placed in the focus of the telescope.

To make the detection of atoms in the lower hyperfine state possible and to reduce the loss in signal due to depumping, a repumping beam is used for both camera systems. Its preparation is simpler than the preparation of the probe beams. First the light of the repumping slave lasers is mixed on a beam cube. The light of one exit port injects the tapered amplifier, while the light from the other exit port is used for the repumping beams. It passes through a shutter and an AOM, is split on a beam cube, expanded in a telescope and sent to the glass cell. The MOT repumping beam is mixed with a horizontal MOT beam using a polarizing cube and is copropagating with the probe beam. This beam is also used for optical pumping before capture in the magnetic trap. The repumping beam for the Ioffe-Pritchard camera system is sent through the cell approximately counter-propagating with the probe beam. This is the advantageous direction since recoils from the probe and repump beam are in opposite directions.

The quality of the absorption images depends also on the smoothness of the spatial profile of the probe beam. To realize this several things can be done. First the probe beam is expanded to a size much larger than the size actually used. Only the nearly flat center region of the gaussian profile is used. Next fibers and pinholes remove higher spatial frequencies in the profile. To reduce interference fringes which are produced by the parallel glass windows of the cell and the entrance window of the camera, the probe beam is always sent at a slight angle through these windows, which makes the interference period too small to be resolved. The most disturbing interference fringes come from dust particles on the optics, especially if they are near a focal plane, for example on the glass cell or on the entrance window of the camera. Careful cleaning is a must to obtain good results.

Another problem arises when the position or the profile of the probe beam has changed between recording of the absorption and the reference image. Such a change can come from mechanic vibrations due to the switch-off of the magnetic trap. To prevent this, the optics of the camera system have to be attached independently from the magnetic trap in a very stable way, paying attention not to form loops for induction currents which would give rise to strong mechanical forces. The absorption and the reference images have to be taken with a time interval much smaller than any mechanical oscillation period or with a time delay for which the vibrating position of the probe beam coincides by chance with its initial position.

A severe problem is also the temperature dependence of the index of refraction of air. The Ioffe bars can be up to 55°C hot, which provokes a laminar air current around them. Upon switch-off of the Ioffe bars the air current becomes turbulent. The distortions induced in the probe beam by these air currents change on a ms scale, making it difficult to take an absorption and a reference image with the same distortions. Luckily it takes about 10 ms for the air current to change from laminar to turbulent, giving some time to take the images.

2.10.4 Two isotope imaging

A special property of the slow scan camera helps to achieve this goal. The CCD chip can be divided in several slices (typically five, then their size is 512 × 204 pixels). Only the uppermost slice is exposed to light, the rest of the chip is screened and serves as analog image memory. After each exposure, the charges of the chip are displaced by the number of lines each slice takes. This displacement can be fast, typically $16\,\mu$s per line. After the displacement is completed, the image is protected in the screened region of the chip and the next picture can be taken until all storage regions are full. This method for recording images is very versatile. We use it to take the reference image only 2 ms after the probe image, which prevents distortions due to changing air currents and vibrations, which would occur for delays longer than ∼10 ms. Another usage is to take images of both isotopes after one experimental run (see figure 2.13). To do this, four pictures are taken. First the ^{7}Li absorption image. This image taking process leaves the ^{6}Li distribution undisturbed. Next the ^{6}Li absorption image is recorded. The next two images are the reference images for the two isotopes. It is important that the probe beam is undisturbed by the atoms for the reference images. For images of the MOT this is obtained by waiting until the atoms have fallen out of the image area. This takes more than 2 ms and hence can not be used, since image distortions would occur for longer waiting times. For this reason we put the atoms out of resonance for the reference images, either by changing the offset magnetic field or by changing the probe beams frequency slightly (by ∼ 20 MHz). Lager detunings can not be used since this would partly disinject the slave laser producing the probe beam, which would strongly affect the probe beam intensity. When the atoms are out of resonance, reference images of both isotopes can be taken one after the other. The speed of transport within the CCD depends on the charge in the well of the CCD chip. If the well is full it spills to the next pixel during an overly rapid transport. Typically we charge the well to $\sim 1/5$ of its capacity of $10^5\,e^-$. This corresponds to a dynamics of 14 bit. Transport time of $16\,\mu$s per line are possible, giving a delay of 1 ms between the images of the two isotopes and a delay of 2 ms between the absorption and the reference image.

Noise images are recorded afterwards. One noise image for ^{7}Li is taken with the ^{6}Li exposures and the inverse, to include the effect of crosstalk between the two beams. Since the noise images change only if the stray light around the camera is changed and since the readout of the camera takes 15 s, the noise images are only recorded once in a while and not after each experimental run.

Taking several images in each experimental run can be used for many purposes. It allowed us to compare the behavior of the bosonic and the fermionic atoms after the same experimental run, which was essential to detect the Fermi pressure. The distribution of the bosons can be used to measure the temperature of the mixture. This is not easy to do by knowing only the fermionic distribution. Without the two isotope imaging technique the sequence used to obtain a stable Bose-Einstein condensate is extremely hard to optimize because of fluctuations in the experiment. Another helpful

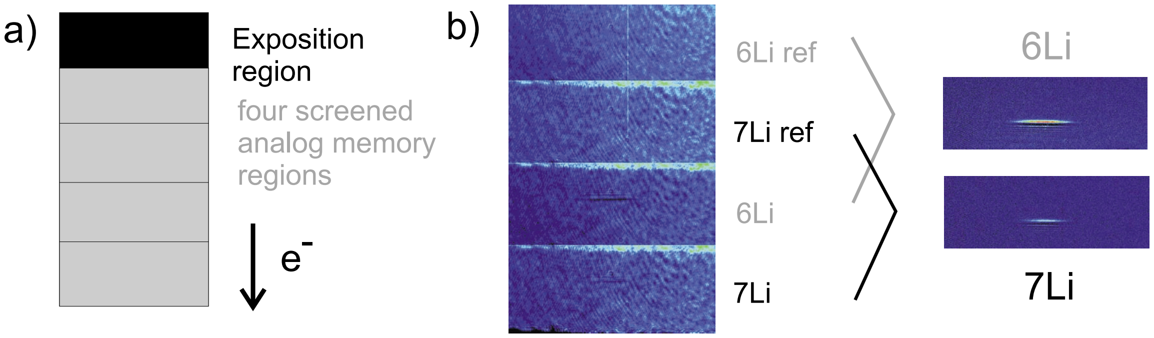

Figure 2.13: *Two isotope imaging. a) The CCD sensor is divided into five regions with the same number of lines: one exposition region and four analog memory regions protected against light by a screen. After the exposition of an image, all images are transferred to the next region away from the exposure region. b) To take absorption images of the two isotopes four pictures are taken: the* ^{7}*Li and* ^{6}*Li absorption picture, and the* ^{7}*Li and* ^{6}*Li reference pictures. The absorption images are normalized by the reference images.*

trick using the two picture technique is to take two images of the same isotope, the first without, the second with repumping beam. If the atoms have initially been prepared in the higher hyperfine state, their image can be obtained already without the repumping beam. If not they will appear only on the second image. Thus this is a nice method to verify the quality of transfer between hyperfine states. If the cloud is dense and hot, two images of the same isotope can be taken after slightly different times after release from the magnetic trap.

Using a phase-contrast imaging technique it is possible to take many images of the same cloud. Thus one can observe *in situ* the temporal development of the cloud, e.g., after changing one parameter, such as the Feshbach magnetic field or the trap oscillation frequencies [177, 39]. Without this capability, one must prepare multiple clouds under exactly the same initial conditions, and allow them to evolve for different amounts of time.

2.10.5 Detection parameters

The intensity of the probe and repumping beam and the exposure time determine the quality of the images taken. We studied the dependence of the absorption images on these quantities. Here I will discuss the dependence of the images on the exposure time, when holding the probe and repumping beam intensities fixed at $90\,\mu\mathrm{W/cm^2}$ and $2\,\mathrm{mW/cm^2}$ respectively.

For short exposure times, the noise is dominated by the shot noise of the probe laser beam. For long exposure times, other noise sources dominate, such as vibrations which can change the intensity profile of the probe beam between the absorption and the reference picture. In figure (2.14a) the signal to noise ratio is plotted versus the exposure time. Here the signal is the total number of charges on the CCD chip (thus proportional to the exposure time) and the noise is the RMS noise of the optical density picture. The signal to noise ratio follows approximately a square root law, demonstrating that the noise is predominantly shot noise in this region. The quantity we are interested in is the measured number of atoms. Since the probe beam is resonant with the higher hyperfine state, each atom will absorbe only a few photons before it is pumped to the lower hyperfine state. To increase the number of scattered photons, a repumping beam transfers the atoms back to the higher hyperfine state. If the atoms are initially in the higher hyperfine state, they will absorb most strongly at the beginning of the exposure. After a while an equilibrium will be established between the population of the higher and lower hyperfine states, depending on the intensities of the probe and repumping beams. The equilibrium can be shifted towards the higher hyperfine state, when using a strong repumping and a weak probe beam. This is the reason why we choose a repumping beam that has nearly the saturation intensity of $2.4\,\mathrm{mW/cm^2}$ for lithium.

The dependence of the measured atom number with the exposition time for atoms in the higher hyperfine state is shown in figure (2.14b) for a cloud of $70\,\mu$K and 2.5×10^6 atoms in the Ioffe-Pritchard trap. If the atoms are initially in the lower hyperfine state, the signal increases from zero with the exposure time to attain approximately the same equilibrium value (not shown in the figure). Thus the atom number measured in the lower states is always smaller than the one in the higher states. It is possible to increase the signal of atoms in the lower state by first pumping all atoms to the higher states before the exposure by switching the repumping beam on $\sim 100\,\mu$s before the probe beam. For exposure times longer than $100\,\mu$s, the spatial shape of the atomic distribution starts to change visibly in the radial direction. This is due to the free expansion of the atomic cloud. Thus the probe beam must have a high enough intensity to permit short exposure times, but smaller then that of the repump beam. The expansion even increases due to the heating that the photon recoil from the detection beams provokes. For very long exposure times, the atoms could even be accelerated so much that they get out of resonance with the probe beam. These effects are all more dramatic for atoms with light mass, such as lithium, in contrast to heavy atoms such as rubidium.

To determine a good compromise between signal to noise ratio and the measured atom number, the two quantities are multiplied and plotted versus the exposure time in figure (2.14c). This quantity increases strongly up to around $20\,\mu$s and saturates. Thus we finally chose an exposure time of $30\,\mu$s and worked with these detection parameters for all experiments in the Ioffe trap discussed in the result section. This exposure time is still in the region where the noise is dominantly shot noise.

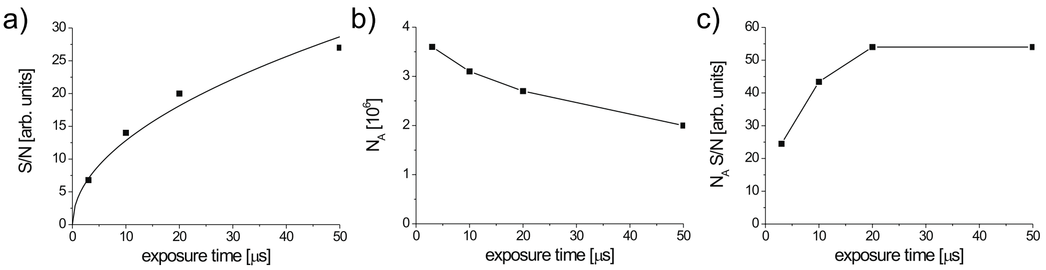

Figure 2.14: *Optimization of the detection system. Signal to noise ratio S/N (a), measured atom number N_A (b) and $N_A\, S/N$ plotted versus the exposure time.*

2.10.6 Using absorption images

At the end of this section, I want to discuss how the different physical parameters such as atom number, temperature, collision rate and so on are obtained from time-of-flight images. The atom number is obtained readily by integration over the optical density (compare to formula 2.18)

$$N = \int dx \int dy \int dz\, n(x,y,z) = \int dx \int dy\, D_{opt}(x,y)/\sigma\,. \tag{2.19}$$

The absorption cross section, $\sigma = C^2\,\lambda^2/(2\pi\left[1+(4\pi\Delta/\Gamma)^2\right])$, depends on the wavelength of the transition λ, its linewidth Γ, the detuning Δ of the probe laser beam from resonance and the Clebsch Gordon coefficient C of the transition. The lithium wavelength is 671 nm and we usually probe at resonance $\Delta = 0$, thus $\sigma = C^2\,\lambda^2/(2\pi)$. Ideally, the cycling transition $|F=2, m_F=2\rangle \rightarrow |F^{'}=3, m_{F'}=3\rangle$ should be used for detection, giving a Clebsch Gordon coefficient $C = 1$. For lithium this is difficult to achieve, since the hyperfine splitting of the $2^2\mathrm{P}_{3/2}$ excited state is 9.2 MHz or less, comparable to the linewidth of 5.9 MHz (see figure 2.4). If the probe beam is not perfectly polarized σ^+, the $|F^{'}=2, m_{F'}=2\rangle$ state is also excited. This state can decay to the lower, $F = 1$ hyperfine state, from which atoms are repumped to any of the higher states. Thus, very soon an equilibrium of the population of the $F = 2$ states is reached. The $F = 1$ states are less populated since the repumping beam has a higher intensity than the probe beam. As an approximation, we use the average of the squared Clebsch Gordon coefficients of all possible transitions for a σ^+ transition from the $F = 2$ state, yielding $C^2 = 7/15$. For ^{6}Li we use $C^2 = 1/2$. These results are the same for a linear or σ^- polarized probe beam. Thus they can be used for any probe beam polarization. This approximation of the Clebsch Gordon coefficients is the main uncertainty in the determination of the atom number, which was estimated to be about a factor of 2.

For the determination of the atom number by integrating over the optical density, attention has to be payed to an eventual offset in the optical density resulting from a slight difference in the probe beam intensity between the absorption image and the reference image. In practice this is taken into account by selecting a subregion of the image in which no atoms are present and calculating the value of the offset from this region.

The temperature can be measured in several ways (see section 3.2.2). The most general is to suddenly release the atoms and take their picture after a time of flight large enough so that the distribution is much larger than the initially trapped distribution. In absence of collisions, the spatial distribution then displays the initial momentum distribution and the temperature can be obtained with an appropriate fit, for example a gaussian fit for a classical cloud. Other parameters, such as collision rate and phase-space density, can be calculated from atom number, temperature and trap frequencies. There are more measurement methods and more sophisticated ways to fit the data, which will be explained in the results section.

2.11 Experiment control and data acquisition

Bose-Einstein condensation experiments go through a complicated experimental sequence each time a degenerate gas is produced. Afterwards an image is recorded on a CCD camera and analyzed. In our experiment both tasks are accomplished by a dedicated computer. The general layout of the system is shown in figure 2.15. The control computer (an old 75 MHz Intel 486 PC) is running under MS-DOS and programmed in Turbo Pascal. Due to this real time operating system a time stability can be reached that would under Windows require an I/O card with integrated memory which stores the whole sequence.

The digital and analog output system has been developed by us and constructed by the LKB electronic technicians. A bus connects the computer with several output boxes. The bus consists of a 16 bit data bus, a 7 bit address bus and a one bit strobe signal. The latter is momentarily put to high when data and address are valid and triggers the reading of the data by the addressed 16 bit latch or digital-analog converter. We use three different types of boxes, one containing 16 TTL outputs, another with four 16 bit analog outputs and yet another with four analog outputs, each having its own floating ground. The boxes are opto-isolated from the bus so that an over-voltage or short-circuit in the experiment does not destroy the computer, a feature that has already proven useful. A box can have an error signal input that has to be on +5 V to enable the outputs. This is used together with the waterflow and temperature monitoring system to switch off the magnetic trap upon malfunction.

Several other devices are connected to the computer using IEEE, especially the synthesizers, signal- and pulse generators. The Nd:YAG laser and the data acquisition computer are connected by serial ports.

The program system managing the control of the experiment has been written by

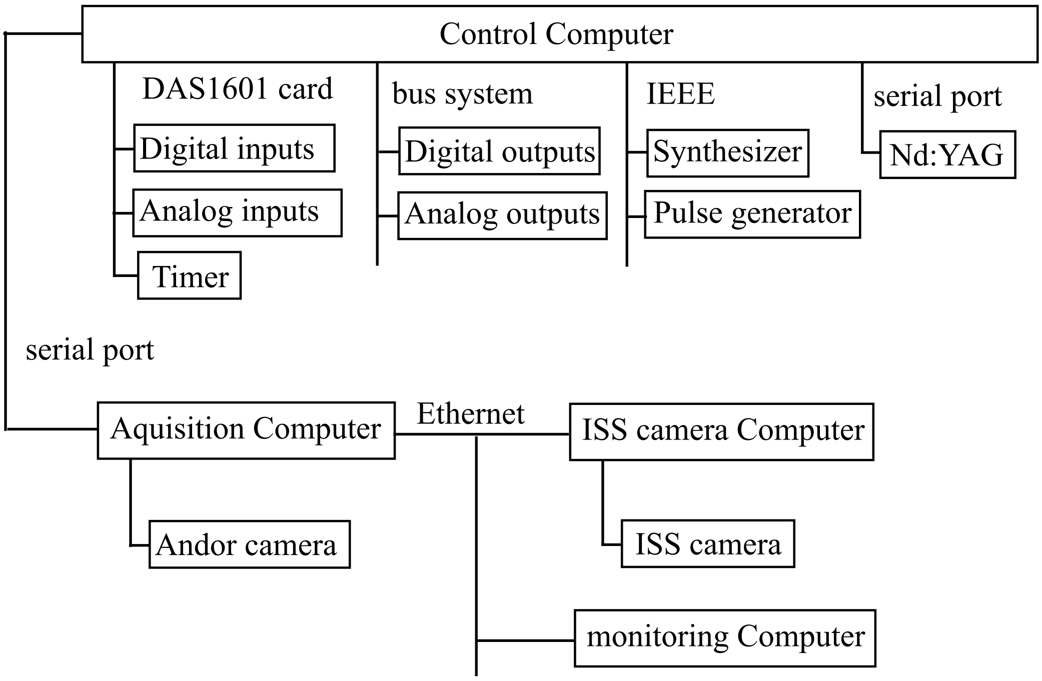

Figure 2.15: *The computer system consists of a control computer and a data aquisition computer. The control computer operates shutters, AOMs, power supplies and so forth by using a digital/analog output system and the IEEE bus and serial ports. It transfers the experimental parameters to the aquisition computer which records, treats and stores absorption images of the atoms.*

us. It provides the user with a user-friendly way to program the experimental sequence. Output ports are managed and obtain names that are easy to understand. Parameters describing the experimental sequence (about 700 at the moment) are handled automatically. After declaration of a parameter, a menu entry is generated for its modification. Parameters can be stored and recalled from disk and are sent to the acquisition computer after each experimental run to be stored together with the acquired images. Experimental series in which one or several parameters are varied from one run to the next can be declared interactively. The order of the experimental runs in a series is mixed pseudo-randomly to prevent drifts in the experiment from being misinterpreted. Several series can be stored in a list and be executed in absence of the experimentator. Each time the experiment is run, the experimental sequence is executed twice. During the first execution, which takes less than a second, nothing is written to the output ports. This execution serves to collect data over the experimental sequence to be executed. The most important of these parameters is the time the sequence will take. And it serves to prepare some devices for the experiment to come. During this pre-execution the order of the execution may get changed. This is used for example to give the command to a shutter earlier than it appears in the programmed sequence, in order to anticipate the delay the shutter has. Only the second execution actually writes to the output ports.

The data acquisition system, also written by us, fulfills several functions. At the beginning of the experimental sequence the control and the acquisition computers are synchronized. About 50 ms before the absorption image is taken, the CCD camera is put into the mode in which it can be triggered externally. This cannot be done earlier, since in this mode unwanted charge will accumulate on the chip. This is the reason why the total time of the experimental sequence has to be calculated by the control computer before the sequence is run and transmitted to the acquisition computer. After the images are taken, they are stored on hard disk and the optical density is calculated. The atom number is calculated and gaussian fits are done on the summed axial and radial distributions. All experimental parameters and the fit results are stored on the hard disk. For experimental series, data such as the atom number or the size versus the varied parameter are already displayed graphically. Several series can be combined and images contributing to a series are easily retrieved by clicking on the corresponding data point. More complicated fits to the data, including two dimensional fits, can be started by user action. Copies of the data acquisition program can also be run in parallel on several other machines. These can be connected to the data acquisition program on the experiment *via* ethernet, to display always the latest measurement results and the status of the machine. In this way, measurement series can be taken in the lab while other work is done in the office while continually checking the quality of the recorded data and the correct operation of the machine.

We use two camera systems, one for the MOT region, one for the Ioffe-Pritchard trap. Since the old frame grabber card of the MOT region camera produces a lot of radiation it would severely disturb images taken with the slow scan camera, if the two frame grabbers would be in the same computer. To solve this problem, we put the old frame grabber in an extra computer which transfers the image data to the main acquisition computer using TCP/IP on the local ethernet.

The control program and especially the data acquisition program are flexible and easily adapted to many cold atom experiments. The acquisition program is used on three BEC machines in Paris and several groups worldwide showed interest in using it. The source code of both programs together with sample data and the user manuals are ready for download on my personal homepage. I will be glad to provide anyone interested in using these programs with additional information.

Chapter 3

Experimental results

In this chapter, I will present the experimental results obtained with our setup. It is divided into four sections.

- The first part follows the steps necessary to prepare a gas of lithium atoms for evaporative and sympathetic cooling. Special attention is payed to the two isotope MOT and the Doppler cooling in the Ioffe-Pritchard trap.

- The second part describes experiments done with the atoms in the higher hyperfine states (^{7}Li $|F = 2, m_F = 2\rangle$, ^{6}Li $|F = 3/2, m_F = 3/2\rangle$). Evaporative cooling of ^{7}Li and sympathetic cooling of ^{6}Li are discussed. The detection of the degenerate Fermi gas is presented.

- The third part is dedicated to experiments done with the atoms in the lower hyperfine states (^{7}Li $|F = 1, m_F = -1\rangle$, ^{6}Li $|F = 1/2, m_F = -1/2\rangle$). The transfer from the higher to the lower states is described. Sympathetic cooling leading to a Bose condensate immersed in a degenerate Fermi sea is presented. It is shown that the produced condensate is one-dimensional.

- In the last section, our first results using the optical trap are presented. We use the Feshbach resonance of the ^{7}Li $|F = 1, m_F = 1\rangle$ state to rethermalize the gas. Evaporative cooling is performed by lowering the optical trap potential. A condensate with tunable scattering length is produced. By tuning the scattering length negative and releasing the condensate in one direction, bright solitons have been produced.

In independent sections our measurement methods are explained and measurements of the lifetime and heating rate in the different states are given.

3.1 On the road to evaporative cooling

3.1.1 The two isotope MOT

The two isotope magneto optical trap (TIMOT) is loaded from a Zeeman slowed atomic beam. The spin-flip Zeeman slower has a capture velocity of $\sim 1000\,\mathrm{m/s}$ and operates at a detuning of $-420\,\mathrm{MHz}$ from resonance (see sections 2.4 and 2.5). The ^{6}Li repumping transition has been changed since our last published work on the TIMOT ([178], appendix B). In the old configuration the D2 transition from $2^2\mathrm{S}_{1/2}$ $F = 1/2$ to $2^2\mathrm{P}_{3/2}$ $F' = 3/2$ was used (see figure 2.4). This transition is about $7\,\Gamma$ to the blue of the D1 $2^2\mathrm{S}_{1/2}$ $F = 2$ to $2^2\mathrm{P}_{1/2}$ $F' = 1$ resonance of ^{7}Li. Thus, use of this ^{6}Li repumping light significantly weakens the confinement of the ^{7}Li MOT and reduces the number of captured bosonic atoms. Since it is essential for sympathetic cooling to start with a large number of bosons, we changed the ^{6}Li repumping to the D1 $2^2\mathrm{S}_{1/2}$ $F = 1/2$ to $2^2\mathrm{P}_{1/2}$ $F' = 3/2$ transition. Since the hyperfine splitting of the excited levels of this transition is only $26.1\,\mathrm{MHz}$, it is essential for a good operation of the ^{6}Li MOT, to reduce the detuning of the repumping laser to only about $-1\,\Gamma = -5.9\,\mathrm{MHz}$ (see figure 3.1). Indeed for detunings around $-3\,\Gamma$, which one would naively expect to be good detunings, the light is blue to the resonance of the D1 $2^2\mathrm{S}_{1/2}$ $F = 1/2 \rightarrow 2^2\mathrm{P}_{1/2}$ $F' = 1/2$ transition and leads to heating of the MOT and to a lower number of captured atoms. Going to the red side of both transitions at about $-5\,\Gamma$ again results in a well behaved MOT with a performance slightly worse than at $-1\,\Gamma$.

After changing the ^{6}Li repumping transition, no influence of the ^{6}Li trapping light on the behavior of the ^{7}Li MOT could be detected any longer. This opened the possibility of studying the influence of the presence of ^{7}Li atoms on the behavior of the ^{6}Li MOT.

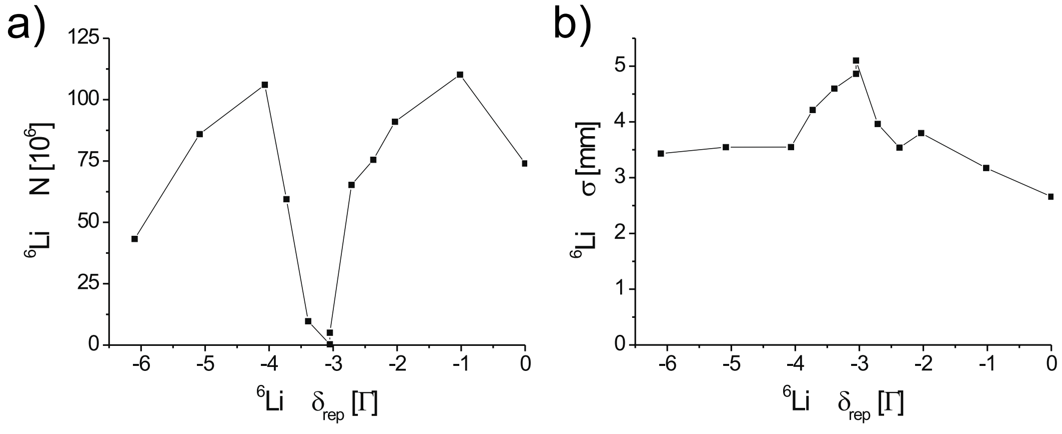

Figure 3.1: *Number of ^{6}Li atoms (a) and size after* 1 *ms of free expansion (b) of the ^{6}Li single isotope MOT versus the repump detuning. For detunings around* $-3\,\Gamma$ ($\Gamma = 5.9\,MHz$)*, the repumper is near the D1* $2^2S_{1/2}$ $F = 1/2 \rightarrow 2^2P_{1/2}$ $F' = 1/2$ *transition. This results in a loss of atoms and heating of the gas. The uncertainty in the x-axis is* $1\,\Gamma$.

To do this, we measure the loading and the lifetime of the ^{6}Li MOT in presence and absence of ^{7}Li atoms. To hinder the loading of bosonic atoms either the principal or the repumping ^{7}Li Zeeman slowing beam is blocked. None of the ^{7}Li frequencies used for the MOT or the Zeeman slower are observed to have any influence on the ^{6}Li MOT. The ^{7}Li MOT used in this experiment containes $\sim 7 \times 10^9$ atoms at a temperature of 1.5 mK and a peak density of $2 \times 10^{11}\mathrm{cm}^{-3}$. The result is shown in figure (3.2). In the absence of ^{7}Li, the ^{6}Li MOT loads to 9×10^8 atoms within 50 s. In the presence of ^{7}Li, the equilibrium number is 4×10^8 atoms. While loading both isotopes simultaneously, the ^{6}Li atom number reaches its maximum of 6×10^8 atoms after 30 s before decreasing again with the increase in ^{7}Li atom number. The lifetime of ^{6}Li in absence of ^{7}Li is 41 s while it is reduced to 21 s in presence of ^{7}Li. We attribute this change in lifetime to light assisted collisions between the bosonic and fermionic isotope.

The loading method of the TIMOT that we use for sympathetic cooling experiments is the following. The intensities of all four beams injecting the tapered amplifier are chosen to give equal intensities in all four frequency components of the beam leaving the amplifier. This is checked using a Fabry-Perot cavity. Now the ^{6}Li injection beams are blocked. Since the tapered amplifier is operated in a highly saturated regime, the total output power of the tapered amplifier drops less than a factor of 2, which is the decrease in the total power of the injecting beams. This increases the power for the ^{7}Li frequency components by $\sim$ 50% and leads to a higher ^{7}Li atom number than achievable with the light equally distributed to all four frequencies. The loading of the ^{7}Li MOT is monitored by measuring the fluorescence. When a given level of

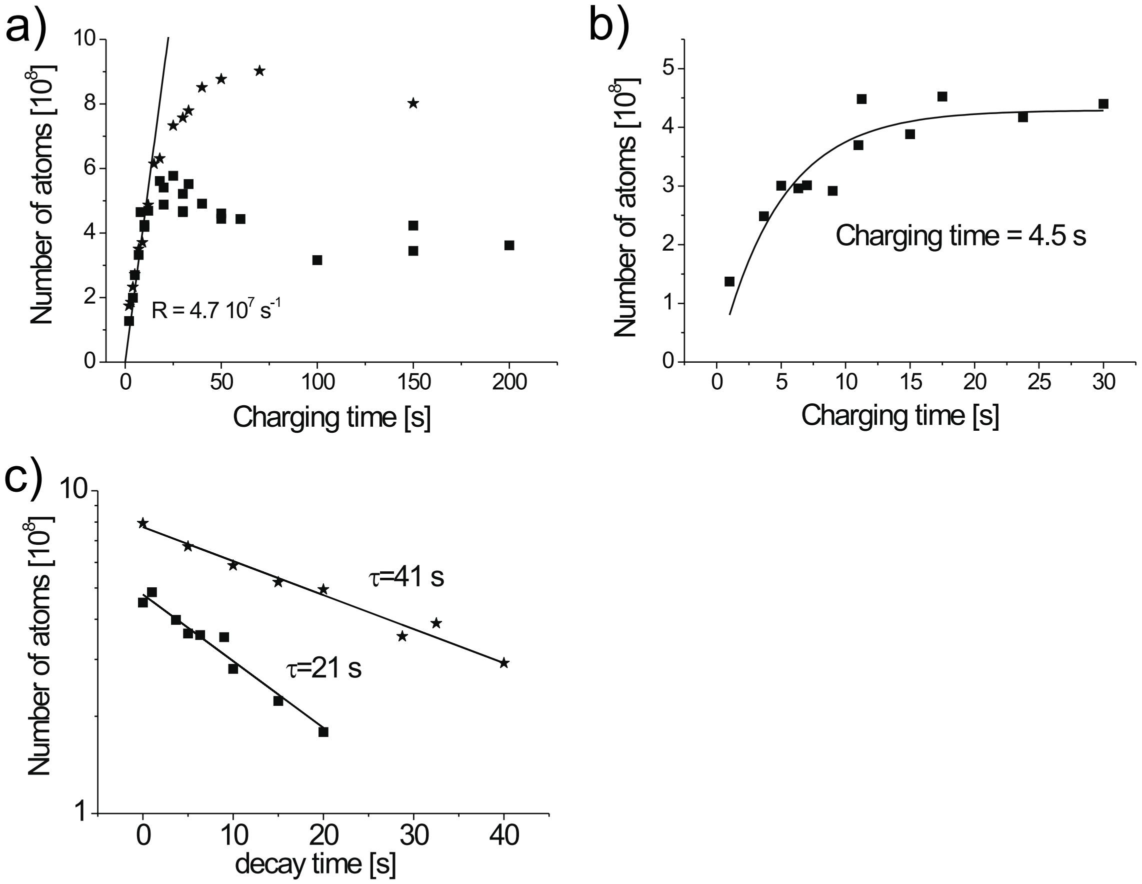

Figure 3.2: *Charging curve (a,b) and lifetime measurement (c) of the* ^{6}*Li MOT in presence (squares) and absence (stars) of* ^{7}*Li atoms. a) The charging of* ^{6}*Li and* ^{7}*Li is started at the same time. This leads to a maximum in the* ^{6}*Li atom number around 30 s, when the* ^{7}*Li MOT is not yet completely charged. b) The* ^{7}*Li MOT is charged before* ^{6}*Li is added. c) The presence of* ^{7}*Li decreases the lifetime of the* ^{6}*Li MOT from 40 s to 21 s.*

fluorescence is reached, the experimental sequence is started. First the ^{6}Li injection beams are unblocked to add about 10^7 fermions to the MOT. This takes a few seconds, but much less time than the lifetime of ^{7}Li under these conditions. By changing this ^{6}Li loading time, the ratio of ^{6}Li to ^{7}Li can be finetuned in a much more reliable way than would be possible by adjusting the relative MOT beam intensities and loading continuously.

The parameters of the TIMOT are optimized on the number of atoms captured from the atomic beam slowed to $\sim 50\,\mathrm{m/s}$. After the completion of the loading process it is no longer necessary to capture atoms with more than a few m/s, thus the operation parameters can be changed to values optimized for a high initial collision rate in the magnetic trap. This phase is called a compressed MOT (CMOT) and takes 3 ms. The light intensity is lowered by a factor 3, the principal detunings are moved towards resonance, and the ^{7}Li repumping detuning is shifted farther away from resonance. This results in a slight compression and a cooling of a factor 2 in comparison with the MOT. A summary of the operation parameters of the MOT and the CMOT and their performances is given in table (3.1).

	single isotope MOT		two isotope MOT	
	^{7}Li	^{6}Li	^{7}Li	^{6}Li
N	6×10^9	1.6×10^9	7.3×10^9	2.7×10^8
$n_0\,[\mathrm{cm}^{-3}]$	1×10^{11}	1.0×10^{11}	2.0×10^{11}	3.4×10^{10}
$T\,[\mathrm{mK}]$	1.5	0.7	1.0	0.7
$\delta_{P7,6}\,[\Gamma]$	-6.4	-6.8	-6.4	-6.8
$\delta_{R7,6}\,[\Gamma]$	-5.3	-1.0	-5.3	-1.0

	single isotope CMOT		two isotope CMOT	
	^{7}Li	^{6}Li	^{7}Li	^{6}Li
N	3.4×10^9	9×10^8	3.2×10^9	2.7×10^8
$n_0\,[\mathrm{cm}^{-3}]$	2×10^{11}	2.7×10^{11}	2×10^{11}	5.9×10^{10}
$T\,[\mathrm{mK}]$	0.6	0.4	0.6	0.7
$\delta_{P7,6}\,[\Gamma]$	-2.9	-2.0	-2.9	-2.0
$\delta_{R7,6}\,[\Gamma]$	-9.8	-0.5	-9.8	-0.5

Table 3.1: *Comparison of atom number N, peak density n_0, temperature T and frequency detunings for the single-isotope and two-isotope MOT and CMOT. The ^{7}Li MOT is charged to the atom number used in the experiment. The maximum atom number in the single isotope ^{7}Li MOT is $> 2 \times 10^{10}$ atoms and 2.2×10^9 for ^{6}Li. The atom number ratio for the two isotope MOT is fixed by choosing a 1.5:5 ratio for the intensities of the ^{6}Li and ^{7}Li frequency components. The detunings are defined in figure (2.4).*

3.1.2 Optical pumping

After switch-off of the MOT, the atoms are pumped to the higher hyperfine state. For both species this is done simultaneously with σ^+ polarized repumping laser beams parallel to a homogeneous magnetic guiding field of about 10 G. After 0.2 ms of optical pumping with a 600 μW/cm^2 beam, the atoms are captured in a magnetic quadrupole field. During the first 200 ms after the capture, the atoms undergo spin relaxation collisions until only atoms in the stretched states are left over (see figure 3.3). This process leads to a loss of about a factor 2 in the number of trapped atoms for ^{7}Li. The transfer efficiency from the MOT to the spin polarized magnetically trapped cloud is about 30% for ^{7}Li and 20% for ^{6}Li.

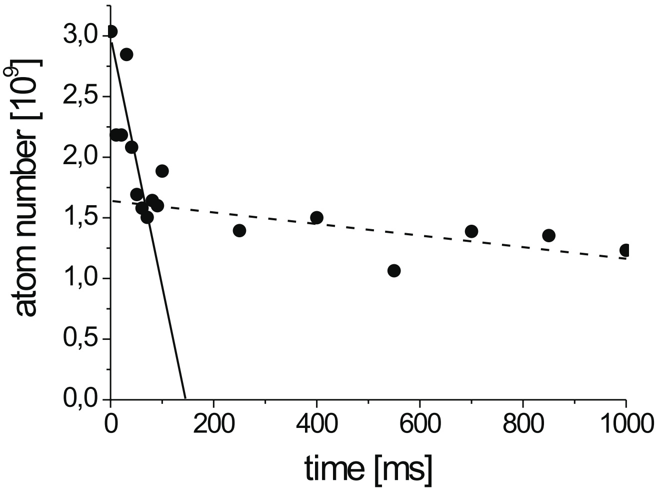

Figure 3.3: *Lifetime measurement after capture in the magnetic trap. The ^{7}Li atoms have been transferred to the $F = 2$ state with a σ^+ polarized optical pumping beam resonant with the D2 $F = 1 \rightarrow F' = 2$ transition. The steep decrease in atom number during the first* 100 *ms is due to spin relaxation of atoms trapped in the* $|F = 2, m_F = 1\rangle$ *state. The timescale of this decrease is compatible with the exchange rate constant predicted in [153] ($\tau = 100$ ms). The decrease in atom number for longer times is due to background gas collisions ($\tau = 17$ s).*

3.1.3 Transfer and capture in the Ioffe trap

Next the quadrupole field is compressed and the trapped atoms are transferred to the Ioffe-Pritchard region by changing the current ratio in the MOT and transfer quadrupole coils as described in the setup section (2.7). The transfer is done with constant acceleration and deceleration of the atoms, resulting in a parabolic flight taking 100 ms. During this transfer 90% of the trapped atoms are lost because the initial 1/e width of the cloud of about 6 mm exceeds the internal dimension of the appendage which is only 3 mm in the smallest direction (see figure 3.4). This loss could be prevented if the initial clouds temperature were smaller. We tried evaporative cooling in the lower quadrupole trap to achieve this. But we had no success because of Majorana spin flips (see section 1.2). These losses are observed by measuring the time dependence of the atom number in different spatial regions of the trap. To be able to observe atoms in the central region, *in situ* images are taken with the quadrupole field on. The Zeeman shift detunes atoms in regions outside the center from resonance. The lifetime in the center is observed to be shorter than the lifetime in regions around the center (see figure 3.5), as it is expected for Majorana losses. In addition the lifetime of clouds with different temperatures are measured. Since colder clouds are smaller, they are more vulnerable to Majorana losses. Therefore the observed lifetime is shorter.

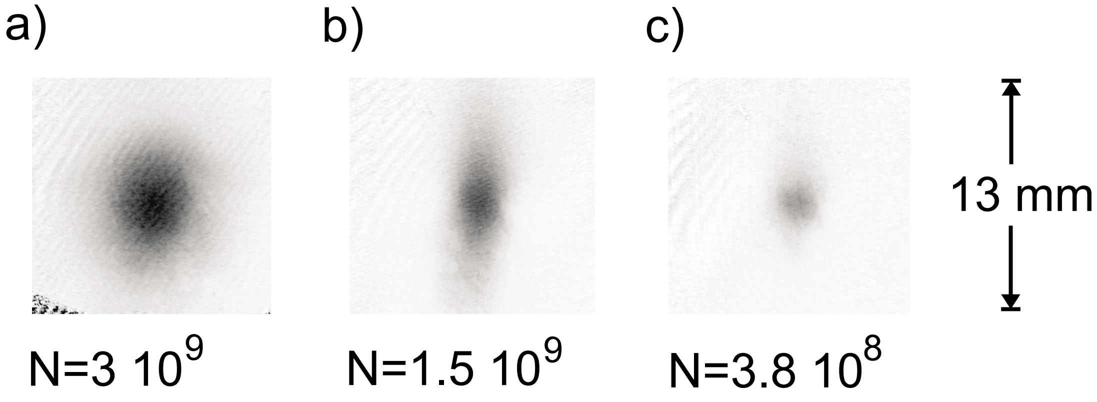

Figure 3.4: *Loss of atoms during the transfer to the appendage. a)* 3×10^9 *atoms after capture in the lower quadrupole trap. b)* 1.5×10^9 *atoms are left after half of the transfer to the appendage and a reversed transfer to the initial position. The glass cell removes atoms mainly in the horizontal direction, resulting in an elliptic cloud. c)* 3.8×10^8 *atoms are left after the full transfer and a transfer back to the initial position. Since mainly highly energetic atoms have been removed by collisions with the glass cell, the temperature is decreased by about a factor 3.*

To improve the transfer efficiency, perhaps an evaporation could be successful in a TOP trap in the region of the MOT. After this precooling the atoms could be transferred without further loss to the Ioffe trap, if the lifetime given by Majorana flips in the quadrupole trap used for the transfer is longer than the duration of the transfer. Another possible approach to improve the transfer efficiency would be to increase the internal size of the appendage. But this would also lead to an increase in the distance of the Ioffe bars from the atoms and thus a decrease in the radial magnetic field gradient. The parameter on which we want to optimize the transfer is the initial elastic collision rate Γ in the Ioffe trap. We calculated Γ as a function of the internal size d of the appendage (for energy independent elastic collision cross section). Γ has an optimum in d, and it turned out that the chosen size of 3 mm is very near this optimum. The

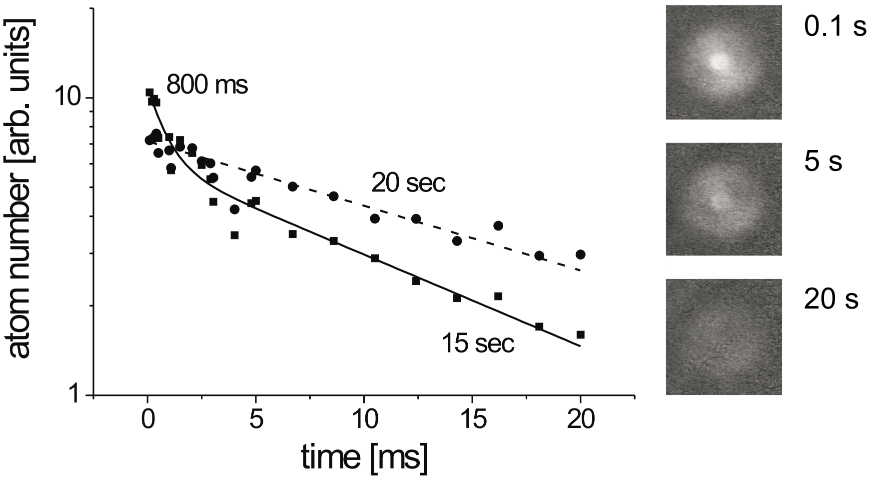

Figure 3.5: *Observation of Majorana losses. Lifetime of atoms in the quadrupole trap after capture from the MOT. The pictures are taken in situ, with the magnetic field on. Due to the Zeeman shift, only atoms near the trap center are visible. The number of atoms in the central region (squares) and of atoms around the central region (circles) is plotted. The lifetime in the center is reduced to* 15 *s in comparison to* 20 *s outside the center. In addition a loss on a shorter timescale is observed during the first seconds. The reduction in lifetime is attributed to Majorana losses.*

calculation predicts a maximum of Γ, which is only 20% higher than the Γ predicted for our size. At the moment we continue to operate with 90% loss of atoms during the transfer.

The loading of the Ioffe trap is done in several steps. Already during the last ten percent of the transfer, the Ioffe bars are ramped to a gradient of 20 G/cm to improve the centering of the atoms with the appendage. When the transfer is completed, the Ioffe bars are switched to a gradient twice the radial gradient of the quadrupole coils. This reverses the direction of the magnetic field in the vertical direction, making it the same direction it will have in the Ioffe trap. Now the cloud is compressed adiabatically in the radial directions while lowering the axial confinement by increasing the current in the Ioffe bars and decreasing the current in the transfer coils. Finally the transfer coils are switched off and the pinch coils are switched on, taking over the axial confinement and creating an offset field to prevent Majorana spin flips.

During the transfer the power supplies' programming mode is "constant voltage" because in this mode they can react faster. After capture in the Ioffe trap, the mode is changed to "constant current" because only in this mode can the magnetic trap be stable even if the coils change their resistance while heating up.

The initial number of atoms in the ^{7}Li MOT of 6×10^9 is reduced to 3.8×10^8 in the Ioffe trap, corresponding to a total transfer efficiency of 6%. The maximum number of atoms possible at this stage is 6×10^8. The temperature is 0.7 mK, comparable to the temperature of the CMOT. The current in the Ioffe bars is 320 A and the current in the pinch coils 193 A. No offset field compensation is done. This corresponds to oscillation frequencies of $\omega_{ax} = 2\pi \times 73\,\mathrm{Hz}$ and $\omega_{rad} = 2\pi \times 200\,\mathrm{Hz}$. The peak density is $2.3 \times 10^{10}\,\mathrm{cm}^{-3}$, the peak phase-space density $\rho_0 = 3.5 \times 10^{-7}$ and the collision rate $\Gamma = 0.7\mathrm{s}^{-1}$ (see also table 3.2). The frequencies are given for the ^{7}Li $|F = 2, m_F = 2\rangle$ state and the collision rate is calculated for an energy independent collision cross section of $a = -27\,a_0$. If not mentioned otherwise, this will be the case for all frequencies and collision rates given in the next sections.

3.1.4 First trials of evaporative cooling

Now the magnetic trap is adiabatically compressed to increase the elastic collision rate. During an adiabatic compression the phase-space density is constant $\rho_0 \propto n_0\lambda_{dB}^3 \propto 1/(\sigma^3 T^{3/2}) = cst$ (when keeping the potential shape unchanged or in absence of collisions; for a counter example see [179]). Here σ is the size of the harmonically trapped cloud, which is linked to the temperature with $k_B T/2 = m\omega^2\sigma^2/2$. From these two relations it can be shown that the temperature is proportional to the oscillator frequencies for an adiabatic compression: $T \propto \omega$. The elastic collision rate Γ scales as $\Gamma \propto n_0\sigma_{el}v \propto T^{1/2}/\sigma^3 \propto \omega^2$, where v is the mean velocity and the relations obtained before have been used. This means that adiabatic compression can increase the elastic collision rate (for energy independent elastic scattering cross section σ_{el}), but it also heats the gas.

The adiabatic compression is done by increasing the gradient of the Ioffe bars and the curvature of the pinch coils while decreasing the offset magnetic field. At maximum compression with 500 A of current in the pinch and compensation coils, 700 A in the Ioffe bars and an offset field of 2 G, the trapping frequencies are $\omega_{ax} = 2\pi \times 118\,\mathrm{Hz}$ and $\omega_{rad} = 2\pi \times 7000\,\mathrm{Hz}$. We capture 3.8×10^8 atoms, which have a temperature of about 2.8 mK after compression. This is less than expected from the scaling law $T \propto \omega$. The reason is that the cloud is far into the anharmonic region of the Ioffe-Pritchard trapping potential. The density is $1.8 \times 10^{11}\,\mathrm{cm}^{-3}$, the phase-space density is still 3.5×10^{-7} and the collision rate is $6\,\mathrm{s}^{-1}$. The trap lifetime was about one minute, giving a ratio of good to bad collisions of 360. This should lead to runaway evaporative cooling. We tried to obtain this, but the “evaporation” was a pure selection of atoms. The reason is the energy dependence of the elastic collision cross section as explained in section (1.3.1) and shown in figure (1.14).

To diminish the effect of the decreasing cross section with increasing energy, the temperature has to be lowered. This can be done by working with a less compressed trap. On the other hand, this decreases the density and thus lowers the elastic collision rate. We tried to find a compromise between these two effects to make evaporative cooling work, but we did not succeed.

3.1.5 Doppler cooling in the Ioffe trap

We could not start evaporative cooling because of the reduced elastic collision cross section for collision energies around $\sim k_B\,6\,\mathrm{mK}$. The solution to this problem was to cool the atoms in the Ioffe-Pritchard trap using Doppler cooling. Doppler cooling works by letting atoms interact with a laser beam red detuned from their resonance. If an atom is counter-propagating the laser beam, it sees the beam frequency shifted closer to resonance due to the Doppler effect and photons can be absorbed, slowing the atom. In the opposite case, if the atom is moving away from the beam, the frequency is even more red detuned and the probability of absorption diminishes. The limit temperature of this process is attaint at low saturation for a detuning of $\delta = -\Gamma/2$ and is $k_B T_{Doppler} = \hbar\Gamma/2$, where Γ is the width of the resonance [180]. This temperature is $140\,\mu\mathrm{K}$ in the case of lithium. Doppler cooling is also the cooling mechanism in the MOT. Why should it be advantageous to cool with the same cooling mechanism again in the magnetic trap? The point is that the magnetic trap can be adiabatically compressed, leading to higher temperatures than the initial temperatures in the MOT (up to 4 mK in comparison with 0.7 mK after the CMOT). In addition, the transfer to the magnetic trap is never completely adiabatic, leading to heating of the gas. Finally, the Doppler limit is not reached in our MOT because of the high densities which lead to multiple scattering and thus heating. This problem is less severe in the magnetic trap for several reasons. We loose 94% of the atoms and thus there is less scattered light. The geometry of the Ioffe trap has a cigar shape, letting scattered light escape in the radial directions with less reabsorption. Atoms outside the center of the trap are detuned away from the laser frequency by the magnetic field, and are thus less susceptible to scattered light.

Implementation of a cooling mechanism involving light in a magnetic trap is not completely obvious, since the light could induce transitions to untrapped states and thus lead to a very short lifetime [165]. To prevent this, the Ioffe-Pritchard trap is operated at a high bias magnetic field (150...600 G) and the cooling laser beam is σ^+ polarized relative to this field and directed parallel to it. The frequency of the beam is detuned about $1\,\Gamma$ to the red of the ^{7}Li D2 $|F = 2, m_F = 2\rangle \rightarrow |F' = 3, m_F = 3\rangle$ transition at this magnetic field. Only atoms in the center of the trap are nearly resonant to this light. Atoms slightly outside the center region see a higher magnetic field and are farther off resonance. That is important because for these atoms the light field has also a σ^- component since the magnetic field orientation is no longer parallel to the beam. If these atoms could absorb light, they could easily be lost. The use of only one on axis beam thus makes the use of a repumping laser unnecessary.

Only a single beam with one frequency component, a diameter of 1 mm and an

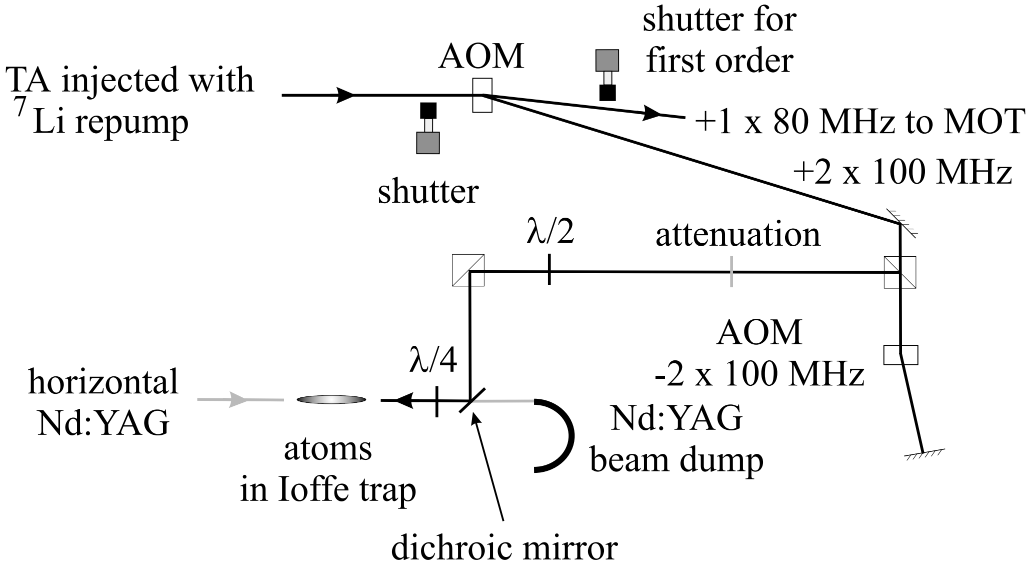

Figure 3.6: *Preparation of the beam used for Doppler cooling in the Ioffe trap. The tapered amplifier is injected only with the* ^{7}*Li repumping light. The output of the tapered amplifier passes through an AOM. Light in the first diffraction order of this AOM, operated at 80 MHz is used for the MOT. Light in the second order of the AOM operated at 100 MHz is used for Doppler cooling. The Doppler cooling beam is frequency shifted by a second AOM, expanded to* 1 *mm diameter, attenuated and directed onto the atoms on axis with the Ioffe-Pritchard trap. A cube and a* $\lambda/4$ *wave plate serve to polarize the light* σ^+. *The Nd:YAG laser beam of the horizontal optical dipole trap is counter-propagating to the Doppler cooling beam. To separate this* 1064 *nm beam from the* 671 *nm Doppler beam, a dichroic mirror is used. The* 5 *W optical trap beam is afterwards dissipated in a beam dump.*

intensity of $25\,\mu\mathrm{W/cm}^2$ is used. It is derived from the tapered amplifier, injected only with the ^{7}Li repumping light. Thus the light is shifted by about the hyperfine splitting of 803.5 MHz to the blue of the principal transition at zero magnetic field. The magnetic field is chosen to overcompensate this shift slightly and puts the D2 $|F = 2, m_F = 2\rangle \rightarrow |F' = 3, m_F = 3\rangle$ resonance to the blue of the light. The exact derivation of the beam is shown in figure (3.6). The second AOM compensates the action of the first. It was used to try out a whole range of different offset magnetic fields for the Doppler cooling. At the end it turned out that all offset fields between 150 G and 600 G work equally well and in principle we could operate without this second AOM.

The Doppler cooling works with only one single beam. This is possible because the atoms are trapped magnetically and oscillate toward and away from the beam. Atoms are cooled when they are moving against the beam and absorb much less photons from

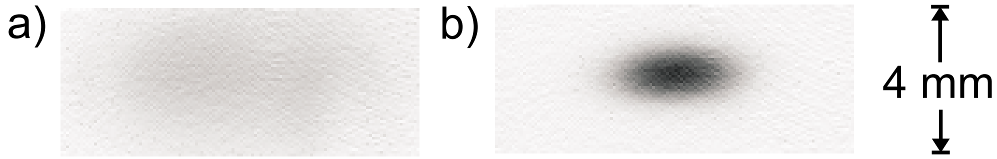

Figure 3.7: *Absorption pictures of the atomic cloud before (a) and after (b) Doppler cooling. Both pictures are taken in the trap configuration of the first Doppler cooling.*

it when they are copropagating with it. This cools the gas in the axial dimension. The radial dimensions are cooled because of mixing of the atomic trajectories in the slightly anharmonic trap. At the end of the cooling process the onsetting elastic collisions also mix the degrees of freedom. When using only one cooling beam, its light pressure is not compensated. Thus it is important to ramp its intensity down smoothly. Not doing so results in a center of mass oscillation of the cloud, leading to heating. This center of mass oscillation has been used for a first calibration of the axial trap frequency.

The exact sequence of the Doppler cooling is the following. First the atoms are captured after the transfer into a trap with 320 A in the Ioffe bars and 193 A in the pinch coils. This results in a trap with oscillation frequencies of $\omega_{ax} = 2\pi \times 73\,\text{Hz}$ and $\omega_{rad} = 2\pi \times 200\,\text{Hz}$ and an offset magnetic field of 480 G. An initial 130 ms Doppler cooling stage with an intensity of $25\,\mu\text{W/cm}^2$ and an adiabatic switch off during 100 ms is performed. This cools the gas only in the axial direction. Almost no atoms are lost during the process.

To also cool the radial directions, a trap geometry with higher anharmonicities has to be used, to allow ergodic mixing of the atomic trajectories. Furthermore, the final temperature reached by Doppler cooling does not depend strongly on the trap oscillation frequencies. Thus lowest temperatures are achieved by Doppler cooling in a steep trap and then adiabatically decompressing. The compression before Doppler cooling is done by increasing the current in the Ioffe bars and in the pinch coils to 850 A and 696 A respectively. The offset field has to be kept constant to keep the atomic resonance near the laser frequency. For this reason, current through the pinch coils is increased by 500 A from the transfer power supplies, which circulates through the pinch coils and the compensation coils (see the circuit of the magnetic trap 2.9). Since the offset field per unit of current has nearly the same magnitude but opposite direction for these coil pairs, the offset field is unchanged. The current of 193 A coming from the MOT power supplies and circulating only the pinch coils is slightly increased to allow for the mismatch in the current compensation between pinch and compensation coils. The current ramps are performed in 500 ms and lead to oscillation frequencies of $\omega_{ax} = 2\pi \times 140\,\text{Hz}$ and $\omega_{rad} = 2\pi \times 537\,\text{Hz}$. Form the change in the oscillation frequencies the increase in temperature can be calculated and is a factor 2 (2.7) in the axial (radial) direction. Now a second Doppler cooling stage is applied, this time

	N	T [mK]	n_0	ρ_0	Γ_0	Γ
Capture	3.8×10^8	0.7	2.3×10^{10}	3.5×10^{-7}	0.7	0.3
Compressed	3.8×10^8	2.8	1.8×10^{11}	3.5×10^{-7}	6	0.6
Doppler	3.2×10^8	0.2	1.3×10^{11}	1.2×10^{-5}	2.2	2
Doppler comp.	3.2×10^8	1.1	1.5×10^{12}	1.2×10^{-5}	33	13

Table 3.2: *Effect of adiabatic compression and Doppler cooling on the cloud in the Ioffe-Pritchard trap. Shown are the atom number N, the temperature T, the peak density n_0, the peak phase-space density ρ_0 and the collision rate Γ calculated for energy independent elastic collision cross section. The capture trap has oscillation frequencies of $\omega_{ax} = 2\pi \times 73\,Hz$ and $\omega_{rad} = 2\pi \times 200\,Hz$ (for $^7Li\ |F = 2, m_F = 2\rangle$) and an offset magnetic field of 480 G. For the compressed trap $\omega_{ax} = 2\pi \times 118\,Hz$ and $\omega_{rad} = 2\pi \times 7000\,Hz$ and the offset magnetic field is 2 G. The collision rate Γ_0 is calculated with an energy independent cross section of $a = -27\,a_0$. Inclusion of the correction given in figure (1.14 b) results in the effective collision rate Γ.*

with an intensity of $35\,\mu$W/cm^2 and a duration of 1 second. Afterwards the beam is ramped off in 100 ms. The cooling stage is long enough to let the ergodic mixing and the collisions work to mix all degrees of freedom. This time the cloud is cooled in all dimensions. After expansion to the initial trap parameters the axial temperature has decreased by nearly a factor 4 from $\sim 700\,\mu$K to $\sim 200\,\mu$K. Only $\sim 15\%$ of the atoms are lost during the Doppler cooling process. The results of the two Doppler cooling stages are shown in picture (3.7) and summarized in table (3.2).

When mixing ^{6}Li to the sample, it can be observed that ^{6}Li has been cooled to the same temperature as ^{7}Li after the second Doppler cooling, while it is unaffected by the first. Since no light near a ^{6}Li resonance is used, this cooling can only be sympathetic cooling, mediated by collisions between ^{6}Li and ^{7}Li. The collision cross section for ^{7}Li collisions is only about a factor 0.5 lower than the inter-isotope collision cross section for temperatures around 0.5 mK. This indicates that collisions between ^{7}Li probably play a role in the mixing of the axial and radial degrees of freedom.

It is not possible to leave out the first Doppler cooling stage. Without it, atoms are lost during the compression, perhaps because of an insufficient trap depth.

After Doppler cooling, the atoms are prepared for evaporative cooling. It is no longer necessary to keep the offset field at 480 G; it can be reduced down to 1.5 G before Majorana losses become important. This strongly increases the radial confinement (see formula 2.9). The reduction is done by ramping off the part of the current flowing through the pinch coils that comes from the MOT power supply. This reduces the axial confinement slightly. The mutual compensation of the bias fields of the pinch and compensation coils is not perfect. An extra pair of Helmholtz coils powered by a low current, high precision power supply provides an additional offset field. This compensates the imbalance and gives us the possibility to choose arbitrary offset fields up to $\sim$ 26 G. The offset field could in principle also be chosen by adding current to the pinch coils using the MOT power supply, as it is done during the Doppler cooling stage, but the stability of the offset field is then not sufficient for evaporative cooling, since the MOT power supply is relatively unstable. The current in the Ioffe bars is reduced from its value of 850 A, which it had during Doppler cooling, to 700 A. This is done because at a current of 850 A the Ioffe bars overheat after $\sim$ 10 s. In the new trap configuration the frequencies are $\omega_{ax} = 2\pi \times 118\,\mathrm{Hz}$ and $\omega_{rad} = 2\pi \times 7000\,\mathrm{Hz}$ for an offset magnetic field of 2 G. The gas has now a temperature of 1.1 mK and a collision rate of $13\,\mathrm{s}^{-1}$, where the energy dependence of the collision cross section has been taken into account (see table 3.2). With a lifetime of about one minute, the ratio of elastic to inelastic collisions is now 780, which is sufficient for runaway evaporative cooling.

3.2 Measurements

Before describing in detail how the evaporative cooling worked after the Doppler cooling was optimized, I want to describe which methods we use to determine the physical parameters of the gas, such as temperature, collision rate and so on.

3.2.1 Measurement of the trap oscillation frequencies

To measure the trap oscillation frequencies we used two methods, one which works for hot clouds, before evaporative cooling is applied and another which works best for very cold clouds, well confined in the harmonic region of the trap. A coarse check of these measurements is given by the comparison with the calculated values for our trap geometry.

The first method measures the axial oscillation frequencies by displacing the cloud axially from its equilibrium position by using the light pressure of the Doppler cooling beam and then suddenly switching off the beam. This leaves the cloud oscillating. By taking images after different delay times after switch-off, the movement can be followed. By measuring out one oscillation period and again another oscillation period, a dozen periods later, the oscillation frequency can be determined with high precision (see figure 3.8).

The radial oscillation frequency could not be determined using this method because of the lack of a pushing beam in the radial direction. But here the resonant character of ergodic mixing helped. We capture the atoms in the Ioffe trap after the transfer. The temperature of the cloud in the axial direction is then much higher than the temperature in the radial direction, because in the axial direction the appendage is large and no selection of the coldest atoms has taken place. After a while the trajectories of the atoms oscillating in the axial direction have turned to a radial oscillation due to anharmonicities in the trapping potential. Now the hot atoms are lost by collisions with the appendage. This can be observed as a loss of atoms and as a decrease in axial size. The timescale of this ergodic mixing depends on the amount of anharmonicities and on the ratio of the radial and axial trapping frequencies. If these frequencies are multiples of each other, small trajectory distortions sum up in phase each oscillation period and lead to a fast ergodic mixing [181]. We measure the axial size of the cloud a given time after capture in the Ioffe trap, and vary the current in the Ioffe bars. A clear resonance can be observed when the oscillation frequencies are multiples of each other (see figure 3.9). Using the known axial oscillation frequency, the radial frequency can be calculated.

These measurements were essential for us to know the oscillation frequencies before the evaporative cooling worked. After we achieved evaporative cooling we improved our measurements, by using parametric heating and shaking of the trap (see picture 3.10). A cloud with a temperature of 6 μK is produced, which guarantees that the gas is

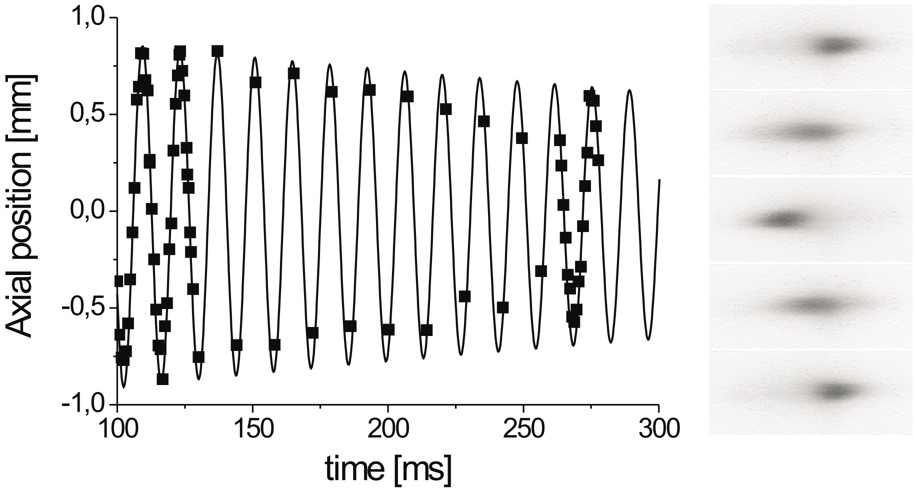

Figure 3.8: *Determination of the axial oscillation frequency. The atomic cloud is pushed out of its equilibrium position using the Doppler cooling beam. After a sudden switch off of the beam, the cloud oscillates in the trapping potential. In this example the oscillation frequency is* $\omega_{ax} = 2\pi \times 72\,Hz$.

well in the harmonic region of the trap. To measure the axial frequency we modulated the position of the trap center in the axial direction by adding a sinusoidally varying quadrupolar field with its axis parallel to the Ioffe-Pritchard trap axis. Heating is observed, when the axial trap oscillation frequency is used as modulation frequency. The radial frequency is determined by modulating the offset magnetic field using a sinusoidal homogeneous magnetic field on axis with the trap. In this way, the radial oscillation frequency is modulated. Parametric heating is observed if the modulation frequency is twice the radial trap frequency. To add the necessary oscillating magnetic fields, the output of a sine wave generator is amplified by a 100 W audio amplifier and put on a coil pair in either Helmholtz or quadrupole configuration. To protect the audio amplifier, a 50 Ω inductance is put in series with the coils.

3.2.2 Temperature measurements

We use three different methods to determine the temperature of the gas. The first uses the free expansion of the cloud after release from the trap. The second involves measuring the energy spectrum and the third consists of fitting *in situ* images of the trapped cloud.

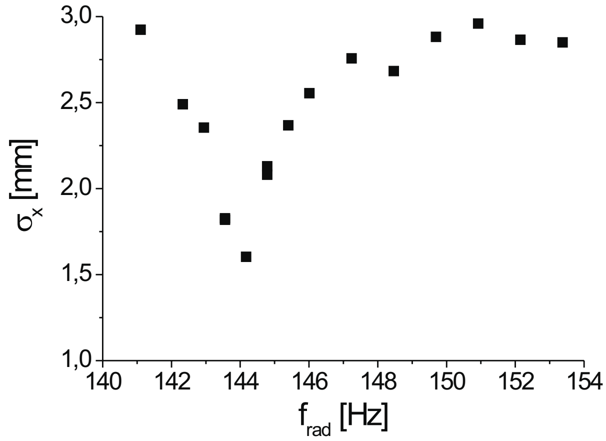

Figure 3.9: *Cross dimensional rethermalization. A cloud with higher axial than radial temperature is prepared. After a delay of* 400 *ms, the axial size is measured. A strong reduction in the axial size is observed if the radial oscillation frequency is the double of the axial frequency. Here the axial oscillation frequency was measured as shown in figure (3.8) and is* 72 *Hz.*

Time of flight

The most universal measurement is the so called *time-of-flight* temperature measurement. It consists in releasing the atoms suddenly from the trap. If the gas is in the collisionless regime, which means that the elastic collision rate is much smaller than the trap oscillation frequencies, the cloud expands freely. Each atom flies in the direction of the momentum it had when the trap was switched off. During the expansion the spatial distribution of the cloud is a convolution of the initial spatial distribution and the momentum distribution. When the cloud has grown much larger than the initial distribution, the spatial distribution is well approximated by the momentum distribution $n(\overrightarrow{r}) = n_p(m\overrightarrow{r}/t)$. In the case of a classical gas the momentum distribution is a Boltzmann distribution $n_p(\overrightarrow{p}) = \exp(-p^2/(2mk_BT))$. Thus a gaussian fit to the spatial distribution after a long time of flight gives the temperature $T = m\sigma^2/k_Bt^2$, where σ is the size of the gaussian fit. If the initial spatial distribution is also a gaussian with the size σ_0 then the distribution stays gaussian during the whole expansion with the size $\sigma(t) = \sqrt{\sigma_0^2 + (vt)^2}$, where $v = \sqrt{k_BT/m}$ is the mean velocity. Since it is not always possible to expand the cloud to sizes much larger than the initial size, *e.g.*, because of a limited field of view or a too severe drop in signal to noise, the temperature is often determined by fitting the time evolution of the size of the cloud using this law. The assumption of an initial gaussian distribution is exact for a classical gas in a harmonic trap and is also well fulfilled for not too dense clouds trapped in a MOT. One condition

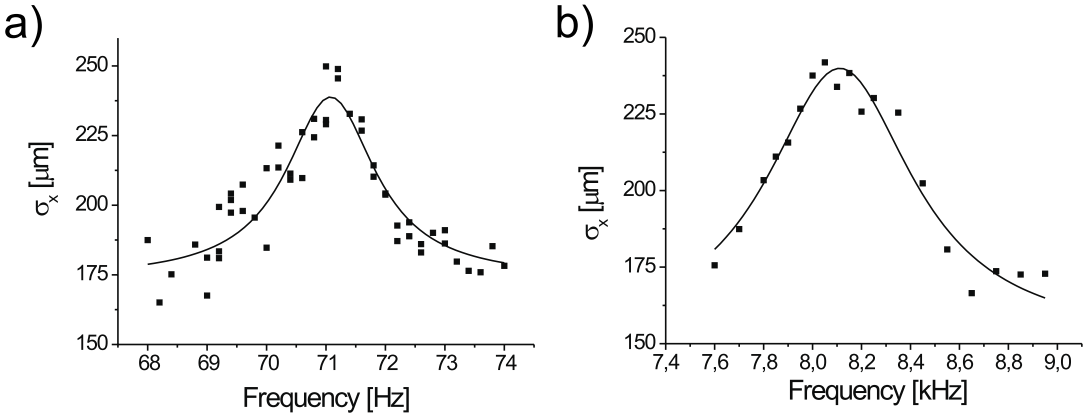

Figure 3.10: *Measurement of the trap oscillation frequencies. The increase in axial size of the trapped gas, reflecting the increase in temperature, is observed after* 10 s *of modulation of the trap. The gas is initially at a temperature of* 6 μK. *a) Measurement of the axial oscillation frequency by moving the trap center axially. b) Measurement of the radial oscillation frequency by modulating the radial oscillation frequencies. The trap oscillation frequency is half the value of the modulation frequency at resonance. Lorentz curves are fitted to the data to extract the trap frequencies of* $\omega_{ax} = 2\pi \times 71.1(5)$ *Hz and* $\omega_{rad} = 2\pi \times 4.05(1)$ *kHz.*

has to be fulfilled for this method to work: the trap has to be released on a timescale shorter than the oscillation period. If this is not the case, the gas will experience an adiabatic expansion during the switch-off and cool down before it is released, giving an underestimate for the temperature measurement. This condition is easy to fulfill for the MOT and for the dipole trap, but much more difficult for the magnetic trap, since the energy of the magnetic field has to be dissipated. In our case we solve the problem by using high current low inductance coils and permitting a switch-off induction voltage of 800 V. The energy is dissipated in varistors parallel to the IGBT switches (see section 2.7.3). The time-of-flight temperature measurement method is very universal since it works for all types of trap. But it often requires several images after different times of flight.

Energy spectrum

The next method probes the energy distribution directly, but can only be applied in a magnetic trap when the gas is collisionless. The high energy tail of the distribution is removed from the trap by a constant radio frequency knife (see section 1.2). The number of remaining atoms is measured in dependence of the radio frequency. Below a certain frequency, no atoms are removed, because the radio frequency knife is below the trap bottom (see figure 1.8). This frequency corresponds to zero energy. The frequency scale can be converted into an energy scale with the known parameters of the transition. With the knife at the trap bottom, no atoms remain trapped. When increasing the cut energy, atoms below the cut energy stay trapped. Thus one is recording the integral of the energy distribution

$$N(E_{cut}) = \int_0^{E_{cut}} d\epsilon\, \rho(\epsilon) f(\epsilon)\,, \tag{3.1}$$

where $\rho(\epsilon)$ is the density of states, $f(\epsilon)$ the energy distribution and E_{cut} the cut energy. The shape of the magnetic trapping potential enters through the density of states (see [137] for the density of states of a Ioffe potential). The temperature determines the energy distribution. A fit to the experimental data determines the temperature. The advantage of this method is, that it requires only measurements of relative atom numbers, which are easy to perform. A limitation of the method is that it works only if the collision rate is much smaller than the trap oscillation period. This is the case for the bosonic gas before Doppler cooling and for a pure polarized fermionic gas at all temperatures. If the condition is not fulfilled, evaporation leads to a higher loss in the number than expected from the removal of the high energy tail.

In situ spatial distribution

The third temperature measurement method in the magnetic trap is measuring the *in situ* spatial distribution of the cloud. It is not completely trivial to record this distribution. When taking images of the cloud with the magnetic trap on, the Zeeman effect can shift atoms in the wings of the cloud out of resonance. This effect was used to see the Majorana losses (figure 3.5). This effect can hinder the recording of the correct spatial distribution. If the energy corresponding to the temperature of the gas is lower than the energy corresponding to the linewidth of the transition used for detection $T \ll 5.9\,\mathrm{MHz}\, h/k_B = 280\,\mu\mathrm{K}$, this effect is small and *in situ* absorption images show the correct spatial distribution. For clouds at higher temperatures or for clouds in magnetic traps with high offset magnetic field, the trap has to be switched off, before the image is taken. The switch-off has to be done in a way that the spatial distribution is not significantly changed. In our magnetic trap, the radial confinement can be switched off in $18\,\mu$s, due to the low inductance of the Ioffe bars. The axial confinement needs $600\,\mu$s for switch-off because of the high inductance of the compensation coils. Thus we switch first the axial confinement off and after $700\,\mu$s we also switch the radial confinement off. The change in spatial size during these switch-off times is negligible. The longer time of flight in the axial direction is not important because of the bigger size of the cloud in this direction. This method of switch-off works only for traps with small offset magnetic field. If it is performed for clouds in a trap with high offset field, the offset field, which comes from the pinch coils, will decrease during the $600\,\mu$s of axial switch-off time. This increases the radial oscillation frequencies and compresses and excites the gas radially. Still some information about the radial temperature is contained in the radial size of the cloud, but the extraction of the exact temperature is difficult. But these images are still useful to compare temperatures of clouds prepared under different conditions and were the kind of measurements on which Doppler cooling was optimized.

After successful recording of the *in situ* spatial distribution, the temperature can be extracted from its form. For classical gases the density profile is linked to the potential U and to the temperature by the Boltzmann law $n(\overrightarrow{r}) = n_0 \exp(-U(\overrightarrow{r})/k_B T)$. For a harmonic trap with trapping frequency ω the distribution is gaussian with size σ and the temperature is $T = m\omega^2\sigma^2/k_B$. In a Ioffe trap the potential is very well approximated by a harmonic potential if the temperature is much lower than the energy corresponding to the offset magnetic field divided by k_B: $k_B T \ll m_F g_F \mu_B B_0$. When this is not the case a two-dimensional fit is performed including the correct Ioffe trapping potential. For temperatures below $\sim\ 200\,\mu$K and a typical radial oscillation frequency of 7 kHz, the radial size of the cloud is smaller than the resolution of our imaging system of about $10\,\mu$m. In this case a two-dimensional fit does not make sense any more. We integrate the optical density along the radial direction and fit the resulting axial distribution to determine the temperature. In the classical regime this is done with a gaussian fit. In the quantum degenerate regime the effect of quantum statistics has to be taken into account (see section 1.1) and the correct fit functions have to be used. For a degenerate Fermi gas the three-dimensional spatial distribution is calculated using equation (1.13) and numerically integrated twice. The resulting 1D distribution is fitted to the experimental data. For a bosonic gas near the phase transition the temperature can be determined from the thermal cloud, if it is visible. The theoretical distribution used as fit function is given by equation (1.56). When no thermal cloud is visible the determination of the temperature using this method becomes impossible. The determination of the temperature of a degenerate Fermi gas is even more difficult. Only the wings of the distribution contain information about the temperature and can be fitted with a gaussian distribution. This method works approximately to degeneracies of $T/T_F = 0.3$. Below that, the temperature has to be deduced from the bosonic gas, thermalized with the fermionic one.

Comparison of the three methods

To cross check our three temperature measurement methods, all three of them have been performed on atomic clouds prepared under the same conditions. The energy spectrum method works only for collisionless clouds. This is the case for a bosonic cloud after capture in the Ioffe trap or for a pure fermionic cloud after sympathetic cooling. This is why we used these conditions for a comparison of all three methods. The time-of-flight method and the method using fits to the *in situ* spatial distribution were compared often under various other experimental conditions. In figure (3.11), the three measurements performed on a bosonic cloud after capture in the Ioffe trap are

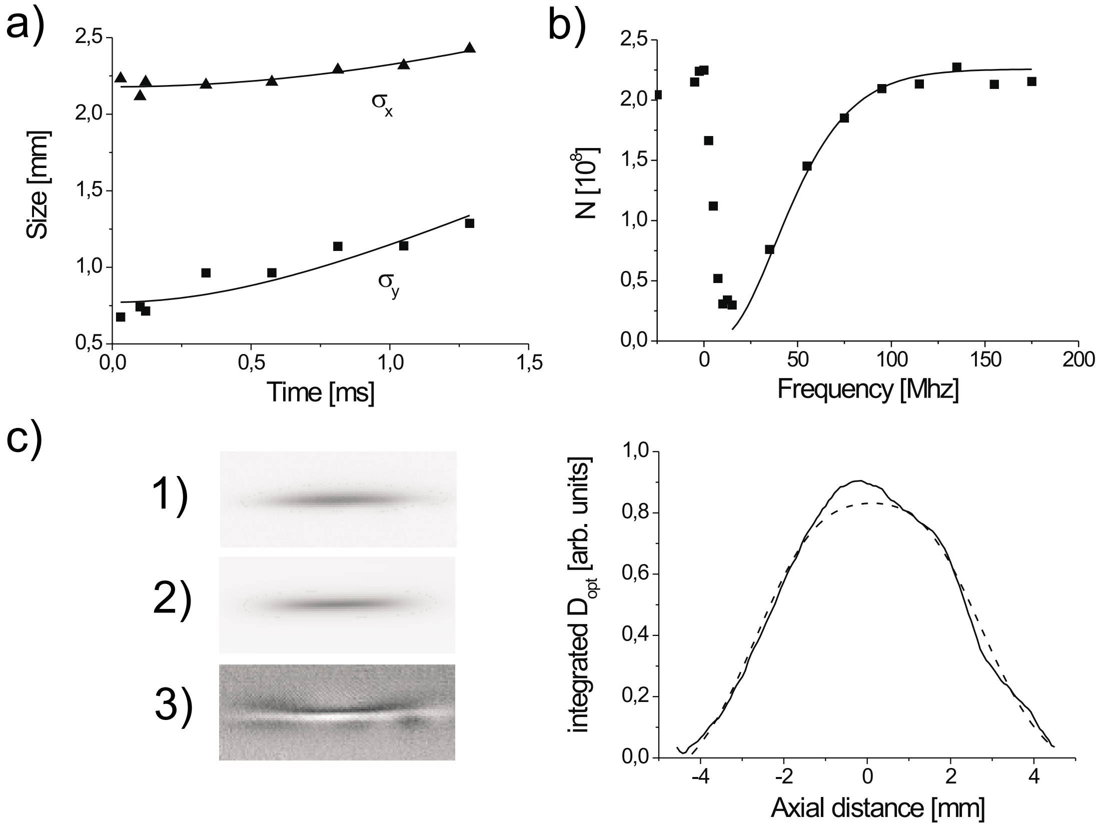

Figure 3.11: *Comparison of three different temperature measurement methods performed with atomic clouds under the same conditions. a) Time of flight measurement. The free expansion of the cloud is observed for* $1.5\,ms$*. The extracted temperature is* $T_{ax} = 620\,\mu K$ *and* $T_{rad} = 640\,\mu K$*. b) Integrated energy spectrum determined by ejection of high energy atoms with a radio frequency knife of varying frequency. The temperature is* $T = 620 \pm 30\,\mu K$*. c) Two-dimensional fit of the distribution after an axial time of flight of* $700\,\mu s$ *and a radial time of flight of* $30\,\mu s$*. Under these conditions the spatial distribution is still very near to the distribution in the trap. In (1) the measured distribution is shown. (2) displays the fit and (3) the 10 times magnified residue of the fit. For comparison the optical density summed over the radial direction is given (solid) and compared to the fit (dashed). The temperature obtained is* $T_{ax} = 500\,\mu K$ *and* $T_{rad} = 780\,\mu K$*. The trap oscillation frequencies for all measurements were* $\omega_{ax} = 2\pi \times 75\,Hz$ *and* $\omega_{rad} = 2\pi \times 1160\,Hz$ *with an offset magnetic field of* $6\,G$*.*

presented. The first two measurements agree within their level of accuracy of 5%. The fit to the initial spatial distribution agrees to a precision of 10% when averaging the temperatures obtained for the axial and radial direction. Treated separately, the error is 20%.

By measuring the temperature with the time-of-flight method, and measuring the *in-situ* size of the cloud, the trap oscillation frequencies can be approximately calculated. This was useful for a first estimation of the confinement of our optical trap.

3.2.3 Measurements of other parameters

The atom number can be determined as discussed in the section on absorption images (2.10) with an uncertainty of less than a factor of 2. After measurement of the number, the temperature and either the size for a MOT or the trap parameters for a magnetic trap, all the other important quantities such as peak density n_0, peak phase-space density ρ_0 and collision rate Γ can be calculated. The collision rate has also been measured directly as explained later in section (3.3.5). To determine if the condition for runaway evaporative cooling $\Gamma_{elastic}/\Gamma_{inelastic} \geq 200$ is fulfilled, the trap lifetime has to be measured. This is done by preparing always the same sample and measuring the remaining number of atoms after a varying storage time. The difficulty in this measurement is the reproducibility with which always the same initial atom number can be prepared. If background gas collisions are dominant, the loss is described by an exponential decay. In our case the $1/e$ lifetime is between one and two minutes. To obtain a good background gas collision limited lifetime measurement, the gas has to be much colder than the trap depth to prevent evaporation, but not too dense to prevent dipolar relaxation and three-body collisions. Good results are obtained after Doppler cooling and storing the atoms in a rather weak trap to reduce density. An example of a lifetime measurement is shown in figure (3.12).

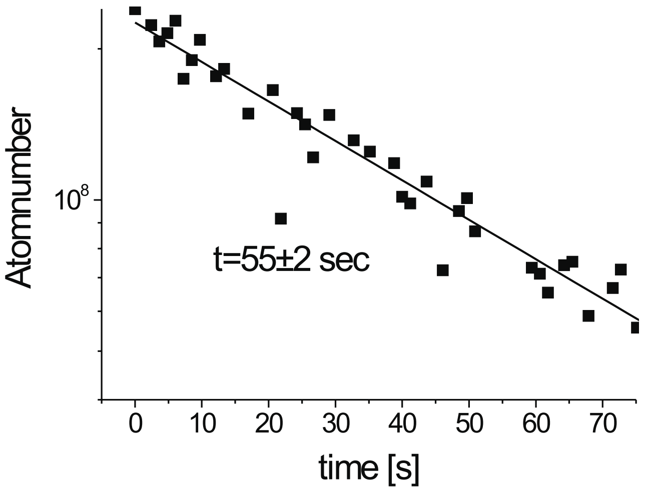

Figure 3.12: *Background gas collision limited lifetime of a gas after Doppler cooling. The gas is stored in a trap with oscillation frequencies of* $\omega_{ax} = 2\pi \times 73\,Hz$ *and* $\omega_{rad} = 2\pi \times 200\,Hz$ *and an offset magnetic field of* $480\,G$*. The lifetime is* $55(2)\,s$*. The best observed lifetime under these conditions has been* $140\,s$*, due to a lower background gas pressure.*

3.3 Experiments in the higher HF states

3.3.1 Evaporative cooling of ^{7}Li

After optimization of the Doppler cooling, evaporative cooling worked immediately. In the following I will discuss in detail the properties of our evaporative cooling process. In the next section the sympathetic cooling will be explained.

Two different transitions can be used to remove atoms during evaporative cooling. The Zeeman transition $|F = 2, m_F = 2\rangle \rightarrow |F = 2, m_F = 0\rangle$ and the hyperfine transition $|F = 2, m_F = 2\rangle \rightarrow |F = 1, m_F = 1\rangle$ (see figure 2.1).

The frequency range of the first depends on the offset magnetic field, and on the initial temperature. For the chosen offset field of 2 G and an initial temperature of 1 mK, the radio frequency sweep used for evaporation goes typically from 50 MHz down to 1.5 MHz. This transition can be considered as consisting of two transitions, $|F = 2, m_F = 2\rangle \rightarrow |F = 2, m_F = 1\rangle$ and $|F = 2, m_F = 1\rangle \rightarrow |F = 2, m_F = 0\rangle$. If the offset magnetic field is too large the second order Zeeman effect lifts the degeneracy between the two transitions, making the evaporation harder [182]. But the real disadvantage of this transition becomes apparent when trying to use it for sympathetic cooling. Due to the level structure of ^{6}Li and ^{7}Li, a given radio frequency corresponds for ^{6}Li to a lower cut energy than for ^{7}Li, see figure (3.13). Thus ^{6}Li is removed from the trap before it can be sympathetically cooled by ^{7}Li and sympathetic cooling does not work.

The hyperfine transition $|F = 2, m_F = 2\rangle \rightarrow |F = 1, m_F = 1\rangle$ has none of the listed disadvantages (see figure 3.14). It is selective for ^{7}Li and a simple one photon transition. The cut energy and the radio frequency are linked by the law $E_{cut} = \hbar(\nu - \nu_{hf})/1.5 - \mu_B B_0$. The factor 1.5 comes from the level structure of the used transition, B_0 is the offset magnetic field and $\nu_{hf} = 803.504$ MHz the hyperfine splitting [183]. The used frequency range is 1 GHz down to ν_{hf}, corresponding to energies of $k_B\,6$ mK to zero.

The optimization of the radio frequency ramp was done in several steps. The principle is the following. As a first starting point the frequency of 1 GHz was chosen, which was both, a reasonable value taking into account the absence of collisions around 6.6 mK and the limit of our microwave amplifier. The initial temperature of the gas in the compressed trap is about 2 mK, so that 1 GHz corresponds to a rather small value of $\eta = 3$ ($E_{cut} = \eta k_B T$). Now a final cut energy was chosen about 3 to 5 times smaller than the initial cut energy. A linear ramp was performed between these two energies and the duration of the ramp was varied. The measurement parameter on which the evaporation was optimized is the collision rate. This is the parameter driving the evaporative cooling. The higher it becomes, the better the cooling will work. It turns out that at low temperatures the elastic collision rate has the same dependence on atom number N and temperature T as the peak optical density. This can be seen in the

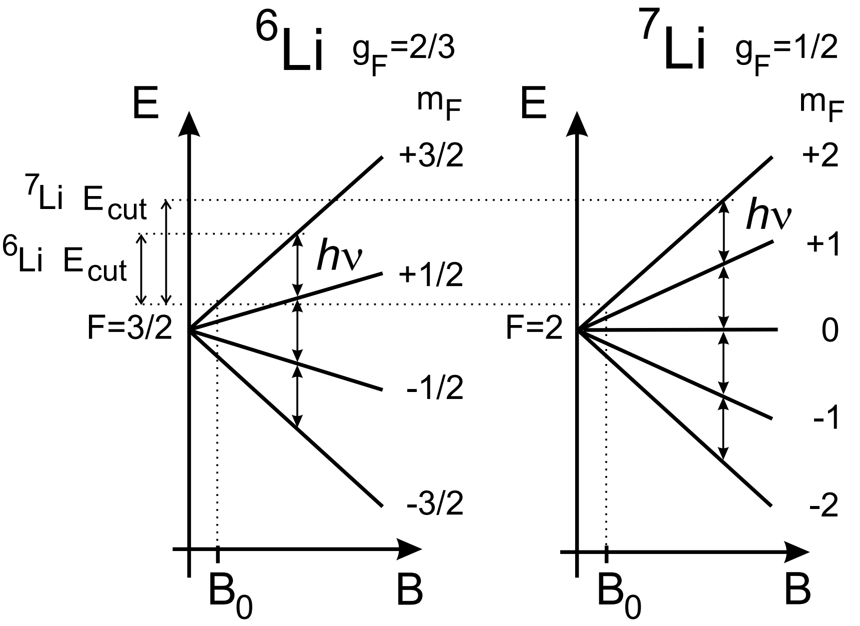

Figure 3.13: *Zeeman radio frequency transition in the higher hyperfine states. Shown is the magnetic field dependence of the* m_F *substates of* ^{6}*Li and* ^{7}*Li for weak magnetic fields.* B_0 *is the offset magnetic field of the trap. A radio frequency wave with frequency* ν *corresponds to a lower cut energy* E_{cut} *for* ^{6}*Li than for* ^{7}*Li. This makes sympathetic cooling of* ^{6}*Li by* ^{7}*Li with a Zeeman transition impossible.*

following way.

$$\begin{aligned} \Gamma &= v n_0 \sigma_{el} \propto \sqrt{T} N/(\sigma_x \sigma_y \sigma_z) \propto N/T \,, \qquad (3.2) \\ D_{opt}(x=0, y=0) &= \int dz\, n(x=0, y=0, z) \propto \sigma_z n_0 \propto \sigma_z N/(\sigma_x \sigma_y \sigma_z) \propto N/T \propto \Gamma \,, \end{aligned}$$

where $\sigma_i = \sqrt{k_B T / m\omega_i^2}$ has been used. The peak optical density is determined with a simple *in situ* measurement of the density distribution. Thus no calculation is needed and the optimization process becomes relatively simple.

Normally the optical density rises steeply to a maximum and falls off rather slowly with the duration of the radio frequency sweep. If a choice had to be made between durations with equivalent results, the shorter duration was chosen. After the optimization of a linear sweep, a new end cut energy, again 3 to 5 times lower than before was chosen and another linear sweep segment to this end frequency was added to the existing sweep. This piecewise linear segment method was pursued until the evaporation stopped working or quantum degeneracy was reached. In a second iteration the whole sweep was optimized globally. The whole evaporation was performed and stretched in time. Also the frequency or the time of the starting point of one of the linear ramps

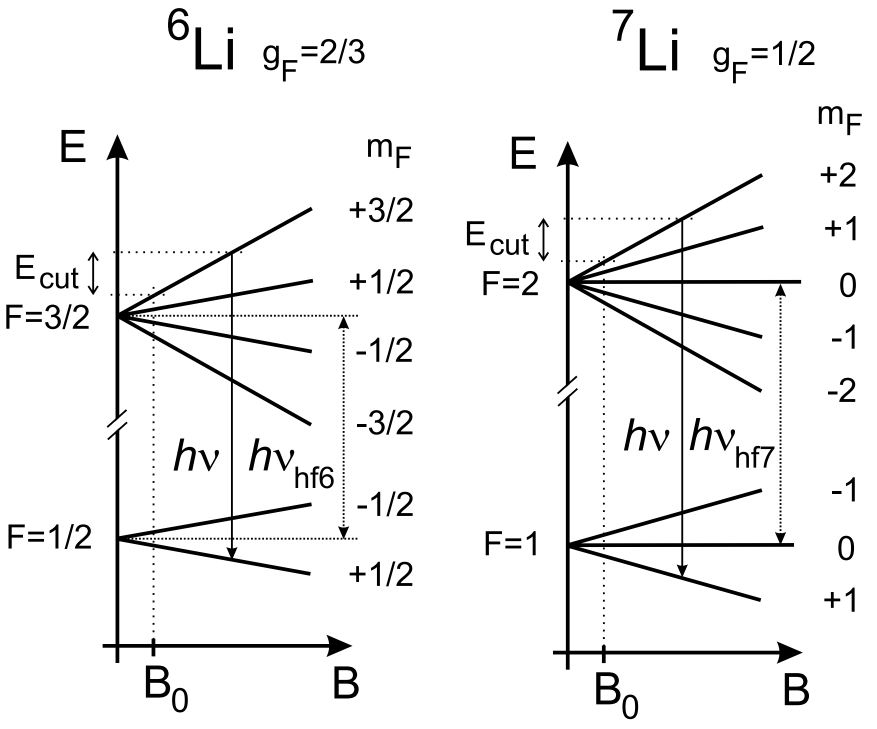

Figure 3.14: *Evaporation on the hyperfine transition of* ^{6}*Li and* ^{7}*Li. Due to the difference in the hyperfine splitting* $\nu_{hf6} = 228.205$ *MHz and* $\nu_{hf7} = 803.504$ *MHz of the two isotopes the evaporation is isotope selective.* B_0 *indicates the offset magnetic field of the trap.*

out of which the sweep consists was varied. It turned out, that it is not useful to start the evaporation above a frequency of $\sim$ 920 MHz. This is probably due to the lack of collisions for higher energies. An attempt has been made to overcome this lack in the following way. The trap was initially not fully compressed, to keep the initial temperatures lower. Now a constant radio frequency knife of for example 920 MHz was used during a slow final compression stage. Another strategy was to optimize part of the ramp in a shallower trap, then the trap was compressed and a new evaporation sweep optimized. Both attempts produced the same results as the first method. Since this method is simpler, we stayed with it.

The characterization of the evaporative cooling process is shown in figures (3.15) and (3.17). The initial conditions are a bosonic gas with 2×10^8 atoms at a temperature of 2 mK in a trap with oscillation frequencies of $\omega_{ax} = 2\pi \times 71.17(5)$ Hz and $\omega_{rad} = 2\pi \times 4050(8)$ Hz. This is not the steepest possible trap, but a further increase in the trapping frequencies did not improve the result. The initial collision rate is about $13\,\mathrm{s}^{-1}$. This value was calculated including the temperature dependence of the elastic collision cross section. With the lifetime of one minute, the elastic to inelastic collision

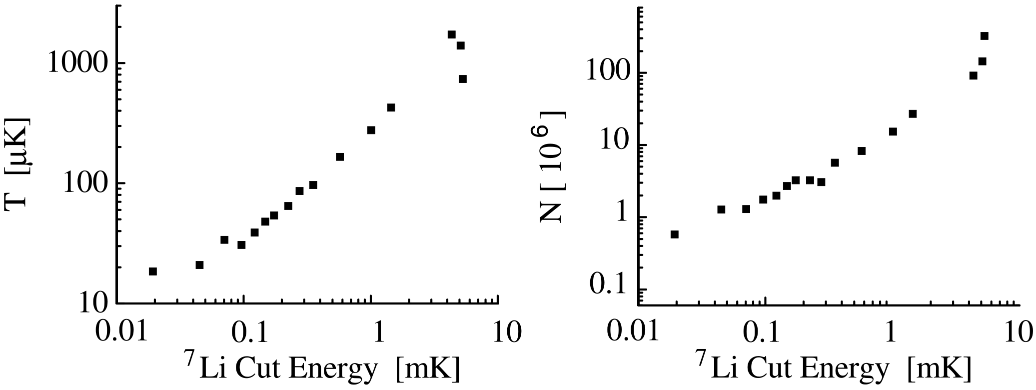

Figure 3.15: *^{7}Li temperature and number as a function of the cut energy during evaporative cooling. Uncertainty in the x-axis is about 0.01 mK.*

ratio is 780, sufficient to start evaporative cooling. A fast evaporative cooling sweep is performed between 1 GHz and 920 MHz during 2.5 s to remove the hottest atoms, which can not participate in the evaporative cooling because of their vanishingly small elastic collision rate. The whole evaporation sweep takes 35 s and is shown in figure (3.16). The result is not strongly dependent on the exact shape of the radio frequency sweep.

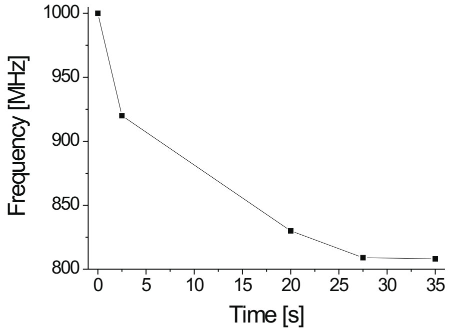

time [s]	ν [MHz]	E_{cut} [μK]
0.0	1000	5800
2.5	920	3400
20.0	830	675
27.5	809	39
35.0	808	9

Figure 3.16: *The typical evaporative cooling sweep for a trap with oscillation frequencies $\omega_{ax} = 2\pi \times 71.17(5)\, s^{-1}$ and $\omega_{rad} = 2\pi \times 4050(8)\, s^{-1}$. The initial number of ^{7}Li atoms for this sweep is between 2×10^8 and 4×10^8 and the initial temperature is $\sim 2\,mK$. For the first experiments with evaporative cooling slightly longer ramps were used.*

The collision rate increases during this ramp to about $50\,\mathrm{s}^{-1}$. The ratio between the measured temperatures and the microwave cut energy is $\eta = 4$. At the end of the evaporation, when the density exceeds $10^{12}\,\mathrm{cm}^{-3}$ dipolar losses start to limit density and lifetime. The evaporation is on the border of runaway evaporative cooling. This can be seen in figure (3.17a), where the peak phase-space density is plotted on a log-log plot versus the atom number. The data points are nearly on a line with slope -2. In section (1.2) it was derived that this is the slope expected for constant collision rate.

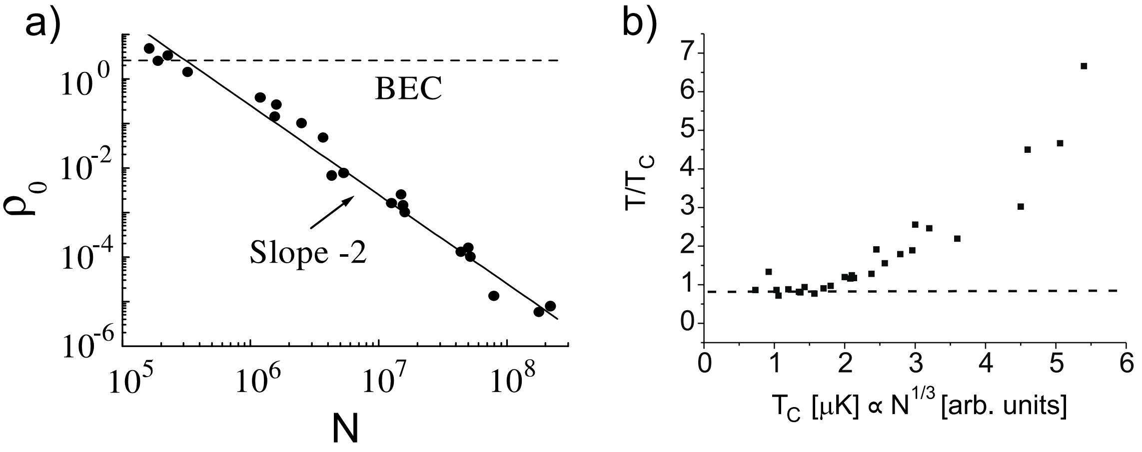

Figure 3.17: *a) ^{7}Li peak phase-space density versus number of atoms N during single-species evaporation of duration* 40 *s. At the end of the evaporation, the peak phase-space density exceeds 2.6, the critical value for Bose-Einstein condensation. The phase-space density is calculated using the measured trap frequencies, atom number and size of the gas in the trap. The uncertainty is a factor 2, coming mainly from the uncertainty in the atom number. b) Indirect signature of the unstable ^{7}Li condensate. The bosonic degeneracy T/T_C is plotted versus the critical temperature, proportional to the cubic root of the atom number during evaporative cooling. The degeneracy never reaches values below 0.9 as a result of the instability of the condensate.*

The peak phase-space density is calculated from the measured trap oscillation frequencies, atom number and axial size of the cloud in the magnetic trap. The uncertainty of a factor 2 comes mainly from the uncertainty in the determination of the atom number. The calculated phase-space density exceeds 2.6 at the end of the evaporation, which means, that a Bose-Einstein condensate should be present. Since the scattering length is negative, the maximum atom number for a metastable condensate under these conditions is about 300 (see section 1.1.8). Our signal to noise ratio is not good enough to resolve such a small condensates on a background of 10^5 thermal atoms. In principle it is possible to construct a sufficiently good detection system, but it takes quite an effort [184]. One of the difficulties is to overcome the spherical abberation resulting from the passage of the probe beam through the wall of the glass vacuum chamber. Without directly seeing the condensate we can still detect its presence indirectly. When the temperature is decreased below the critical temperature, a condensate is created. If the temperature is decreased slightly, the condensate atom number will grow beyond the critical atom number and the condensate will collapse and decay in dipolar relaxation collisions and three-body recombination. This has been extensively studied experimentally and theoretically in [184, 12, 185, 186, 187, 188]. Thus the condensate is the origin of a new loss process appearing slightly below T_C. This can be seen in figure (3.17b), where the degeneracy T/T_C is plotted versus the critical temperature (which is proportional to $N^{1/3}$) during the evaporation. The temperature is determined from the axial size of the distribution and ω_{ax}. The critical temperature is calculated from the trap oscillation frequencies and the atom number using formula (1.31). The error in the determination of T/T_C comes mainly from the error in the measured atom number and is about 15%. T/T_C never goes below $\sim$ 0.9, a signature of an additional loss process appearing at T_C. We will see in section (3.3.4) that the fact that the condensate is unstable for $N_0 \gtrsim 300$ limits the fermionic degeneracies achievable in a boson-fermion mixture with sympathetic cooling. Later on we found ways to produce condensates stable for arbitrary atomnumbers. How this was done is explained in section (3.4.4).

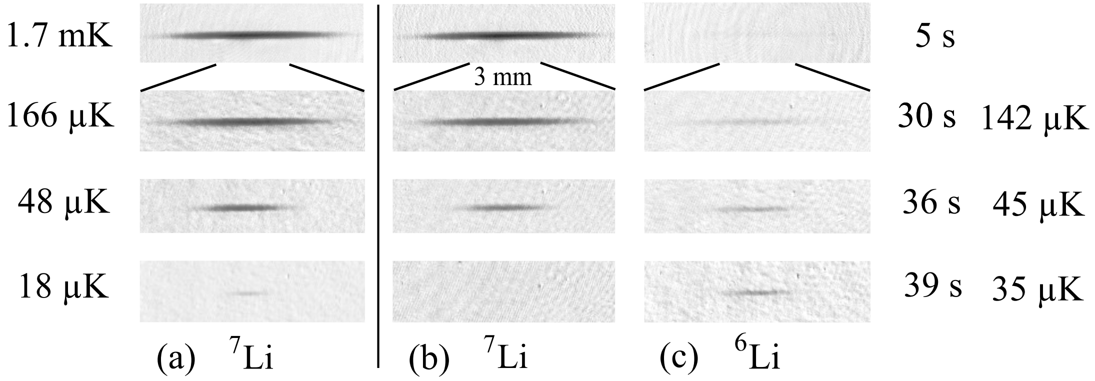

Figure 3.18: *Images of ^{6}Li and ^{7}Li atom clouds at various stages of sympathetic cooling (b,c) and during single-species evaporation (a) with identical initial numbers of ^{7}Li atoms. Top images are 1 cm long, the others 3 mm. Temperatures of ^{7}Li (resp. ^{6}Li alone) are given on the left (right).*

3.3.2 Sympathetic cooling of ^{6}Li by ^{7}Li

After optimization of the ^{7}Li evaporative cooling method, we added 2.5×10^6 ^{6}Li atoms to the trap. An evaporative cooling ramp lasting 40 s is performed. In situ images of both isotopes during the evaporation are shown in figure (3.18). In column a) the behavior of ^{7}Li alone is shown. Sympathetic cooling is shown in columns b) (^{7}Li) and c) (^{6}Li). The initial ^{7}Li atom number is chosen to be the same when cooling both the pure bosonic cloud as well as when cooling the mixture of the bosons and fermions.

The first feature that can be observed is that the cloud's axial size shrinks with ongoing evaporation. This reflects the decrease in temperature. The sizes of all clouds are equal at each stage of the cooling process, showing that the temperatures are the same and that ^{6}Li is in thermal equilibrium with ^{7}Li. The number of ^{6}Li atoms stays roughly constant since evaporation is only performed on ^{7}Li. Thus with lowering temperature the density increases strongly. During the first three stages shown, ^{7}Li behaves the same with or without ^{6}Li present. This is expected as $N_7 \gg N_6$: the thermal capacity of ^{7}Li is then much bigger than the thermal capacity of ^{6}Li. But at the last stage, when cooling a mixture, no ^{7}Li remains having been completely evaporated. As explained in section (1.2.2) this is because the fermionic thermal capacity has become larger than the bosonic. The bosons were no longer able to cool the fermions significantly. Since bosons and fermions are in thermal equilibrium, this also prevents the temperature of the bosons from decreasing further, and since the radio frequency knife is still lowered, all bosons are lost. For the example shown in figure (3.18) this breakdown of sympathetic cooling is reached already in the classical regime, for $T \sim 3\,T_C$. In this regime the heat capacities are equal, when equal number of atoms are reached. Without the ^{6}Li present, ^{7}Li could be cooled under the same conditions to $18\,\mu$K which is below the temperature of 35 μK reached for ^{6}Li at the breakdown.

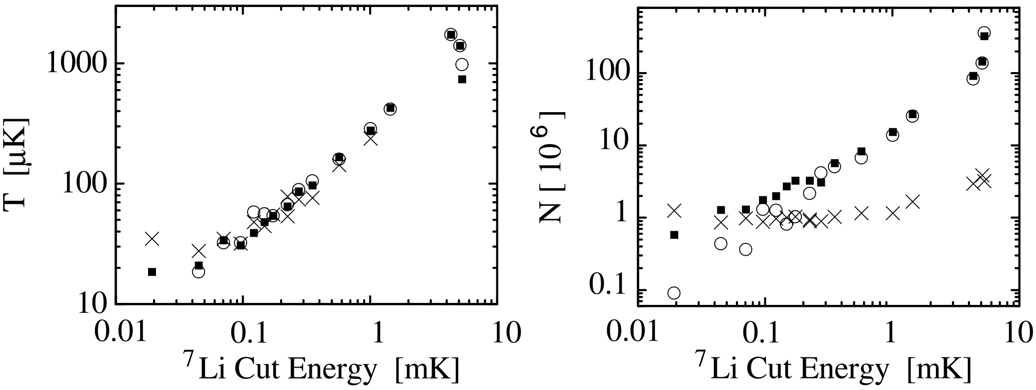

Figure 3.19: *^{6}Li (crosses) and ^{7}Li (open circles) temperatures and numbers as a function of the ^{7}Li cut energy. During sympathetic cooling, temperatures of ^{6}Li and ^{7}Li are the same down to a limit below which ^{6}Li is no longer cooled. Black squares show ^{7}Li alone with identical parameters. Uncertainty in the x-axis is about 0.01 mK.*

More quantitatively, temperatures and numbers of ^{6}Li and ^{7}Li atoms as a function of the microwave cut energy are plotted in figure (3.19). Above $40\,\mu$K, the temperatures of all three clouds are nearly identical, indicating that the collision cross-section between ^{7}Li $|F = 2, m_F = 2\rangle$ and ^{6}Li $|F = \frac{3}{2}, m_F = \frac{3}{2}\rangle$ is not significantly smaller than that of ^{7}Li $|F = 2, m_F = 2\rangle$ with itself. This is consistent with the prediction that the inter-isotope scattering length is (40.8 ± 0.2) a_0 [153]. The initial evaporation of ^{7}Li behaves the same with or without ^{6}Li present, as expected because the ^{6}Li number is a very small fraction of the ^{7}Li number. At a temperature around 35 μK, the number of ^{7}Li atoms (N_7) has been reduced to the number of ^{6}Li atoms (N_6). As a result the ^{6}Li cloud is no longer cooled and remains at 35 μK.

The temperature and atom number at different steps during the experimental sequence is summarized in table (3.3).

	^{7}Li		^{6}Li
	N	T [mK]	N
Compressed MOT	6×10^9	0.8	1.6×10^8
Lower Quadrupole	2.5×10^9	1	8×10^7
Capture I-P trap	3.8×10^8	0.7	1.3×10^7
Compressed I-P	3.2×10^8	2	2.5×10^6
End symp. cool.	1.7×10^6	0.03	1.2×10^6

Table 3.3: *Typical atom numbers and temperatures before and during sympathetic cooling*

3.3.3 Detection of Fermi degeneracy

For classical gases, the temperature, T_S, at which sympathetic cooling stops is reached when $N_7 \approx N_6$. In the case of ^{7}Li alone, the final temperature obtainable, T_7, is approximately proportional to N_7 and so $T_S \propto N_6$. Since $T_\mathrm{F} \propto N_6^{1/3}$, the degeneracy parameter $T_S/T_\mathrm{F} \propto N_6^{2/3}$, and Fermi degeneracy can be approached by reducing the number of ^{6}Li. After having improved the resolution of the imaging system this was done. The first signs of a degenerate Fermi sea were seen in time-of-flight measurements of the fermionic distribution. For these images, a simple method to detect the degeneracy consists of fitting gaussians to the wings of the distribution. In figure (3.20), the size of the Gaussian fit, σ, is plotted versus the fitting interval, parameterized by r. The center up to a distance of $r\,\sigma_0$ is not fitted, only the wings outside are. σ_0 is the size of a complete gaussian fit ($r = 0$). For a classical cloud, the resulting fit size does not depend on the fit region. A fermionic cloud, by contrast, has a suppression of population at low energies. Thus, when fitting a gaussian distribution to the whole cloud the size is overestimated. It goes down when fitting only the wings. The opposite is true for the bosonic cloud, produced under the same conditions. For the bosonic and the fermionic cloud the sizes are the same for $r = 1$, reflecting that they are thermalized. For larger values for r the signal to noise is too low to provide a reliable fit. The fit of the wings for $r = 1$ gives the temperature and together with the atom number and the trapping frequencies the degeneracy can be calculated. The highest observed degeneracy using this method was $T/T_F = 0.3$. Using the fermionic distribution to determine the temperature, it is not possible to obtain a higher degeneracy as a result.

Indeed, when doing the same treatment for a theoretically calculated distribution with $T = 0$, the degeneracy obtained with this method using $r = 1$ is $T/T_F = 0.3$ and not $T/T_F = 0$. Clearly a better method to measure the temperature is needed.

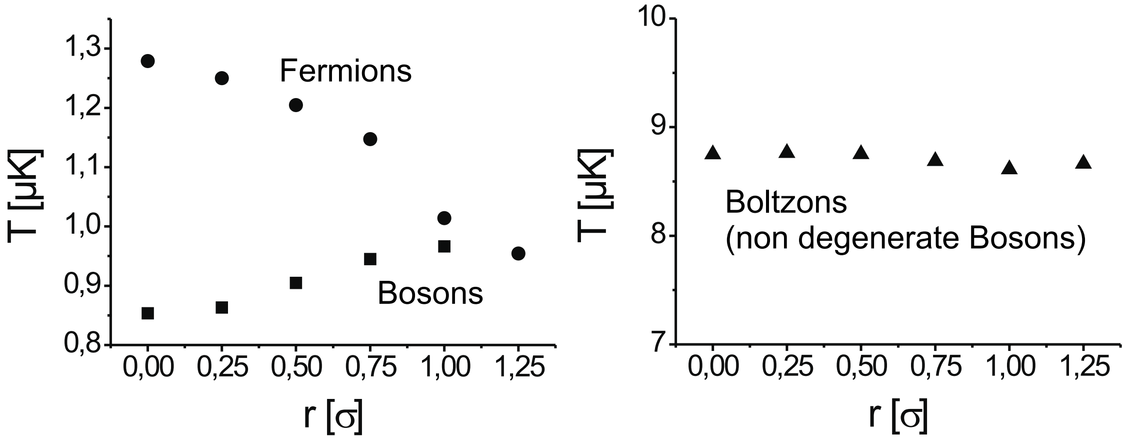

Figure 3.20: *Detection of quantum degeneracy. Gaussians are fitted to the momentum distributions of a degenerate bosonic (square) and fermionic (disks) cloud and the temperature is deduced from the found size. A gaussian fit to the whole distribution over (under) estimates the temperature for the fermionic (bosonic) distribution, because of the non-gaussian distributions in the regime of degeneracy. By excluding the central part* $\{-r, r\}$ *from the fit, only the more classical high energy regions of the distribution are probed and the temperatures deduced from the fit approach their real values. Here* r *is given in units of the RMS size* σ *of the gaussian fit to the whole distribution. The dependence of the fit result of the fit region is characteristic for distributions of degenerate gases. For comparison the same fit procedure is applied to a non-degenerate bosonic gas (triangles) giving nearly no change in the temperature with* r.

3.3.4 Detection of Fermi pressure

The solution is to measure the temperature of the bosonic component. To be sure that this temperature is the same as the temperature of the fermionic component, the thermalization rate between the two was measured (see section 3.3.5) and the clouds are left to thermalize for a 7 times longer timespan (1 s) than the thermalization time (150 ms) after the end of the evaporation, before the images are taken. It was also essential to modify the imaging system to be able to take images of the fermionic and bosonic component after the same experimental run (see section 2.10).

First the system was studied using time-of-flight images and a degeneracy of better than $T/T_F = 0.3$ was found. The disadvantage of the time-of-flight technique is, that the spatial extension depends on mass and the time of free flight. And both are different for ^{6}Li and ^{7}Li. The time of flight is different because the camera needs at least 0.5 ms to prepare itself for a new exposure. Thus the degeneracy is not evident, but has to be extracted by fits and calculation.

Much more direct visual information can be obtained, when *in situ* images of both isotopes are taken. The imaging of one component does not disturb the distribution of the second in the axial direction, which is used to determine the degeneracy. This is because the delay of 1 ms between the two images is shorter than the period of the axial oscillation, which is 13 ms. This was verified by exchanging the isotope sequence during the imaging process. Later on the image of ^{7}Li was always taken second, just to make sure that if a heating occurred it could only decrease the measured degeneracy.

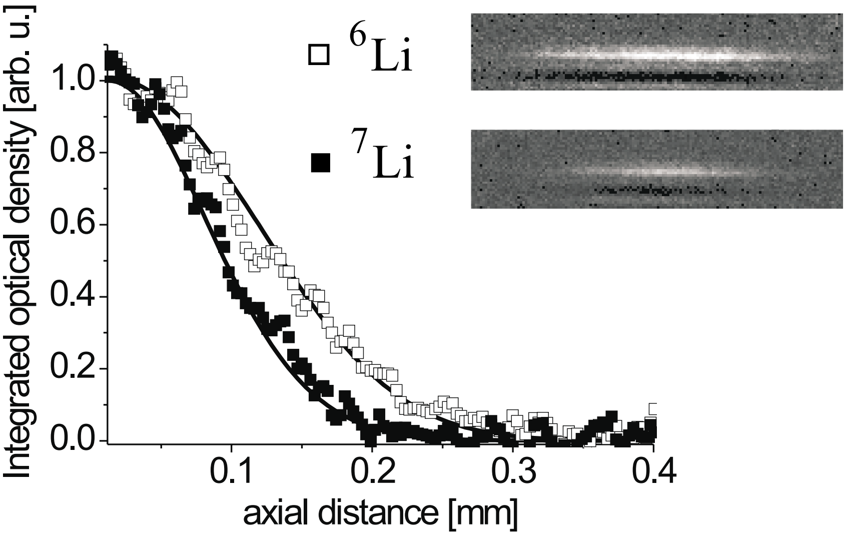

Figure 3.21: *Observation of Fermi pressure. Absorption images in the trap and spatial distributions integrated over the vertical direction of* 8.1×10^4 ^{6}*Li and* 2.7×10^4 ^{7}*Li atoms in their higher hyperfine states. The temperature is* $1.4(1)\,\mu K$ *corresponding to* $1.1(2)\,T_\mathrm{C}$ *for the bosons and* $0.33(5)\,T_\mathrm{F}$ *for the fermions. Solid lines are the expected Bose and Fermi distributions.*

This method has the advantage that it requires simply two images of each cloud under the the same conditions. Since the magnetic moments μ of both isotopes, each in the stretched state, are the same, they experience the same trapping potential. If the gases are in the classical regime and if they are in thermal equilibrium, their spatial distributions are gaussians with the same width $\sigma = \sqrt{k_B T/(\mu C)}$ (where C is the magnetic field curvature). The mass does not enter, contrary to momentum distributions. The detection of degeneracy is now very simple. If a difference in the axial distribution is detected between two well thermalized clouds, the only reason for this comes from their different quantum statistics. Typical images are shown in figure (3.21). Axial profiles of the distributions summed up in the radial directions are shown. The fermionic distribution is clearly broader than the bosonic distribution, indicating the effect of Fermi pressure. Here the fermionic degeneracy can be seen directly without any calculation or fit involved. For the shown example the temperature measured from the bosonic distribution is $1.4(1)\,\mu$K and $T/T_F = 0.33(5)$, where T_F is again calculated from the fermionic atom number and the trap oscillation frequencies. Both distributions are well described by theory (the twice integrated bosonic distribution (1.56) and a double integral over the fermionic distribution (1.13), shown in solid lines.

Our highest degeneracy achieved in the ^{6}Li $F = 3/2$ state is $T/T_F = 0.25(5)$ with $T_F = 4\,\mu$K, very similar to [61]. This limit is set by the fact that the condensate is unstable as discussed in section (1.2.2). By going to the highest trap oscillation frequencies ($\omega_{ax} = 2\pi \times 112\,$Hz and $\omega_{rad} = 2\pi \times 7101\,$Hz for ^{7}Li $|F = 2, m_F = 2\rangle$) and with 2.5×10^5 fermions, Fermi temperatures of $T_F = 11\,\mu$K are reached with a degeneracy of $T/T_F = 0.36(5)$. This Fermi temperature is 3 times higher than the photon recoil of $3.5\,\mu$K, a situation favorable to the observation of modifications of the scattering of light of this quantum gas (see section 1.1.4).

The behavior of bosons and fermions is compared in figure (3.22a). The axial bosonic and fermionic distributions were fit to Gaussians, and the ratio of their RMS sizes is plotted versus the fermionic degeneracy T/T_F. The data is compared to a theoretical curve. In the classical regime, both sizes are the same. Below the degeneracy of $T/T_F = 1$ the fermionic cloud stays bigger than the bosonic cloud due to the Fermi pressure, but also due to the bosonic degeneracy. To extract the action of just the Fermi pressure, the RMS size of the fit to the fermionic distribution is compared to the Fermi radius $R_F = \sqrt{2k_B T_F/m\omega_{ax}^2}$ in figure (3.22b). The ratio of the two sizes squared is plotted versus the degeneracy T/T_F. Again the data is compared to a theoretical curve. The straight line going through the origin describes the behavior in the absence of Fermi pressure. In the quantum regime, the Fermi pressure makes the size saturate at a nonzero value ($\sigma^2/R_F^2 = 0.15$ instead of zero, see section 1.1.2). This is also apparent in the experimental results, but the data points are not in perfect agreement with the theoretical curve. At the moment we can not explain this difference. We did check, however, that it does not come from a bad calibration of the imaging system, nor from the uncertainty in the atom number or the trap frequencies. It might be due to the effect of the bosonic mean field on the fermions which was excluded from the numerical calculation described in section (1.1.13) and from [75].

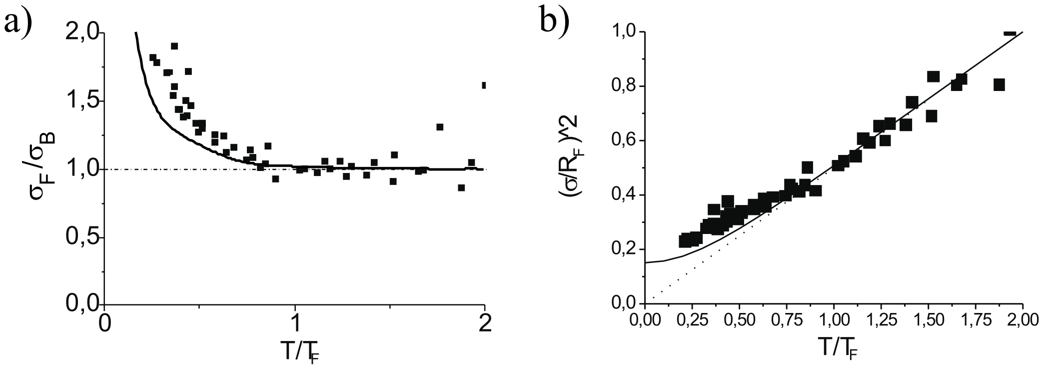

Figure 3.22: *Fermi pressure versus the degeneracy parameter* T/T_F*. Squares: data, dashed line: classically expected behavior, solid line: theory including quantum effects. a) The ratio of the RMS sizes of gaussian fits to thermalized fermionic and bosonic distributions is plotted versus the fermionic degeneracy. In the classical region* $T/T_F > 1$ *the distributions have the same size. In the degenerate region* $T/T_F < 1$*, the fermionic distribution exceeds the bosonic in size. b) The same data, but here the RMS size of a gaussian fit to the fermionic distribution is normalized by the Fermi radius* $R_F = \sqrt{2k_BT_F/m\omega_{ax}^2}$ *and the square of this ratio is plotted versus the fermionic degeneracy.*

3.3.5 Thermalization measurement

For the results discussed above, it is essential to know that the bosonic and fermionic gases are in thermal equilibrium. To ensure this, we let the system thermalize for 1 s after the end of the cooling ramp and before taking the images. To determine if this is sufficient, the thermalization timescale was measured for a fermionic cloud with a degeneracy of $T/T_F = 0.5$. Initially a mixture of a bosonic gas with 10^5 atoms and a fermionic gas with 1.5×10^5 atoms and a common temperature of 2.6 μK was produced. A radio frequency knife was switched on during 10 ms to remove suddenly the hottest 80% of the bosonic atoms. As will be shown, this cut is 15 times faster than the thermalization timescale. After the cut the bosons are not in thermal equilibrium, neither with themselves, nor with the fermions. The axial profile is non-gaussian, the high energy wings are missing. This distribution has no well defined temperature since it is not thermalized. For simplicity a gaussian fit is also performed on it and used to determine an effective temperature, which is slightly lower than the temperature of 1 μK reached after some 100 ms of thermalization without fermions present. In the presence of fermions, the bosons thermalize to a final temperature of 2.4 μK with an exponential timescale of 150 ms as is shown in figure (3.23). This temperature is slightly lower than the initial temperature of the fermions, since these are cooled during the thermalization by about 0.2 μK. The whole process has been simulated as described in section (1.2.4). Two theoretical curves are shown in the figure, one including Pauli suppression, the other without. The parameters entering the simulation are the trap oscillation frequencies, the atom numbers and the cut energy of the radio frequency knife. The initial temperature of the Fermi gas is adapted to obtain the measured temperature after thermalization. The expected difference in the initial slope is only 20% which is below the signal to noise ratio of the experiment. That is why this measurement gives no indication for Pauli blocking. But it can be interpreted as a measurement for the inter-isotope scattering cross section. The calculation is done with the value $41\,a_0$ from reference [153] and agrees well with the experimental data. The uncertainty in this value is certainly less than $\sqrt{2}$ corresponding to a change in the elastic scattering cross section by a factor 2. This would change the initial slope of the rethermalization curve by a factor 2, which is incompatible with the experimental data. For a degeneracy of $T/T_F = 0.25$, the difference in initial slope is also a factor 2, which should be observable (see section 1.1.4). But it will also be more difficult to do the measurement in these conditions, since the number of atoms will be lower, if the experimental setup is not improved. Even at the highest degeneracy reached in the higher hyperfine states, the thermalization time is with 300 ms still 3 times shorter than the time we allowed for thermalization in the experiment. All this proves that the assumption of thermal equilibrium is justified for all measurements.

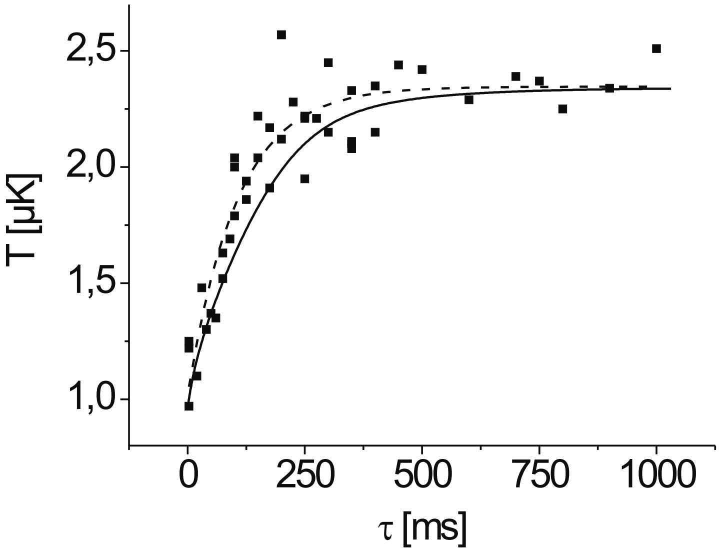

Figure 3.23: *Rethermalization of a bosonic cloud immersed in a Fermi sea at* $T/T_F = 0.5$. *The temperature of the bosonic cloud is plotted versus the rethermalization time. The theoretical predictions for thermalization with a classical gas (dashed) and with a degenerate Fermi gas (solid) are given.*

3.4 Experiments in the lower HF states

3.4.1 State transfer

As we have seen before (sections 1.2.2 and 3.3.4), the best achievable Fermi degeneracy in the higher hyperfine states is limited because the intrinsic instability of the condensate prevents any cooling below the critical temperature. To overcome this limitation we searched for a situation where the Bose gas has a positive scattering length $a > 0$. As discussed in section (2.2.2), only the ^{7}Li $|F = 2, m_F = 2\rangle$ and $|F = 1, m_F = -1\rangle$ states are immune to spin relaxation in a magnetic trap. And of those the $|F = 1, m_F = -1\rangle$ state has a small but positive scattering length of $a = 5.1\, a_0$. When using this state for the bosons, the fermions have to be in the $|F = 1/2, m_F = -1/2\rangle$ state to obtain a stable mixture at the densities of interest [153]. The disadvantages of the lower hyperfine states in comparison with the stretched states are their smaller magnetic moments, the limited trap depth (2.4 mK for ^{7}Li and 330 μK for ^{6}Li) and the small bosonic scattering length. For these reasons it is not possible to start evaporation in the lower hyperfine states. But after a precooling stage using evaporation in the stretched states, the atoms can be transferred to the lower states and evaporation cooling can be continued.

Thus, we searched for a method to transfer the atoms to the lower hyperfine states. To understand the transfer, take a look at the level scheme of the ground states of lithium figure (2.1). We start with both atoms in the stretched state ($|2, 2\rangle$ and $|3/2, 3/2\rangle$). It is then necessary to precool to at least 50 μK before executing the transfer to the lower states. This corresponds to $\eta = E_{cut}/k_B T = 4$ for ^{6}Li after the transfer. If less precooling is performed, the ^{6}Li atoms are lost without significant cooling effect. We choose radio frequency transitions to change the internal states. For ^{7}Li the transfer requires a three photon transition. For the first series of experiments presented in the following, resonant π pulses are used. Later on the method of adiabatic transfer is applied (see section 3.6.1). A first π pulse is applied on the hyperfine transition $|2, 2\rangle \rightarrow |1, 1\rangle$. Then a two photon π pulse on the Zeeman transition transfers the atoms to the $|1, -1\rangle$ state. The intermediate $|1, 1\rangle$ state is an untrapped state. The atom could gain energy or even be ejected from the trap if it stayed in this state for a significant fraction of the trap oscillation period. Fortunately these can be made very long by opening the trap adiabatically without loosing in phase-space density, giving more time for the π pulses. We open from $\omega_{ax} = 2\pi \times 75.0(1)\,\mathrm{s}^{-1}$ and $\omega_{rad} = 2\pi \times 4000(10)\,\mathrm{s}^{-1}$ to frequencies of $\omega_{ax} \approx 2\pi \times 5\,\mathrm{s}^{-1}$ and $\omega_{rad} = 2\pi \times 100\,\mathrm{s}^{-1}$. The adiabatic opening is done in two steps, each taking 500 ms. Two steps have been chosen, to slow down the opening at the end when the oscillation frequencies are already low. So the opening is always adiabatic. It has been verified that the process is adiabatic by recompressing with the same scheme and measuring the temperature. The adiabatic opening has two other beneficial effects. The temperature of the gas is decreased by a factor 40 from initially 10 μK to 0.25 μK. This reduces the energy spread of the resonance. Since the width of the transition is linked to the duration of the π pulse with $\Delta\nu = 2\pi/\Delta t$ resulting from the Fourier transform of the pulse, a smaller energy spread allows for longer pulses. For a π pulse the pulse area, the amplitude integrated over time, has to be conserved, thus a longer pulse time weakens the demands on the amplifier and antenna, thus simplifying the system. The second advantage is that the trap bottom becomes very stable, since the trapping coils are run at a current of 1 A (pinch coils) or 10 A (Ioffe bars) and the main contribution to the offset field comes from the very stable coils installed for this purpose. Transformers and other electronic equipment may produce a fluctuating magnetic field in phase with the line current which is oscillating with 50 Hz in Europe. To remove those fluctuations, the emission of the pulse sequence is synchronized to the phase of the power lines of the lab.

Transition	ν [MHz]	t [μs]
^{7}Li $\|2,2\rangle \rightarrow \|1,1\rangle$	806.335	17
^{7}Li $\|1,1\rangle \rightarrow \|1,-1\rangle$	0.951	12
^{6}Li $\|3/2,3/2\rangle \rightarrow \|1/2,1/2\rangle$	230.740	7
^{6}Li $\|1/2,1/2\rangle \rightarrow \|1/2,-1/2\rangle$	1.268	12

Table 3.4: *The pulse sequence used to transfer the atoms from the higher to the lower hyperfine state. A maximum delay of* 70 μs *with no radiation exists between pulses. The pulse power is adapted to achieve* π *pulses. If the pulse sequence is run backwards, atoms are transferred from the lower to the higher hyperfine states.*

The exact pulse sequence is shown in table (3.4). For optimization of the parameters of the pulses, it is essential to use a Stern-Gerlach separation of the internal states during a time-of-flight measurement. After the last radio frequency pulse, the trap is switched off and a field gradient in the vertical direction is switched on using a special Stern-Gerlach field coil (see section 2.7.3). The states with different magnetic moment are accelerated differently, resulting in a separation of these states after 0.7 ms time of flight. From these images, the reason of a badly working transfer is immediately apparent. If for example the frequency of the pulse is too high, the resonance condition is only fulfilled for atoms in the wings of the distribution. The images show that atoms are mainly transferred at the the outer rims of the cloud in the axial direction. If the duration of the pulse is not correct, not all atoms are transferred. If the energy spread of the cloud is too large, only the central part of the cloud is transferred.

The Rabi oscillation of the optimized transition using the Stern-Gerlach method is shown in figure (3.24). Graph a) shows the hyperfine transfer of ^{7}Li. The transfer efficiency is nearly 100%. Graph b) shows the Zeeman oscillation between the three $|F = 1, m_F = 1, 0, -1\rangle$ levels. One can see that the population is not first completely transferred to the $m_F = 0$ state and than to the $m_F = -1$ state. Instead at each moment the rotated spin 1 decomposes into a superposition of all three m_F states. On

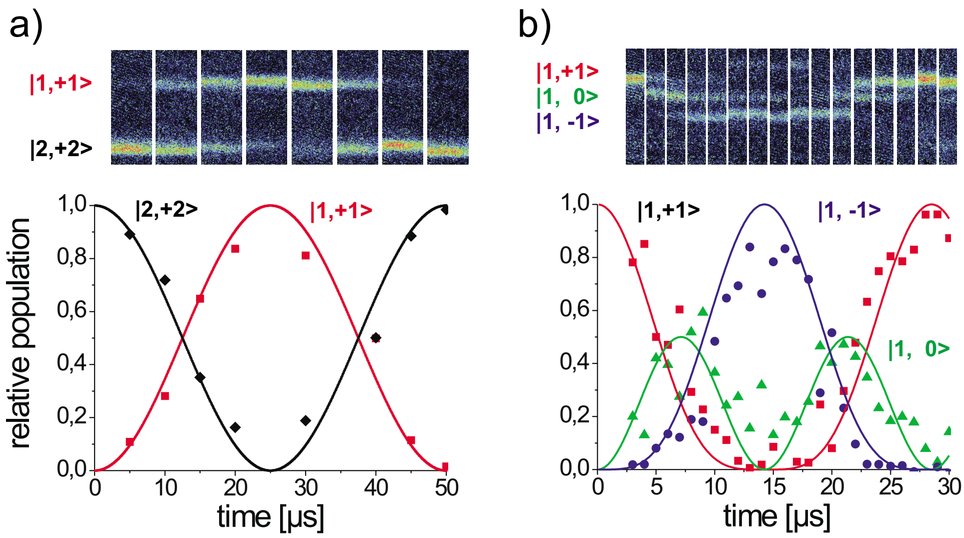

Figure 3.24: *Rabi oscillations. The population of different states is detected by using a magnetic field gradient during a free expansion. a) Rabi oscillation between the ^{7}Li $|F = 2, m_F = 2\rangle$ and the $|F = 1, m_F = 1\rangle$ states. b) Rabi oscillation between the ^{7}Li $|F = 1, m_F = -1, 0, 1\rangle$ states.*

the images one has the impression, that the total atom number has been reduced, when going to the $m_F = -1$ state, but since all atoms reappear after one Rabi oscillation, this can not be true. Presumably the absorption of the probe beam by atoms in different states is just different. In figure (3.25) the whole transfer process is shown. The total transfer efficiency depends on the initial temperature of the gas and is better than 75% for an initial temperature of $10\,\mu$K.

When changing to the lower hyperfine states, the magnetic moments of the atoms stay no longer $\mu = 1\,\mu_B$. They become $\mu = 1/2\,\mu_B$ for ^{7}Li and $\mu = 1/3\,\mu_B$ for ^{6}Li. This results in a nonadiabatic change of the trapping potential. It is possible to compensate for this for one isotope by increasing the confinement of the trap after the state transfer faster than the oscillation period. Doing this does not improve the conditions of the gas after the transfer, so we do not use this option anymore. After the transfer, the trap is recompressed adiabatically. This time, we compress to the steepest possible confinement resulting in trapping frequencies of $\omega_{rad} = 2\pi \times 4970(10)\,\mathrm{s}^{-1}$ and $\omega_{ax} = 2\pi \times 83(1)\,\mathrm{s}^{-1}$ for ^{7}Li $|1, -1\rangle$, compensating for the reduced magnetic moment.

Finally I would like to mention a nice trick which permits in everyday life a fast verification of the transfer process. Two images of the same isotope are taken after the same experimental run, the first without, the second with repumping laser present. If the atoms are in the higher hyperfine state, they show up on the first image. If they are in the lower state they are only visible after having been optically pumped to the

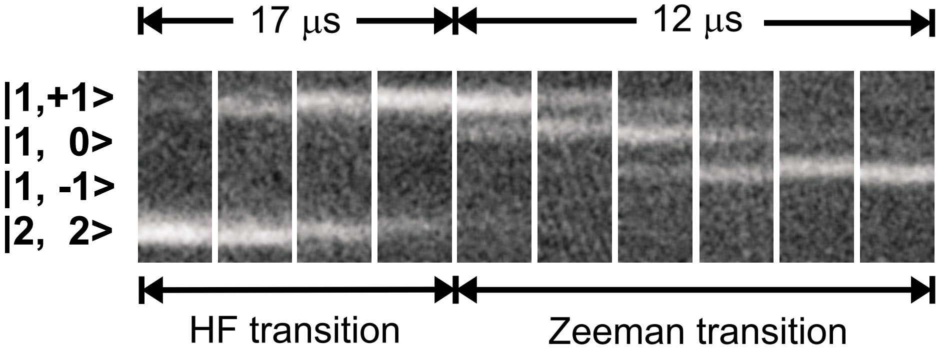

Figure 3.25: *Population of the ^{7}Li ground states during the transfer from the $|F = 2, m_F = 2\rangle$ to the $|F = 1, m_F = -1\rangle$ state. The states are separated by applying a magnetic field gradient during the free expansion. A first π pulse resonant with the hyperfine transition transfers the atoms to the $|F = 1, m_F = 1\rangle$ state. A second π pulse resonant with the Zeeman transition transfers the atom to the final state $|F = 1, m_F = -1\rangle$.*

higher state by the repumper and thus show up only on the second image.

3.4.2 Evaporative cooling of ^{7}Li

After optimization of the transfer to the lower hyperfine state for ^{7}Li we tried to produce a condensate by continuing the evaporation. Now the $|1, -1\rangle \rightarrow |2, -2\rangle$ transition is used for evaporation, resulting in a radio frequency ramp increasing from 795 MHz to 799 MHz for an offset field of 2 G (see figure 3.26). The ramp is optimized with the method described above (section 3.3.1) and the peak phase-space density of the resulting cloud depends clearly on the duration of the ramp. Thus collisions are present. But the optical density and collision rate always decrease during the evaporation, making it impossible to reach the transition temperature.

This is due to two facts. First the scattering length in the $|1, -1\rangle$ state is with $5.1\, a_0 = 0.27\,\mathrm{nm}$ very small. The cross section is decreased by a factor 27 in comparison with the higher hyperfine state and is over 400 times smaller than for ^{87}Rb. In addition the lifetime does not increase significantly when going to the lower hyperfine state. Initially we expected this. The lifetime in the higher state is limited by the dipolar loss rate. The dipolar loss rate depends on the density of energy states accessible after the loss process (Fermis golden rule). The density of states depends on the released energy, which is the hyperfine energy for the higher hyperfine state, but only the Zeeman energy for the lower state. Thus the dipolar loss rate should decrease if the coupling matrix element stays constant. Apparently this is not the case.

In the end, the ratio of good to bad collisions is slightly too small to permit the

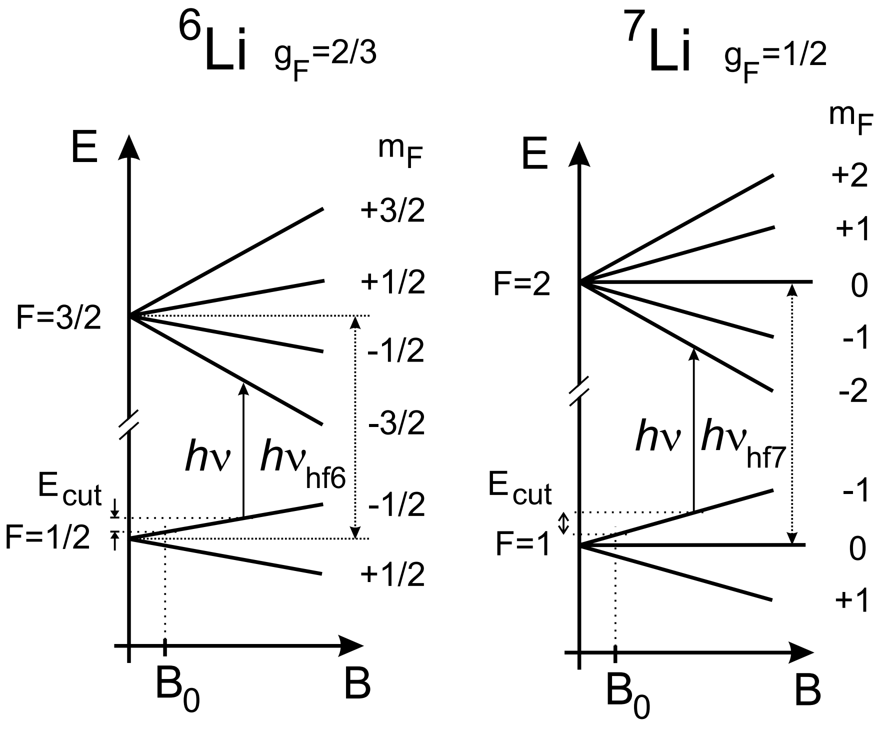

Figure 3.26: *Evaporation out of the lower hyperfine states of* ^{6}*Li and* ^{7}*Li. The cut energy increases with decreasing radio frequency.* B_0 *is the offset magnetic field of the trap and* $\nu_{hf6} = 228.205\,MHz$ *and* $\nu_{hf7} = 803.504\,MHz$ *the hyperfine splittings of the two isotopes.*

continuation of evaporative cooling.

3.4.3 Sympathetic cooling of ^{7}Li by ^{6}Li

The solution to this problem is to use the elastic scattering between the bosons and the fermions in the lower hyperfine states to rethermalize the gas during evaporative cooling. Indeed the ^{6}Li - ^{7}Li scattering cross section is nearly the same in the higher and lower hyperfine states ($\sigma_{67high} = 4\pi(41a_0)^2 = 6724\,\pi\,a_0^2$ and $\sigma_{67low} = 4\pi(38a_0)^2 = 5776\,\pi\,a_0^2$) and close to the ^{7}Li - ^{7}Li cross section in the higher state ($\sigma_{77high} = 8\pi(-27a_0)^2 = 5837\,\pi\,a_0^2$). How do we have to choose the isotope ratio to make optimum use of this situation? In the experiment the total number of atoms $N_B + N_F$ is more or less fixed. Between the fermions no s-wave collisions are possible and the collisions between the bosons are negligible. Thus the optimum ratio of $N_B : N_F$ for collisions is a $1:1$ ratio. It is adjusted by changing the initial isotope ratio in the TIMOT by changing the ^{6}Li loading time.

The optimum ratio has to be kept during the whole evaporation. One way to achieve this is with a dual evaporation ramp in parallel on both isotopes. The two ramps on the $|1/2,-1/2\rangle \rightarrow |3/2,-3/2\rangle$ transition for ^{6}Li and the $|1,-1\rangle \rightarrow |2,-2\rangle$ transition for ^{7}Li have to be balanced to maintain roughly equal numbers of both isotopes. After 10 s of evaporative cooling, Bose-Einstein condensation of ^{7}Li occurs together with a ^{6}Li degenerate Fermi gas. Surprisingly, a single 25 s ramp performed only on ^{6}Li achieves the same results (figure 3.27). In this case the equal number condition is fulfilled because of the reduced lifetime of the ^{7}Li cloud that we attribute to dipolar collisional loss [153]. The duration of the RF evaporation ramp is matched to this loss rate.

In the following we concentrate on this second evaporation scheme, sympathetic cooling of ^{7}Li by evaporative cooling of ^{6}Li. This cooling scheme is simpler for several reasons. First, there is no need to balance two ramps, which can be difficult. Next, since the bosons are cooled by the fermions, the bosonic temperature is never lower than the fermionic one. Thus a temperature measurement of the thermal bosonic cloud in the worst case leads to an underestimation of the quantum degeneracy of ^{6}Li. The last advantage I point out here is somewhat technical, but in the daily work with the experiment it is a very important point and concerns the fine tuning of the isotope ratio. The error signal for a too high or too low fraction of ^{6}Li is a completely missing bosonic or fermionic cloud at the end of the experimental sequence. If the fraction of ^{6}Li is too high, a breakdown of sympathetic cooling appears during the first cooling ramp in the higher hyperfine states, and no ^{7}Li is left. During the second ramp on ^{6}Li, no collisions are present and we are left either with a very dilute ^{6}Li cloud or no cloud at all. If too few ^{6}Li atoms have been present, the second ramp will not work and we are left with no ^{6}Li and a hot ^{7}Li cloud. These signals are simple to interpret and give a clear idea of the direction in which the isotope ratio has to be changed. But if a double ramp on both isotopes were used, an error as those described above could also have originated from a misbalance of the two evaporation ramps. Thus it is much less complicated to diagnose and optimize the isotope ratio with a single evaporation cut of the bosonic cloud. The regulation of the isotope ratio is something that has to be done continuously because of the insufficient stability of our lasers (which has been improved since the data presented here was taken).

Now we will discuss the outcome of the evaporation in the lower hyperfine states. In figure (3.27) *in situ* absorption images of bosons and fermions at the end of the evaporation are shown. The bosonic distribution shows the typical double structure: a strong and narrow peak forms the condensate at the center, surrounded by a much broader distribution, the thermal cloud. As the Fermi distribution is very insensitive to temperature, this thermal cloud is a very useful tool for the determination of the common temperature. To determine N_B, N_F, the condensate fraction N_0/N_B, and the temperature, the distributions are fitted appropriately (see section 1.1). From this and the measured trap frequencies $\bar{\omega}$, we determine the quantum degeneracy of the Bose and Fermi gases. In figure (3.27 top), the temperature is just below T_C, $T = 1.6\,\mu$K $=0.87\,T_C = 0.57\,T_F$. In figure (3.27 bottom) on the contrary, the condensate is quasi-

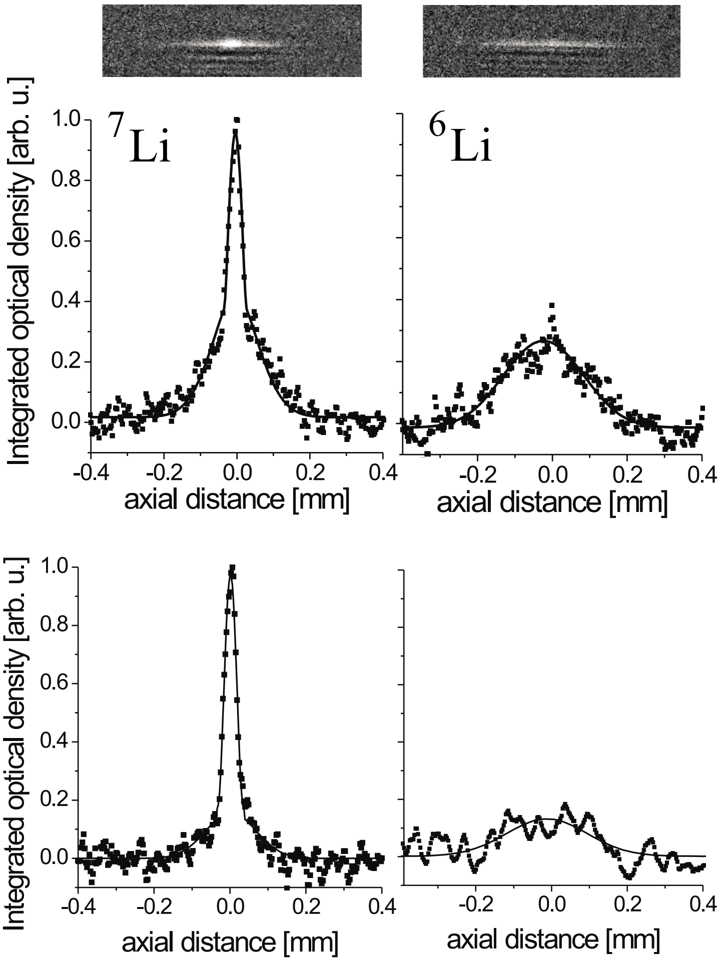

Figure 3.27: *Mixture of Bose and Fermi gases. Top: In situ spatial distributions after sympathetic cooling with* $N_{\mathrm{B}} = 3.5 \times 10^4$ *and* $N_{\mathrm{F}} = 2.5 \times 10^4$. *The Bose condensed peak (*8.5×10^3 *atoms) is surrounded by the thermal cloud which allows the determination of the common temperature.* $T = 1.6\mu K = 0.87\,T_{\mathrm{C}} = 0.57\,T_{\mathrm{F}}$. *The Fermi distribution is wider because of the smaller magnetic moment and Fermi pressure. Bottom: profiles with a quasi-pure condensate, with* $N_{\mathrm{B}} = 1.5 \times 10^4$, $N_{\mathrm{F}} = 4 \times 10^3$. *The barely detectable thermal cloud indicates a temperature of* $\simeq 0.28\,\mu K \simeq 0.2(1)\,T_{\mathrm{C}} = 0.2(1)\,T_{\mathrm{F}}$.

pure; $N_0/N_B = 0.77$; the thermal fraction is near our detection limit, indicating a temperature of $\approx 0.28\,\mu\mathrm{K} \leq 0.2(1)\,T_C = 0.2(1)\,T_F$ with $N = 8.2 \times 10^3$ bosons and 4×10^3 fermions. Note that the fermionic distribution is wider because of both, the smaller magnetic moment and the Fermi pressure. For degeneracies $T/T_F < 0.2$ no bosonic thermal cloud is visible. A more sensitive method to determine the temperature is needed to investigate this regime. This could be a thermalization measurement detecting the Pauli blocking as described in section (1.1.4).

3.4.4 A stable lithium condensate

In this section we discuss the properties of the condensate. The condensate fraction N_0/N as a function T/T_C is shown in figure (3.28). With the strong anisotropy ($\omega_{rad}/\omega_{ax} = 59$) of our trap, the theory including anisotropy and finite number effects differs significantly from the thermodynamic limit (see section 1.1.6), and is in good agreement with our measurements. T_C is determined by measuring the trap oscillation frequencies and the atom number. The error in the first quantity is below 1% but the atom number is known only to a factor 2 (see section 2.10.6). Since the atom number enters with the cubic root in $T_C \propto \bar{\omega} N^{1/3}$, T_C has a systematic uncertainty of about 20%. The uncertainty in the determination of the temperature from the spatial extension of the thermal cloud and the axial trap frequency is less. Since the critical temperature determined with our data is well in accordance with the theoretical prediction, the error in the determination of the atom number is possibly even less than the conservative estimation of a factor 2.

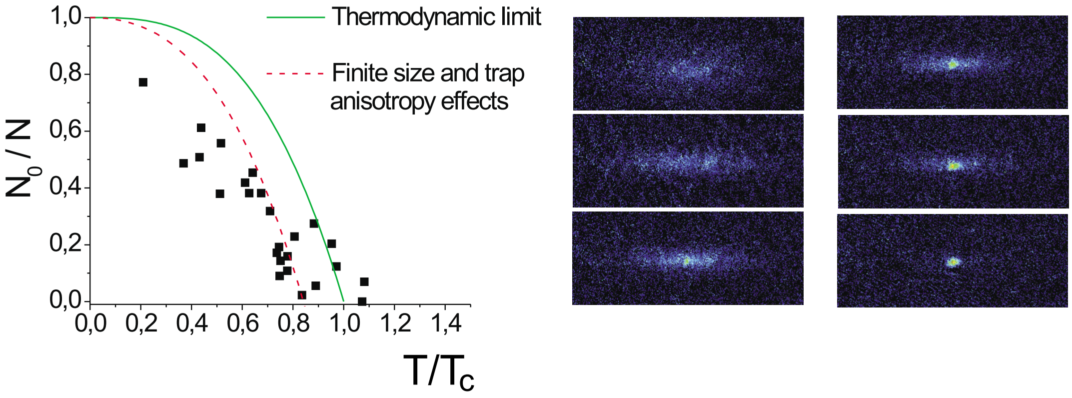

Figure 3.28: *Normalized BEC fraction as a function of T/T_C. Dashed line: theory in the thermodynamic limit. Solid line: theory including finite size and trap anisotropy [82].*

Because of the small scattering length, this ^{7}Li condensate has special properties. Figure (3.29) shows images of a condensate with 10^4 atoms after $0-10\,$ms expansion time after the release from a trap with frequencies $\omega_{rad} = 2\pi \times 1.4\,$kHz and $\omega_{ax} = 2\pi \times 37\,$Hz. These images reveal that the condensate is one-dimensional. Gaussian fits to the radial distribution agree to better than 5% with the time development of the radial ground state wavefunction in the harmonic magnetic trap. The wavefunction

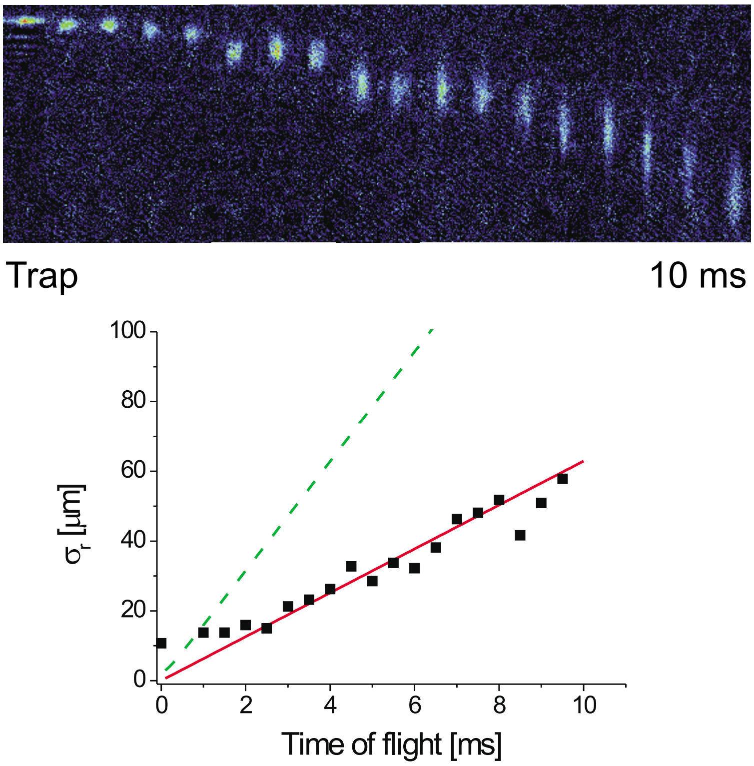

Figure 3.29: *Signature of 1D condensate. Radial size of expanding condensates with* 10^4 *atoms as a function of time of flight. For short times, the size is given by the resolution of our imaging system. The straight line is the expected behavior for the expansion of the ground state radial harmonic oscillator (3.3). The dashed line shows the theoretical prediction using the Thomas-Fermi approximation after formula (1.41). The trap oscillation frequencies for the initial trap are* $\omega_{rad} = 2\pi \times 1.4\,kHz$ *and* $\omega_{ax} = 2\pi \times 37\,Hz$*.*

stays gaussian during the expansion and its RMS size changes as

$$\sigma_{rad}(t) = \sqrt{\frac{\hbar}{2m\omega_{rad}} + \frac{\hbar\omega_{rad}}{2m}t^2}\,. \tag{3.3}$$

This is in contrast to the expansion of a typical condensate in the Thomas-Fermi regime, where the release of interaction energy leads to a faster increase in radial size (formula 1.41). The condensate is one dimensional, when its radial wavefunction is well approximated by the radial one-particle harmonic oscillator wavefunction. This is the case when the chemical potential μ_{1D} is not sufficient to populate excited states, $\mu_{1D} \ll \hbar\omega_{rad}$ [89]. The axial wavefunction of our condensate can still be described with the Thomas-Fermi profile. To verify the validity of these approximations, we minimize in section (1.1.10) the energy of an ansatz for the wavefunction with gaussian profile in the radial and TF shape in the axial direction, parametrized by the RMS size of the gaussian and the Thomas-Fermi radius. We find that the mean field interaction increases the size of the Gaussian by ≈ 3% for our parameters (formula (1.46)). The calculated TF radius in the axial direction (formula (1.47)) is 28 μm or 7 times the axial harmonic oscillator size and is in good agreement with the measured radius, 30 μm in figure (3.27). Also the relation $\mu_{1D} = 0.45\,\hbar\omega_{rad}$ for our parameters shows, that we are in the 1D regime. This 1D regime was also realized about the same time in sodium condensates, by going to low atom number and extreme aspect ratios [31]. Since μ_{1D} is proportional to $a^{2/3}$, the 1D regime is much easier to reach with ^{7}Li (small a) than with Na or ^{87}Rb which have much larger scattering length.

3.4.5 The Fermi sea

In figure (3.27 bottom) the degeneracy factor is $T/T_F = 0.2(1)$, which is the best degeneracy we could measure. The size of the Fermi gas as a function of T/T_F is shown in figure (3.30) in analogy with figure (3.22b) for the higher hyperfine states. Again the data points show a saturation of the size for high degeneracies due to the Fermi pressure. Data and theory are again slightly offset.

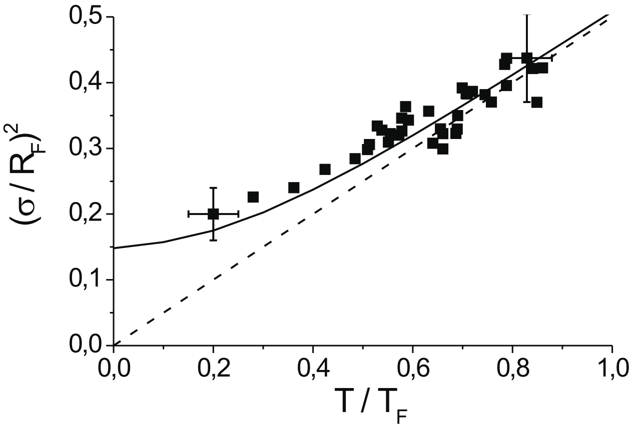

Figure 3.30: *Fermion cloud size: variance of gaussian fit divided by the square of the Fermi radius* $R_F^2 = 2k_B T_F / M\omega_{ax}^2$ *as a function of* T/T_F*. Solid line: theory as explained in section (1.1.2). Dashed line: Boltzmann gas.*

The limit in the degeneracy is not imposed by a limit in the cooling mechanism, but due to the limitation of the temperature measurement method. Each of the limits discussed in section (1.2.2) slow down the cooling process at much higher degeneracies.

Although the fermionic distribution is predicted to be slightly modified by the bosonic mean field, no phase separation between the condensate and the Fermi sea has been detected as expected (see section 1.1.13). The sound velocity of our pure condensate is $\approx 0.9\,\mathrm{cm/s}$, corresponding to a temperature of 100 nK, a factor of 10 below our typical Fermi temperature of $\approx 1\,\mu\mathrm{K}$.

3.5 Loss rates

The loss rate often determines the failure or success of evaporative cooling. We have measured loss rates for ^{6}Li and ^{7}Li for each of the trapped states for mixtures and for pure gases under various conditions of temperature and density. The background gas limited lifetime was measured after Doppler cooling to increase the ratio between trap depth and temperature. An open trap ($\omega_{ax} = 2\pi \times 73\,\mathrm{Hz}$ and $\omega_{rad} = 2\pi \times 200\,\mathrm{Hz}$ with an offset magnetic field of 480 G) is used to reduce density and thus two and three-body collisions. The lifetime was found to be between 50 s and 140 s, depending on the vacuum quality (see figure 3.12). All the sympathetic cooling experiments have been done with a background gas limited lifetime of about 70 s.

A further measurement compares the lifetimes and heating rates of ^{6}Li and ^{7}Li under the conditions of sympathetic cooling in the higher hyperfine states and is shown in figure (3.31). The decay of 10^5 fermions at $3.7\,\mu$K with a peak density of $6 \times 10^{12}\,\mathrm{cm}^{-3}$ is well described by an exponential decay on a timescale of $50\,s$. No heating could be observed with a measurement uncertainty less than $\sim 50\,\mathrm{nK/s}$. This is due to the lack of collisions for a polarized fermionic gas. This measurement proves also, that the heating due to fluctuations in the potential is very weak.

Under the same conditions as the ^{6}Li measurement, the decay of 3.3×10^5 bosons at a temperature of $11.7\,\mu$K and a density of $3.7 \times 10^{12}\,\mathrm{cm}^{-3}$ is measured. A heating rate of 110 nK/s is detected. If the decay is interpreted as an exponential decay, the lifetime is only 25 s, much shorter than the background gas limited lifetime. This and the heating can be explained by the existence of dipolar loss described by the decay rate constant β defined by the differential equation

$$\dot{N}(t) = -\frac{\beta n_0}{\sqrt{2}N(0)}(N(t))^2 - \Gamma N(t)\,. \tag{3.4}$$

This equation has the solution

$$N(t) = \frac{\Gamma N(0)}{(\Gamma + bN(0))\exp(\Gamma t) - bN(0)}\,, \tag{3.5}$$

with $b = \beta n_0/(\sqrt{2}N(0))$, where n_0 is the peak density at $t = 0$. By fitting the data with this equation we find a rate constant of $\beta = 1.6(5) \times 10^{-14}\mathrm{cm}^3\mathrm{s}^{-1}$ when as background gas limited lifetime $1/\Gamma = 50\,\mathrm{s}$ is chosen, as measured with the fermions. This measurement is in accordance with the theoretical prediction of $1.6 \times 10^{-14}\,\mathrm{cm}^3\mathrm{s}^{-1}$ [189] and measurements in high magnetic fields [190].

We searched for interspecies losses by recording the ^{6}Li trap lifetime in the presence and absence of ^{7}Li atoms at a peak density $n_0(^7\mathrm{Li}) = 2 \times 10^{11}\,\mathrm{at/cm}^3$ and a common temperature of $530\,\mu$K. With $n_0(^7\mathrm{Li}) = 4.6\,n_0(^6\mathrm{Li})$, the lifetimes are respectively 73(10) s and 73(8) s, showing no significant difference. We deduce an upper limit for dipolar decay rates $\beta_{6-7} \leq 10^{-13}\,\mathrm{cm}^3\mathrm{s}^{-1}$ and $\beta_{6-6} \leq 4.6 \times 10^{-13}\,\mathrm{cm}^3\mathrm{s}^{-1}$.

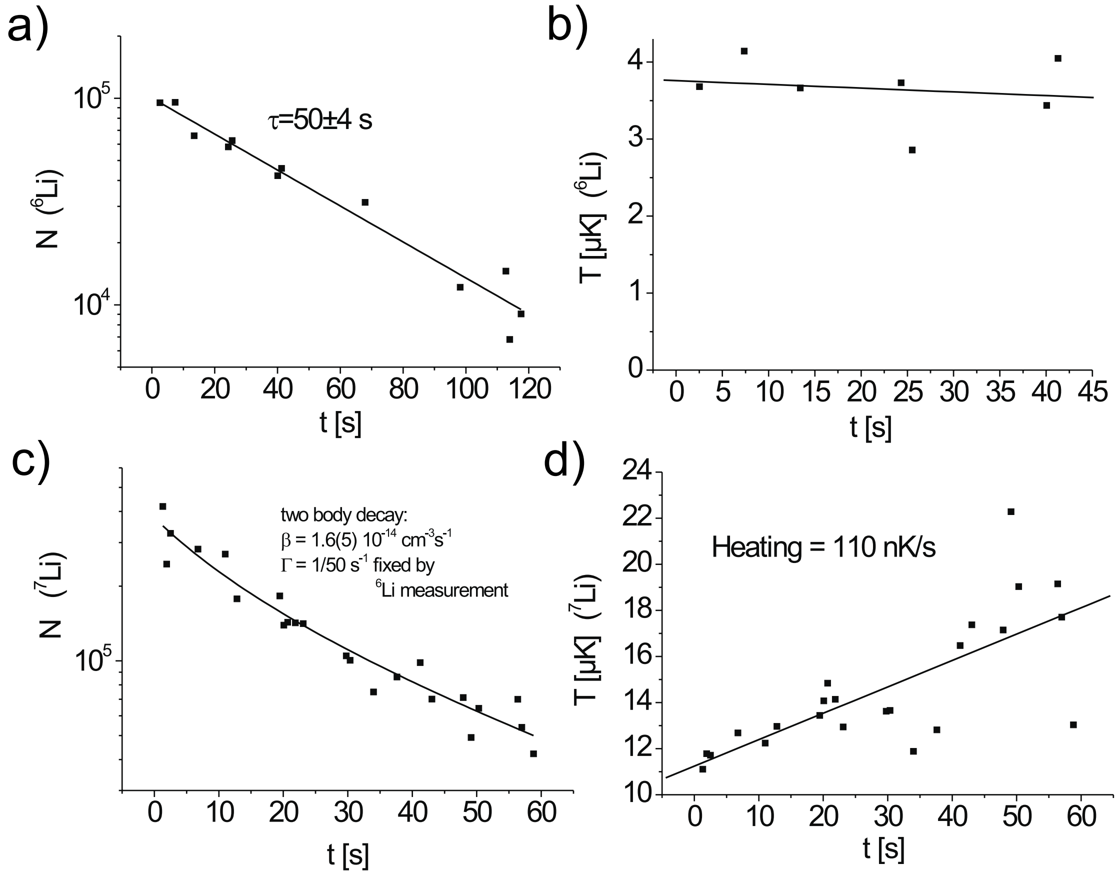

Figure 3.31: *Atom number and temperature of* $^6Li\ |F = 3/2, m_F = 3/2\rangle$ *(a,b) and* $^7Li\ |F = 2, m_F = 2\rangle$ *(c,d) as a function of the storage time in the magnetic trap. The parameters at* $t = 0$ *are:* ^6Li*: atom number* $N_6 = 10^5$*, temperature* $T = 3.7\,\mu K$*, peak density* $n_0 = 5.9 \times 10^{12}\ cm^{-3}$*, Fermi temperature* $T_F = 4.8\,\mu K$*;* ^7Li*:* $N_7 = 3.3 \times 10^5$*,* $T = 11.7\,\mu K$*,* $n_0 = 3.7 \times 10^{12}\ cm^{-3}$*, critical temperature* $T_C = 3.6\,\mu K$*. The lifetime of* ^6Li *is exponential with a decay constant of* $\tau = 50(4)\ s$*. The heating rate is below the measurement uncertainty of less than* $\sim 50\,nK/s$*. The loss of* ^7Li *can be better approximated by including two-body losses. By fixing the background gas limited lifetime to* $50\,s$*, the value measured for* ^6Li*, the two-body decay rate* $\beta = 1.6(5) \times 10^{-14}\ cm^{-3}s^{-1}$ *is obtained. The heating rate is* $110 \pm 20\,nK/s$*.*

We performed a lifetime measurement for the ^{7}Li $|1, -1\rangle$ state which is shown in figure (3.32). An exponential fit to the data gives a lifetime of 20 s, which is too short to be explained by background gas collisions. Fitting with formula (3.5), gives a dipolar decay rate constant of $\beta = (3.8 \pm 1.6) \times 10^{-14}\mathrm{s}^{-1}$, when fixing the background gas limited lifetime at 50 s.

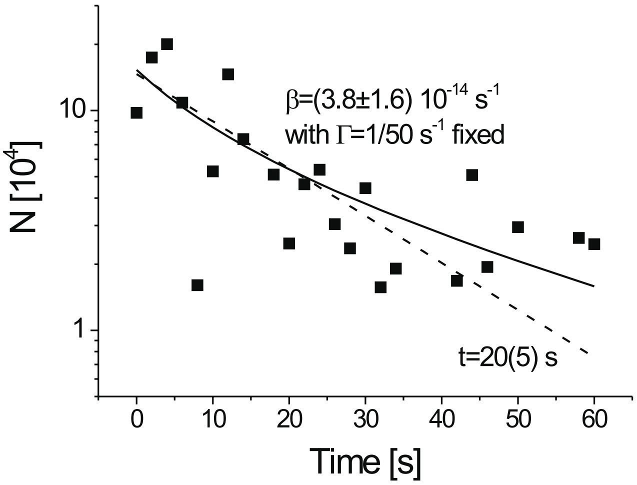

Figure 3.32: *Lifetime of* ^7Li $|F=1, m_F=-1\rangle$ *in a trap with frequencies* $\omega_{ax} = 2\pi \times 84\,s^{-1}$ *and* $\omega_{rad} = 2\pi \times 4970\,s^{-1}$*. The initial density is* $n_0 = 2 \times 10^{12} cm^{-3}$*. An exponential fit (dashed) gives a lifetime of* 20(5) *s, which can not be explained by background gas collisions. Fixing the background gas collisions to the independently measured* $50\,s^{-1}$*, the dipolar decay rate constant is* $\beta = (3.8 \pm 1.6) \times 10^{-14} cm^3 s^{-1}$ *(solid line).*

The decay of ^{6}Li in the $|1/2, -1/2\rangle$ state was not measured, but is longer than that of ^{7}Li under the same conditions, which can be seen by the fact, that ^{6}Li has to be evaporated to compensate the dipolar loss of ^{7}Li to keep the equal number condition during the second cooling ramp.

The lifetime of the condensate was not measured precisely, but we could observe condensates after a ~ 1 s storage time after the radio frequency knife was switched off. Thus the lifetime should be at least of this order of magnitude.

3.6 Experiments with the optical trap

During the time I was mainly writing this thesis, the work on the experiment did not stop. The other members of our group, Thomas Bourdel, Julien Cubizolles, Lev Khaykovich and Gabriele Ferrari who was visiting during three months, pursued new experiments. A first optical trap, with only one, horizontal beam had already been installed. The confinement in the axial direction is weak ($\omega_{ax} \sim 2\pi \times 20\,\mathrm{Hz}$), and is weaker than the magnetic trap which can confine with up to 130 Hz. A vertical dipole trap was added to increase the confinement in this direction and to make evaporative cooling in the dipole trap easier. In the following I will describe the results obtained with this dipole trap. First, a more reliable method of state transfer, an adiabatic passage, was implemented. Next the Feshbach resonance in the ^{7}Li $|1,1\rangle$ state was detected and then exploited to produce a condensate. Due to the Feshbach resonance the condensate has a tunable scattering length. It was possible to produce a bright soliton by using a negative scattering length and removing the confinement in the axial direction.

3.6.1 Adiabatic transfer

In the magnetic trap, radio frequency π pulses were used to transfer the atoms between different hyperfine states (see section 3.4.1). For a two-level system of a ground state $|g\rangle$ and an excited state $|e\rangle$, the states are coupled by the radio frequency pulse with the matrix element $\hbar\Omega_R/2$, where Ω_R is the Rabi frequency. During the pulse with duration τ, the ground state evolves into a superposition state $t|g\rangle + r|e\rangle$ with $t = \cos(\Omega_R\tau/2)$ and $r = \sin(\Omega_R\tau/2)$. For $\Omega_R\tau/2 = \pi$ the population is transferred to state $|e\rangle$. This method has the advantage of being very fast ($\sim 20\,\mu$s), much faster than the oscillation period of the trap of 10 ms. Thus the atoms can easily pass through untrapped states. The drawback is that the transfer depends crucially on the detuning of the radio frequency from the atomic transition. And this in turn depends on the value of the magnetic field, which depends on the position of the atoms in the magnetic trap and which may fluctuate in time.

A more reliable way to transfer the atoms is an adiabatic passage between the energy states by sweeping the radio frequency over the resonance (see figure 3.33). For a sweep with constant rate $d\omega_{rf}/dt$, the population is distributed to the two states with $|r|^2 = 1 - e^{-2\pi\Gamma}$ and $|t|^2 = e^{-2\pi\Gamma}$, with the Landau-Zener parameter $\Gamma = \Omega_R^2(4d\omega_{rf}/dt)^{-1}$ [16, 191]. All atoms will be transferred as long as the sweep is slow enough and as long as the transition frequency is well within the frequency sweep. Thus, fluctuations in the offset magnetic field are less important. Incoherent processes, mainly collisions, can hinder the adiabatic passage. For this reason, the adiabatic passage is experimentally done in a rather weak trap to reduce density. The parameters used in the experiment for the adiabatic transfer in the optical trap are a 10 ms sweep over an 1 MHz interval across the transition.

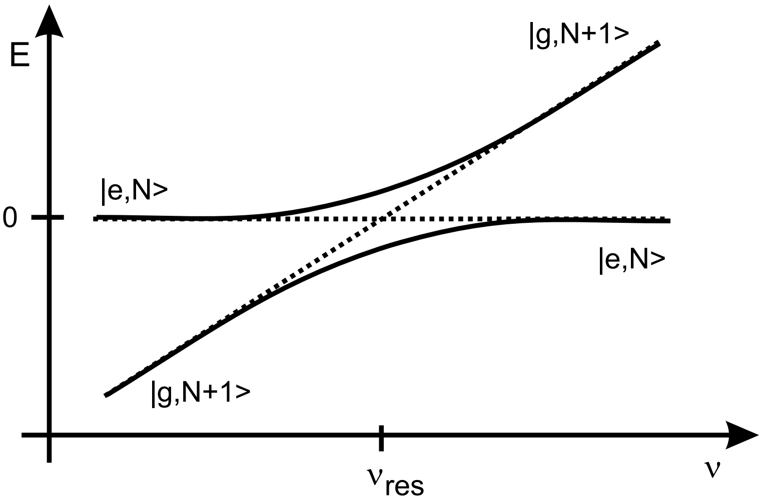

Figure 3.33: *Dressed atom picture of the energy states versus the radio frequency. Represented are the ground state in presence of N+1 photons* $|g, N+1\rangle$ *and the excited state in presence of N photons* $|e, N\rangle$. *The energy difference of these states and the* $|e, N\rangle$ *state is plotted around the transition frequency (dashed lines). For an adiabatic sweep of the radio frequency the crossing of the energy levels is avoided and the* $|g, N+1\rangle$ *state is transferred to the* $|e, N\rangle$ *state.*

3.6.2 Detection of the ^{7}Li $|F = 1, m_F = 1\rangle$ Feshbach resonance

The first goal when working with atoms in the optical trap was to detect the Feshbach resonance in the ^{7}Li $|F = 1, m_F = 1\rangle$ state (see section 1.3.3). For this, a sample of ^{7}Li atoms is evaporatively cooled in the magnetic trap down to a temperature of $10\,\mu$K. Next the intensity of the crossed dipole trap is increased from 0 W to $\sim$ 1 W per beam by a linear 200 ms ramp. In the next 200 ms, the magnetic trap is ramped off. Only a bias magnetic field of 7.5 G is left on. Now the adiabatic passage from the $|F = 2, m_F = 2\rangle$ to the $|F = 1, m_F = 1\rangle$ state follows, using a radio frequency sweep from 819 MHz to 820 MHz and a duration of 10 ms. This transfer has an efficiency of $\sim$ 95%. Afterwards the optical trap is ramped to its full power of $\sim$ 3 W per beam. The next step is the increase of the offset field to the desired value using the pinch coils as described in section (2.7.3). The pinch coils produce a magnetic field with curvature in the axial direction. For atoms in the $|F = 2, m_F = 2\rangle$ state, this curvature produces an additional axial trapping potential. For atoms in the strong field seeking $|F = 1, m_F = 1\rangle$ state, the potential is “anti-trapping”, it reduces the axial confinement coming from the dipole trap. The magnetic field spread experienced by the atoms across the cloud is about 10 mG. This is small in comparison with the width of the Feshbach resonance, so that all atoms obtain the same scattering length.

The first signal of the Feshbach resonance was an enhanced loss of atoms in the vicinity of a specific magnetic field. Since the $|F = 1, m_F = 1\rangle$ is the absolute ground state, two-body relaxation can be excluded as loss mechanism. Three body recombination is the dominating loss process. The result is shown in figure (3.34). A sample of atoms is prepared in the optical trap and left 200 ms at constant magnetic offset field. The number of remaining atoms is recorded. The loss depends strongly on the magnetic field value. In the range between 700 G and 725 G the lifetime is so short, that no atoms can be detected after the experimental sequence. For values of the magnetic field above the Feshbach resonance, the number of atoms never regains its value below the resonance. This is due to the loss during the passage through the resonance when ramping to the final field value. The value of the magnetic field up to 90 G is measured by searching for the frequency of the $|F = 1, m_F = 1\rangle \rightarrow |F = 2, m_F = 2\rangle$ transition for different currents in the pinch coils. Then the result is extrapolated to higher fields. The resonance lays within our measurement uncertainty (~ 20 G) on the theoretically predicted resonance at 745 G (see figure 1.16).

3.6.3 Condensation in the ^{7}Li $|F = 1, m_F = 1\rangle$ state

Now the question arises if it would be possible to use the elastic collisions near the Feshbach resonance to perform evaporative cooling in the dipole trap and produce a condensate in the $|F = 1, m_F = 1\rangle$ state. Two problems arise. In the dipole trap all internal states are trapped. Thus it is not possible to selectively remove atoms by using radio frequency transitions to untrapped states as in the case of a magnetic trap. One method for performing evaporative cooling is to reduce instead the potential depth, in order to remove energetic atoms over the potential barrier of the dipole trap. But this results in a decrease in the confinement, reducing the density and thus the elastic collision rate. This loss has to be compensated by an efficient evaporation, meaning a good ratio of elastic to inelastic collisions.

The second problem is that loss through three-body collisions increases strongly near the resonance. In a simple approximation the three-body recombination rate scales with the elastic scattering cross section squared [150]. In order to make the evaporation work, a compromise between the elastic and the inelastic collision rate has to be found by choosing the right value of the magnetic field. It is not *a priori* clear that a regime exists in which evaporation will work.

To find this out, an offset field of 665 G is applied for which a reasonable scattering length of about $40\,a_0$ is theoretically predicted and the measured lifetime is about 1 s. The intensity of the horizontal dipole trap beam is lowered in two consecutive linear ramps. In this case, the evaporation is caused mainly by atoms falling out of the trap along the weak direction of the vertical beam. The potential barrier here is

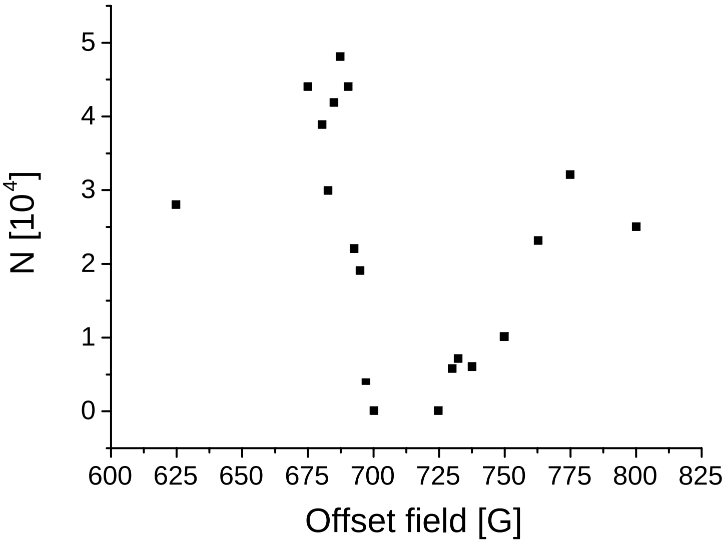

Figure 3.34: *Loss of atoms near the* ^7Li $|F = 1, m_F = 1\rangle$ *Feshbach resonance.* 5×10^5 *atoms are kept during* 200 *ms at a magnetic field value near the Feshbach resonance. Three body collisions reduce the number of atoms. The magnetic field is reduced in* 50 *ms and the atom number recorded. The atom numbers at the right hand side of the resonance are systematically smaller, since the sample passed through the magnetic field region of the resonance, when ramping on and off the magnetic field.*

lowered because of gravity. In addition this method only slightly changes the horizontal confinement, which is determined mainly by the unchanged vertical beam. Because of this it is possible to extract the change in temperature from the axial size of the trapped cloud. The duration and the final intensity of the evaporation ramps are optimized on the increase in phase-space density, determined by measuring the number of atoms and the size of the cloud in horizontal direction. After some optimization the typical double structure of the thermal cloud with condensate is detected (see figure 3.35).

The evaporation ramp is afterwards further optimized by changing also the intensity of the vertical beam and the offset magnetic field. As expected, the timescale for successful evaporation becomes shorter when approaching the Feshbach resonance because of the increasing collision rate. It turns out, that the atom number of the resulting condensate is more stable for short evaporation times, probably due to the feedback on the atom number, that three-body recombination provides. If the initial number is higher than usual, the density becomes higher during the evaporation and more atoms are lost because of three-body recombination. If the number is smaller, less losses take place. The atom number at the end of the evaporation fluctuates less

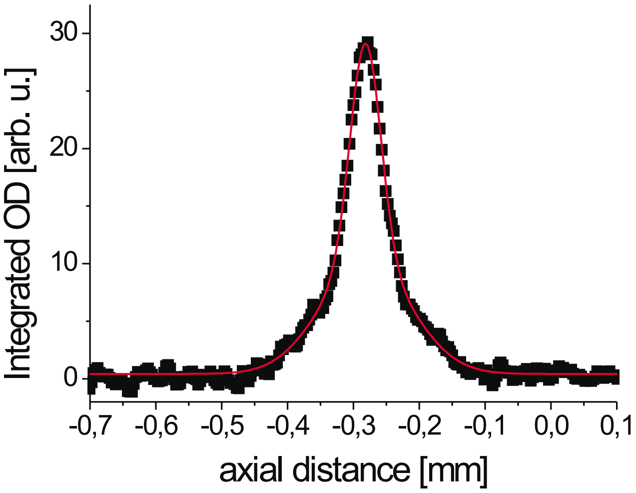

Figure 3.35: *Integrated density profile of a condensate produced by evaporation in the optical trap. The double structure of the condensate and the thermal cloud is clearly visible.*

than at the beginning. This is the reason, why for the following experiments a short evaporation ramp was chosen. The optimized ramp consists of two consecutive linear ramps of the power of both beams. After the creation of the condensate, the scattering length is adapted as necessary by changing the offset field and then further experiments are done with the sample prepared in this way.

In the following I will summarize the typical operation conditions. First a sample of 5×10^5 ^{7}Li atoms at $10\,\mu$K is prepared by evaporation in the magnetic trap. After transfer to the optical trap and change of the internal state to the $|F = 1, m_F = 1\rangle$ state, an offset field of 665 G is applied. The initial Nd:YAG intensities are lowered during 100 ms in a linear ramp to 20% (35%) of the initial value for the horizontal (vertical) beam. A second ramp is executed during 150 ms, lowering the intensities to 4% (8%) of their initial values. This procedure results reliably in the production of a condensate with 2×10^4 atoms. The lifetime of the condensate under these conditions is a few 10 ms. This time is sufficient to reduce the offset field which lowers the scattering rate and results in a longer lifetime.

We observe that the $|F = 2, m_F = 2\rangle$ atoms left over from the not 100% efficient adiabatic transfer, thermalize with the $|F = 1, m_F = 1\rangle$ atoms and are sympathetically cooled by them. This is possible because the $|F = 2, m_F = 2\rangle$, $|F = 1, m_F = 1\rangle$ mixture is stable against spin relaxation. The ratio of $F = 2$ to $F = 1$ atoms increased during the evaporation, which means that the $F = 2$ atoms are not as effectively removed as the $F = 1$ atoms. This is probably due to the magnetic potential coming from the pinch coils, which is confining for the $F = 2$ atoms and reduces the axial confinement for the $F = 1$ atoms. We did not look for a condensate in the $F = 2$ state yet. Since the scattering length between the $F = 2$ atoms is $-27\,a_0$ only a limited number of atoms is permitted in the $F = 2$ condensate. Since the final oscillation frequencies in the optical trap are lower than in the magnetic trap used for evaporation, the critical number of atoms is higher and the condensate might be observable.

Since the $F = 2$ atoms are an unnecessary thermal load for the cooling of the $F = 1$ atoms, we remove as many of them as possible after the adiabatic passage. To do this, a magnetic field gradient produced by the compensation coils is ramped on and off in the 0.5 s following the adiabatic passage. The atoms experience a potential consisting of the optical potential and a linear magnetic potential. The resulting trap has a reduced depth in comparison with the optical trap alone. The reduction in trap depth depends on the slope of the magnetic potential which depends on the magnetic moment of the atom. The magnetic moment is twice as high for the $m_F = 2$ atoms than for the $m_F = 1$ atoms. Thus the trap depth is reduced more for the $F = 2$ atoms than for the $F = 1$ atoms. In reducing the trap depth for the $m_F = 2$ atoms to zero, these atoms can be removed while keeping nearly all $m_F = 1$ atoms.

3.6.4 A condensate with tunable scattering length

One of the special properties of the condensate produced in this manner, is that the scattering length can be easily tuned. For this, the value of the offset field is changed right after the end of the intensity sweeps. Again, an exponential current ramp $I(t) = I_{init} + (I_{final} - I_{init})(1 - \exp(-t/\tau))/(1 - \exp(-\eta))$ for $t = 0...\eta\tau$ is used to avoid oscillations of the current as a reaction of the stabilization electronics of the power supply to fast changes of the programmed current. The lifetime of the condensate for different offset fields can be measured, giving the inelastic collision rate. The elastic collision rate can possibly be determined by measuring the release of mean field energy during a time-of-flight expansion. It is important that the offset magnetic field is applied during the whole time of flight, since the scattering length should not be changed while the mean field energy is being released.

3.6.5 The bright soliton

For magnetic field values between 150 G and 510 G the scattering length in the $|F = 1, m_F = 1\rangle$ state is negative and as low as $-4.4\,a_0$. This is used to produce a bright soliton (section 1.1.11 and figure 3.36). The offset field is tuned between 100 G and 600 G. After switch-off of the vertical dipole trap beam, the $F = 1$ atoms are confined in the radial directions by the horizontal dipole trap beam. In the axial direction, they experience a repulsive harmonic potential, resulting from the superposition of the weak confining potential of the dipole trap and the “anti-trapping” potential from the pinch coils used to produce the offset magnetic field. We observe the change in position and size of the atomic cloud under these conditions. For zero scattering length, the cloud behaves as an ideal gas, expanding due to the curvature of the potential (see figure 3.37). As the scattering length is made negative, the expansion rate decreases due to the attractive mean field. For scattering length below $a =\sim -3\,a_0$, the cloud does not change its size while it is sliding in the radial potential given by the horizontal dipole trap beam (figure 3.36). This is the signature for a bright soliton. Further information on this experiment and a theoretical model describing the region of stability of the soliton can be found in [192].

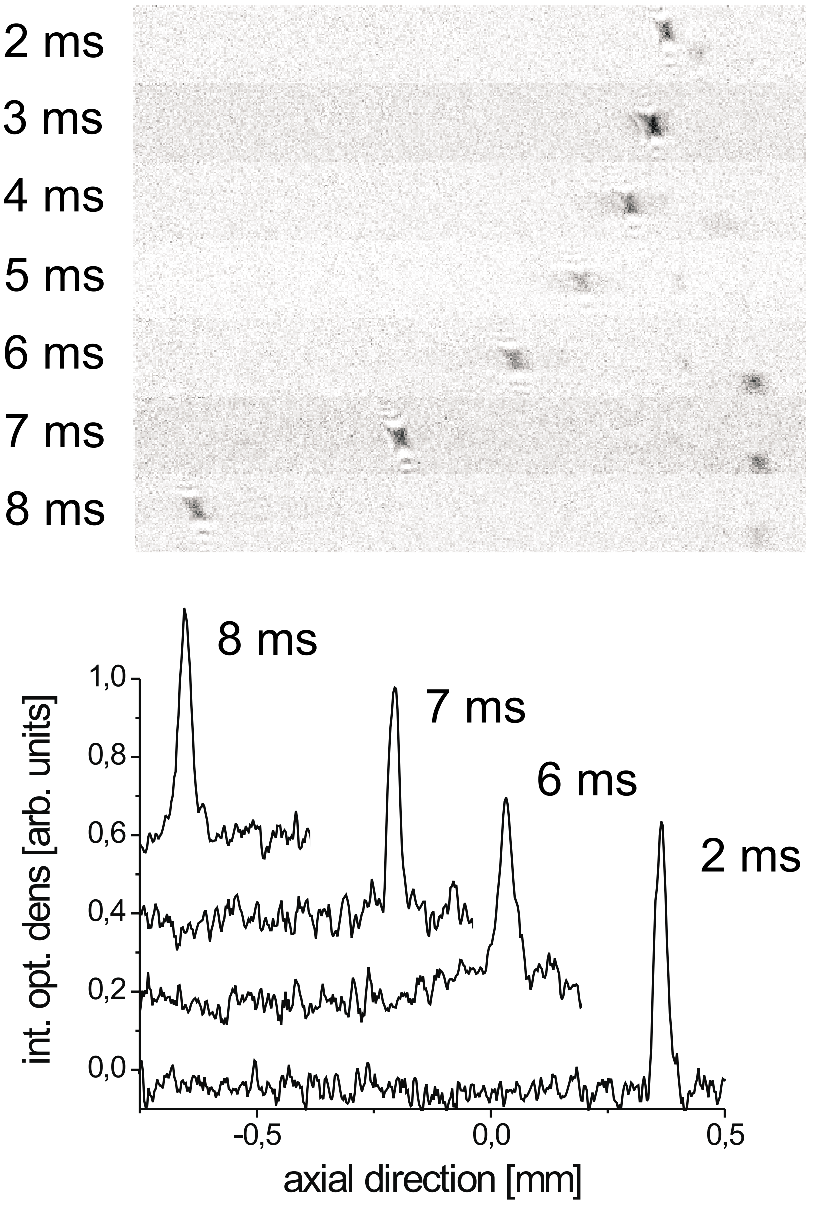

Figure 3.36: *A soliton travelling in the horizontal optical trap. Shown are absorption images of the soliton and axial profiles of the integrated optical density. The soliton travels to the left, driven by the curvature of the magnetic field provided by the pinch coils. The scattering length has been tuned to* $-4\,a_0$*, producing an attractive meanfield which holds the soliton together. The size does not change during the time of flight. The cloud of atoms visible at the right hand side around* 7 *ms are atoms in the* $F = 2$ *state which stay confined in the axial direction by the pinch coils and in the radial direction by the horizontal dipole trap beam. Due to the non-adiabatic switch-off of the vertical dipole trap beam, they oscillate with a frequency of* 65 *Hz. Their oscillatory movement brings them in and out of the focal plane of the imaging system. This is perhaps one reason, why they are not visible before* 6 *ms.*

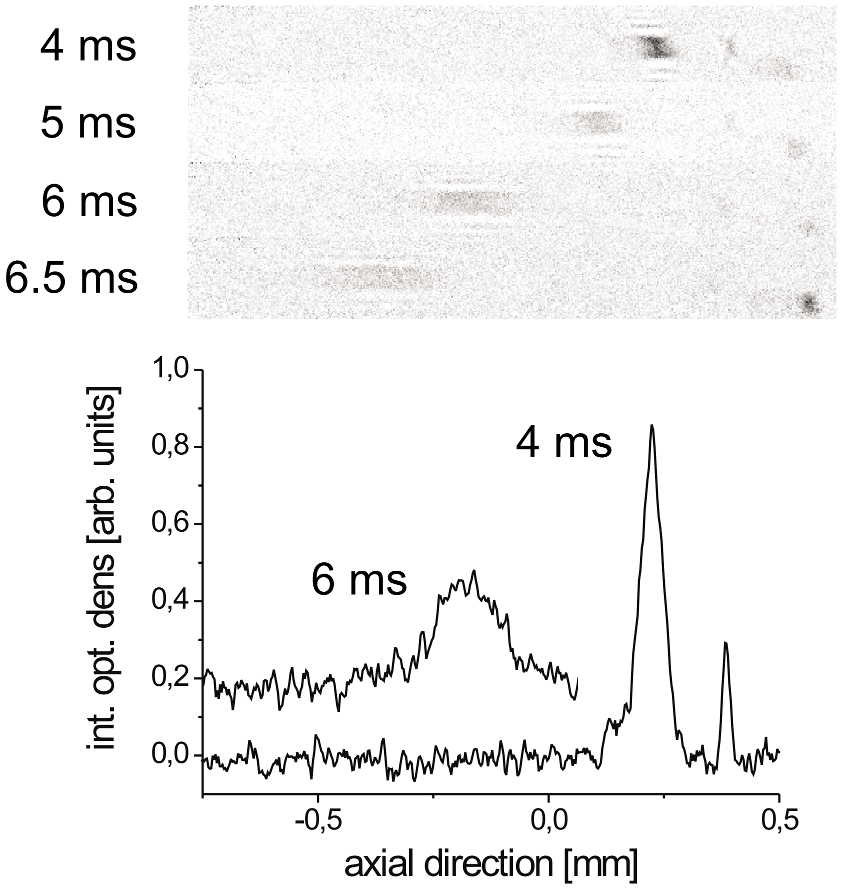

Figure 3.37: *The same experiment as shown in figure (3.36) but performed for a scattering length* $a \sim 0$*. The cloud expands due to the curvature of the magnetic field.*

Conclusion and outlook

During the last four years, we have planned and constructed a machine, capable of producing degenerate gases of fermionic and bosonic lithium. During the construction, we encountered various challenges and solved them in original ways. Some of them, for example the construction of the strongly confining magnetic trap and the laser system for a two isotope MOT (which was simplified by the use of one amplifier for all the necessary frequencies), had a more technical nature. One of the most important fundamental challenges was the reduction of the elastic collision cross section of ^{7}Li at just the temperature that the cloud had in the magnetic trap. This prevented the success of a straight forward evaporative cooling scheme. The problem was overcome by implementing a Doppler cooling stage in the magnetic trap. After surmounting this obstacle, the evaporative cooling and also the sympathetic cooling of ^{6}Li by ^{7}Li worked and was studied in detail. This result was obtained about one year ago, in October 2000. During the next months, the performance of the system was improved. The stability of the laser system and the mechanical and electrical stability of the magnetic trap were enhanced. A better version of the detection system was constructed, featuring especially a two isotope imaging method. This imaging method was essential for all further work with ^{6}Li, ^{7}Li mixtures. An immediate result due to the new detection system was the evidence for Fermi pressure by the comparison of the behavior of fermionic and bosonic gases in the region of degeneracy. The best fermionic degeneracy that we could reach at that point was $T/T_F = 0.25(5)$. We were not able to see the condensate, since it was unstable for atom numbers exceeding a few hundred. There was hope to improve the fermionic degeneracy when working with a stable condensate. And also a stable lithium condensate was itself interesting. To achieve this, the scattering length of ^{7}Li had to be positive as it is the case in the $|F = 1, m_F = -1\rangle$ state. We developed a method to achieve the transfer from the initial $|F = 2, m_F = 2\rangle$ state to this state in a magnetic trap. Now evaporative cooling in this state was optimized. As it turned out, the evaporation required some ^{6}Li atoms in the the lower hyperfine state to drive thermalization via the collisions between the two isotopes. Finally a stable Bose-Einstein condensate immersed in a degenerate Fermi sea could be produced. The fermionic degeneracy achieved was at least $T/T_F = 0.2(1)$. This time, the degeneracy was limited by our detection method. The condensate was one dimensional due to the small scattering length. The next step was the installation of the optical dipole trap. This enabled us to first observe and then use the Feshbach resonance in the ^{7}Li $|F = 1, m_F = 1\rangle$ state to produce a condensate with tunable scattering length. By tuning the scattering length negative and releasing the condensate in the horizontal dipole trap beam, we were able to produce and observe bright solitons.

A lot of physics of degenerate lithium can now be explored with the machine as it is.

- **Bright soliton.** Now that we know how to produce bright solitons in a reliable way, we can study their properties. First we will try to observe them on a longer timescale than the 8 ms that we have done until now, by trapping them in a waveguide without axial curvature. This will also permit to produce solitons with a weaker mean-field attraction giving rise to a higher number of atoms in the soliton and an axial size above our resolution limit. An exciting and relatively simple experiment is the creation of two solitons in a crossed dipole trap with two vertical beams. By confining the solitons in a waveguide with a slight axial confinement, the solitons will oscillate against each other and we will hopefully be able to verify that they cross each other without disturbance.

- **Feshbach resonance in ^{6}Li.** Just around the corner lays the detection of the Feshbach resonance in the $|F = 1/2, m_F = \pm 1/2\rangle$ states of ^{6}Li. All technical requirements are given. The losses accompanying the resonance can be measured and the change in spatial size of the fermionic sample due to the mean field can probably be observed. The resonance enhanced elastic scattering cross section can be used to perform evaporative cooling in the optical trap as was done with ^{7}Li. This method produces two interacting degenerate Fermi gases, a prerequisite for Cooper pairing. The ^{7}Li can serve as a probe to measure the properties of the fermionic gas.

- **BCS transition.** These two interacting Fermi gases can possibly undergo a

BCS transition. The production, detection and study of this transition is a great challenge, but there is reason to hope that this may be possible with this machine. Eventually new techniques to increase the phase-space density have to be used, for example an adiabatic deformation of the trap as proposed in [193].

- **Phase separation.** A Feshbach resonance is predicted between the ^{6}Li $|F = 1/2, m_F = -1/2\rangle$ and the ^{7}Li $|F = 1, m_F = -1\rangle$ state. Spin exchange decay is allowed for this mixture for magnetic fields above 150 G. But the rate is predicted to be low at the positive scattering length side of the Feshbach resonance [153]. This resonance could not only be used to drive evaporative cooling, but possibly also to produce a phase separation between the bosons and the fermions as described in section (1.1.13).
- **Low dimensional systems.** We have already produced a one dimensional condensate. Also in the optical trap this should be possible by using an extreme ratio of the oscillation frequencies and tuning the scattering length to a low value. Two dimensional condensates could be produced by using a standing optical wave. These low dimensional condensates are interesting study objects in their own right [89]. Their phase coherence properties or the influence of the mean field on their vibration frequencies could be studied. An especially interesting domain would be reached, if the scattering length is bigger than the harmonic oscillator length in one or two directions. The scattering length is then reduced in comparison with the scattering length for non confined atoms [74].

These are only the research topics which appear to be interesting at the moment. It would be astonishing if there would be no surprises or new ideas on the way to reach some of these goals. These surprises and ideas can lead to new directions for our research. It seems reasonable to assume, that work with the machine that we have built will provide new insights into fascinating physics for several years to come.

Thanks

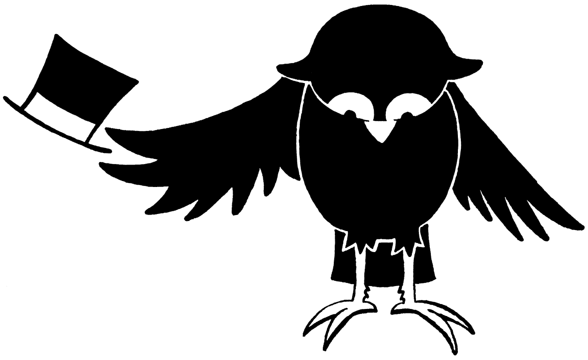

The work described here would not have been possible without the involvement of many people. I would like to mention and thank those of special importance to myself and to the project.

My plan to study in Paris became a reality when Christophe Salomon invited me to undertake my Ph.D. in his research group. I met him in Konstanz while working on my diploma thesis with Gerhard Rempe, which resulted in the first Bose-Einstein condensate outside the United States and gave me a fascination for experimental quantum physics. Christophe believed in me. Even when I hesitated, because I wasn't sure I could stand living in such a big city as Paris, he was very kind. He invited me on a bicycle trip along the riverside with his family to show me the enjoyable sides of Paris. Now I am very glad that I came. Paris is the loveliest city I have known. Christophe infects everybody with his optimism even when the experiment is completely non-operational and no solution is in sight. I have enjoyed being a part of his group, which does not make an artificial separation between work and private life. I will always remember our trip to Sologne with all the Salomons. It was a great opportunity for me. Christophe gave me confidence and freedom, which made the work pleasurable. When necessary he was always available and willing to discuss any aspect of the experiment. His experience allowed us to solve many problems we could not have overcome otherwise.

When I joined the Lithium group at the ENS, Marc-Oliver Mewes and Gabriele Ferrari were already working on the project. They had built a first version of the vacuum chamber and a basic optical system for ^{7}Li alone. We profited from the experience which Marc-Oliver had gained during his Ph.D. in the group of W. Ketterle at MIT. It was his idea to separate the MOT and the Ioffe-Pritchard trap spatially. He also enriched discussions during lunch, especially when Isabelle Bouchoule was present. Gabriele was always thinking beyond what we were constructing at the moment. So he not only did a very good job in designing the optical system and the magnetic trap, but also came up with new ideas that often proved useful afterwards, such as the amplification of several frequencies with one tapered amplifier. We not only worked together but also spent a lot of our free time together and became good friends. When Marc-Oliver left, Kristan Corwin joined the team. The experiment was in a difficult situation at that time, because we were blocked by the loss of atoms during the transfer to the Ioffe-Pritchard region and by the decrease in the elastic collision cross section to zero for the temperatures we started with in the compressed magnetic trap. All the same, Kristan wasn't discouraged and invested herself a lot to contribute to the project. She is a very nice and open-hearted person. I enjoy thinking back on our lovely dinners just before returning to the lab for the last hours before midnight, which often turned out to be dinners after work until midnight! With some overlap with Kristan, Lev Khaykovich joined the team as a Postdoc. I enjoyed very much working with him and we soon became friends. We also spent parts of our free time together, mainly inline skating or swimming. It was with him that I passed the greatest days of the experiment, the moment when the first visible condensate appeared on the computer screen and the first evidence of a bright soliton. Julien Cubizolles started working with us in the year 2000 and later joined the team as a Ph.D. student. A year later Thomas Bourdel joined. They are the first French persons (besides Christophe) working on the project. Both are very helpful and learn quickly. I think the future of the experiment is in good hands. I would like to thank the trainees which helped us during the years: Dan Israel, Fabrice Gerbier and Alice Sinatra.

The success of our experiment also depended, of course, on the work environment. I would like to thank the directors of the laboratoire Kastler Brossel, Michèle Leduc, Elisabeth Giacobino and Franck Laloë for receiving me. The members of the cold atom group are of special importance. Claude Cohen-Tannoudji, the founding father of the group, was always very kind and interested in my work. His courses at the Collège de France will stay with me. Jean Dalibard's presence and advice was crucial at least on two occasions: when he pointed out to us the fatal temperature dependence of the ^{7}Li scattering cross section; and when he mentioned that in the rubidium experiment some atoms survived a 2π pulse passing through a magnetically untrapped state. The latter encouraged us to work on state transfer in the magnetic trap, which was initially planned in the optical trap, for which the laser was delivered with a delay of more than three months. Yvan Castin used to come to the lab whenever we had new or unexpected results, as for example the time-of-flight expansion of the condensate, and to search for theoretical models describing our observations. He was also a very good teacher at the 1999 Les Houches summer school. Gora Shlyapnikov always pointed out which directions we ought to investigate from a theoretical point of view. I enjoyed discussions with him at the Aspen workshop 2001, where we shared an office. David Guery-Odelin was always friendly and helpful. I remember well that he was the first person from outside the lithium group to invited me out one evening. I was also fortunate to meet Kirk Madison, who worked as a post-doc on the vortex experiment and became a friend. I would like to thank the other members from the cold atom group, for being there, creating a pleasant atmosphere and helping out when technical material was missing: Frédéric Chevy and Franck Pereira dos Santos who started their PhDs together with me, Isabelle Bouchoule and Helene Perrin whom I remember from my first visit to LKB in 1997, Pierre Desbiolles, Maxime Dahan, Denis Boiron, Jérémie Léonard, Erwan Jahier, Lincoln Carr, Peter Rosenbusch, Philippe Cren, Christian Roos, Wendel Wohlleben, Johannes Söding, Vincent Bretin, Ernst Rasel, Carl Barrelet, Sylvain Schwartz, Iacoppo Carusotto, Markus Holzmann, Anna Minguzzi, Franceso Pavone, Francisco Perales, Sinha Subhasis, Unni Krishnan, Makoto Morinaga and Junmin Wang. Some of the persons mentioned here helped me in the correction of this manuscript : David Guery-Odelin, Thomas Bourdel, Julien Cubizolle, Kristan Corwin, Kirk Madison, Joseph Thywissen and Lincoln Carr.

I would like to thank the members of my jury, Alain Aspect, Rudi Grimm, Claude Cohen-Tannoudji, Gora Shlyapnikov, Roland Combescot and Christophe Salomon, for their participation in the jury and for the excellent remarks they made concerning my manuscript.

The laboratory could not function without people who are a bit behind the scenes but all the more important to construct a machine or make smooth scientific work at all possible. As administrative assistants we are fortunate to have Nicole Neveux, Geneviève Piard, Zohra Ouassyoun and Corinne Palescandolo. I thank André Clouqueur, Lionel Pérenes and Patrick Giron for the design and the construction of our electronics and Yvan Cabirou, Didier Courtiade, Frank Deutertre, Xavier Dollat, Denis Douillet, Rémi Fert, Benoît Lemaire, Jack Olejenik, Jean Outrequin, Jean-Claude Paindorge, Jean-François Point, Michel Quindu and Pascal Travers for designing, manufacturing and installing the various mechanical parts out of which our machine consists. Bruno Fabre, Patricia Celton, and Denis Jaggi were always there when I needed material for the experiment.

Some companies helped more than required of them, especially Andor technologies, Climatelec and Aimants Calamit.

During the last years I had occasion to travel extensively and visited laboratories around the world. I was always very well received and I would like to thank the people who showed me their laboratories and often also invited me out during the evenings or weekends. I can not mention everybody here, so I will just give a list of the directors of some of the groups which I would like to thank for their hospitality: A. Aspect, R.

Blatt, S. Chu, E. Cornell, J. Close, J. Doyle, T. Esslinger, C. Foot, P. Fromherz, G. Gabrielse, R. Grimm, P. Hannaford, T. Hänsch, D. Heinzen, R. Hulet, M. Kasevich, W. Ketterle, D. Kleppner, R. McLean, D. Meschede, M. Prentis, D. Pritchard, M. Raizen, G. Rempe, A. Sidorov, V. Vuletic, J.T.M. Walraven, C. Wieman, and P. Zoller.

Life would not be worth living without good friends. This was especially difficult for me when I came to Paris and had none here for some time. So I particularly appreciated when new friends appeared in my life. I want to thank them for having made my life outside the lab enjoyable. I would like to mention especially Bernadette, Phillipe, Godefroy, Eunyong, Sang Wuk, Carmen, Mirko, Trinh, Yvan, Joseph, Tibault, Vincent, Nynke, Sylvia, Milo, Julika, Frauke, Franziska, Julia, Ania, Klaus, Björn, and Audrey.

I especially like to thank my parents, my brother Mathias and my sister Katharina. The owl pictures throughout the thesis are Katharina's creation. Mathias helped with animations necessary for the thesis defence and the PHARAO space-clock project. It was always great when Mathias or Katharina stayed with me in Paris.

Thanks to everybody!

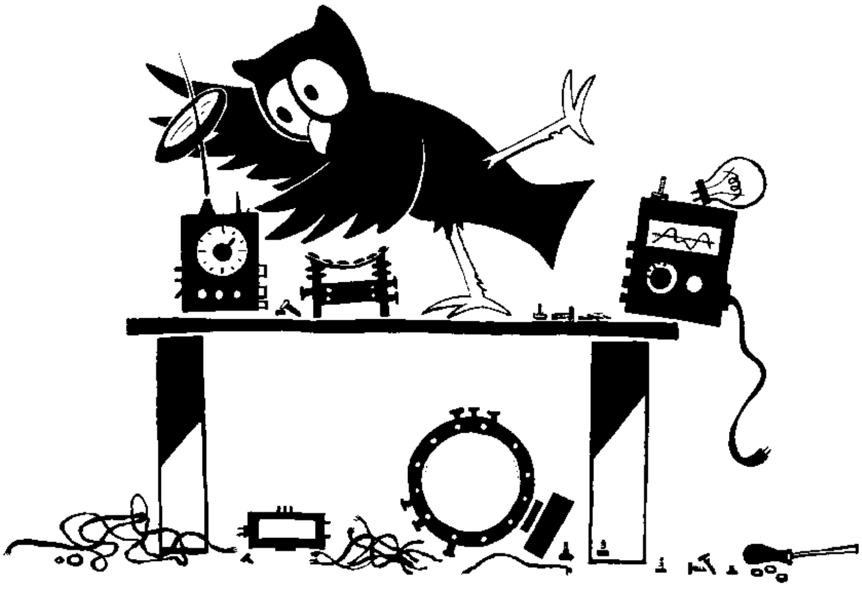

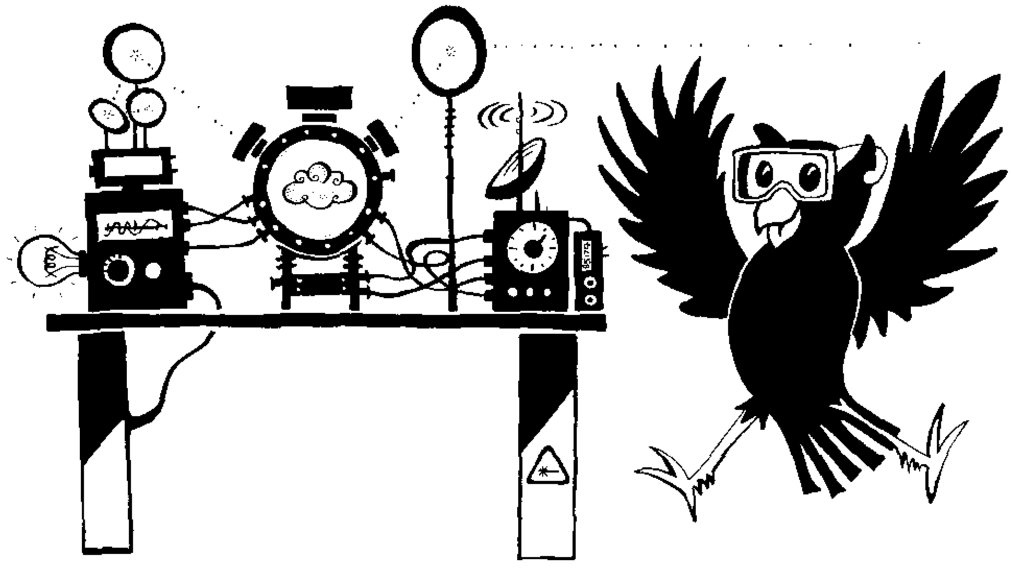

Appendix A

High-power multiple-frequency narrow-linewidth laser source based on a semiconductor tapered amplifier

G. Ferrari, M.-O. Mewes, F. Schreck and C. Salomon
Optics Letters,
Volume **24**, Numéro 3, pages 151-153, Février 1999.

High-power multiple-frequency narrow-linewidth laser source based on a semiconductor tapered amplifier

Gabriele Ferrari, Marc-Oliver Mewes, Florian Schreck, and Christophe Salomon

Laboratoire Kastler Brossel, Département de Physique de l'Ecole Normale Supérieure, 24 rue Lhomond, 75231 Paris Cedex 05, France

Received October 12, 1998

The output of two grating-stabilized external-cavity diode lasers was injected into a semiconductor tapered amplifier in a master oscillator–power amplifier (MOPA) configuration. At a wavelength of 671 nm this configuration produced 210 mW of power in a diffraction-limited mode with two frequency components of narrow linewidth. The frequency difference δ was varied from 20 MHz to 12 GHz, while the power ratio of the two components was freely adjustable. For $\delta < 2$ GHz additional frequency sidebands appear in the output of the MOPA. This configuration is a flexible and simple high-power cw laser source for light with multiple narrow-linewidth frequency components. © 1999 Optical Society of America

OCIS codes: 140.0140, 140.3280, 140.3600, 140.4480, 140.5960.

Narrow-linewidth semiconductor lasers have become a standard tool in high-resolution spectroscopy as well as in laser cooling.[1] The key advantages of semiconductor lasers compared with dye and solid-state lasers are their price, reliability, and ease of maintenance. The main disadvantages are relatively low power and a limited wavelength coverage. For instance, at 671 nm, single-mode laser diodes can deliver only 30 mW of power. Recently semiconductor tapered power amplifiers[2] (TA's) for many wavelengths from 650 nm to 1.0 μm have become commercially available.[3] These devices overcome the power limitations of traditional laser diodes and are able to provide several hundred milliwatts of single-mode laser power. Injection of a few milliwatts of narrow-linewidth laser light yields a TA linewidth that is identical to the linewidth of the injecting master laser,[4–6] typically less than 100 kHz.

For several applications in atomic physics, such as optical pumping and the simultaneous laser cooling of different isotopes, it is useful to have a single beam with several narrow-linewidth frequency components of identical polarization. Also, magneto-optical trapping of alkali atoms requires two frequencies to excite the atoms in both hyperfine levels of the ground state, which can be achieved by addition of sidebands to the carrier frequency through phase or intensity modulation. This method is, however, inflexible because of its limited range of modulation frequencies. One also loses power into other sidebands. Another method, the geometrical superposition of beams with different frequencies through a nonpolarizing beam splitter, is highly sensitive to alignment.

Here we present a flexible method for producing a single high-power beam with two narrow-linewidth frequency components of adjustable frequency difference and intensity. It consists of a simple master oscillator–power amplifier (MOPA) configuration operating at 671 nm, which produces 210 mW of two narrow-linewidth frequency components with identical polarization in a Gaussian mode. The superposition of the two frequency components is produced by injection of the amplifier chip with the light of two narrow-linewidth low-power laser diodes simultaneously. The power ratio between the two components as well as their frequency difference is adjustable. The system has been characterized for frequency differences from 20 MHz to 12 GHz. At differences of less than 2 GHz significant additional frequency sidebands that were due to nonlinearities in the TA were observed. These sidebands are characterized as a function of frequency difference and carrier intensities.

The setup is shown in Fig. 1. It consists of two 30-mW extended cavity diode lasers, L1 and L2 (Spectra Diode Laboratories Model SDL-7311-G1), operated in Littrow configuration with an emission linewidth of a few hundred kilohertz. The light emitted by each laser is collimated by a Geltech molded glass aspheric lens ($f = 4.5$ mm; N.A., 0.55). The frequency ν_1 of L1 is stabilized at the $2S_{1/2} \rightarrow 2P_{3/2}$ optical transition of ^{7}Li (671 nm). The frequency ν_2 of L2 can be detuned from ν_1.

The beams of the two lasers pass through separate optical Faraday isolators with more than 40-dB isolation and telescopes that reduce the beam waist

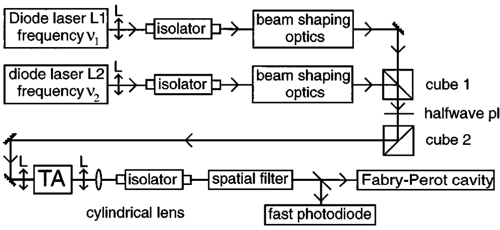

Fig. 1. Experimental setup. Two beams from low-power narrow-linewidth diode lasers L1 and L2 are superposed upon a polarizing cube. Components with identical polarizations are selected with the second polarizing cube and injected into the TA. The output of the TA is spatially filtered. The frequency and intensity components of the output are measured with a fast photodiode and a Fabry–Perot cavity, respectively. L's, Geltec aspheric lenses with a N.A. of 0.55.

0146-9592/99/030151-03$15.00/0 © 1999 Optical Society of America

to 4.4 mm vertically and 0.9 mm horizontally. The beams are then superposed with a polarizing cube. The two overlapping beams have orthogonal linear polarizations. By passing the light through a half-wave plate and a second polarization beam splitter we select components of the beams with vertical polarization. The half-wave plate allows us to adjust the intensity ratio of the components. The two superposed beams with different frequencies are then injected into the TA chip (Spectral Diode Laboratories Model SDL-8630). The input facet of the amplifier emits a few milliwatts of amplified spontaneous emission (ASE) in the backward direction, i.e., toward the injecting beam. For good injection the shape and divergence of the input beam and the ASE need to be matched. The two divergences of the ASE and the injecting laser diodes are anisotropic but nearly identical. We therefore did not need to correct the ellipticity of the laser beams. We chose a Geltech aspheric lens, which is identical to the collimating lenses that are used in the master lasers, to focus the light into the TA. The TA chip itself is connected to a metal block for mounting and heat sinking. This assembly is attached to a horizontal base and kept at a temperature of 22 °C with a stability of 1 mK by use of a water-cooled Peltier element. The amplifier has a center wavelength of 672 nm at 21 °C and a tuning range from 667 to 677 nm. We supplied it with a current of 1.25 A with a relative stability of 10^{-4}. The total injection power is 15–16 mW, depending on the relative contributions of L1 and L2. Thus the TA output power is saturated and the ASE relative power is reduced.

The output beam of the TA is vertically collimated by an aspheric lens identical to the one used for injection. In the horizontal direction we use an additional cylindrical lens ($f = 150$ mm) to compensate for the large astigmatism of the output beam. The frequency spectrum of the output beam is analyzed with a fast photodiode with a bandwidth of 6 GHz (New Focus photodiode 1515) and a spectrum analyzer. With this diode, frequency differences δ of as much as 12 GHz can be measured. The relative intensity of the frequency components is measured by a Fabry–Perot spectrum analyzer with a resolution of ~5 MHz and a free spectral range of 800 MHz. The total power obtained after spatial filtering is 210 mW in a nearly diffraction-limited Gaussian mode with a 2:3 aspect ratio (a focal length of 100 mm for the cylindrical lens would produce an almost circular beam). The spatial filter also suppresses the broadband ASE in the filtered mode to less than 2% of the total power. To prevent backreflection into the TA chip, all optics on the output side are antireflection coated and the beam is passed through a Faraday optical isolator with more than 40-dB isolation after the cylindrical lens.

For a frequency difference δ larger than 2 GHz the output beam of the MOPA consists essentially of the two amplified frequency components, ν_1 and ν_2, as illustrated in Fig. 2a for $\delta = 10$ GHz, a frequency difference comparable with the isotopic shift of the $2S_{1/2} \rightarrow 2P_{3/2}$ optical transition in ^{6}Li and ^{7}Li. By changing the relative intensities of the injection beams we can vary the power ratio R between the two amplified components. It should be pointed out that R is proportional to the power ratio of the injecting beams even though the total injection power saturates the amplifier. Using the fast photodiode, we checked that the beat note at δ of the TA output was identical to the beat note between the two injecting lasers L1 and L2 within the 10-Hz resolution bandwidth of our spectrum analyzer.

For a power ratio $R = 1$ we observe weak sidebands at $\nu_1 - \delta$ and $\nu_2 + \delta$, each with 0.1% of the total power. This generation of new frequencies becomes more pronounced with decreasing frequency difference, as illustrated in Fig. 2b for $\delta = 100$ MHz: Sidebands at $\nu_1 - \delta$, $\nu_1 - 2\delta$, $\nu_1 - 3\delta$, and at $\nu_2 + \delta$, $\nu_2 + 2\delta$ appear. When $R = 1$, ~40% of the total power is contained in these sidebands. Because the amplifier gain is frequency independent for the frequency range investigated, we consider only power ratios R between 0 and 1.

The sidebands are probably due to a beating of the two injection frequencies ν_1 and ν_2 that modulate the injected intensity with frequency δ. The relative amplitude of the intensity modulation is $2\sqrt{R}/(1 + R)$, which is maximized when the two injecting intensities are equal ($R = 1$). For small frequency differences (<2 GHz) this intensity modulation affects both the amplitude and the phase of the main frequency components because of nonlinearities in the gain medium.[7] This modulation is reflected in sidebands at multiples of δ in the amplified light. Because of simultaneous phase and amplitude modulation, sidebands of the same order (e.g., at $\nu_1 - \delta$ and at $\nu_2 + \delta$) may not have the same intensity for $R = 1$.[8]

Frequency components other than the injected frequencies in the output can have significant implications for experiments. They lower the intensity

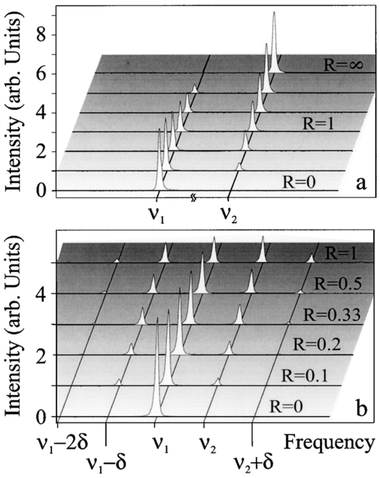

Fig. 2. Intensity spectrum of the MOPA output measured with a Fabry–Perot spectrum analyzer with a frequency resolution of 5 MHz. ν_1 is the frequency of the $2S_{1/2} \rightarrow 2P_{3/2}$ optical transition in ^{7}Li. a, The spectra were recorded for different power ratios R and $\delta = \nu_2 - \nu_1 = 10$ GHz. For equal power at ν_1 and ν_2, ~0.2% of the total power was coupled into sidebands at $\nu_1 - \delta$ and $\nu_2 + \delta$. b, Spectra are shown for $\delta = 100$ MHz. The appearance of sidebands can be observed as R is changed from 0 to 1.

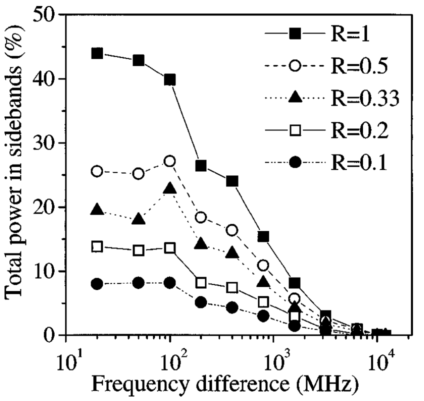

Fig. 3. Fraction of the total power coupled into all sidebands at the MOPA output as a function of frequency difference δ for different power ratios R in the injected frequencies.

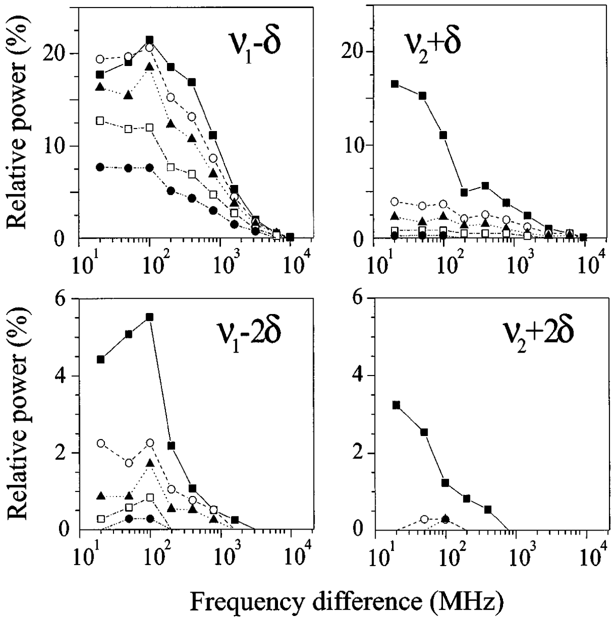

Fig. 4. Fraction of the total power coupled into each sideband at the MOPA output as a function of frequency difference δ for different power ratios R in the injected frequencies. Significant sidebands appear at $\nu_1 - \delta$, $\nu_2 + \delta$, $\nu_1 - 2\delta$, and $\nu_2 + 2\delta$.[9] Symbols are the same as in Fig. 3.

available at the injected frequencies and could excite unwanted transitions. We have therefore studied the sideband characteristics for frequency differences from 20 MHz to 12 GHz and several values of R. We measured the fraction of total power coupled into all sidebands (Fig. 3) as well as the fraction of power in each sideband for different values of R and δ (Fig. 4). It is evident that the power in the sidebands increases with R for $R \leq 1$ and decreases with δ. For $\delta = 20$ MHz and $R = 1$, ~45% of the total power is coupled into the sidebands, whereas for frequency differences δ above 1 GHz the sideband fraction is below 10% and for $\delta > 11$ GHz it drops to below 0.1%. The roll-off at frequencies above ~1 GHz is typical of the electron–hole recombination time in semiconductor devices. Spectra for $\delta < 10$ MHz could not be resolved because of limitations in the finesse of the Fabry–Perot cavity.

In all the previous experiments the TA was operated in the saturated regime. Because sidebands are a result of nonlinearities of the gain medium, we tried to operate the TA in a less saturated, more linear regime. For $R = 1$ and $\delta = 800$ MHz, after decreasing the injecting power by a factor of 5 (from 15 to 3 mW) and increasing the current from 1.25 to 1.45 A we decreased the sideband power by 45% (from 36 to 20 mW) while preserving 94% (155 mW) of the power at the injecting frequencies. However, the result of this operation was to double the contribution of broadband ASE in the spatially filtered mode to 4%.

We have presented a flexible and convenient semiconductor source of high-power narrow-linewidth light of several frequency components. The MOPA consists only of standard optical elements and semiconductor lasers. Analogous configurations could be realized with TA's centered at different wavelengths, and we believe that the observations reported here are general features of semiconductor TA's. Finally, more than two frequencies could in principle be injected.

We are grateful to R. Grimm for providing the design of the external-cavity diode laser supports and to M. Welling for designing the support for the TA chip. M.-O. Mewes acknowledges support from a Marie Curie research fellowship of the European Community [Training and Mobility of Researchers (TMR)]. Laboratoire Kastler Brossel is a Unité de Recherche de l'Ecole Normale Supérieure et de l'Université Pierre et Marie Curie, Associée au Centre National de la Recherche Scientifique (CNRS). This research was partially supported by the CNRS Collège de France and by the European Community the (TMR network ERB FMRX-CT96-0002). G. Ferrari's e-mail address is gferrari@physique.ens.fr.

References

1. L. Hollberg and C. Wieman, Rev. Sci. Instrum. **62,** 1 (1991).
2. J. N. Walpole, Opt. Quantum Electron. **28,** 623 (1996).
3. Spectra Diode Laboratories, *1998 Semiconductor Laser Product Catalog* (Spectra Diode Laboratories, San Jose, Calif., 1998).
4. D. Mehuys, D. F. Welch, and L. Goldberg, Electron. Lett. **28,** 1944 (1992).
5. F. Z. Cruz, M. Rauner, J. H. Marquart, L. Hollberg, and J. C. Bergquist, in *Proceedings of the Fifth Symposium on Frequency Standards and Metrology,* J. C. Bergquist, ed. (World Scientific, Singapore, 1995), p. 511.
6. A. C. Wilson, J. C. Sharpe, C. R. McKenzie, P. J. Manson, and D. M. Warrington, Appl. Opt. **37,** 4871 (1998).
7. W. W. Chow, S. W. Koch, and M. Sargent III, *Semiconductor-Laser Physics* (Springer-Verlag, Berlin, 1994), p. 286.
8. W. Lenth, Opt. Lett. **8,** 575 (1983).
9. In some cases it is possible to detect third-order sidebands: For $R = 1$ the relative power at $\nu_1 - 3\delta$ was ~1% for frequency differences δ from 20 to 100 MHz, whereas for $R = 0.5$ it was 0.3% at $\delta = 100$ MHz. Only for $\delta = 20$ MHz and $R = 1$ was it possible to detect a component at $\nu_2 + 3\delta$ with a relative power of 1%.

Appendix B

Simultaneous magneto-optical trapping of two lithium isotopes

M.-O. Mewes, G. Ferrari, F. Schreck, A. Sinatra, and C. Salomon
Physical Review A,
Volume **61**, pages 11403-1-11403-4, 8 Décembre 1999.

PHYSICAL REVIEW A, VOLUME 61, 011403(R)

Simultaneous magneto-optical trapping of two lithium isotopes

Marc-Oliver Mewes, Gabriele Ferrari, Florian Schreck, Alice Sinatra, and Christophe Salomon
Laboratoire Kastler Brossel, Ecole Normale Supérieure, 24 rue Lhomond, 75231 Paris Cedex 05, France

(Received 27 July 1999; published 8 December 1999)

We confine 4×10^8 fermionic ^{6}Li atoms simultaneously with 9×10^9 bosonic ^{7}Li atoms in a magneto-optical trap based on an all-semiconductor laser system. We optimize the two-isotope sample for sympathetic evaporative cooling. This is an essential step towards the production of a quantum-degenerate gas of *fermionic* lithium atoms.

PACS number(s): 32.80.Pj

The observation of Bose-Einstein condensation in atomic vapors [1] has made dilute *bosonic* quantum gases experimentally accessible and the study of these systems has thus been very fruitful. Quantum degenerate gases of fermions also offer novel physical properties. At temperatures below the Fermi temperature, energy and momentum transfer is modified by Fermi statistics [2,3]. One striking prediction is the partial suppression of spontaneous emission [4]. Also, a Fermi gas of atoms in a mixture of different hyperfine (HF) states might undergo a BCS pairing transition and exhibit long-range coherence and superfluid behavior [5]. Recently the onset of quantum degeneracy of a gas of *fermionic* ^{40}K atoms has been observed by DeMarco and Jin, and a temperature half of the Fermi temperature has been reached [6].

Evaporative cooling of polarized atoms has so far been essential for the production of quantum degenerate gases [7]. It is driven by elastic collisions. At ultralow temperature T, i.e., below a few millikelvin for lithium, collisions between bosons or distinguishable particles are predominantly s-wave collisions, while Pauli exclusion prohibits s partial waves of polarized fermions. In an ultracold gas of indistinguishable fermions the elastic collision rate diminishes proportionally to T^2, as recently confirmed in [8]. Fermionic atoms can be cooled *sympathetically* by collisions in a mixture of different internal states [6,9] or of different species, which are yet to be implemented.

We intend to sympathetically cool fermionic ^{6}Li with the bosonic ^{7}Li isotope. This could produce not only a quantum degenerate Fermi gas but also a Bose-Einstein condensate of ^{7}Li in both HF ground states as well as a mixture of quantum degenerate gases of fermions and bosons [10]. One can also employ ultracold bosons to probe collisional properties of a degenerate Fermi gas [3].

Previously several groups have studied samples of two atomic species in a magneto-optical trap (MOT) [14]. In this article we describe realization of a MOT containing both fermionic and bosonic lithium and its optimization for sympathetic cooling. 4×10^8 ^{6}Li atoms and 9×10^9 ^{7}Li atoms are simultaneously confined. These numbers together with the density and temperature achieved should be sufficient to produce a Fermi gas with a Fermi temperature on the order of 10 μK in a harmonic magnetic trap of frequency $\overline{\omega}/2\pi=400\ \mathrm{s}^{-1}$. The phase-space density $\mathcal{D}=n_0\Lambda^3/f$ of unpolarized atoms (f internal states) with a peak density n_0 and temperature T is the number of identical atoms per cubic thermal De Broglie wavelength $\Lambda=(2\pi\hbar^2/mk_BT)^{1/2}$. The achieved phase-space density in the two-isotope magneto-optical trap is 4×10^{-6} for ^{7}Li($f=3$) and 0.8×10^{-6} for ^{6}Li($f=2$). In single-isotope traps, the number of fermions (1.5×10^9) exceeds the best previous realization of laser-cooled fermions by one order of magnitude [6,11]. The number of trapped ^{7}Li (1.8×10^{10}) is also a factor of 10 improvement [12].

In future experiments, this two-isotope sample will be polarized and transferred into a magnetic trap. Bosonic lithium will be evaporatively cooled. Fermionic lithium thermalizes with the bosons via elastic collisions. Neglecting inelastic losses for mixtures of $^7\mathrm{Li}(F=2,m_F=2)+{}^6\mathrm{Li}(F=3/2,m_F=3/2)$ [and $^7\mathrm{Li}(F=1,m_F=-1)+{}^6\mathrm{Li}(F=1/2,m_F=-1/2)$], as justified in [13], all initially confined fermions should reach the quantum degenerate regime, i.e., $T\leqslant T_F$. Note that reaching $T\ll T_F$ might become difficult because Fermi blocking will slow down the thermalization process since only fermions near the Fermi surface contribute [6,3,10]. In a typical evaporative cooling sequence the phase-space density $\mathcal{D}$ is increased by $\sim10^6$ by decreasing the atom number by ~100 [7]. For sympathetic cooling this implies that N initially confined ^{7}Li atoms can sympathetically cool a sample of $N/100$ ^{6}Li atoms into the quantum degenerate regime. We therefore aim to maximize the number N of ^{7}Li atoms in the two-isotope trap while simultaneously confining on the order of $N/100$ ^{6}Li atoms. It is equally crucial that atoms thermalize quickly during the trap lifetime. Thus the initial elastic collision rate Γ_i between ^{7}Li atoms in the magnetic trap must be maximized. For a linear trapping potential in three dimensions Γ_i can be related to quantities of the MOT as follows:

$$\Gamma_i\propto N^{4/9}\mathcal{D}_i^{5/9}\propto NT^{-5/6}\sigma^{-5/3}, \tag{1}$$

where N is the number of trapped atoms, T is the temperature of the sample and σ the width of the Gaussian density distribution $n(r)=[N/(\sqrt{2\pi}\sigma)^3]\exp(-r^2/2\sigma^2)$ in the MOT. We have optimized the laser-cooled sample of ^{7}Li with respect to Γ_i in the presence of ^{6}Li.

In the experiment, the MOT is loaded from a Zeeman slowed lithium beam. ^{6}Li in the beam is enriched and has an abundance of about 20%. Both isotopes are slowed and confined in the MOT with 671-nm light that is near resonant with the $D2$ line, the $2S_{1/2}\rightarrow2P_{3/2}$ optical transition. The isotopic shift for this transition is 10 GHz. Each isotope re-

©1999 The American Physical Society

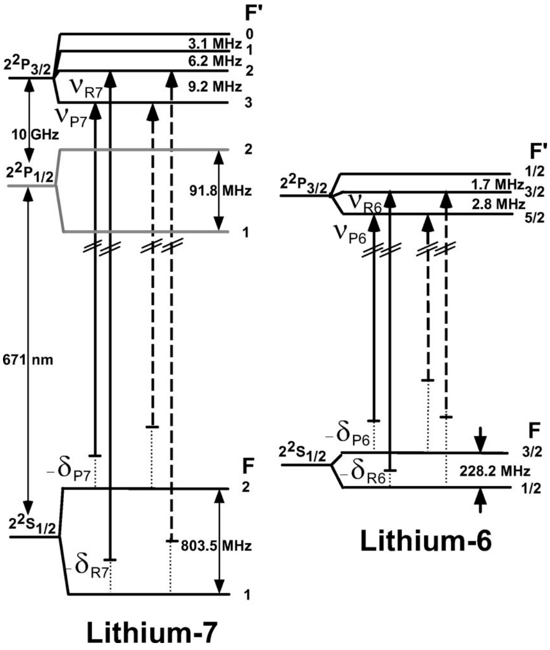

FIG. 1. Frequencies employed to slow (dashed arrows) and magneto-optically trap (solid arrows) both lithium isotopes. The detunings of the frequencies from the respective resonances are marked with a dotted line. The detuning of the slowing light from the respective zero magnetic field transitions for ^{7}Li is -426 MHz and -447 MHz for ^{6}Li.

quires two frequencies to excite from the two HF ground states. The HF splitting is 803.5 MHz for ^{7}Li and 228.2 MHz for ^{6}Li. Hence simultaneous laser cooling of both lithium isotopes requires *eight* different laser frequencies: four frequencies for Zeeman slowing and four frequencies for magneto-optical trapping, as shown in Fig. 1.

All frequencies are derived with acousto-optical modulators from two grating-stabilized external-cavity diode lasers based on 30-mW laser diodes. The lasers are frequency locked in saturated absorption to the $D2$ lines of ^{6}Li and ^{7}Li, respectively. The slowing light is produced by geometrical superposition of the output of four injection seeded 30-mW laser diodes. Four trapping frequency components are geometrically superposed and 15 mW of this light is injected into a tapered semiconductor amplifier chip. After spatial filtering, the chip produces up to 140 mW of trapping light containing the four frequency components in a Gaussian mode at an identical polarization, as described in [15]. The intensity ratio of the frequency components in the trapping beams can be adjusted. This light is split up into six independent Gaussian trapping beams, each with a maximum peak intensity of $I_{max}=6$ mW/cm^2, a $1/e^2$ intensity width of 3 cm, and an apertured diameter of 2 cm. The MOT is operated in a 4cm × 4cm × 10 cm Vycor glass cell of optical quality $\lambda/2$. Background gas collisions limit the $1/e$ MOT lifetime τ to about 25 s.

The trapped atom clouds of both isotopes are separately observed in absorption imaging. For observation, the trapping light and magnetic field are switched off abruptly. The induction limited $1/e$ decay time of the magnetic field is less than 50 μs. After free ballistic expansion with an adjustable time of flight between 150 μs and 7 ms the sample is illuminated for 80 μs by a probe beam. This probe excites either ^{7}Li from the $F=2$ ground state or ^{6}Li from the $F=3/2$ ground state to the $2P_{3/2}$ excited-state manifold. The absorption shadow of the sample is imaged onto a charge-coupled device (CCD) camera. A separate repumping beam that is not projected onto the camera excites atoms in the other HF ground state to avoid hyperfine optical pumping. The density distribution, atom number, and temperature of the sample are obtained from absorption images for different ballistic expansion times.

TABLE I. Comparison of atom number N, peak density n_0, temperature T, and frequency detunings for the single-isotope and two-isotope MOT.

	Single-isotope MOT		Two-isotope MOT	
	^{7}Li	^{6}Li	^{7}Li	^{6}Li
N	1.8×10^{10}	1.5×10^{9}	9×10^{9}	4×10^{8}
n (cm^{-3})	3×10^{11}	1.0×10^{11}	2.5×10^{11}	5×10^{10}
T (mK)	1.5	0.7	1.0	0.7
$\delta_{P7,6}$ (units of Γ)	-8.0	-2.7	-8.0	-2.7
$\delta_{R7,6}$ (units of Γ)	-5.8	-5.1	-5.8	-5.1

Both isotopes are magneto-optically trapped in two steps: In the first step, *the loading phase*, the capture volume and velocity of the trap are large, such that the number of trapped atoms is maximized. In the second step, *the compression phase*, the already trapped atoms are compressed in phase space, such that the initial elastic collision rate Γ_i is maximized.

All four frequencies ν_{P7}, ν_{R7}, ν_{P6}, and ν_{R6} of the MOT are exciting on the $D2$ line. We maximized the number of ^{7}Li atoms and ^{6}Li atoms in separate MOTs as well as the number of ^{7}Li atoms in the two-isotope trap. The maximization involved the detunings $\delta_{P7},\delta_{R7},\delta_{P6},\delta_{R6}$ of the light components from the cooling and repumping transitions of the two isotopes (Fig. 1), the intensities of all frequency components, and the strength of the magnetic field of the MOT.

First, the atom number was optimized in separate *single-isotope* MOTs with only the two frequencies for the respective isotopes present. We were able to capture up to 1.8×10^{10} ^{7}Li atoms and 1.5×10^{9} ^{6}Li atoms. The atom number N, peak density n_0, temperature T, and the respective detunings are listed in Table I. The atom number is accurate to within a factor of 2, and this dominates the uncertainty in the density determination. This uncertainty arises from a conservative estimate for the absorption cross section because the probe beam polarization is not well defined with respect to the local magnetic field and the HF structure splitting in the excited state is small. The temperature uncertainty is 0.2 mK. For both isotopes the atom number is maximized at large frequency detunings and equal intensities in both frequency components. The optimum magnetic-field gradient B' along the symmetry axis of the magnetic quadrupole field of the MOT is about 35 G/cm for both isotopes. The MOT was operated at maximum intensity $I_{max}=6$ mW/cm^2 in each of the six beams.

In the ^{7}Li trap, at low atom number ($\leqslant10^9$) the temperature is the Doppler temperature (1.1 mK at $\delta_{P7}=-8\Gamma$), as shown in Fig. 2. At large atom numbers, for 5×10^9 to 2×10^{10} trapped atoms, the temperature is 1.5(2) mK and

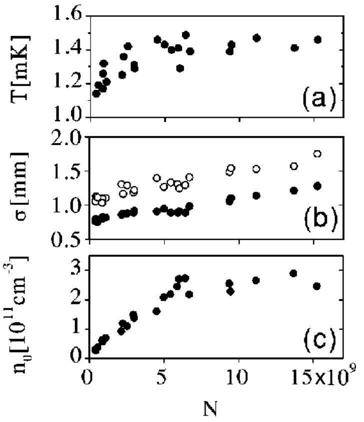

FIG. 2. Temperature T, one-dimensional rms width σ and peak density n_0 in a ^{7}Li MOT versus atom number N. N was varied by changing the loading time. In (b) the width along the symmetry axis z of the magnetic field (solid data points) is $\sim$40% smaller than in the radial direction (hollow points) as expected from a simple MOT model $(1/\sqrt{2})$.

nearly constant, while the density typically saturates at $n_0 = 3\times10^{11}$ cm^{-3}. In this regime the number of trapped ^{7}Li atoms is limited by loss due to inelastic radiative escape (RE) or fine-structure (FS) changing collisions. In steady state, the flux of slow atoms $\mathcal{F} = 2\times10^9$ s^{-1} is balanced by the trap loss according to

$$\mathcal{F} = N/\tau + \beta n_0 N/\sqrt{8}, \tag{2}$$

$\tau = 25$ s is the background-gas-limited lifetime of the MOT. The two-body loss coefficient $\beta = 6\times10^{-13}$ cm^3/s was experimentally determined and is consistent with previous studies of trap loss in a ^{7}Li MOT [16].

In ^{7}Li the HF splitting between the $F'=3$ and the $F'=2$ excited states is 1.6 Γ, and in ^{6}Li, 0.5 Γ between the $F'=5/2$ and the $F'=3/2$ excited states, where $\Gamma = 5.9$ MHz is the natural width of the lithium D lines. Despite the inverted excited-state HF structure of both lithium isotopes, the small HF splitting leads to off-resonant excitation of the $F=2 \rightarrow F'=2$ transition in ^{7}Li, and the $F=3/2 \rightarrow F'=3/2$ transition in ^{6}Li and frequent decay into the lower HF ground state. The repumping light component is therefore of equal importance as the principal trapping light. In fact, we only obtained a MOT with the repumping light also in a six-beam MOT configuration. This is not required in MOTs of other alkali metals with larger HF splitting, such as Cs, Na, or Rb.

For the two-isotope trap, the ^{6}Li repumping transition $F=1/2 \rightarrow F'=3/2$ is about 7 Γ to the blue of the $F=2 \rightarrow F'=1$ resonance in the $D1$ line of ^{7}Li. If both lithium isotopes are simultaneously confined, the ^{6}Li repumping light component ν_{R6} frequently excites this *noncooling* transition and significantly weakens the confinement of the trap for ^{7}Li. This leads to a smaller number of trapped ^{7}Li atoms in the presence of ^{6}Li light. We reduce this harmful effect by detuning towards the $D1$ resonance while reducing the ^{6}Li repumping intensity. The coincidence could also be avoided by repumping ^{6}Li on the $D1$ line instead. Aside from the light-induced trap loss we do not observe mutual effects due to the presence of both isotopes (such as collision-induced trap loss, heating, or a modification of the spatial distribution). With an intensity relation between the four frequency components ν_{P7}, ν_{R7}, ν_{P6}, and ν_{R6} of 8:8:2:1, we are able to confine 9×10^9 ^{7}Li atoms together with 4×10^8 ^{6}Li atoms. This ratio of $\sim$20 between the two isotopes can obviously be increased without loss of ^{7}Li atoms. N, n_0, T, and the respective detunings for the two-isotope MOT are listed in Table I.

TABLE II. Comparison of atom number N, peak density n_0, temperature T, and frequency detunings for the single-isotope and two-isotope compressed MOT.

	Single-isotope CMOT ^{7}Li	Single-isotope CMOT ^{6}Li	Two-isotope CMOT ^{7}Li	Two-isotope CMOT ^{6}Li
N	7×10^9	5×10^8	6×10^9	3×10^8
n (cm^{-3})	4×10^{11}	1.5×10^{11}	4×10^{11}	6.5×10^{10}
T (mK)	0.6	0.4	0.6	0.7
$\delta_{P7,6}$ (units of Γ)	-3.0	-2.7	-3.0	-2.7
$\delta_{R7,6}$ (units of Γ)	-9.0	-2.7	-9.0	-5.8

After loading the trap it is possible to further compress the sample in phase space and maximize the initial elastic collision rate Γ_i by changing the laser parameters for the duration of a few milliseconds. From Eq. (1) follows that in the case of *no* loss of atoms during compression a maximization of Γ_i also maximizes $\mathcal{D}_i$. For the compression, we optimize Γ_i with respect to the total laser intensity and the frequency detunings δ_{P6}, δ_{P7}, δ_{R6}, δ_{R7} while keeping B' constant at 35 G/cm. We compress the single-isotope MOTs as well as the two-isotope sample. For sympathetic cooling we are especially interested in maximizing Γ_i for ^{7}Li in the presence of ^{6}Li. As shown in Table II, decreasing δ_{R7}, i.e., detuning ν_{R7} further to the red of the transition, and approaching ν_{P7} towards resonance while reducing the overall laser intensity to $0.3 I_{max} = 1.8$ mW/cm^2, results in a 40% drop in temperature and increases the density by 70% (see Fig. 3). 30% of the initially confined atoms are lost during the first 3 ms of compression. This loss is probably due to FS- and RE-collision-induced heating during the initial compression stage. According to Eq. (1) compression increases Γ_i by 60%. After compressing the two-isotope trap for 3 ms, we

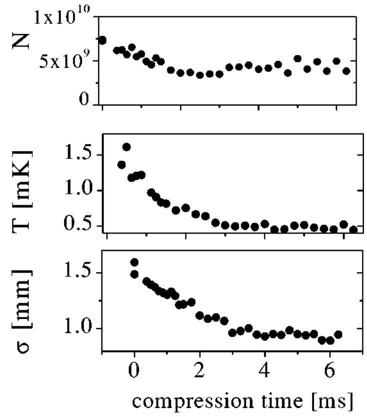

FIG. 3. Temporal dynamics of the compression phase of a ^{7}Li MOT. Atom number N, temperature T, and rms width σ_z after an abrupt change of the laser parameters at $t=0$.

obtain a maximum of 6×10^9 ^{7}Li atoms at a peak density of 4×10^{11} cm^{-3} and a temperature of 0.6 mK together with ^{6}Li at a density 6.5×10^{10} cm^{-3} and a temperature of 0.7 mK. Aside from the initial loss during the first few milliseconds, the 1/*e* trap lifetime also decreases to about 30 ms for both isotopes.

Figure 3 shows the typical temporal dynamics of atom number, width, and temperature of the ^{7}Li compressed MOT (CMOT) for the first 6.5 ms of compression. Γ_i and $\mathcal{D}_i$ reach a maximum after about 3 ms. The CMOT is rather insensitive to the repumping frequency ν_{R7}: detuning by $2\,\Gamma$ above and below the optimized value of $5.8\,\Gamma$ decreases Γ_i by less than 25%. The CMOT is much more sensitive to the detuning ν_{P7} of the trapping light. We optimized Γ_i with respect to the duration *t* of the compression phase and the detuning. The maxima of Γ_i and $\mathcal{D}_i$ remain at a constant value for $t \geqslant 3$ ms but shift to different detuning parameters with increasing CMOT duration.

To summarize, we showed that it is possible to trap about 6×10^9 ^{7}Li atoms together with 3×10^8 ^{6}Li atoms in the two-isotope MOT at at phase-space densities of $\sim10^{-6}$. These results are comparable to results achieved with single isotopes of Na or Cs in a *dark* SPOT [17]. In combination with a strong confining magnetic trap we expect an initial elastic collision rate well above 10 s^{-1}, despite the small triplet scattering length of 1.4 nm (^{7}Li-^{7}Li) and 2.0 nm (^{6}Li-^{7}Li) [18]. This can lead to the production of quantum degenerate Bose and Fermi gases of lithium by forced evaporation and sympathetic cooling within a few seconds.

We are grateful for the experimental assistance of Fabrice Gerbier. We thank C. Cohen-Tannoudji and J. Dalibard for discussions and Kirk Madison for a careful reading of the manuscript. M.-O.M. and F.S. were supported by the EC and DAAD(HSP 3), respectively. This work was partially supported by the CNRS, Collège de France, DRED, and the EC (TMR Network No. ERB FMRX-CT96-0002). Laboratoire Kastler Brossel is ''Unité de recherche de l'Ecole Normale Supérieure et de l'Université Pierre et Marie Curie, associée au CNRS.''

---

[1] M.H. Anderson *et al.*, Science **269**, 198 (1995); K.B. Davis *et al.*, Phys. Rev. Lett. **75**, 3969 (1995); C.C. Bradley, C.A. Sackett, and R.G. Hulet, *ibid.* **78**, 985 (1997); D.G. Fried *et al.*, *ibid.* **81**, 3811 (1998).

[2] J.M.K.V.A. Koelman *et al.*, Phys. Rev. Lett. **59**, 676 (1987); A. Imamoglu and L. You, Phys. Rev. A **50**, 2642 (1994); J. Javanainen and J. Roustekoski, *ibid.* **52**, 3033 (1995); B. DeMarco and D.S. Jin, *ibid.* **58**, R4267 (1998).

[3] G. Ferrari, Phys. Rev. A **59**, R4125 (1999).

[4] T. Busch *et al.*, Europhys. Lett. **44**, 1 (1998).

[5] A.J. Leggett, J. Phys. C **7**, 19 (1980); H.T.C. Stoof *et al.*, Phys. Rev. Lett. **76**, 10 (1996); M.A. Baranov, Y. Kagan, and M.Y. Kagan, Pis'ma Zh. Eksp. Teor. Fiz. **64**, 304 (1996) [JETP Lett. **64**, 301 (1996)]; A.G.W. Modavi, and A.J. Leggett, J. Low Temp. Phys. **109**, 625 (1998).

[6] B. DeMarco and D. Jin, Science **285**, 1703 (1999).

[7] W. Ketterle and K.J. van Druten, in *Advances in Atomic, Molecular, and Optical Physics*, edited by B. Bederson and H. Walther (Academic Press, San Diego, 1996), Vol. 37, p. 181.

[8] B. DeMarco *et al.*, Phys. Rev. Lett. **82**, 4208 (1999).

[9] C.J. Myatt *et al.*, Phys. Rev. Lett. **78**, 586 (1997).

[10] K. Moelmer, Phys. Rev. Lett. **80**, 1804 (1998); E. Timmermans and R. Côté, *ibid.* **80**, 3419 (1998); W. Geist, L. You, and T.A.B. Kennedy, Phys. Rev. A **59**, 1500 (1999).

[11] G. Modugno *et al.*, Phys. Rev. A (to be published).

[12] U. Schünemann *et al.*, Opt. Commun. **158**, 263 (1998).

[13] F. van Abeelen, B. Verhaar, and A. Moerdijk, Phys. Rev. A **55**, 4377 (1997).

[14] W. Süptitz *et al.*, Opt. Lett. **19**, 1124 (1994); M.S. Santos *et al.*, Phys. Rev. A **52**, R4340 (1995); G.D. Telles *et al.*, *ibid.* **59**, R23 (1999); J.P. Shaffer, W. Chalupczak, and N.P. Bigelow, Phys. Rev. Lett. **82**, 1124 (1999); U. Schlöder *et al.* (unpublished).

[15] G. Ferrari, M.-O. Mewes, F. Schreck, and C. Salomon, Opt. Lett. **24**, 151 (1999).

[16] J. Kawanake, K. Shimizu, H. Tanaka, and F. Shimizu, Phys. Rev. A **48**, R883 (1993); N.W.M. Ritchie *et al.*, *ibid.* **51**, 961 (1995).

[17] W. Ketterle *et al.*, Phys. Rev. Lett. **70**, 2253 (1993).

[18] E.R.I. Abraham, W.I. McAlexander, C.A. Sackett, and R.G. Hulet, Phys. Rev. A **55**, R3299 (1997).

Appendix C

Sympathetic cooling of bosonic and fermionic lithium gases towards quantum degeneracy

F. Schreck, G. Ferrari, K. L. Corwin, J. Cubizolles, L. Khaykovich,
M.-O. Mewes, and C. Salomon
Physical Review A,
Volume **64**, page 011402(R), 8 June 2001.

RAPID COMMUNICATIONS

PHYSICAL REVIEW A, VOLUME 64, 011402(R)

Sympathetic cooling of bosonic and fermionic lithium gases towards quantum degeneracy

F. Schreck, G. Ferrari, K. L. Corwin, J. Cubizolles, L. Khaykovich, M.-O. Mewes, and C. Salomon
Laboratoire Kastler Brossel, Ecole Normale Supérieure, 24 rue Lhomond, 75231 Paris CEDEX 05, France

(Received 16 November 2000; published 8 June 2001)

Sympathetic cooling of two atomic isotopes is experimentally investigated. Using forced evaporation of a bosonic ^{7}Li gas in a magnetic trap, a sample of 1.3×10^5 ^{6}Li fermions has been sympathetically cooled to 9(3) μK, corresponding to 2.2(0.8) times the Fermi temperature. The measured rate constant for two-body inelastic collisions of the ^{7}Li $|2,2\rangle$ state at low magnetic field is $1.0^{+0.8}_{-0.5}\times10^{-14}$ cm^3 s^{-1}.

DOI: 10.1103/PhysRevA.64.011402 PACS number(s): 32.80.Pj, 05.20.Dd, 05.30.Jp, 05.30.Fk

In atomic physics, the combination of laser cooling and evaporative cooling in magnetic traps has been successfully used to reach Bose-Einstein condensation (BEC) in dilute vapors [1,2]. These techniques, however, are not universal. Producing laser light at appropriate wavelengths is sometimes difficult, and laser cooling of molecules remains a challenge. Relying on elastic collisions [3], evaporative cooling fails for fermions at low temperature. Indeed no *s*-wave scattering is allowed for identical fermions, and when the temperature T decreases, the *p*-wave cross section vanishes as T^2 [4].

Sympathetic cooling allows one to overcome these limitations. It uses a buffer gas to cool another species via collisions and was first proposed for two-component plasmas [5]. Often used for cooling ions confined in electromagnetic traps [6,7], it has been applied recently to cool neutral atoms and molecules via cryogenically cooled helium [8]. Sympathetic cooling using ^{87}Rb atoms in two different internal states has led to the production of two overlapping condensates [9]. For fermions, the *s*-wave scattering limitation was overcome by using two distinct Zeeman substates, both of which were evaporatively cooled. This method has been used to reach temperatures on the order of ~300 nK~0.4 T_F [10], where T_F is the Fermi temperature below which quantum effects become prominent. Cold collisions between ^{6}Li and ^{7}Li were analyzed theoretically in [11] and it was predicted that sympathetic cooling of ^{6}Li by contact with ^{7}Li should work efficiently.

In this Rapid Communication, we report on the experimental demonstration of sympathetic cooling of ^{6}Li fermions via collisions with evaporatively cooled ^{7}Li bosons in a magnetic trap. Both species were cooled from 2 mK to $\sim9(3)$ μK, corresponding to $T\sim2.2(0.8)T_F$ where $T_F=(\hbar\overline{\omega}/k_B)(6N)^{1/3}$, $\overline{\omega}$ is the geometric mean of the three oscillation frequencies in the trap, and N is the number of fermions. For these experimental conditions, $T_F\sim4$ μK. This method represents a crucial step towards the production of a strongly degenerate Fermi gas of ^{6}Li and the study of its optical and collisional properties [12,13]. It also opens the way to interesting studies on mixtures of Bose condensates and Fermi gases [14–16]. Finally ^{6}Li is considered a good candidate for the observation of BCS transition [17–19].

A sketch of our apparatus is shown in Fig. 1. First the ^{7}Li and ^{6}Li isotopes are simultaneously captured from a slowed atomic beam and cooled in a magneto-optical trap (MOT) at the center of a Vycor glass cell [20]. On top of this cell is located a small appendage of external dimensions $20\times7\times40$ mm and a wall thickness of 2 mm. The small dimension along y permits the construction of a strongly confining Ioffe-Pritchard (IP) trap using electromagnets. The two-dimensional quadrupole field is created by four copper Ioffe bars (IBs), each consisting of three conductors running at a maximum current of 700 A. Axial confinement is provided by two pinch coils (PCs) in series with two compensation coils (CCs) at 500 A in order to reduce the bias magnetic field. For these currents, the radial gradient is 2.38 kG/cm and the axial curvature is 695 G/cm^2. With a bias field of 15 G, the trap frequencies for ^{7}Li are $\omega_{\rm rad}/2\pi=2.57(4)$ kHz and $\omega_{\rm ax}/2\pi=118(1)$ Hz. The background-limited trap lifetime is 130 s. Atoms are transferred from the MOT region to the IP trap in a magnetic elevator quadrupole trap. The elevator consists of lower quadrupole (LQ) coils (identical with the MOT coils) and upper quadrupole (UQ) coils centered on the IP trap axis, 50 mm above the LQ trap center. The current ratio between the two sets of coils determines the center of the resulting quadrupole trap, allowing the atoms to be lifted by adjusting this ratio.

This trap design allows for both large compression and high atom numbers, two crucial parameters for evaporative cooling. This is particularly important for lithium atoms, since the *s*-wave cross sections at zero energy are at least 16 times smaller than for ^{87}Rb. The scattering length for ^{7}Li in state $|F=2,m_F=2\rangle$ used in our experiments is $-27a_0$ [21]. Finally, all coil currents can be switched off rapidly, allowing the potentials to be turned off nonadiabatically for time-of-flight absorption imaging. In contrast, early Bose-Einstein condensation experiments with ^{7}Li used a permanent magnet trap [22].

We describe now the main steps of our sympathetic cooling experiments (parameters are summarized in Table I). 6×10^9 ^{7}Li and 1.6×10^8 ^{6}Li atoms are captured in ~1 min in the MOT. The relative numbers of ^{7}Li and ^{6}Li can be adjusted by changing the light intensity tuned to each isotope with the laser setup described in [23]. Both isotopes are cooled to ~0.8 mK, optically pumped to the upper hyperfine state, $F=2$ (respectively, $F=3/2$) and captured in the LQ trap with an axial gradient of 400 G/cm. Characterization of the LQ trap with ^{7}Li revealed two time scales for trap losses: a fast one (100 ms) that we attribute to spin relaxation and a slow one (50 s) due to Majorana transitions near the

©2001 The American Physical Society

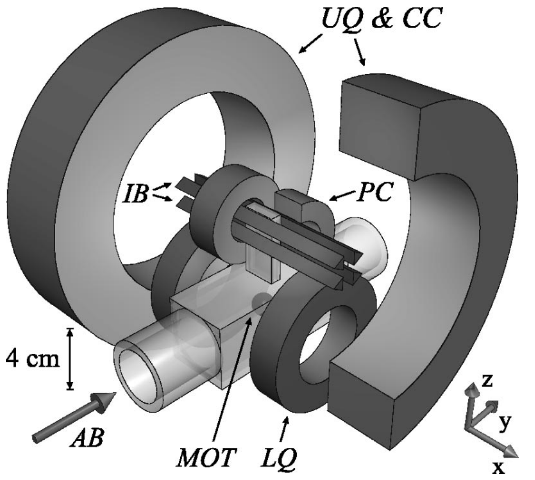

FIG. 1. Experimental setup. Both lithium isotopes are collected from a slow atomic beam (AB) in a magneto-optical trap (MOT) at the center of a glass cell. Atoms are magnetically elevated using lower quadrupole (LQ) and upper quadrupole (UQ) coils in a small appendage. At this site, a strongly confining Ioffe-Pritchard trap consisting of four Ioffe bars (IBs), two pinch coils (PCs) and two compensation coils (CCs) allow evaporative cooling of ^{7}Li to quantum degeneracy and sympathetic cooling of ^{6}Li-^{7}Li mixtures.

trap center. Just before the magnetic elevator stage about 40% of both isotopes remain trapped.

The transfer to the UQ trap is done by increasing the current in the UQ coils to 480 A in 50 ms and ramping off the current in the LQ coils in the next 50 ms. Nearly mode-matched transfer into the IP trap is accomplished by simultaneously switching on the IBs and the PCs while switching off the UQ coils. The transfer efficiency from LQ trap to the IP trap is 15% and is limited by the energy cut due to the narrow dimension of the appendage (3 mm) in the radial direction. High-energy atoms hit the glass cell and are lost. A wider appendage would allow a higher transfer efficiency but at the expense of a reduced radial gradient. Our simulation shows that the chosen size is optimum with respect to the initial collision rate in the IP trap for a temperature of 1 mK in the LQ trap.

After compressing the IP trap to maximum currents and reducing the bias field to 15 G, we obtain 2.5×10^8 ^{7}Li atoms and 1.8×10^7 ^{6}Li atoms at a temperature of 7(3) mK. In these conditions, we have been unsuccessful in reaching runaway evaporation (i.e., increase of collision rate) on ^{7}Li in the presence or absence of ^{6}Li. Because the $|2,2\rangle$ state of ^{7}Li has a negative scattering length, as the collision energy increases, the scattering cross section falls to zero. This occurs at $T_0=8$ mK, i.e., within the *s*-wave energy range [24]. To overcome this limitation, we apply a stage of one-dimensional Doppler cooling of ^{7}Li in the IP trap with a bias field of 430 G using a σ^+-σ^+ laser standing wave aligned along the *x* axis. Each beam has an intensity of 25 μW/cm^2 and is detuned about one natural linewidth below the resonance in the trap. In 1 s of cooling, the temperature in all three dimensions drops by a factor of 4 and the loss of atoms is 15%. In the compressed IP trap, the temperature is now $\sim$2 mK, sufficiently below T_0. Thus at the start of the evaporation, the collision rate is $\sim$15 s^{-1}, i.e., 2000 times the background gas collision rate.

TABLE I. Typical atom numbers and temperatures before and during sympathetic cooling.

	^{7}Li		^{6}Li
	N	T (mK)	*N*
Compressed MOT	6×10^9	0.8	1.6×10^8
Lower quadrupole	2.5×10^9	1	8×10^7
Capture IP trap	3.8×10^8	0.7	1.3×10^7
Compressed IP	3.2×10^8	2	2.5×10^6
End symp. cool.	1.7×10^6	0.03	1.2×10^6

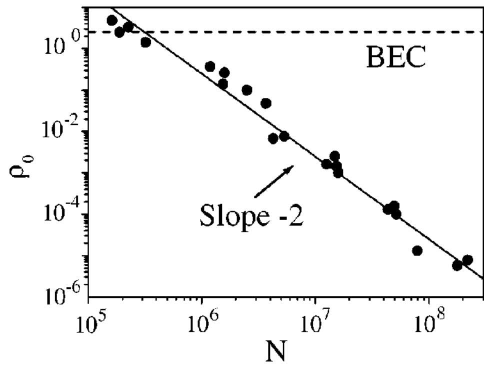

FIG. 2. ^{7}Li peak phase-space density vs number of atoms *N* during single-species evaporation.

Absorption images are taken with 10-μs exposure time, immediately after the trap is turned off and before the cloud can expand. Independent laser systems provide isotope selective probe beams. From these images, the total number of atoms is found, to an accuracy of a factor of 2. The temperature is then deduced from a fit of the cloud size in the axial direction by a Gaussian of standard deviation σ_{ax} and the measured oscillation frequency ω_{ax}. This temperature measurement agrees to within 15% with a time-of-flight measurement of the kinetic energy.

Evaporation is performed exclusively on ^{7}Li. We apply a tunable microwave field near the ^{7}Li hyperfine transition at 803.5 MHz to couple the $|F=2,m_F=2\rangle$ trapped state to the $|F=1,m_F=1\rangle$ untrapped state. To verify the effectiveness of the evaporation process, we first cool ^{7}Li alone in the trap down to the regime of quantum degeneracy; after 15 s of compression of the cloud with a microwave knife fixed at 5.4 mK, we have 2×10^8 atoms at a temperature of 1.2 mK [25]. We then lower the microwave cut energy from this value to $\sim$5 μK in 45 s. The central phase-space density is $\rho_0=n_0\Lambda^3$ where $\Lambda=h(2\pi m k_B T)^{-1/2}$ and n_0 is the peak density. In Fig. 2, ρ_0 is plotted vs atom number at various stages of the evaporation scan. $\rho_0(N)$ is well fitted by a line of slope -2 on a log-log scale, indicating a nearly constant collision rate during forced evaporation. We reached phase-space densities exceeding 2.6 with 5×10^4 atoms at 1.2 μK, meeting the condition for Bose-Einstein condensation. However, due to the effective attractive interaction, the trapped

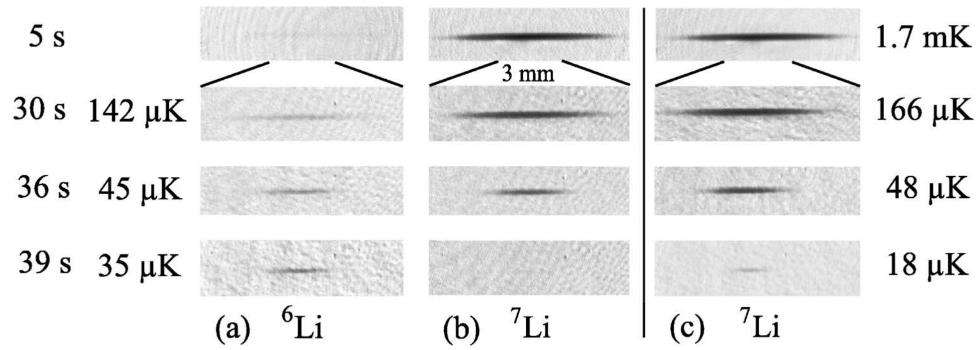

FIG. 3. Images of ^{6}Li and ^{7}Li atom clouds at various stages of sympathetic cooling (a),(b) and during single-species evaporation (c) with identical initial numbers of ^{7}Li atoms. Top images are 1 cm long, the others 3 mm. Temperatures of ^{6}Li (respectively, ^{7}Li alone) are given on the left (right).

condensate is expected to be stable only for atom numbers up to a critical value [26,27], which, in our trap geometry, is limited to a few hundred. Our current imaging system is unable to detect such a small sample. We also observe that the trap lifetime is reduced to 22(4) s at a peak density of 4×10^{12} at/cm^3 and a temperature of 21 μK, well above BEC. We attribute this reduction to dipolar relaxation and obtain a dipolar relaxation rate $\beta_{7-7}=1.0^{+0.8}_{-0.5}10^{-14}$ cm^3 s^{-1} in agreement with the theoretical value 1.6×10^{-14} cm^3 s^{-1} predicted in [28] and comparable to that measured in high magnetic field [29,30].

Using a similar evaporation ramp lasting 40 s with 2.5×10^6 ^{6}Li atoms and 3.2×10^8 ^{7}Li atoms, sympathetic cooling of fermionic ^{6}Li is clearly shown in Fig. 3. The displayed images recorded at various stages of the evaporation ramp for mixtures [(a) and (b)] or for ^{7}Li alone with identical initial number (c). In (a), the optical density of the ^{6}Li cloud is seen to increase considerably because of the reduction in size without apparent loss of atoms, a signature of sympathetic cooling. Comparisons of the cloud sizes between (a) and (b) indicate that ^{6}Li and ^{7}Li are in thermal equilibrium, except for the end of the evaporation. At 39 s, ^{6}Li is at 40 μK, ^{7}Li is not detectable (b), while ^{7}Li alone is at 20 μK (c). This indicates that between 36 and 39 s, the numbers of ^{6}Li and ^{7}Li have become equal. Beyond this point, the temperature of ^{6}Li no longer decreases significantly. The thermal capacity of ^{6}Li soon exceeds that of ^{7}Li, resulting in heating and loss of ^{7}Li during the final stage of forced evaporation (b). Under the same conditions but without ^{6}Li, normal evaporative cooling of ^{7}Li proceeds to a temperature of 18 μK (c) that is below that obtained for ^{6}Li at 39 s, 35 μK (a).

More quantitatively, temperatures and numbers of ^{6}Li and ^{7}Li atoms as a function of the microwave cut energy are plotted in Fig. 4. Above 40 μK, the temperatures of all three clouds are nearly identical, indicating that the collision cross section between the ^{7}Li $|2,2\rangle$ and ^{6}Li $|\frac{3}{2},\frac{3}{2}\rangle$ is not significantly smaller than that of the ^{7}Li $|2,2\rangle$ with itself. This is consistent with the prediction that the scattering length between these states of ^{6}Li and ^{7}Li is $(40.8\pm0.2)a_0$ [11]. In addition, close thermal contact implies that the microwave knife acts the same on the ^{7}Li cloud with or without ^{6}Li present, as expected because the ^{6}Li number is initially a very small fraction of the ^{7}Li number. The ratio between the measured temperatures and the microwave cut energy is 4. At a temperature around 35 μK, the number of ^{7}Li atoms (N_7) has been reduced to the number of ^{6}Li atoms (N_6). As a result the ^{6}Li cloud is no longer cooled and remains at 35 μK.

For classical gases, the decoupling temperature T_D is reached when $N_7\approx N_6$. In the case of ^{7}Li alone, T_7 is approximately proportional to N_7 and so $T_D\propto N_6$. Since $T_F\propto N_6^{1/3}$, the degeneracy parameter $T_D/T_F\propto N_6^{2/3}$, and Fermi degeneracy can be approached by reducing the number of ^{6}Li. Doing this, the highest degeneracy reached after a complete sympathetic cooling evaporation ramp was $T/T_F=2.2(0.8)$ at a temperature of $9(3)\mu$K with 1.3×10^5 ^{6}Li atoms. At this stage we are limited by the detection efficiency of our imaging system.

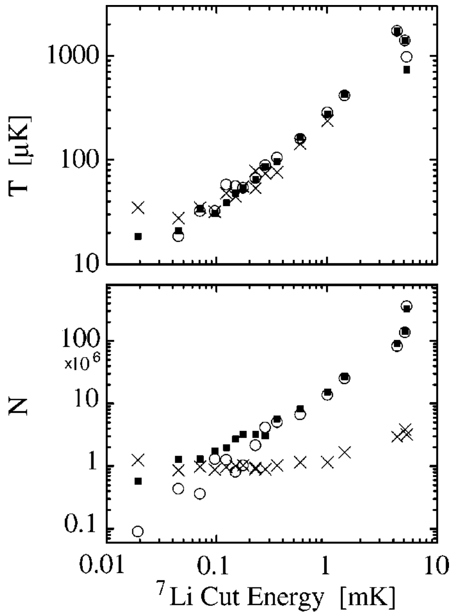

FIG. 4. ^{6}Li (crosses) and ^{7}Li (open circles) temperatures and numbers as a function of the ^{7}Li cut energy. During sympathetic cooling, temperatures are the same down to a decoupling region below which ^{6}Li is no longer cooled. Black squares show ^{7}Li alone with identical parameters. Uncertainty in the x axis is about 0.01 mK.

Finally an important question for studies of mixtures of these degenerate gases is the possibility of interspecies loss mechanisms. We have searched for such losses by recording the ^{6}Li trap lifetimes in the presence and absence of ^{7}Li atoms at a peak density $n_0(^7\mathrm{Li})=2\times10^{11}$ at/cm^3 and a common temperature of 530 μK. With $n_0(^7\mathrm{Li})=4.6n_0(^6\mathrm{Li})$, the lifetimes were, respectively, 73(10) s and 73(8) s, showing no significant difference. We deduce an upper limit for dipolar decay rates, $\beta_{6-7}\leqslant1\times10^{-13}$ cm^{3}s^{-1},$\beta_{6-6}\leqslant4.6\times10^{-13}$ cm^{3}s^{-1}.

In summary we have demonstrated sympathetic cooling of fermionic lithium via evaporation performed on the bosonic Li isotope and obtained temperatures of $2.2(0.8)T_F$. Recently, we have achieved Fermi degeneracy and temperatures of 0.3 T_F. This work will be the subject of a future publication.

We are grateful for the experimental assistance of Fabrice Gerbier and A. Sinatra-Castin, to ANDOR technology for loaning us a camera, and to J. Dalibard, C. Cohen-Tannoudji, G. Shlyapnikov, and D. Guéry-Odelin for discussions. M.-O. M., F. S., and K. C. were financially supported by the EU, by the DAAD, and by MENRT. This work was partially supported by CNRS, Collège de France, DRED, and the EC (TMR Network No. ERB FMRX-CT96-0002). Laboratoire Kastler Brossel is Unité de recherche de l'Ecole Normale Supérieure et de l'Université Pierre et Marie Curie, associée au CNRS.

---

[1] M.H. Anderson *et al.*, Science **269**, 198 (1995).

[2] *Bose-Einstein Condensation in Atomic Gases*, Proceedings of the International School of Physics ''Enrico Fermi,'' edited by M. Inguscio, S. Stringari, and C. Wieman (IOS Press, Amsterdam, 1999).

[3] H.F. Hess, Phys. Rev. B **34**, 3476 (1986).

[4] B. DeMarco *et al.*, Phys. Rev. Lett. **82**, 4208 (1999).

[5] L. Spitzer, *Physics of Fully Ionized Gases* (Interscience, New York, 1962).

[6] R.E. Drullinger *et al.*, Appl. Phys. **22**, 365 (1980).

[7] D.J. Larson *et al.*, Phys. Rev. Lett. **57**, 70 (1986).

[8] J. Kim *et al.*, Phys. Rev. Lett. **78**, 3665 (1997).

[9] C.J. Myatt *et al.*, Phys. Rev. Lett. **78**, 586 (1997).

[10] B. DeMarco and D.S. Jin, Science **285**, 1703 (1999).

[11] F.A. VanAbeleen, B.J. Verhaar, and A.J. Moerdijk, Phys. Rev. A **55**, 4377 (1997).

[12] B. DeMarco and D.S. Jin, Phys. Rev. A **58**, R4267 (1998).

[13] G. Ferrari, Phys. Rev. A **59**, R4125 (1999).

[14] L. Viverit, C.J. Pethick, and H. Smith, Phys. Rev. A **61**, 053605 (1999), and references therein.

[15] K. Molmer, Phys. Rev. Lett. **80**, 1804 (1998).

[16] W. Geist, L. You, and T.A. Kennedy, Phys. Rev. A **59**, 1500 (1999).

[17] H.T. Stoof *et al.*, Phys. Rev. Lett. **76**, 10 (1996).

[18] R. Combescot, Phys. Rev. Lett. **83**, 3766 (1999).

[19] M. Houbiers and H.T.C. Stoof, Phys. Rev. A **59**, 1556 (1999).

[20] M.-O. Mewes, G. Ferrari, F. Schreck, A. Sinatra, and C. Salomon, Phys. Rev. A **61**, 011403(R) (1999).

[21] E.R.I. Abraham, C.A. Sackett, and R.G. Hulet, Phys. Rev. A **55**, R3299 (1997).

[22] C.C. Bradley *et al.*, Phys. Rev. Lett. **75**, 1687 (1995).

[23] G. Ferrari, M.-O. Mewes, F. Schreck, and C. Salomon, Opt. Lett. **24**, 151 (1999).

[24] J. Dalibard, in *Bose-Einstein Condensation in Atomic Gases* (Ref. [2]).

[25] This compression phase was not used in ^{6}Li cooling.

[26] P.A. Ruprecht *et al.*, Phys. Rev. A **51**, 4704 (1995).

[27] C.C. Bradley, C.A. Sackett, and R.G. Hulet, Phys. Rev. Lett. **78**, 985 (1997).

[28] A.J. Moerdijk and B.J. Verhaar, Phys. Rev. A **53**, R19 (1996).

[29] J.M. Gerton, C.A. Sackett, B.J. Frew, and R.G. Hulet, Phys. Rev. A **59**, 1514 (1999).

[30] The definition of β is given by $\dot{N}=-\beta n_0 N/\sqrt{2}-\alpha N$.

Appendix D

Quasipure Bose-Einstein Condensate Immersed in a Fermi Sea

F. SCHRECK, L. KHAYKOVICH, K. L. CORWIN, G. FERRARI, T. BOURDEL, J. CUBIZOLLES, AND C. SALOMON
Physical Review Letters,
Volume **87**, page 080403, 7 August 2001.

Quasipure Bose-Einstein Condensate Immersed in a Fermi Sea

F. Schreck, L. Khaykovich, K. L. Corwin, G. Ferrari,* T. Bourdel, J. Cubizolles, and C. Salomon
Laboratoire Kastler Brossel, Ecole Normale Supérieure, 24 rue Lhomond, 75231 Paris CEDEX 05, France

(Received 13 July 2001; published 7 August 2001)

We report the observation of coexisting Bose-Einstein condensate (BEC) and Fermi gas in a magnetic trap. With a very small fraction of thermal atoms, the ^{7}Li condensate is quasipure and in thermal contact with a ^{6}Li Fermi gas. The lowest common temperature is 0.28 μK $\simeq 0.2(1)T_C = 0.2(1)T_F$ where T_C is the BEC critical temperature and T_F the Fermi temperature. The ^{7}Li condensate has a one-dimensional character.

DOI: 10.1103/PhysRevLett.87.080403 PACS numbers: 05.30.Fk, 03.75.–b, 05.30.Jp, 32.80.Pj

Bose-Einstein condensation (BEC) of atomic gases has been very actively studied in recent years [1,2]. The dilute character of the samples and the ability to control the atom-atom interactions allowed a detailed comparison with the theories of quantum gases. Atomic Fermi gases, on the other hand, have only been investigated experimentally for two years [3–5]. They are predicted to possess intriguing properties and may offer an interesting link with the behavior of electrons in metals and semiconductors, and the possibility of Cooper pairing [6] such as in superconductors and neutron stars. Mixtures of bosonic and fermionic quantum systems, with the prominent example of ^{4}He-^{3}He fluids, have also stimulated intense theoretical and experimental activity [7]. This has led to new physical effects including phase separation, influence of the superfluidity of the Bose system on the Fermi degeneracy, and to new applications such as the dilution refrigerator [7–9].

In this paper, we present a new mixture of bosonic and fermionic systems, a stable Bose-condensed gas of ^{7}Li atoms in the internal state $|F = 1, m_F = -1\rangle$ immersed in a Fermi sea of ^{6}Li atoms in $|F = 1/2, m_F = -1/2\rangle$ (Fig. 1). Confined in the same magnetic trap, both atomic species are in thermal equilibrium with a temperature of $0.2(1)T_F \ll T_C$. All previous experiments performed with ^{7}Li in $|F = 2, m_F = 2\rangle$ had condensate numbers limited to $N \leq 1400$ because of the negative scattering length, $a = -1.4$ nm, in this state [10,11]. Our condensate is produced in a state which has a positive, but small, scattering length, $a = +0.27$ nm [12]. The number of condensed atoms is typically 10^4, and BEC appears unambiguously both in the position distribution in the trap and in the standard time of flight images.

Because of the symmetrization postulate, colliding fermions have no s-wave scattering at low energy. In the low temperature domain of interest, the p-wave contribution vanishes. Our method for producing simultaneous quantum degeneracy for both isotopes of lithium is sympathetic cooling [4,5]; s-wave collisions between two different atomic isotopes are allowed and rf evaporation selectively removes from the trap high energy atoms of one species. Elastic collisions subsequently restore thermal equilibrium of the two-component gas at a lower temperature.

Our experimental setup has been described in detail in [4,13]. A mixture of ^{6}Li and ^{7}Li atoms is loaded from a magneto-optical trap into a strongly confining Ioffe-Pritchard trap at a temperature of about 2 mK. As depicted in Fig. 1, this relatively high temperature precludes direct magnetic trapping of the atoms in their lower hyperfine state because of the shallow magnetic trap depth, 2.4 mK for ^{7}Li in $|F = 1, m_F = -1\rangle$ and 0.2 mK for ^{6}Li in $|F = 1/2, m_F = -1/2\rangle$. Therefore we proceed in two steps. Both isotopes are first trapped and cooled in their upper hyperfine states. The ^{7}Li $|F = 2, m_F = 2\rangle$ and ^{6}Li $|F = 3/2, m_F = 3/2\rangle$ states have no energy maximum as a function of the magnetic field (Fig. 1). Thus the trap depth can be large. Evaporation is performed selectively on ^{7}Li using a microwave field near 803 MHz that couples $|F = 2, m_F = 2\rangle$ to $|F = 1, m_F = 1\rangle$. When both gases are cooled to a common temperature of about 9 μK, atoms are transferred using a combination of microwave and rf pulses into states $|F = 1, m_F = -1\rangle$ and $|F = 1/2, m_F = -1/2\rangle$ with an energy far below their respective trap depths. Evaporative cooling is then resumed until ^{7}Li reaches the BEC threshold.

In the first series of experiments, both Li isotopes are trapped in their higher hf states. ^{6}Li is sympathetically cooled to Fermi degeneracy by performing 30 s of

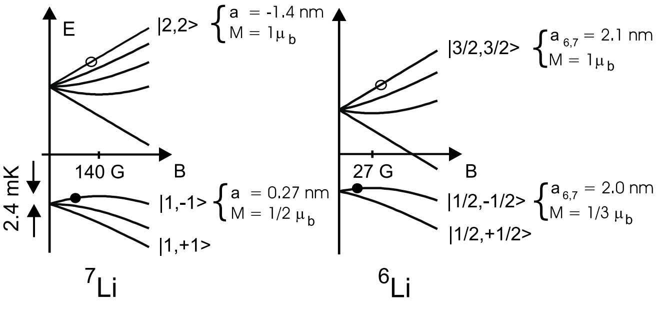

FIG. 1. Energy levels of ^{7}Li and ^{6}Li ground states in a magnetic field. Relevant scattering lengths, a, and magnetic moments, M, are given. μ_b is the Bohr magneton. The $|1, -1\rangle$ state (respectively, $|1/2, -1/2\rangle$) is trapped only in fields weaker than 140 G (respectively, 27 G). Open circles: first cooling stage; black circles: second cooling stage.

0031-9007/01/87(8)/080403(4)$15.00

© 2001 The American Physical Society

evaporative cooling on ^{7}Li [4]. Trap frequencies for ^{7}Li are $\omega_{\rm rad} = 2\pi \times 4000(10)$ s^{-1} and $\omega_{\rm ax} = 2\pi \times 75.0(1)$ s^{-1} with a bias field of 2 G. Absorption images of both isotopes are recorded on a single CCD camera with a resolution of 10 μm. Images are taken quasisimultaneously (only 1 ms apart) in the trap or after a time of flight expansion. Probe beams have an intensity below saturation and a common duration of 30 μs. Typical *in situ* absorption images in the quantum regime can be seen in Fig. 2. Here the temperature T is 1.4(1) μK and $T/T_{\rm F} = 0.33(5)$, where the Fermi temperature $T_{\rm F}$ is $(\hbar\bar{\omega}/k_{\rm B})(6N_{\rm F})^{1/3}$, with $\bar{\omega}$ the geometric mean of the three oscillation frequencies in the trap and $N_{\rm F}$ the number of fermions. For images recorded in the magnetic trap, the common temperature is measured from the spatial extent of the bosonic cloud in the axial direction since the shape of the Fermi cloud is much less sensitive to temperature changes when $T/T_{\rm F} < 1$ [14]. The spatial distributions of bosons and fermions are recorded after a 1 s thermalization stage at the end of the evaporation. As the measured thermalization time constant between the two gases, 0.15 s, is much shorter than 1 s, the two clouds are in thermal equilibrium [15]. Both isotopes experience the same trapping potential. Thus the striking difference between the sizes of the Fermi and Bose gases [5] is a direct consequence of Fermi pressure. The measured axial profiles in Fig. 2 are in excellent agreement with the calculated ones (solid lines) for a Bose distribution at the critical temperature $T_{\rm C}$. In our steepest traps, Fermi temperatures as high as 11 μK with a degeneracy of $T/T_{\rm F} = 0.36$ are obtained. This $T_{\rm F}$ is a factor of 3 larger than the single photon recoil temperature at 671 nm, opening interesting possibilities for light scattering experiments [16].

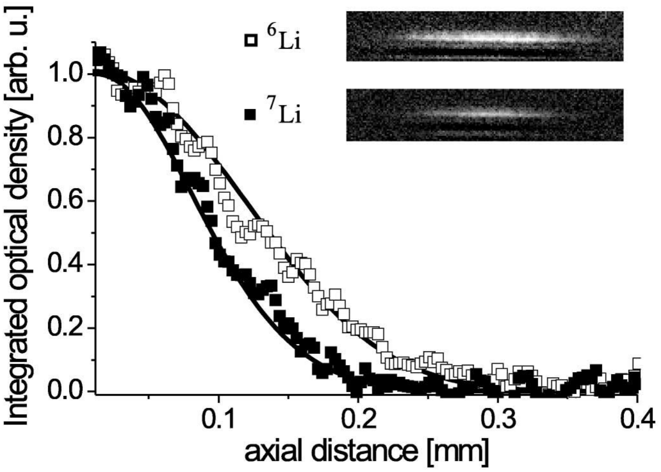

FIG. 2. Observation of Fermi pressure. Absorption images in the trap and spatial distributions integrated over the vertical direction of 8.1×10^4 ^{6}Li and 2.7×10^4 ^{7}Li atoms in their higher hyperfine states. The temperature is 1.4(1) μK $= 1.1(2)T_{\rm C}$ for the bosons and $0.33(5)T_{\rm F}$ for the fermions. Solid lines are the expected Bose and Fermi distributions.

Our highest Fermi degeneracy in ^{6}Li $|F = 3/2, m_F = 3/2\rangle$, achieved by cooling with ^{7}Li $|F = 2, m_F = 2\rangle$, is $T/T_{\rm F} = 0.25(5)$ with $T_{\rm F} = 4$ μK, very similar to Ref. [5]. We observe that the boson temperature cannot be lowered below $T_{\rm C}$. Indeed, because of the negative scattering length in ^{7}Li $|F = 2, m_F = 2\rangle$, for our trap parameters, collapse of the condensate occurs when its number reaches ~300 [10]. Since sympathetic cooling stops when the heat capacity of the bosons becomes lower than that of the fermions, this limits the Fermi degeneracy to about 0.3 [5].

In order to explore the behavior of a Fermi sea in the presence of a BEC with a temperature well below $T_{\rm C}$, we perform another series of experiments with both isotopes trapped in their lower hf state where the positive ^{7}Li scattering length (Fig. 1) allows the formation of a stable BEC with high atom numbers. To avoid large dipolar relaxation, ^{6}Li must also be in its lower hf state [17]. First, sympathetic cooling down to ~9 μK is performed on the ^{7}Li $|F = 2, m_F = 2\rangle$, ^{6}Li $|F = 3/2, m_F = 3/2\rangle$ mixture as before. Then, to facilitate state transfer, the trap is adiabatically opened to frequencies $\omega_{\rm rad} = 2\pi \times 100$ s^{-1} and $\omega_{\rm ax} = 2\pi \times 5$ s^{-1} (for ^{7}Li, $F = 2$).

The transfer of each isotope uses two radio frequency π pulses. The first pulse at 803 MHz for ^{7}Li (228 MHz for ^{6}Li) transfers the bosons from $|2, 2\rangle$ to $|1, 1\rangle$ (the fermions from $|3/2, 3/2\rangle$ to $|1/2, 1/2\rangle$). These states are magnetically untrapped states (see Fig. 1). The second π pulse at 1 MHz for ^{7}Li (1.3 MHz for ^{6}Li) transfers the bosons to $|1, -1\rangle$, a magnetically trapped state (the fermions to $|1/2, -1/2\rangle$). Adiabatic opening of the trap cools the cloud. It decreases the energy broadening of the resonance and gives more time for the passage through untrapped states. The durations of the π pulses are 17 and 13 μs and more than 70% of each isotope is transferred. Finally the trap is adiabatically recompressed to the steepest confinement giving $\omega_{\rm rad} = 2\pi \times 4970(10)$ s^{-1} and $\omega_{\rm ax} = 2\pi \times 83(1)$ s^{-1} for ^{7}Li $|F = 1, m_F = -1\rangle$, compensating for the reduced magnetic moment.

Because of the very large reduction of the ^{7}Li s-wave scattering cross section from the $F = 2$ to the $F = 1$ state (a factor ~27 [17]), we were unable to reach runaway evaporation with ^{7}Li atoms alone in $F = 1$. In contrast, the ^{6}Li/^{7}Li cross section is ~27 times higher than the ^{7}Li/^{7}Li one [12,17]. We therefore use ^{6}Li atoms as a mediating gas to increase the thermalization rate of both gases. Two different methods were used to perform the evaporation. The first consists of using two rf ramps on the hf transitions of ^{6}Li (from $|1/2, -1/2\rangle$ to $|3/2, -3/2\rangle$) and ^{7}Li (from $|1, -1\rangle$ to $|2, -2\rangle$), which we balanced to maintain roughly equal numbers of both isotopes. After 10 s of evaporative cooling, Bose-Einstein condensation of ^{7}Li occurs together with a ^{6}Li degenerate Fermi gas (Fig. 3). Surprisingly, a single 25 s ramp performed only on ^{6}Li achieved the same results. In this case the equal number condition was fulfilled because of the reduced lifetime of the ^{7}Li cloud that we attribute to dipolar collisional loss [17]. The duration of the rf evaporation was matched to

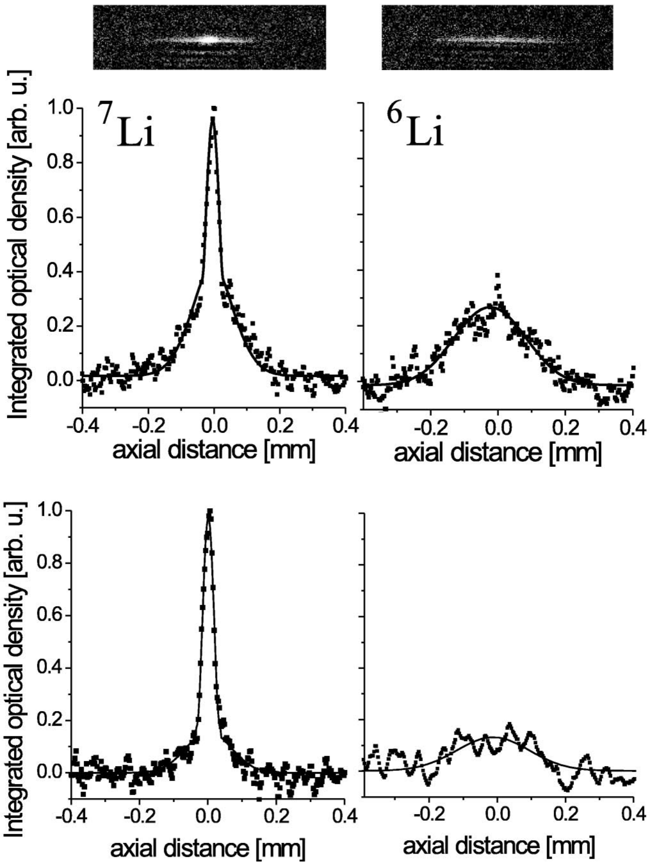

FIG. 3. Mixture of Bose and Fermi gases. Top: *In situ* spatial distributions after sympathetic cooling with $N_B = 3.5 \times 10^4$ and $N_F = 2.5 \times 10^4$. The Bose condensed peak (8.5×10^3 atoms) is surrounded by the thermal cloud which allows the determination of the common temperature: $T = 1.6\ \mu K = 0.87 T_C = 0.57 T_F$. The Fermi distribution is wider because of the smaller magnetic moment and Fermi pressure. Bottom: profiles with a *quasipure* condensate, with $N_B = 10^4$, $N_F = 4 \times 10^3$. The barely detectable thermal cloud indicates a temperature of $\simeq 0.28\ \mu K \simeq 0.2(1) T_C = 0.2(1) T_F$.

this loss rate. In the following we concentrate on this second, and simpler, evaporation scheme, sympathetic cooling of ^{7}Li by evaporative cooling of ^{6}Li.

In Fig. 3 *in situ* absorption images of bosons and fermions at the end of the evaporation are shown. The bosonic distribution shows the typical double structure: a strong and narrow peak forms the condensate at the center, surrounded by a much broader distribution, the thermal cloud. As the Fermi distribution is very insensitive to temperature, this thermal cloud is a very useful tool for the determination of the common temperature. Note that, as cooling was performed only on ^{6}Li atoms, the temperature measured on ^{7}Li cannot be lower than the temperature of the fermions. Measuring N_B, N_F, the condensate fraction N_0/N_B, and $\bar{\omega}$, we determine the quantum degeneracy of the Bose and Fermi gases. In Fig. 3 (top), the temperature is just below T_C, $T = 1.6\ \mu K = 0.87 T_C = 0.57 T_F$. In Fig. 3 (bottom) on the contrary, the condensate is quasipure; $N_0/N_B = 0.77$; the thermal fraction is near our detectivity limit, indicating a temperature of $\simeq 0.28\ \mu K \leq 0.2 T_C = 0.2(1) T_F$ with $N_B = 10^4$ bosons and 4×10^3 fermions. The condensate fraction N_0/N_B as a function of T/T_C is shown in Fig. 4(a), while the size of the fermi gas as a function of T/T_F is shown in Fig. 4(b). With the strong anisotropy ($\omega_{rad}/\omega_{ax} = 59$) of our trap, the theory including anisotropy and finite number effects differs significantly from the thermodynamic limit [2], in agreement with our measurements even though there is a 20% systematic uncertainty on our determination of T_C and T_F. We have also obtained samples colder than those presented in Fig. 4, for which the ^{7}Li thermal fraction is below our detectivity floor, indicating $T < 0.2 T_C \simeq 0.2 T_F$. Clearly a more sensitive thermal probe is required now to investigate this temperature domain. An elegant method relies on the measurement of thermalization rates with impurity atoms including Pauli blocking [18,19].

Because of the small scattering length, this ^{7}Li condensate has interesting properties. Time of flight images, performed after expansion times of 0–10 ms with $N_0 = 10^4$ condensed atoms, reveal that the condensate is one dimensional (1D). In contrast to condensates in the Thomas-Fermi (TF) regime, where the release of interaction energy

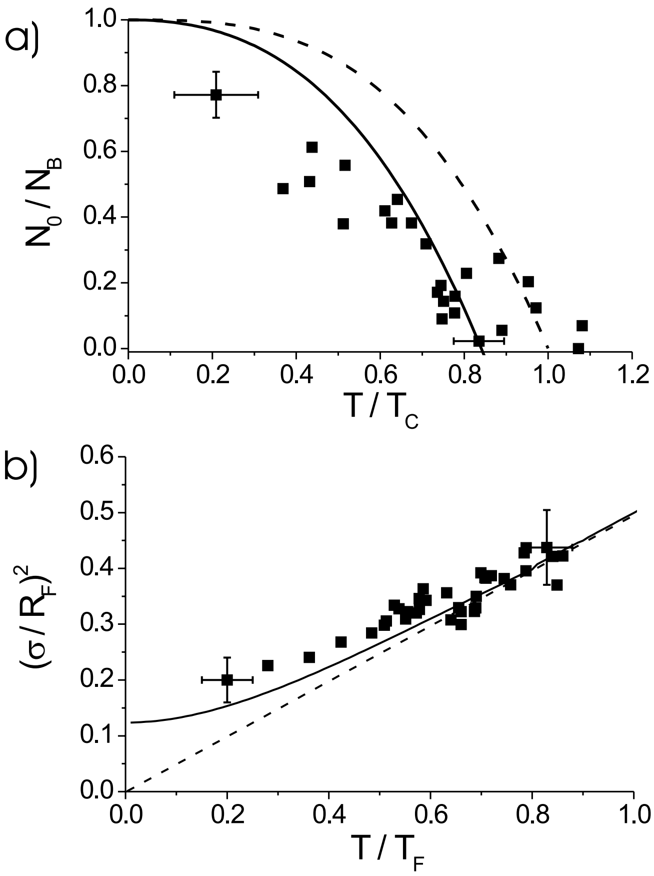

FIG. 4. Temperature dependence of mixtures of quantum gases: (a) normalized BEC fraction as a function of T/T_C. Dashed line: theory in the thermodynamic limit. Solid line: theory including finite size and trap anisotropy [2]; (b) fermion cloud size: variance of Gaussian fit divided by the square of Fermi radius $R_F^2 = 2 k_B T_F / M \omega_{ax}^2$ as a function of T/T_F. Solid line: theory. Dashed line: Boltzmann gas.

leads to a fast increase in radial size, our measurements agree to better than 5% with the time development of the radial ground state wave function in the harmonic magnetic trap (Fig. 5). This behavior is expected when the chemical potential μ satisfies $\mu < \hbar\omega_{\mathrm{rad}}$ [20]. Searching for the ground state energy of the many-body system with a Gaussian ansatz radially and TF shape axially [20], we find that the mean field interaction increases the size of the Gaussian by ≈3%. The calculated TF radius is 28 μm or 7 times the axial harmonic oscillator size and is in good agreement with the measured radius, 30 μm in Fig. 3. Thus with $\mu = 0.45\hbar\omega_{\mathrm{rad}}$, the gas is described as an ideal gas radially but is in the TF regime axially. This 1D situation has also been realized recently in sodium condensates [21].

What are the limits of this BEC-Fermi gas cooling scheme? First, the $1/e$ condensate lifetime of about 3 s in this steep trap will limit the available BEC-Fermi gas interaction time. Second, the boson-fermion mean field interaction can induce a spatial phase separation [8] that prevents thermal contact between ^{7}Li and ^{6}Li. Using the method of [8] developed for $T = 0$, we expect, for the parameters of Fig. 3 (top), that the density of fermions is only very slightly modified by the presence of the condensate in accordance with our observations. Third, because of the superfluidity of the condensate, impurity atoms (such as ^{6}Li), which move through the BEC slower than the sound velocity v_c, are no longer scattered [9,22]. When the Fermi velocity v_F becomes smaller than v_c, cooling occurs only through collisions with the bosonic thermal cloud, thus slowing down drastically. With 10^4 condensed atoms, $v_c \simeq 0.9$ cm/s. The corresponding temperature where superfluid decoupling should occur is ≃100 nK, a factor of 14 lower than T_F.

In summary, we have produced a new mixture of Bose and Fermi quantum gases. Future work will explore the degeneracy limits of this mixture. Phase fluctuations of the 1D ^{7}Li condensate should also be detectable via density fluctuations in time of flight images, as recently reported in [23]. The transfer of the BEC into $|F = 2, m_F = 2\rangle$ with negative a should allow the production of bright solitons and of large unstable condensates where interesting and still unexplained dynamics has been recently observed [11,24]. Finally, the large effective attractive interaction between ^{6}Li $|F = 1/2, m_F = +1/2\rangle$ and $|F = 1/2, m_F = -1/2\rangle$ makes this atom an attractive candidate for searching for BCS pairing at lower temperatures [6].

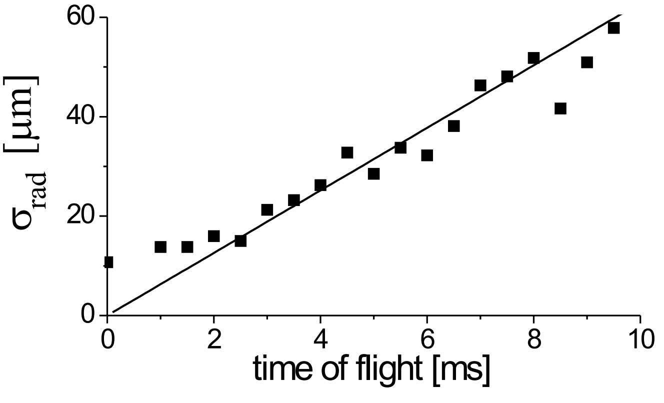

FIG. 5. Signature of 1D condensate. Radial size of expanding condensates with 10^4 atoms as a function of time of flight. The straight line is the expected behavior for the expansion of the ground state radial harmonic oscillator.

We are grateful to Y. Castin, J. Dalibard, C. Cohen-Tannoudji, and G. Shlyapnikov for useful discussions. F. S. and K. L. C. were supported by the DAAD and by MENRT. This work was supported by CNRS, Collège de France and Région Ile de France. Laboratoire Kastler Brossel is *Unité de recherche de l'Ecole Normale Supérieure et de l'Université Pierre et Marie Curie, associée au CNRS.*

---

*Present address: LENS-INFM, Largo E. Fermi 2, Firenze 50125 Italy.

[1] *Bose-Einstein Condensation in Atomic Gases,* Proceedings of the International School of Physics "Enrico Fermi," edited by M. Inguscio, S. Stringari, and C. E. Wieman (IOS Press, Amsterdam, 1999).
[2] F. Dalfovo *et al.,* Rev. Mod. Phys. **71**, 463 (1999).
[3] B. DeMarco and D. S. Jin, Science **285**, 1703 (1999).
[4] F. Schreck *et al.,* Phys. Rev. A **64**, 011402R (2001).
[5] A. G. Truscott *et al.,* Science **291**, 2570 (2001).
[6] H. T. C. Stoof and M. Houbiers, in *Bose-Einstein Condensation in Atomic Gases* (Ref. [1]), p. 537; R. Micnas *et al.,* Rev. Mod. Phys. **62**, 113 (1990).
[7] C. Ebner and D. O. Edwards, Phys. Rep. **2C**, 77 (1970).
[8] K. Mølmer, Phys. Rev. Lett. **80**, 1804 (1998).
[9] E. Timmermans and R. Côté, Phys. Rev. Lett. **80**, 3419 (1998).
[10] C. C. Bradley, C. A. Sackett, and R. G. Hulet, Phys. Rev. Lett. **78**, 985 (1997).
[11] J. M. Gerton *et al.,* Nature (London) **408**, 692 (2000).
[12] R. G. Hulet (private communication).
[13] M.-O. Mewes *et al.,* Phys. Rev. A **61**, 011403R (2000).
[14] D. A. Butts and D. S. Rokhsar, Phys. Rev. A **55**, 4346 (1997).
[15] In this measurement, we abruptly prepare an out of equilibrium ^{7}Li energy distribution in the trap using the microwave evaporation knife and measure the time needed to restore thermal equilibrium through the evolution of the axial size of the ^{7}Li and ^{6}Li clouds.
[16] T. Busch *et al.,* Europhys. Lett. **44**, 755 (1998); B. DeMarco and D. S. Jin, Phys. Rev. A **58**, 4267 (1998).
[17] F. A. Van Abeelen, B. J. Verhaar, and A. J. Moerdijk, Phys. Rev. A **55**, 4377 (1997).
[18] G. Ferrari, Phys. Rev. A **59**, R4125 (1999).
[19] B. DeMarco, S. B. Papp, and D. S. Jin, Phys. Rev. Lett. **86**, 5409 (2001).
[20] D. S. Petrov, G. V. Shlyapnikov, and J. T. M. Walraven, Phys. Rev. Lett. **85**, 3745 (2000).
[21] A. Görlitz *et al.,* cond-mat/0104549.
[22] A. P. Chikkatur *et al.,* Phys. Rev. Lett. **85**, 483 (2000).
[23] S. Dettmer *et al.,* cond-mat/0105525.
[24] J. L. Roberts *et al.,* Phys. Rev. Lett. **86**, 4211 (2001).

.

Bibliography

[1] S.N. Bose. Plancks Gesetz und Lichtquantenhypothese. *Z. Phys.*, **26**, 178, (1924).

[2] A. Einstein. Quantentheorie des einatomigen idealen Gases. *Kgl. Preuss. Akad. Wiss.*, , 261, (1924).

[3] A. Einstein. Quantentheorie des einatomigen idealen Gases. Zweite Abhandlung. *Sitzungsberg. Kgl. Preuss. Akad. Wiss.*, , 3, (1925).

[4] V. Bagnato, D. E. Pritchard, and D. Klepner. Bose-Einstein condensation in an external potential. *Phys. Rev. A*, **35**, 4354, (1987).

[5] C. Ebner and D.O. Edwards. *Phys. Rep.*, **2C**, 77, (1970).

[6] P. G. de Gennes. *Superconductivity of Metals and Alloys.* Advanced Book Classics, (1989).

[7] M. H. Anderson, J. R. Ensher, M. R. Matthews, C. E. Wieman, and E. A. Cornell. Obervation of Bose-Einstein condensation in a dilute atomic vapor. *Science*, **269**, 198, (1995).

[8] K. B. Davis, M.-O. Mewes, M. R. Andrews, N. J. van Druten, D. S. Durfee, D. M. Kurn, and W. Ketterle. Bose-Einstein condensation in a gas of sodium atoms. *Phys. Rev. Lett.*, **75**, 3969, (1995).

[9] E.P. Gross. *Nuovo Cimento*, **20**, 454, (1961).

[10] L.P. Pitaevski. *Sov. Phys. JETP*, **13**, 451, (1961).

[11] J. M. Gerton, D. Strekalov, I. Prodan, and R. G. Hulet. Direct Observation of Growth and Collapse of a Bose-Einstein Condensate with Attractive Interactions. *Nature*, **408**, 692, (2000).

[12] J. L. Roberts, N. R. Claussen, S. L. Cornish, E. A. Donley, E. A. Cornell, and C. E. Wieman. Controlled Collapse of a Bose-Einstein Condensate. *Phys. Rev. Lett.*, **86**, 4211, (2001).

[13] J. R. Ensher, D. S. Jin, M. R. Matthews, C. E. Wieman, and E. A. Cornell. Bose-Einstein Condensation in a Dilute Gas: Measurement of Energy and Ground-State Occupation. *Phys. Rev. Lett.*, **77**, 4984, (1996).

[14] Y. Castin and R. Dum. Bose-Einstein Condensates in Time Dependant Traps. *Phys. Rev. Lett.*, **77**, 5315, (1996).

[15] M. R. Andrews, C. G. Townsend, H.-J. Miesner, D. S. Durfee, D. M. Kurn, and W. Ketterle. Observation of Interference Between Two Bose Condensates. *Science*, **275**, 637, (1997).

[16] M.-O. Mewes, M. R. Andrews, D. M. Kurn, D. S. Durfee, C. G. Townsend, and W. Ketterle. Output Coupler for Bose-Einstein Condensed Atoms. *Phys. Rev. Lett.*, **78**, 582, (1997).

[17] I. Bloch, T. W. Hänsch, and T. Esslinger. Atom Laser with a cw Output Coupler. *Phys. Rev. Lett.*, **82**, 3008, (1999).

[18] M.-O. Mewes, M. R. Andrews, N. J. van Druten, D. M. Kurn, D. S. Durfee, C. G. Townsend, and W. Ketterle. Collective Excitations of a Bose-Einstein Condensate in a Magnetic Trap. *Phys. Rev. Lett.*, **77**, 988, (1996).

[19] O. M. Maragò, S. A. Hopkins, J. Arlt, E. Hodby, G. Hechenblaikner, and C. J. Foot. Observation of the Scissors Mode and Evidence for Superfluidity of a Trapped Bose-Einstein Condensed Gas. *Phys. Rev. Lett.*, **84**, 2056, (2000).

[20] L. Deng, E. W. Hagley, J. Denschlag, J. E. Simsarian, Mark Edwards, Charles W. Clark, K. Helmerson, S. L. Rolston, and W. D. Phillips. Temporal, Matter-Wave-Dispersion Talbot Effect. *Phys. Rev. Lett.*, **83**, 5407, (1999).

[21] S. Inouye, R. F. Löw, S. Gupta, T. Pfau, A. Görlitz, T. L. Gustavson, D. E. Pritchard, and W. Ketterle. Amplification of Light and Atoms in a Bose-Einstein Condensate. *Phys. Rev. Lett.*, **85**, 4225, (2000).

[22] C. Raman, M. Köhl, R. Onofrio, D. S. Durfee, C. E. Kuklewicz, Z. Hadzibabic, and W. Ketterle. Evidence for a Critical Velocity in a Bose-Einstein Condensed Gas. *Phys. Rev. Lett.*, **83**, 2502, (1999).

[23] D. S. Hall, M. R. Matthews, J. R. Ensher, C. E. Wieman, and E. A. Cornell. Dynamics of Component Separation in a Binary Mixture of Bose-Einstein Condensates. *Phys. Rev. Lett.*, **81**, 1539, (1998).

[24] J. Stenger, S. Inouye, D. M. Stamper-Kurn, H.-J. Miesner, A. P. Chikkatur, and W. Ketterle. Spin domains in ground-state Bose-Einstein condensates. *Nature*, **396**, 345, (1998).

[25] S. Burger, K. Bongs, S. Dettmer, W. Ertmer, , A. Sanpera K. Sengstock, G. V. Shlyapnikov, and M. Lewenstein. Dark Solitons in Bose-Einstein Condensates. *Phys. Rev. Lett.*, **83**, 5198, (1999).

[26] J.E. Simsarian J. Denschlag, D.L. Feder, C.W. Clark, L.A. Collins, J. Cubizolles, L. Deng, E.W. Hagley, K. Helmerson, W.P. Reinhardt, S.L. Rolston, B.I. Schneider, and W.D. Phillips. Generating solitons by phase engineering of a Bose-Einstein condensate. *Science*, **287**, 97, (2000).

[27] Z. Dutton, M. Budde, C. Slowe, and L. V. Hau. Observation of Quantum Shock Waves Created with Ultra- Compressed Slow Light Pulses in a Bose-Einstein Condensate. *Science*, **293**, 663, (2001).

[28] M. R. Matthews, B. P. Anderson, P. C. Haljan, D. S. Hall, C. E. Wieman, and E. A. Cornell. Vortices in a Bose-Einstein Condensate. *Phys. Rev. Lett.*, **83**, 2498, (1999).

[29] K. W. Madison, F. Chevy, W. Wohlleben, and J. Dalibard. Vortex Formation in a Stirred Bose-Einstein Condensate. *Phys. Rev. Lett.*, **84**, 806, (2000).

[30] J. R. Abo-Shaeer, C. Raman, J. M. Vogels, and W. Ketterle. Observation of Vortex Lattices in Bose-Einstein Condensates. *Science*, **292**, 476, (2001).

[31] A. Görlitz, J.M. Vogels, A.E. Leanhardt, C. Raman, T.L. Gustavson, J.R. Abo-Shaeer, A.P. Chikkatur, S. Gupta, S. Inouye, T.P. Rosenband, D.E. Pritchard, and W. Ketterle. Realization of Bose-Einstein condensates in lower dimensions. *Phys. Rev. Lett.*, **87**, 130402, (2001).

[32] F. Schreck, L. Khaykovich, K. L. Corwin, G. Ferrari, T. Bourdel, J. Cubizolles, and C. Salomon. Quasipure Bose-Einstein Condensate Immersed in a Fermi Sea. *Phys. Rev. Lett.*, **87**, 080403, (2001).

[33] M. Greiner, I. Bloch, O. Mandel, T. W. Hänsch, and T. Esslinger. Exploring Phase Coherence in a 2D Lattice of Bose-Einstein Condensates. *Phys. Rev. Lett.*, **87**, 160405, (2001).

[34] M. D. Barrett, J. A. Sauer, and M. S. Chapman. All-Optical Formation of an Atomic Bose-Einstein Condensate. *Phys. Rev. Lett.*, **87**, 010404, (2001).

[35] H. Ott, J. Fortagh, A. Grossmann, and C. Zimmermann. Bose-Einstein Condensation in a Surface Micro Trap. *Phys. Rev. Lett.*, **87**, 230401, (2001).

[36] W. Hänsel, P. Hommelhoff, T. W. Hänsch, and J. Reichel. Bose-Einstein condensation on a microelectronic chip. *Nature*, **413**, 498, (2001).

[37] D. Müller, D. Z. Anderson, R. J. Grow, P. D. D. Schwindt, and E. A. Cornell. Guiding Neutral Atoms Around Curves with Lithographically Patterned Current-Carrying Wires. *Phys. Rev. Lett.*, **83**, 5194, (1999).

[38] M.-O. Mewes, M. R. Andrews, N. J. van Druten, D. M. Kurn, D. S. Durfee, and W. Ketterle. Bose-Einstein Condensation in a Tightly Confining dc Magnetic Trap. *Phys. Rev. Lett.*, **77**, 416, (1996).

[39] C. C. Bradley, C. A. Sackett, and R. G. Hulet. Analysis of *in situ* images of Bose-Einstein condensates of lithium. *Phys. Rev. A*, **55**, 3951, (1997).

[40] D. G. Fried, T. C. Killian, L. Willmann, D. Landhuis, S. C. Moss, D. Kleppner, and T.J. Greytak. Bose-Einstein Condensation of Atomic Hydrogen. *Phys. Rev. Lett.*, **81**, 3811, (1998).

[41] A. Robert, O. Sirjean, A. Browaeys, J. Poupard, S. Nowak, D. Boiron, C. I. Westbrook, and A. Aspect. A Bose-Einstein Condensate of Metastable Atoms. *Phys. Rev. Lett.*, **292**, 461, (2001).

[42] F. Pereira Dos Santos, J. Léonard, Junmin Wang, C. J. Barrelet, F. Perales, E. Rasel, C. S. Unnikrishnan, M. Leduc, and C. Cohen-Tannoudji. Bose-Einstein Condensation of Metastable Helium. *Phys. Rev. Lett.*, **86**, 3459, (2001).

[43] G. Modugno, G. Ferrari, G. Roati, R. J. Brecha, A. Simoni, and M. Inguscio. Bose-Einstein Condensation of Potassium Atoms by Sympathetic Cooling. *Science*, **294**, 1320, (2001).

[44] M. Edwards. The Bose-Einstein Condensation (BEC) Homepage at Georgia Southern University (GSU). *http://bec01.phy.gasou.edu/bec.html.*

[45] R. Grimm. Research groups working with atom traps. *http://www.uibk.ac.at/c/c7/c704/ultracold/atomtraps.html.*

[46] E. Fermi. Sulla quantizzazione del gas perfetto monoatomico. *Rend. Lincei*, **3**, 145, (1926).

[47] E. Fermi. Zur Quantelung das idealen einatomigen Gases. *Z. Phys.*, **36**, 902, (1926).

[48] I. F. Silvera and J. T. M. Walraven. Spin-polarized atomic hydrogen: A magnetic gas. *J. Appl. Phys.*, **52**, 2304, (1981).

[49] L. N. Cooper. Bound Electron Pairs in a Degenerate Fermi Gas. *Phys. Rev.*, **104**, 1189, (1956).

[50] J. Bardeen, L. N. Cooper, and J. R. Schrieffer. Theory of Superconductivity. *Phys. Rev.*, **108**, 1175, (1957).

[51] L. Spitzer. *Physics of Fully Ionized Gases.* Interscience, New York, (1962).

[52] R.E. Drullinger *et al. Appl. Phys.*, **22**, 365, (1980).

[53] D. J. Larson, J. C. Bergquist, J. J. Bollinger, Wayne M. Itano, and D. J. Wineland. Sympathetic cooling of trapped ions: A laser-cooled two-species nonneutral ion plasma. *Phys. Rev. Lett.*, **57**, 70, (1986).

[54] J. Kim, B. Friedrich, D. P. Katz, D. Patterson, J. D. Weinstein, R. DeCarvalho, and J. M. Doyle. Buffer-Gas Loading and Magnetic Trapping of Atomic Europium. *Phys. Rev. Lett.*, **78**, 3665, (1997).

[55] J. D. Weinstein, R. DeCarvalho, J. Kim, D. Patterson, B. Friedrich, and J. M. Doyle. Magnetic trapping of atomic chromium. *Phys. Rev. A*, **57**, (R3173), (1998).

[56] D. Egorov, J. D. Weinstein, D. Patterson, B. Friedrich, and J. M. Doyle. Spectroscopy of laser-ablated buffer-gas-cooled PbO at 4 K and the prospects for measuring the electric dipole moment of the electron. *Phys. Rev. A*, **63**, 030501(R), (2001).

[57] C. J. Myatt, E. A. Burt, R. W. Ghrist, E. A. Cornell, and C. E. Wieman. Production of Two Overlapping Bose-Einstein Condensates by Sympathetic Cooling. *Phys. Rev. Lett.*, **78**, 586, (1997).

[58] I. Bloch, M. Greiner, O. Mandel, T. W. Hänsch, and T. Esslinger. Sympathetic cooling of ^{85}Rb and ^{87}Rb. *Phys. Rev. A*, **64**, 021402(R), (2001).

[59] G. Delannoy, S. G. Murdoch, V. Boyer, V. Josse, P. Bouyer, and A. Aspect. Understanding the production of dual Bose-Einstein condensation with sympathetic cooling. *Phys. Rev. A*, **63**, 051602, (2001).

[60] B. DeMarco and D. S. Jin. Onset of Fermi Degeneracy in a Trapped Atomic Gas. *Science*, **285**, 1703, (1999).

[61] A. G. Truscott, K. E. Strecker, W. I. McAlexander, G. B. Partridge, and R. G. Hulet. Observation of Fermi Pressure in a Gas of Trapped Atoms. *Science*, **291**, 2570, (2001).

[62] M. Mudrich, S. Kraft, K. Singer, R. Grimm, A. Mosk, and M. Weidemüller. Sympathetic Cooling with Two Atomic Species in an Optical Trap. *submitted to Phys. Rev. Lett. arXiv:physics/0111213*, (2001).

[63] Z. Hadzibabic, C. A. Stan, K. Dieckmann, S. Gupta, M. W. Zwierlein, A. Görlitz, and W. Ketterle. Two-species mixture of quantum degenerate Bose and Fermi gases. *cond-mat/0112425*, (2001).

[64] S. R. Granade, M. E. Gehm, K. M. O'Hara, and J. E. Thomas. All-Optical Production of a Degenerate Fermi Gas. *Phys. Rev. Lett.*, **88**, 120405, (2002).

[65] G. Ferrari. Collisional relaxation in a fermionic gas. *Phys. Rev. A*, **59**, R4125, (1999).

[66] B. DeMarco, S. B. Papp, and D. S. Jin. Pauli Blocking of Collisions in a Quantum Degenerate Atomic Fermi Gas. *Phys. Rev. Lett.*, **86**, 5409, (2001).

[67] B. DeMarco and D. S. Jin. Exploring a quantum degenerate gas of fermionic atoms. *Phys. Rev. A Rapid Comm.*, **76**, 10, (1998).

[68] T. Busch, J. R. Anglin, J. I. Cirac, and P. Zoller. Inhibition of spontaneous emission in Fermi gases. *Europhys. Lett.*, **44**, 1, (1998).

[69] J. Ruostekoski and J. Javanainen. Optical Linewidth of a Low Density Fermi-Dirac Gas. *Phys. Rev. Lett.*, **82**, 4741, (1999).

[70] E. Tiesinga, B. J. Verhaar, and H. T. C. Stoof. Threshold and resonance phenomena in ultracold ground-state collisions. *Phys. Rev. A*, **47**, 4114, (1993).

[71] R. Combescot. Trapped ^{6}Li: A High T_C Superfluid? *Phys. Rev. Lett.*, **83**, 3766, (1999).

[72] M. Holland, S. J. J. M. F. Kokkelmans, M. L. Chiofalo, and R. Walser. Resonance Superfluidity in a Quantum Degenerate Fermi Gas. *Phys. Rev. Lett.*, **87**, 120406, (2001).

[73] R. G. Hulet. Scattering length of ^{7}Li $|F = 1, m_F = -1\rangle$ state is $a = 5.1\, a_0$. *private communication*, (2001).

[74] D. S. Petrov and G. V. Shlyapnikov. Interatomic collisions in a tightly confined Bose gas. *Phys. Rev. A*, **64**, 012706, (2001).

[75] Z. Akdeniz, P. Vignolo, A. Minguzzi, and M.P. Tosi. Phase separation in a boson-fermion mixture of Lithium atoms. *cond-mat/0112183*, (2001).

[76] K. Huang. *Statistical Mechanics*. Wiley, London, (1966).

[77] D. A. Butts and D. S. Rokhsar. Trapped Fermi gases. *Phys. Rev. A*, **55**, 4346, (1997).

[78] J. Schneider and H. Wallis. Mesoscopic Fermi gas in a harmonic trap. *Phys. Rev. A*, **57**, 1253, (1998).

[79] G. M. Bruum and K. Burnett. Interacting Fermi gas in a harmonic trapp. *Phys. Rev. A*, **58**, 2427, (1998).

[80] K. Mølmer. Bose Condensates and Fermi Gases at Zero Temperature. *Phys. Rev. Lett.*, **80**, 1804, (1998).

[81] R.G. Hulet, E.S. Hilfer, and D. Kleppner. Inhibited spontaneous emission by a Rydberg atom. *Phys. Rev. Lett.*, **55**, 2137, (1985).

[82] F. Dalfovo, S. Giorgini, L. P. Pitaevskii, and S. Stringari. Theory of Bose-Einstein condensation in trapped gases. *Rev. Mod. Phys.*, **71**, 463, (1999).

[83] R. Kaiser, C. Westbrook, and F. David. Coherent atomic matter waves. (2000).

[84] U. Ernst, J. Schuster, F. Schreck, A. Marte, A. Kuhn, and G. Rempe. Free expansion of a Bose-Einstein condensate from an Ioffe-Pritchard magnetic trap. *Appl. Phys. B*, **67**, 719, (1998).

[85] Yu. Kagan, E. L. Surkov, and G. V. Shlyapnikov. Evolution of a Bose gas in anisotropic time-dependent traps. *Phys. Rev. A*, **55**, 18, (1997).

[86] T.D. Lee, K. Huang, and C.N. Yang. Eigenvalues and Eigenfunctions of a Bose System of Hard Spheres and Its Low-Temperature Properties. *Phys. Rev.*, **106**, 1135, (1957).

[87] P. A. Ruprecht, M. J. Holland, K. Burnett, and M. Edwards. Time-dependent solution of the non-linear Schrödinger equation for Bose-condensed trapped neutral atoms. *Phys. Rev. A*, **51**, 4704, (1995).

[88] J.H. Thywissen, M. Olshanii, G. Zabow, M. Drndié, K.S. Johnson, R.M. Westervelt, and M. Prentiss. Microfabricated magnetic waveguides for neutral atoms. *Eur. Phys. J. D*, **7**, 361, (1999).

[89] D.S. Petrov, G.V. Shlyapnikov, and J.T.M. Walraven. Regimes of Quantum Degeneracy in Trapped 1D Gases. *Phys. Rev. Lett.*, **85**, 3745, (2000).

[90] D. S. Petrov, G. V. Shlyapnikov, and J. T. M. Walraven. Phase-Fluctuating 3D Bose-Einstein Condensates in Elongated Traps. *Phys. Rev. Lett.*, **87**, 050404, (2001).

[91] S. Dettmer, D. Hellweg, P. Ryytty, J. J. Arlt, W. Ertmer, D. S. Petrov K. Sengstock, G. V. Shlyapnikov, H. Kreutzmann, L. Santos, and M. Lewenstein. Observation of Phase Fluctuations in Elongated Bose-Einstein Condensates. *Phys. Rev. Lett.*, **87**, 160406, (2001).

[92] Y. Castin. 1D condensate wavefunction. *private communication*, (2001).

[93] G. P. Agrawal. *Nonlinear Fiber Optics.* Academic Press, San Diego, 2nd édition, 1995.

[94] J. S. Russell. Report on Waves. *Report of the fourteenth meeting of the British Association for the Advancement of Science, York, September 1844, page 311: "I was observing the motion of a boat which was rapidly drawn along a narrow channel by a pair of horses, when the boat suddenly stopped - not so the mass of water in the channel which it had put in motion; it accumulated round the prow of the vessel in a state of violent agitation, then suddenly leaving it behind, rolled forward with great velocity, assuming the form of a large solitary elevation, a rounded, smooth and well-defined heap of water, which continued its course along the channel apparently without change of form or diminution of speed. I followed it on horseback, and overtook it still rolling on at a rate of some eight or nine miles an hour, preserving its original figure some thirty feet long and a foot to a foot and a half in height. Its height gradually diminished, and after a chase of one or two miles I lost it in the windings of the channel. Such, in the month of August 1834, was my first chance interview with that singular and beautiful phenomenon which I have called the Wave of Translation"* .

[95] L. D. Carr, J. N. Kutz, and W. P. Reinhardt. Stability of stationary states in the cubic nonlinear Schrödinger equation: Applications to the Bose-Einstein condensate. *Phys. Rev. E*, **63**, 066604, (2001).

[96] S. Burger, L. D. Carr, P. Öhberg, K. Sengstock, and A. Sanpera. Generation and interaction of solitons in Bose-Einstein Condensates. *cond-mat/0201155*, (2002).

[97] D. S. Hall, M. R. Matthews, J. R. Ensher, C. E. Wieman, and E. A. Cornell. Dynamics of Component Separation in a Binary Mixture of Bose-Einstein Condensates. *Phys. Rev. Lett.*, **81**, 1539, (1998).

[98] J. Stenger, S. INouye, D.M. Stamper-Kurn, H.-J. Miesner, A.P. Chikkatur, and W. Ketterle. Spin domains in ground-state Bose-Einstein condensates. *Nature*, **396**, 345, (1998).

[99] L. Viverit, C. J. Pethick, and H. Smith. Zero-temperature phase diagram of binary boson-fermion mixtures. *Phys. Rev. A*, **61**, 053605, (2000).

[100] M. Tinkham. *Introduction to Superconductivity.* Robert E. Krieger publishing Company, (1975).

[101] H. T. C. Stoof. Macroscopic Quantum Tunneling of a Bose Condensate. *J. Stat. Phys.*, **87**, 1353, (1997).

[102] L. You and M. Marinescu. Prospects for p-wave paired Bardeen-Cooper-Schrieffer states of fermionic atoms. *Phys. Rev. A*, **60**, 2324, (1999).

[103] M. A. Baranov, Y. Kagan, and M. Kagan. On the possibility of a superfluid transition in a Fermi gas of neutral particles at ultra low temperatures. *Sov. Phys. JETP*, **64**, 301, (1996).

[104] H. Heiselberg, C. J. Pethick, H. Smith, and L. Viverit. Influence of Induced Interactions on the Superfluid Transition in Dilute Fermi Gases. *Phys. Rev. Lett.*, **85**, 2418, (2000).

[105] L.P. Gor'kov and T.K. Melik-Barkhudarov. *Sov. Phys. JETP*, **13**, 1018, (1961).

[106] G.M. Bruun and C.W. Clark. Detection of the BCS transition of a trapped Fermi Gas. *cond-mat/9906392*, (1999).

[107] W. Zhang, C. A. Sackett, and R. G. Hulet. Optical detection of a Bardeen-Cooper-Schrieffer phase transition in a trapped gas of fermionic atoms. *Phys. Rev. A*, **60**, 504, (1999).

[108] F. Weig and W. Zwerger. Optical detection of a BCS transition of lithium-6 in harmonic traps. *Europhys. Lett.*, **49**, 282, (2000).

[109] J. Ruostekoski. Optical response of a superfluid state in dilute atomic Fermi-Dirac gases. *Phys. Rev. A Rapid Comm.*, **60**, 1775, (1999).

[110] J. Ruostekoski. Scattering of light and atoms in a Fermi-Dirac gas with Bardeen-Cooper-Schrieffer pairing. *Phys. Rev. A*, **61**, 033605, (2000).

[111] P. Törmä and P. Zoller. Laser Probing of Atomic Cooper Pairs. *Phys. Rev. Lett.*, **85**, 487, (2000).

[112] D. M. Stamper-Kurn, A. P. Chikkatur, A. Görlitz, S. Inouye, S. Gupta, D. E. Pritchard, and W. Ketterle. Excitation of Phonons in a Bose-Einstein Condensate by Light Scattering. *Phys. Rev. Lett.*, **83**, 2876, (1999).

[113] A. P. Chikkatur, A. Görlitz, D. M. Stamper-Kurn, S. Inouye, S. Gupta, and W. Ketterle. Excitation of Phonons in a Bose-Einstein Condensate by Light Scattering. *Phys. Rev. Lett.*, **85**, 483, (2000).

[114] A. Minguzzi, G. Ferrari, and Y. Castin. Dynamic structure factor of a superfluid Fermi gas. *cons-mat/0103591*, (2001).

[115] M. A. Baranov and D. S. Petrov. Low-energy collective excitations in a superfluid trapped Fermi gas. *Phys. Rev. A Rapid Comm.*, **62**, 041601(R), (2000).

[116] A. Minguzzi and M. P. Tosi. Scissors mode in a superfluid Fermi gas. *cond-mat*, page 0005098, (2000).

[117] D. Guéry-Odelin and S. Stringari. Scissors Mode and Superfluidity of a Trapped Bose-Einstein Condensed Gas. *Phys. Rev. Lett.*, **83**, 4452, (1999).

[118] M. Farine, P. Schuck, and X. Vi nas. Moment of inertia of a trapped superfluid gas of atomic fermions. *Phys. Rev. A*, **62**, 013608, (2000).

[119] M.L. Chiofalo, S.J.J.M.F. Kokkelmans, J.N. Milstein, and M.J. Holland. Signatures of resonance superfluidity in a quantum Fermi gas. *cond-mat/0110119*, (2001).

[120] H. F. Hess. *Bull. Am. Phys. Soc.*, **30**, 854, (1985).

[121] H. F. Hess. Evaporative cooling of magnetically trapped and compressed spin-polarized hydrogen. *Phys. Rev. B*, **34**, 3476, (1986).

[122] N. Masuhara, J. M. Doyle, J. C. Sandberg, D. Kleppner, T. J. Greytak, H. F. Hess, and G. P. Kochanski. Evaporative Cooling of Spin-Polarized Atomic Hydrogen. *Phys. Rev. Lett.*, **61**, 935, (1988).

[123] C. C. Bradley, C. A. Sackett, and R. G. Hulet. Evidence of Bose-Einstein Condensation in an Atomic Gas with Attractive Interactions. *Phys. Rev. Lett.*, **75**, 1687, (1995).

[124] P. C. Haljan, I. Coddington, P. Engels, and E. A. Cornell. Driving Bose-Einstein-Condensate Vorticity with a Rotating Normal Cloud. *Phys. Rev. Lett.*, **87**, 210403, (2001).

[125] W. Ketterle and N. J. Van Druten. Evaporative cooling of trapped atoms. *Advances in atomic, molecular, and optical physics*, **37**, 181, (1996).

[126] J. Schuster, A. Marte, S. Amtage, B. Sang, , G. Rempe, and H. C. W. Beijerinck. Avalanches in a Bose-Einstein Condensate. *Phys. Rev. Lett.*, **87**, 170404, (2001).

[127] R.E. Drullinger *et al. Appl. Phys.*, **22**, 365, (1980).

[128] J. Stuhler, P. O. Schmidt, S. Hensler, J. Werner, J. Mlynek, and T. Pfau. Continuous loading of a magnetic trap. *Phys. Rev. A*, **64**, 031405(R), (2001).

[129] M. Marinescu and L. You. Controlling Atom-Atom Interaction at Ultralow Temperatures by dc Electric Fields. *Phys. Rev. Lett.*, **81**, 4596, (1998).

[130] D. Jin et al. Sympathetic cooling of ^{40}K with ^{87}Rb. *private communication*, (2001).

[131] J. Close et al. Sympathetic cooling of ^{40}K with ^{87}Rb. *private communication*, (2001).

[132] T. Loftus, J.R. Bochinski, and T.W. Mossberg. Simultaneous multi-isotope trapping of ytterbium. *Phys. Rev. A*, **63**, 053401, (2001).

[133] S. Grossmann and M. Holthaus. On Bose-Einstein condensation in harmonic traps. *Phys. Lett. A*, **208**, 188, (1995).

[134] M. Li, Z. Yan, J. Chen, L. Chen, and C. Chen. Thermodynamic properties of an ideal Fermi gas in an external potential with $U = br^t$ in any dimensional space. *Phys. Rev. A*, **58**, 1445, (1998).

[135] E. Timmermans and R. Côté. Superfluidity in Sympathetic Cooling with Atomic Bose-Einstein Condensates. *Phys. Rev. Lett.*, **80**, 3419, (1998).

[136] E. Timmermans. Degenerate Fermion Gas Heating by Hole Creation. *Phys. Rev. Lett.*, **87**, 240403, (2001).

[137] O. J. Luiten, M. W. Reynolds, and J. T. M. Walraven. Kinetic theory of evaporative cooling of a trapped gas. *Phys. Rev. A*, **53**, 381, (1996).

[138] C. Cohen-Tannoudji, B. Diu, and F. Laloë. *Mécanique Quantique.* Hermann, (1973).

[139] J. Vigué. Possibility of applying laser-cooling techniques to the observation of collective quantum effects. *Phys. Rev. A*, **34**, 4476, (1986).

[140] C. Cohen-Tannoudji. Condensation de gaz atomiques dilués. *Cours de physique atomique et moléculaire, Collège de France, année scolaire 98-99.*

[141] E. R. I. Abraham, C. A. Sackett, and R. G. Hulet. Triplet s-wave resonance in ^{6}Li collisions and scattering lengths of 6Li and ^{7}Li. *Phys. Rev. A (Rapid. Comm.)*, **55**, 3299, (1997).

[142] S. Inouye, M. R. Andrews, J. Stenger, H.-J. Miesner, D. M. Stamper-Kurn, and W. Ketterle. Observation of Feshbach resonances in a Bose-Einstein condensate. *Nature*, **392**, 151, (1998).

[143] J. L. Roberts, N. R. Claussen, James P. Burke Jr., Chris H. Greene, E. A. Cornell, and C. E. Wieman. Resonant Magnetic Field Control of Elastic Scattering in Cold ^{85}Rb. *Phys. Rev. Lett.*, **81**, 5109, (1998).

[144] J. L. Roberts, N. R. Claussen, James P. Burke Jr., Chris H. Greene, E. A. Cornell, and C. E. Wieman. Resonant Magnetic Field Control of Elastic Scattering in Cold ^{85}Rb. *Phys. Rev. Lett.*, **81**, 5109, (1998).

[145] S. L. Cornish, N. R. Claussen, J. L. Roberts, E. A. Cornell, and C. E. Wieman. Stable ^{85}Rb Bose-Einstein Condensates with Widely Tunable Interactions. *Phys. Rev. Lett.*, **85**, 1795, (2000).

[146] C. Chin, V. Vuleti, A. J. Kerman, and S. Chu. High Resolution Feshbach Spectroscopy of Cesium. *Phys. Rev. Lett.*, **85**, 2717, (2000).

[147] P. J. Leo, C. J. Williams, and P. S. Julienne. Collision Properties of Ultracold ^{133}Cs Atoms. *Phys. Rev. Lett.*, **85**, 2721, (2000).

[148] P. J. Leo, P. S. Julienne, F. H. Mies, and C. J. Williams. Collisional Frequency Shifts in ^{133}Cs Fountain Clocks. *Phys. Rev. Lett.*, **86**, 3743, (2001).

[149] J. Stenger, S. Inouye, M. R. Andrews, H.-J. Miesner, D. M. Stamper-Kurn, and W. Ketterle. Strongly Enhanced Inelastic Collisions in a Bose-Einstein Condensate near Feshbach Resonances. *Phys. Rev. Lett.*, **82**, 2422, (1999).

[150] P. O. Fedichev, M. W. Reynolds, and G. V. Shlyapnikov. Three-Body recombination of ultracold atoms to a weakly bound s level. *Phys. Rev. Lett.*, **77**, 2921, (1996).

[151] B. D. Esry, Chris H. Greene, and James P. Burke Jr. Recombination of Three Atoms in the Ultracold Limit. *Phys. Rev. Lett.*, **83**, 1751, (1999).

[152] A. J. Moerdijk, B. J. Verhaar, and A. Axelsson. Resonances in ultracold colllisions of ^{6}Li,^{7}Li, and ^{23}Na. *Phys. Rev. A*, **51**, 4852, (1995).

[153] F. A. van Abeelen, B. J. Verhaar, and A. J. Moerdijk. Sympathetic cooling of ^{6}Li atoms. *Phys. Rev. A*, **55**, 4377, (1997).

[154] Gabriele Ferrari. *Piégeage simultané des isotopes fermionique et bosonique du lithium*
Étude théorique de la relaxation collisionnelle dans un gaz de Fermi dégénéré. Thèse de Doctorat, Université Paris VI, july 2000.

[155] R. Rhodes. *The making of the atomic bomb.* Touchstone, (1986).

[156] V. Venturi and C.Williams. Feshbach resonances in lithium. *private communication.*

[157] A. Mosk, S. Jochim, H. Moritz, Th. Elsser, M. Weidemller, and R. Grimm. Resonator-enhanced optical dipole trap for fermionic lithium atoms. *Optics Letters*, **26**, 1837, (2001).

[158] William D. Phillips and Harold Metcalf. Laser Deceleration of an Atomic Beam. *Phys. Rev. Lett.*, **48**, 596, (1982).

[159] G. Ferrari, M.-O. Mewes, F. Schreck, and C. Salomon. High-power multiple-frequency narrow-linewidth laser source based on a semiconductor tapered amplifier. *Optics Letters*, **24**, 151, (1999).

[160] H. Katori, T. Ido, Y. Isoya, and M. Kuwata-Gonokami. Magneto-Optical Trapping and Cooling of Strontium Atoms down to the Photon Recoil Temperature. *Phys. Rev. Lett.*, **82**, 1116, (1999).

[161] E. Arimondo, W. D. Phillips, and F. Strumia. *Proceeding of the International School of Physics "Enrico Fermi", Course CXVIII: "Laser Manipulation of Atoms and Ions".* North Holland, Amsterdam, (1992).

[162] W. Petrich, M. Anderson, J. Ensher, and E. Cornell. Stable, Tightly Confining Magnetic Trap for Evaporative Cooling of Neutral Atoms. *Phys. Rev. Lett.*, **74**, 3352, (1995).

[163] D. E. Pritchard. Cooling of neutral atoms in a magnetic trap for precision spectroscopy. *Phys. Rev. Lett.*, **51**, 1336, (1983).

[164] T. Esslinger, I. Bloch, and T. W. Hänsch. Bose-Einstein condensation in a quadrupole-Ioffe-configuration trap. *Phys. Rev. A*, **58**, R2664, (1998).

[165] J. J. Tollett, C. C. Bradley, C. A. Sackett, and R. G. Hulet. Permanent magnet trap for cold atoms. *Phys. Rev. A Rapid Comm.*, **51**, 22, (1995).

[166] B. Desruelle, V. Boyer, P. Bouyer, G. Birkl, M. Lécrivain, F. Alves, C.I. Westbrook, and A. Aspect. Trapping cold neutral atoms with an iron-core electromagnet. *Eur. Phys. D*, **1**, 255, (1998).

[167] Powerex. Driving IGBT Modules. *Application Note of Powerex http://www.pwrx.com.*

[168] Powerex. General Considerations: IGBT & IPM modules. *Application Note of Powerex http://www.pwrx.com.*

[169] S. Chu, J. E. Bjorkholm, A. Ashkin, and A. Cable. Experimental Observation of Optically Trapped Atoms. *Phys. Rev. Lett.*, **57**, 314, (1986).

[170] R. Grimm, M. Weidemueller, and Y. Ovchinnikov. Optical dipole traps for neutral atoms. *Adv. at. mol. opt. phys.*, **42**, 95, (2000).

[171] K. L. Corwin, S. J. M. Kuppens, D. Cho, and C. E. Wieman. Spin-Polarized Atoms in a Circularly Polarized Optical Dipole Trap. *Phys. Rev. Lett.*, **83**, 1311, (1999).

[172] A.E. Siegman. *Lasers.* University Science Books, Mill Valley, CA, (1986).

[173] D. Cho. *J. Korean Phys. Soc.*, **30**, 373, (1997).

[174] N.F. Ramsey. *Molecular Beams.* Clarendon Press Ed., Oxford, (1969).

[175] A. Rauschenbeutel, G. Nogues, S. Osnaghi, P. Bertet, M. Brune, J. M. Raimond, and S. Haroche. Coherent Operation of a Tunable Quantum Phase Gate in Cavity QED. *Phys. Rev. Lett.*, **83**, 5166, (1999).

[176] Mark A. Kasevich, Erling Riis, Steven Chu, and Ralph G. DeVoe. rf spectroscopy in an atomic fountain. *Phys. Rev. Lett.*, **63**, 612, (1989).

[177] M.R. Andrews, M.-O. Mewes, N.J. van Druten, D.S. Durfee, D.M. Kurn, and W. Ketterle. Direct, Nondestructive Observation of a Bose Condensate. *Science*, **273**, 84, (1996).

[178] M.-O. Mewes, G. Ferrari, F. Schreck, A. Sinatra, and C. Salomon. Simultaneous magneto-optical trapping of two lithium isotopes. *Phys. Rev. A*, **61**, 11403, (1999).

[179] D. M. Stamper-Kurn, H.-J. Miesner, A. P. Chikkatur, S. Inouye, J. Stenger, and W. Ketterle. Reversible Formation of a Bose-Einstein Condensate. *Phys. Rev. Lett.*, **81**, 2194, (1998).

[180] J. Dalibard and C. Cohen-Tannoudji. Laser cooling below the Doppler limit by polarization gradients: simple theoretical models. *J. Opt. Soc. Am. B*, **6**, 2023, (1989).

[181] E. L. Surkov, J. T. M. Walraven, and G. V. Shlyapnikov. Collisionless motion and evaporative cooling of atoms in magnetic traps. *Phys. Rev. A*, **53**, 3403, (1996).

[182] B. Desruelle, V. Boyer, S. G. Murdoch, G. Delannoy, P. Bouyer, , A. Aspect, and M. Lécrivain. Interrupted evaporative cooling of ^{87}Rb atoms trapped in a high magnetic field. *Phys. Rev. A*, **60**, R1759, (1999).

[183] E. Arimondo, M. Inguscio, and P. Violino. *Rev. Mod. Phys.*, **49**, 31, (1977).

[184] C. C. Bradley, C. A. Sackett, and R. G. Hulet. Bose-Einstein Condensation of Lithium : Obervation of Limited Condensate Number. *Phys. Rev. Lett.*, **78**, 985, (1997).

[185] C. A. Sackett, H. T. C. Stoof, and R. G. Hulet. Growth and Collapse of a Bose-Einstein Condensate with Attractive Interactions. *Phys. Rev. Lett.*, **80**, 2031, (1998).

[186] C. A. Sackett, J. M. Gerton, M. Welling, and R. G. Hulet. Measurements of Collective Collapse in a Bose-Einstein Condensate with Attractive Interactions. *Phys. Rev. Lett.*, **82**, 876, (1999).

[187] F. A. van Abeelen and B. J. Verhaar. Time-Dependent Feshbach Resonance Scattering and Anomalous Decay of a Na Bose-Einstein Condensate. *Phys. Rev. Lett.*, **83**, 1550, (1999).

[188] H. Saito and M. Ueda. Intermittent Implosion and Pattern Formation of Trapped Bose-Einstein Condensates with an Attractive Interaction. *Phys. Rev. Lett.*, **86**, 1406, (2001).

[189] A. J. Moerdijk and B. J. Verhaar. Collisional two- and three-body decay rates of dilute quantum gases at ultralow temperatures. *Phys. Rev. A*, **53**, R19, (1996).

[190] J. M. Gerton, C. A. Sackett, B. J. Frew, and R. G. Hulet. Dipolar relaxation collisions in magnetically trapped ^{7}Li. *Phys. Rev. A*, **59**, 1514, (1999).

[191] J. R. Rubbmark, M. M. Kash, M. G. Littman, and D. Kleppner. Dynamical effects at avoided level crossings: A study of the Landau-Zener effect using Rydberg atoms. *Phys. Rev. A*, **23**, 3107, (1981).

[192] L. Khaykovich, F. Schreck, G. Ferrari, T. Bourdel, J. Cubizolles, L.D. Carr, Y. Castin, and C. Salomon. Formation of a Matter-Wave Bright Soliton. *submitted to Science*, (2002).

[193] L. Viverit, S. Giorgini, L. P. Pitaevskii, and S. Stringari. Adiabatic compression of a trapped Fermi gas. *Phys. Rev. A*, **63**, 033603, (2001).

.

Abstract: This thesis presents studies of quantum degenerate atomic gases of fermionic ^{6}Li and bosonic ^{7}Li. Degeneracy is reached by evaporative cooling of ^{7}Li in a strongly confining magnetic trap. Since at low temperatures direct evaporative cooling is not possible for a polarized fermionic gas, ^{6}Li is sympathetically cooled by thermal contact with ^{7}Li. In a first series of experiments both isotopes are trapped in their low-field seeking higher hyperfine states. A Fermi degeneracy of $T/T_F = 0.25(5)$ is achieved for 10^5 fermions. For more than ~ 300 atoms, the ^{7}Li condensate collapses, due to the attractive interatomic interaction in this state. This limits the degeneracy reached for both species. To overcome this limit, in a second series of experiments ^{7}Li and ^{6}Li atoms are transferred to their low field seeking lower hyperfine states, where the boson-boson interaction is repulsive but weak. The inter-isotope collisions are used to thermalize the mixture. A ^{7}Li Bose-Einstein condensate (BEC) of 10^4 atoms immersed in a Fermi sea is produced. The BEC is quasi-one-dimensional and the thermal fraction can be negligible. The measured degeneracies are $T/T_C = T/T_F = 0.2(1)$. The temperature is measured using the bosonic thermal fraction, which vanishes at the lowest temperatures, limiting our measurement sensitivity. In a third series of experiments, the bosons are transferred into an optical trap and their internal state is changed to $|F = 1, m_F = 1\rangle$, the lowest energy state. A Feshbach resonance is detected and used to produce a BEC with tunable atomic interactions. When the effective interaction between atoms is tuned to be small and attractive, we observe the formation of a matter-wave bright soliton. Propagation of the soliton without spreading over a macroscopic distance of 1.1 mm is observed.

Keywords: Bose-Einstein condensation, Fermi sea, degenerate quantum gases, soliton, lithium, cold atoms, magnetic trapping, optical trapping, magneto-optical trapping, evaporative cooling, sympathetic cooling

Cette thèse décrit l'étude des gaz de fermions ^{6}Li et de bosons ^{7}Li dans le régime quantique à très basse température. Le refroidissement est obtenu par évaporation du ^{7}Li dans un piège magnétique très confinant. Puisque le refroidissement évaporatif d'un gaz de fermion polarisé est quasiment impossible, le ^{6}Li est refroidi sympathiquement par contact thermique avec le ^{7}Li. Dans une première série d'expériences, les propriétés des gaz quantiques dans les états hyperfins les plus élevés, piégés magnétiquement, sont étudiées. Un gaz de 10^5 fermions a une température de 0.25(5) fois la température de Fermi (T_F) est obtenu. L'instabilité du condensat pour plus de 300 atomes condensés, à cause des interactions attractives, limite la dégénérescence que l'on peut atteindre. Pour s'affranchir de cette limite, une autre série d'expérience est menée dans les états hyperfins bas, piégeable magnétiquement, où les interactions entre bosons sont faiblement répulsives. Les collisions inter-isotopiques permettent alors la thermalisation du mélange. Le mélange d'un condensat de Bose-Einstein (CBE) de ^{7}Li et d'un mer de Fermi de ^{6}Li est produit. Le condensat est quasi unidimensionnel et la fraction thermique peut être négligeable. La dégénérescence atteinte correspond à $T/T_C = T/T_F = 0.2(1)$. La température est mesurée à partir de la fraction thermique des bosons qui disparaît aux plus basses températures, et limite notre précision de mesure. Dans une troisième série d'expérience, les bosons sont transférés dans un piège optique, et placé dans l'état interne $|F = 1, m_F = 1\rangle$, l'état fondamental pour les bosons. Une résonance de Feshbach est repérée puis exploitée pour former un condensai où les interactions sont ajustables. Quand les interactions effectives entre les atomes sont attractives, on observe la formation d'un soliton brillant de matière. La propagation de ce soliton sans dispersion sur une distance de 1.1 mm est observée.

Mots clés: condensation de Bose-Einstein, mer de Fermi, gaz quantiques dégénérés, soliton, lithium, atomes froids, piégeage magnétique, piégeage optique, piège magnéto optique, refroidissement évaporative, refroidissement sympathique